INTEGRATED AERODYNAMIC AND CONTROL SYSTEM DESIGN OF OBLIQUE WING AIRCRAFT

A DISSERTATION
SUBMITTED TO THE DEPARTMENT OF AERONAUTICS AND ASTRONAUTICS
AND THE COMMITTEE ON GRADUATE STUDIES
OF STANFORD UNIVERSITY
IN PARTIAL FULFILLMENT OF THE REQUIREMENTS
FOR THE DEGREE OF
DOCTOR OF PHILOSOPHY

By
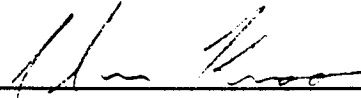Stephen James Morris
January 1990

INTEGRATED AERODYNAMIC AND CONTROL SYSTEM DESIGN OF OBLIQUE WING AIRCRAFT

A DISSERTATION
SUBMITTED TO THE DEPARTMENT OF AERONAUTICS AND ASTRONAUTICS
AND THE COMMITTEE ON GRADUATE STUDIES
OF STANFORD UNIVERSITY
IN PARTIAL FULFILLMENT OF THE REQUIREMENTS
FOR THE DEGREE OF
DOCTOR OF PHILOSOPHY

By
Stephen James Morris
January 1990

I certify that I have read this thesis and that in my opinion it is fully adequate, in scope and in quality, as a dissertation for the degree of Doctor of Philosophy.

_____

Ilan Kroo (Principal Advisor)

I certify that I have read this thesis and that in my opinion it is fully adequate, in scope and in quality, as a dissertation for the degree of Doctor of Philosophy.

_____

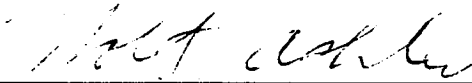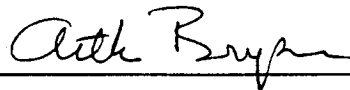Holt Ashley

I certify that I have read this thesis and that in my opinion it is fully adequate, in scope and in quality, as a dissertation for the degree of Doctor of Philosophy.

_____

Arthur Bryson

Approved for the University Committee on Graduate Studies:

_____

Dean of Graduate Studies

Abstract

An efficient high speed aircraft design must achieve a high lift to drag ratio at transonic and supersonic speeds. In 1952 Dr. R. T. Jones proved that for any flight Mach number minimum drag at a fixed lift is achieved by an elliptic wing planform with an appropriate oblique sweep angle. Since then, wind tunnel tests and numerical flow models have confirmed that the compressibility drag of oblique wing aircraft is lower than similar symmetrical sweep designs.

At oblique sweep angles above thirty degrees the highly asymmetric planform gives rise to aerodynamic and inertia couplings which affect stability and degrade the aircraft's handling qualities. In the case of the NASA-Rockwell Oblique Wing Research Aircraft, attempts to improve the handling qualities by implementing a stability augmentation system have produced unsatisfactory results because of an inherent lack of controllability in the proposed design. The present work focuses on improving the handling qualities of oblique wing aircraft by including aerodynamic configuration parameters as variables in the control system synthesis to provide additional degrees of freedom with which to further decouple the aircraft's response. Handling qualities are measured using a quadratic cost function identical to that considered in optimal control problems, but the controller architecture is not restricted to full state feedback. An optimization procedure is used to simultaneously solve for the aircraft configuration and control gains which maximize a handling qualities measure, while meeting imposed constraints on trim. In some designs wing flexibility is also modeled and reduced order controllers are implemented. Oblique wing aircraft synthesized by this integrated design method show significant improvement in handling qualities when compared to the originally proposed closed loop aircraft.

The integrated design synthesis method is then extended to show how handling qualities may be traded for other types of mission performance (drag, weight, etc.). Examples are presented which show how performance can be maximized while maintaining a desired level of handling quality.

Acknowledgements

I consider myself fortunate to have had Professor Ilan Kroo as my advisor during my graduate studies at Stanford. His expert advice and creative approach to problem solving helped me throughout my research. Few students are lucky enough to have an advisor who is not only an excellent teacher but is also a good friend. Now that my graduate studies are finished I will miss our trips to the mountains where we would hang glide and discuss airplanes for many hours.

My father instilled in me the importance of an education. He passed away during my first year of graduate study and would have very much liked to see me finish this work. I am indebted to him for supporting and encouraging me to continue with higher education. My sister , mother, and grandmother have been a major source of moral support in the years since my father's death.

The most difficult part of being a graduate student is surviving the many lonely times when one feels isolated from a world which seemingly could care less about the detailed study of a specific topic. I am thankful for the few close friends I have made while at Stanford. Without their friendship it would have been impossible to complete this thesis. I would like to mention some of their names here: Darrell and Cindy Hill, Ilan and Sharon Kroo, John and Judy Gallman, Geoff Phipps, Fred Vaachss, Chris Uhlik and Kathy Baganoff, Alec Proudfoot, Pat and Rose Hayes.

Table of Contents

List of Tables

List of Figures

List of Principal Symbols

[A]	dynamics matrix
AR	aspect ratio
A.C.	aerodynamic center
[AIC]	aerodynamic influence coefficient matrix
b	wingspan
{B}	boundary condition vector, Eq. 2.20
[B]	control input matrix
bref	reference span
b_s	wing structural span
c	local wing chord
C.G.	center of gravity
C.M.	mass center
C/4	wing quarter chord
C_L	lift coefficient
C_Y	sideforce coefficient
C_D	drag coefficient
C_l	rolling moment coefficient, section lift coefficient
C_M	pitching moment coefficient
C_N	yawing moment coefficient
C_X	X- aerodynamic force coefficient
C_Z	Z - aerodynamic force coefficient
C_{Di}	induced drag coefficient
$C_{L\alpha}$	lift curve slope
$C_{Y\alpha}$	sideforce coefficient derivative w.r.t. angle of attack
$C_{l\alpha}$	rolling moment coefficient derivative w.r.t. angle of attack
$C_{N\alpha}$	yawing moment coefficient derivative w.r.t. angle of attack
$C_{M\alpha}$	pitching moment coefficient derivative w.r.t. angle of attack
{d}	control vector

E	modulus of elasticity
EI	bending stiffness
e	span efficiency factor
$\{F\}$	total force vector $\{F_x, F_y, F_z\}$
f_i	ith bending mode shape function
g	gravitational acceleration
g_y	lateral acceleration
g_z	normal acceleration
I_{xx}, I_{xy}, etc.	inertia tensor elements
I_{11}, I_{101}, etc.	spanwise wing flexibility integral, Eq. 6.1 - 6.48
[I]	identity matrix
J_d	dynamic cost
J_{tot}	total cost
J_{nd}	non-dynamic cost
[K]	controller gain matrix
$[K_{ff}]$	feedforward gain matrix
$[K_{pc}]$	pre-compensator gain matrix
$[K_{fc}]$	feedback compensator gain matrix
K_d	dynamic cost weighting factor
L	aerodynamic lift, Eq. 2.4, rolling moment
$L_{(...)}$	change in rolling moment w.r.t. (...), Eq. 3.14
$\{M\}$	total moment vector $\{M_x, M_y, M_z\}$
M	pitching moment, Mach number, total mass, Eq. 6.1 - 6.49
$M_{(...)}$	change in pitching moment w.r.t. (...), Eq. 3.14
M_w	wing total mass, Eq. 6.1 - 6.49
m	mass per unit span
N	yawing moment
$N_{(...)}$	change in yawing moment w.r.t. (...), Eq. 3.14
N.A.	neutral axis
n	unit normal vector
p	x-body axis angular velocity (roll rate)
P.F.	penalty function

q	y-body axis angular velocity (pitch rate), dynamic pressure
$[Q]$	output error weighting matrix
Q_{Ni}	ith non-conservative generalized force
q_i	ith generalized coordinate, Eq. 6.1 - 6.48
r	z-body axis angular velocity (yaw rate)
$[R]$	control effort weighting matrix
R^{cm-p}	distance from the undeformed aircraft C.M. to material point (p)
S_{ref}	reference area
S_w	wing area
S'	spanwise location along the neutral axis
$T_{(...)-(...)}$	coordinate transform matrix
u	x-body axis perturbation velocity
U_o	nominal x component of the freestream velocity
u_o	nominal x component of the inertial velocity
U	potential energy, Eq. 6.1 - 6.48
u_i	ith generalized speed
$\{u\}$	controls vector
v	y-body axis perturbation velocity
$\{V\}$	local flowfield velocity vector, Eq. 2.17
V_0	freestream velocity
V_N	freestream velocity component normal to the C/4
V_T	freestream velocity component tangential to the C/4
V	inertial velocity
$[VIC]_{(...)}$	velocity influence coefficient matrix, (...) component
w	z-body axis perturbation velocity
w_o	nominal z component of the inertial velocity
$\{x\}$	state vector
X_{pw}	wing pivot location along wing root chord
X_{pf}	wing pivot location along fuselage
$\{y\}$	output vector
α	angle of attack
β	angle of sideslip

Δ	vortex filament length
$\{\delta\}$	control vector
$\{\varepsilon\}$	output error vector
ε	command washout pole location
Φ	velocity potential
ϕ	roll Euler angle
ϕ_b	wing bank angle
$[\Gamma]$	vortex filament circulation strength
η_i	ith mode shape amplitude
Λ	oblique wing sweep angle
θ	pitch Euler angle
$\theta_{1,2}$	wing pivot axis Euler angles
ρ	air density, material density, Eq. 6.1 - 6.48
$\{\omega\}$	angular velocity vector
ψ	yaw Euler angle
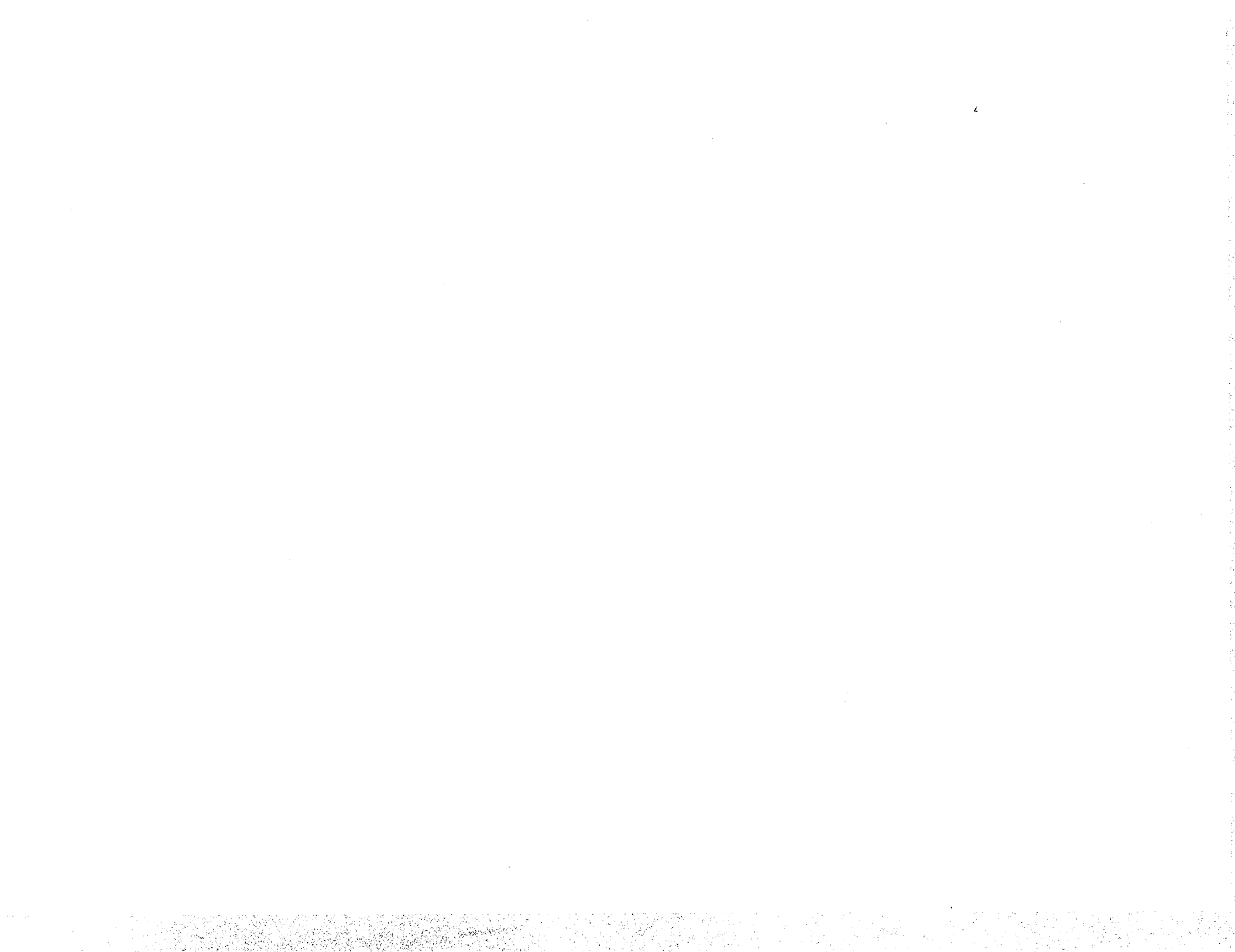
Chapter 1

Introduction

For reduced operating cost, an efficient high speed aircraft design must achieve a high lift to drag ratio at transonic and possibly supersonic speeds. In 1952 Dr. R. T. Jones proved that for any flight Mach number, minimum drag at a fixed lift is achieved by an elliptic wing planform with an appropriate oblique sweep angle. Since then, wind tunnel tests and numerical flow models have confirmed that the compressibility drag of oblique wing aircraft is lower than similar symmetrical sweep designs (Fig. 1.1). The advantages of oblique wing sweep extend beyond drag reduction. High speed aircraft designs must achieve a compromise between the conflicting demands of performance in the subsonic flight regime (i.e. takeoff, climb to cruise, and landing) and reduced compressibility drag at transonic and supersonic speeds. Configurations which employ variable wing sweep often show improved performance when the subsonic and supersonic performance requirements are stringent. The oblique wing configuration is ideally suited for variable sweep because only a single wing pivot loaded primarily in tension is required (Fig. 1.2), whereas symmetric variable sweep configurations require two pivots, each loaded in bending and torsion by its respective wing panel. As a result, symmetric variable sweep designs suffer increased complexity and structural weight when compared with oblique designs. Kroo [Ref. 1] and Nelms [Ref. 2] describe in greater detail these and other advantages of the oblique wing configuration and give a more complete historical description of the concept's evolution. A summary of the key advantages are listed below.

Advantages of Oblique Wing Configurations

1) Reduced transonic and supersonic drag
2) Reduced structural weight for a variable sweep configuration
3) Reduced aerodynamic center shift as wing is swept
4) Lower sonic boom strength due to reduced wave drag
5) Low storage space requirements if wing is overswept for storage

Despite the advantages of reduced compressibility drag and variable wing sweep with low structural weight, no oblique wing aircraft has achieved operational status. Several unmanned demonstrators have been flown [Ref. 2] to prove the feasibility of the asymmetric configuration. A subsonic manned demonstrator, the AD-1, was built and flown by NASA in 1979 to evaluate the handling qualities with oblique wing sweep. Flight tests of radio controlled models and remotely piloted vehicles (RPV's) (Fig. 1.5) indicated that aircraft with oblique wing sweep as high as 65 degrees could be flown without a stability augmentation system. Subsequent flight testing of the AD-1 proved that, although the AD-1 could be flown safely, the handling qualities deteriorated rapidly as oblique sweep and flight dynamic pressure increased [Ref. 3]. Aerodynamic and inertia couplings inherent to the design's asymmetry cause the handling qualities to degrade. A feasible oblique wing design would therefore require a stability augmentation system (SAS) to restore acceptable handling qualities over the flight envelope. From 1984 - 1988 NASA and Rockwell studied the possibility of converting NASA's F-8 fly-by-wire research aircraft into a supersonic oblique wing demonstrator which would investigate handling qualities with an onboard SAS.

The F-8 Oblique Wing Research Aircraft (OWRA) was designed to operate at Mach numbers as high as 1.6 and oblique sweep angles up to 65 degrees. Although the OWRA has not yet flown, estimates of its closed loop handling qualities were obtained from piloted flight simulations conducted in NASA's Vertical Motion Simulator (VMS) [Ref. 4]. A SAS designed by Honeywell [Ref. 5] using a 'loop shaping' technique was implemented in the simulation trials. Pilots flew the aircraft through various maneuvers including abrupt pitch-ups and wind up turns and issued Cooper Harper ratings ranging from 3 (acceptable) to 7 (unacceptable) for the tasks performed. Pilots were most critical of the severe lateral accelerations during pitch maneuvers and the asymmetry in roll tendencies during turns. In general, handling quality ratings decreased with increasing oblique sweep and flight dynamic pressure. The studies showed that even with a SAS onboard the OWRA lacked sufficient controllability to achieve acceptable handling qualities. The OWRA configuration must be changed to improve its controllability, but the impact of aerodynamic and inertia coupling on handling qualities is non-intuitive and therefore complicates the redesign procedure.
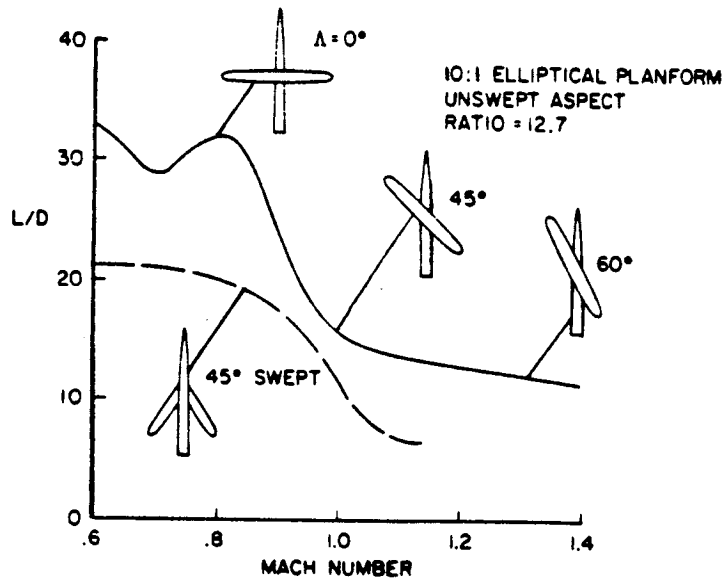
Figure 1.1 Maximum lift to drag ratio, oblique wing vs. symmetric sweep
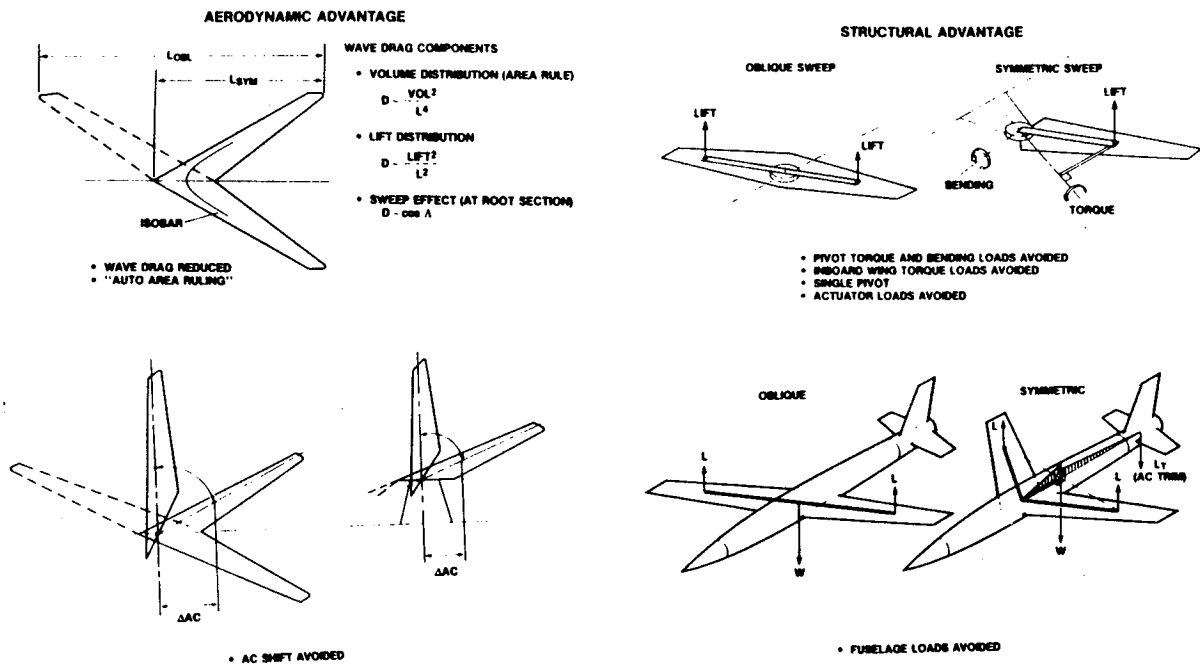
Figure 1.2 Summary of oblique wing advantages

3

The VMS studies of the F-8 OWRA did not account for the influences of elastic wing deformation on the aircraft's dynamic response. Flight tests of the AD-1 subsonic manned demonstrator showed that wing flexibility can significantly influence the aerodynamic coupling and in some cases reverse the coupling present in the rigid aircraft [Ref. 6]. In addition to influencing handling qualities, the combination of wing elasticity and planform asymmetries leads to unusual modes of aeroelastic instability. Jones and Nisbet [Ref. 7] studied a simple mathematical model for an elastic oblique wing with infinite roll degree-of-freedom. Previous to their study, designers felt that oblique wing aeroelastic stability would be limited by the divergence speed of the forward swept wing panel. Jones and Nisbet showed that the aeroelastic instability was not a divergence, but a flutter mode consisting of combined wing bending and fuselage rolling motion. Most significantly, this instability occurs at a dynamic pressure considerably higher than the clamped divergence dynamic pressure of the forward swept wing panel.

The success of the oblique wing concept depends upon improving the aircraft's closed loop handling qualities without increasing its drag or structural weight significantly. This thesis will show how this can be achieved and will also introduce a new approach to the integrated design of aircraft and their control system. Improving the handling qualities of oblique wing aircraft is a highly integrated design problem because the disciplines of aerodynamics, structures, and controls must be considered simultaneously to evaluate performance. A design synthesis which accounts for these effects and systematically alters the configuration of a proposed oblique wing design to improve its handling qualities is presented in this work.

The integrated design of aircraft and their control systems has been previously investigated by Zeiler and Weisshaar [Ref. 8] and Sakawi et. al. [Ref. 9]. In both of these works handling qualities are measured in terms of a dynamic cost function identical to that used in optimal control regulator theory (LQR design). The design variables which define the aircraft's configuration are treated as additional degrees of freedom with which to further improve the aircraft's handling qualities. Sakawi et al. optimized the wing and tail geometry of an actively-controlled aircraft excited by gust disturbances. The synthesis assumed a full-state feedback control architecture and used a random search procedure to solve for the
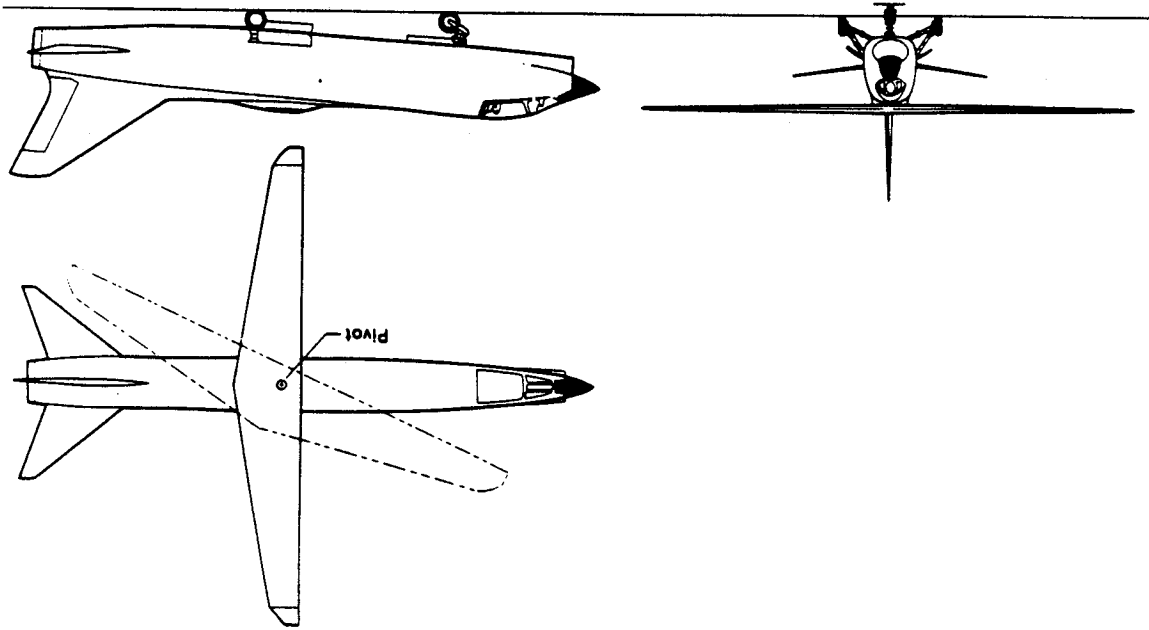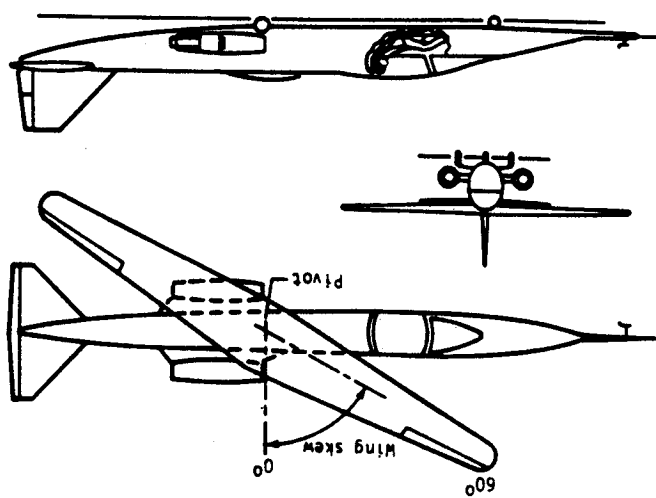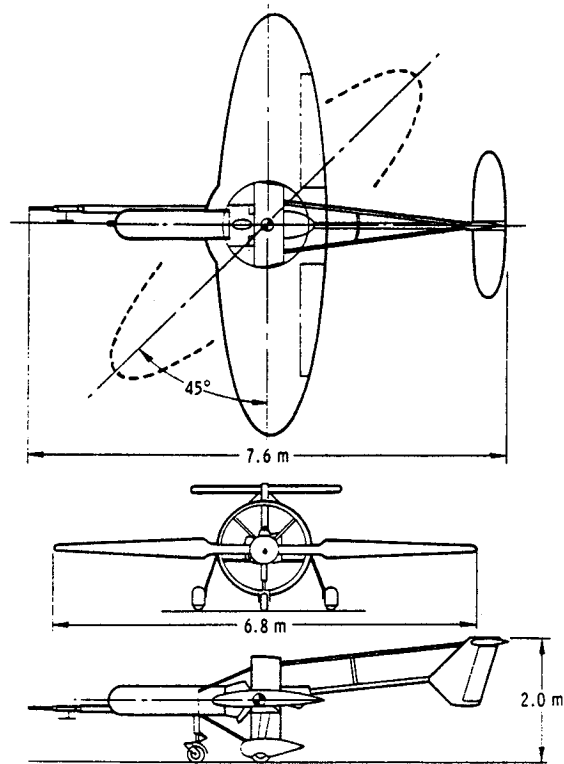
Figure 1.5 Oblique wing RPV 3-view

global minimum. Zeiler and Weisshaar describe the integrated design of a four degree-of-freedom aeroservoelastic system. The design variables consisted of the elastic axis location and the full state feedback control gains. A multi-level linear decomposition scheme was used to solve for the optimal system variables.

In the work presented here, an integrated synthesis procedure is extended to handle any linear control system architecture including reduced-order controllers and passive (no controller) designs. The procedure is used to optimize the system commanded response as well as its unforced response. Multidisciplinary performance indices are considered, illustrating the trade-offs between handling qualities and other measures of performance. Chapter 4 introduces the integrated design procedure and demonstrates its application in two example syntheses: the design of a wing-tail system for minimum trimmed drag with handling quality constraints and the design of a tailless aircraft for minimum weight with aeroelastic constraints. The results show how that this method can solve a variety of highly integrated problems and achieve performance that sequential design procedures would have overlooked.

6

Before an integrated design procedure can be implemented, all of the analyses required to calculate performance (given the design variables) must be available. Aerodynamic, controls, and aeroelastic analyses used to model the F-8 OWRA are described in the initial chapters of this thesis. The aerodynamic characteristics of oblique wing aircraft are discussed in chapter 2 and a vortex lattice model is presented which estimates the forces and moments acting on the aircraft with a minimum computation time. Chapter 3 describes the full-state feedback and reduced-order controller architectures considered for the SAS. The six degree-of-freedom equations of motion for a free flying aircraft with an elastic wing are derived to model wing flexibility effects in chapter 6. All of these analyses are implemented in the integrated synthesis design.

The integrated synthesis method is then applied to the design of the F-8 OWRA in chapter 5. Five configuration variables which define the placement of the wing relative to the fuselage are included along with the controller gains to further decouple the aircraft's dynamic response. The changes in the configuration are limited to ensure that the aircraft's drag and weight is not affected and that trim in 1-g level flight may be achieved with small control deflections. Initially, OWRA designs are synthesized assuming a rigid aircraft with a full-state feedback explicit model following SAS. Multiple flight conditions, reduced-order-controllers, and wing elasticity are included in the integrated synthesis procedure and the OWRA configuration is re-synthesized. In all cases, the resulting optimal integrated designs show improved handling qualities when compared with the original OWRA configuration.

Chapter 2

Oblique Wing Aerodynamics

The aerodynamic coupling experienced by oblique wing aircraft at high sweep angles (greater than 30 degrees) is a key factor in the degradation of handling qualities. A method of accurately estimating the aerodynamic loads with low computation cost is required by the integrated design synthesis so that the influence of configuration geometry changes on handling qualities can be calculated. In this chapter the origin of the aerodynamic coupling are studied using wind tunnel data and numerical modelling results. A vortex lattice method which calculates the forces and moments for the complete aircraft with sufficient accuracy and efficiency are discussed. The results from this code are compared with other more elaborate numerical methods and wind tunnel results.

When R. T. Jones initially proposed the concept of oblique wing sweep [Ref. 10], The reduction of supersonic wave drag was the perceived major advantage of the configuration. A simplified expression for the supersonic drag of an aircraft is given by Jones:

$$(2.1) \qquad \text{Drag} = q \, S \, C_{Dp} + \frac{L^2}{q \, \pi \, b^2} + \frac{(M^2 - 1)}{2 \, \pi \, q} \, \frac{L^2}{X_1^2} + \frac{128 \, q \, \text{Vol}^2}{\pi \, X_2^4}$$

where (Vol) is the aircraft volume and X_1, X_2 are averaged lengths computed from supersonic area rules. If the wing lies near the Mach cone, X_1 and X_2 are essentially equal to the vehicle length, which has a powerful effect on the lift and volume dependent wave drag (the third and fourth terms in equation 2.1, respectively). For a fixed aerodynamic span (b) the total drag is minimized by a configuration with the greatest length. From figure 1.2 it is obvious that for equal spans and sweeps, the oblique sweep configuration has nearly twice the length of the symmetric sweep planform, and therefore lower wave drag. When an oblique wing with a fuselage is considered, the distribution of wing volume along the fuselage length provides a natural area ruling effect, which creates a favorable volume distribution for low wave drag without altering the fuselage cross sectional area near the wing root

8

(i.e. 'coke bottle fuselage').

2.1 Wind Tunnel Test Results

The advantages of reduced wave drag are to some extent countered by the disadvantages of aerodynamic coupling inherent to the asymmetric planform. Extensive wind tunnel tests of the F-8 OWRA configuration (Fig. 2.1-2.2) have been conducted in the NASA Ames transonic wind tunnel [Ref. 11-14] to help analyze the magnitude and nature of the coupling terms. These tests investigated several wing designs in combination with the F-8 fuselage and empennage. Table 2.1 summarizes the configurations tested and figures 2.1-2.2 display isometric drawings of the different versions.

Configuration	Wing Area	Airfoil	L.E. Sweep	Planform	Skew Pivot
1	250 (sq. ft.)	SC(2)-0714	0°	sym.	no
2	250	OW70 14/12	4°	asym.	no
3	300	OW70 14/12	4°	sym.	yes
4	300	SC(2)-0714	0°	sym.	yes

Table 2.1 F-8 OWRA wind tunnel test configurations

Initially, a design with small wing area (250 sq. ft.) and supercritical airfoil was considered (configuration 1). Studies by Kroo and Kennelly showed that an asymmetric planform, and improved airfoil sections resulted in reduced drag when swept obliquely (configuration 2). Wing planform asymmetry, however, complicates the wing construction and a version with a symmetric wing planform was designed as a simpler alternative. Configuration 3 is the updated version of Kroo and Kennelly's design which incorporates the symmetric planform and has 300 square feet of wing area for an expanded flight envelope. Configuration 4 has the same wing area as configuration 3, but the planform has reduced leading edge sweep and different supercritical airfoil sections are used. Configurations 3 and 4 employ a skewed wing pivot which allows the wing to bank relative to the fuselage as the wing is swept obliquely. Wing bank reduces the sideforce produced by leading edge suction at large oblique sweep angles.

9
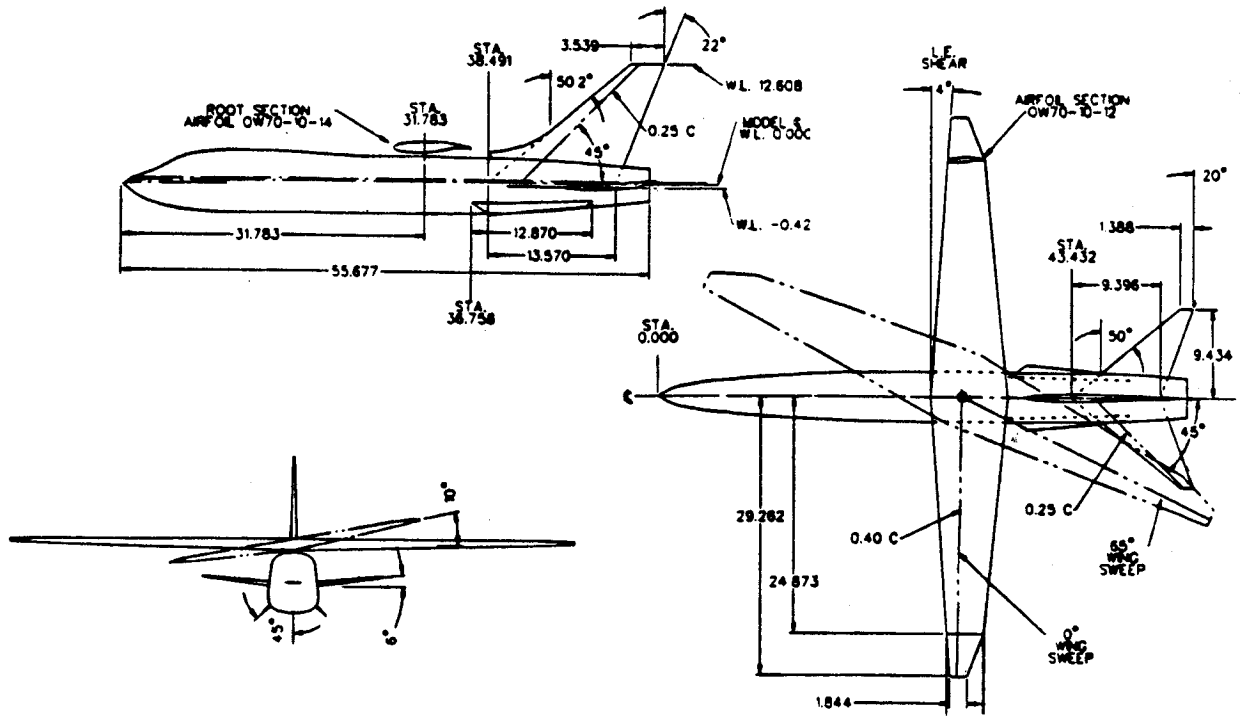
Figure 2.1 F-8 OWRA wind tunnel model (configuration 3 shown)

Configuration #   1&4   2   3
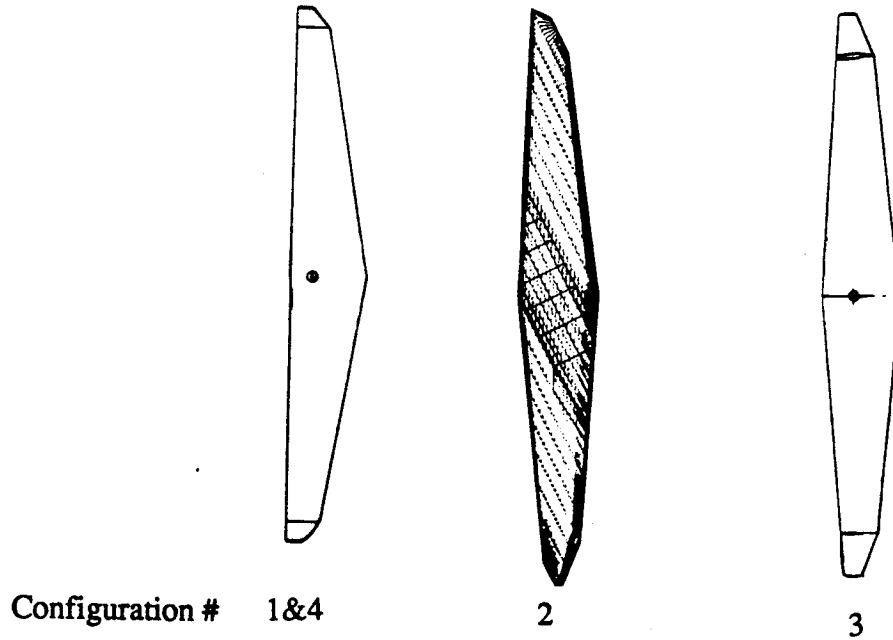
Figure 2.2 F-8 OWRA wing planforms tested

10

Results from the wind tunnel tests of OWRA configuration 3 at Mach 0.8 and 45 degrees oblique sweep are shown in figures 2.3-2.8. This data clearly shows the nonzero values of the coupling terms C_Y, C_l, and C_N and their nonlinear variation with changing angle of attack.

Lift Coefficient vs Angle of Attack
45 deg. sweep, M=0.8
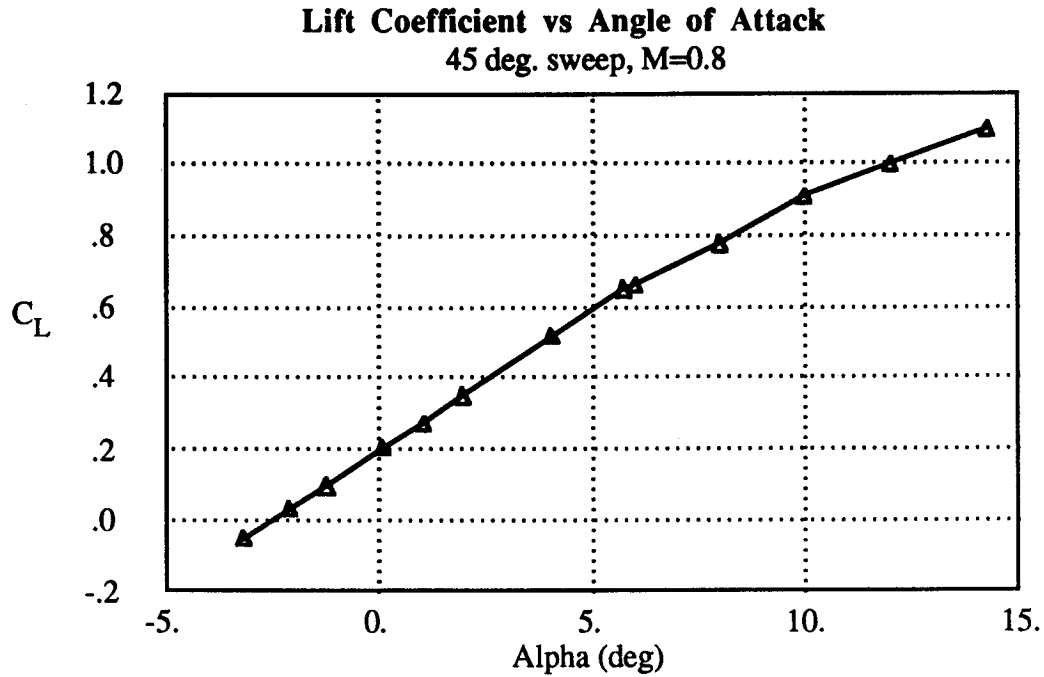
Figure 2.3 lift coefficient vs. angle of attack

Drag Coefficient vs Lift Coefficient
45 deg. sweep, M=0.8
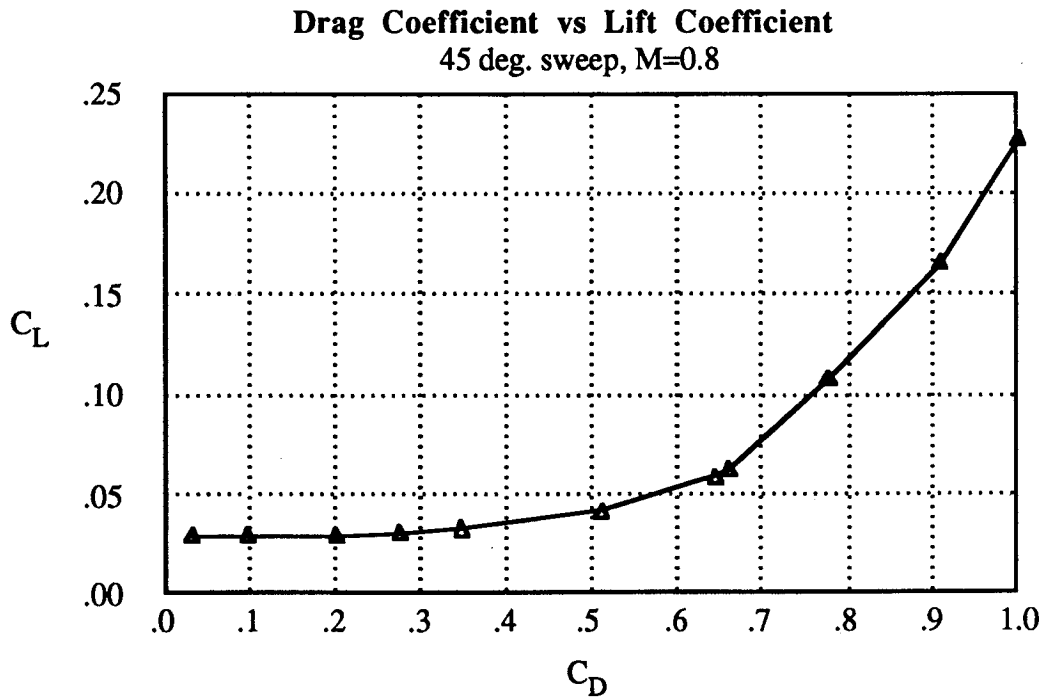
Figure 2.4 lift coefficient vs. drag coefficient

11

Sideforce Coefficient vs Lift Coefficient
45 deg. sweep, M=0.8
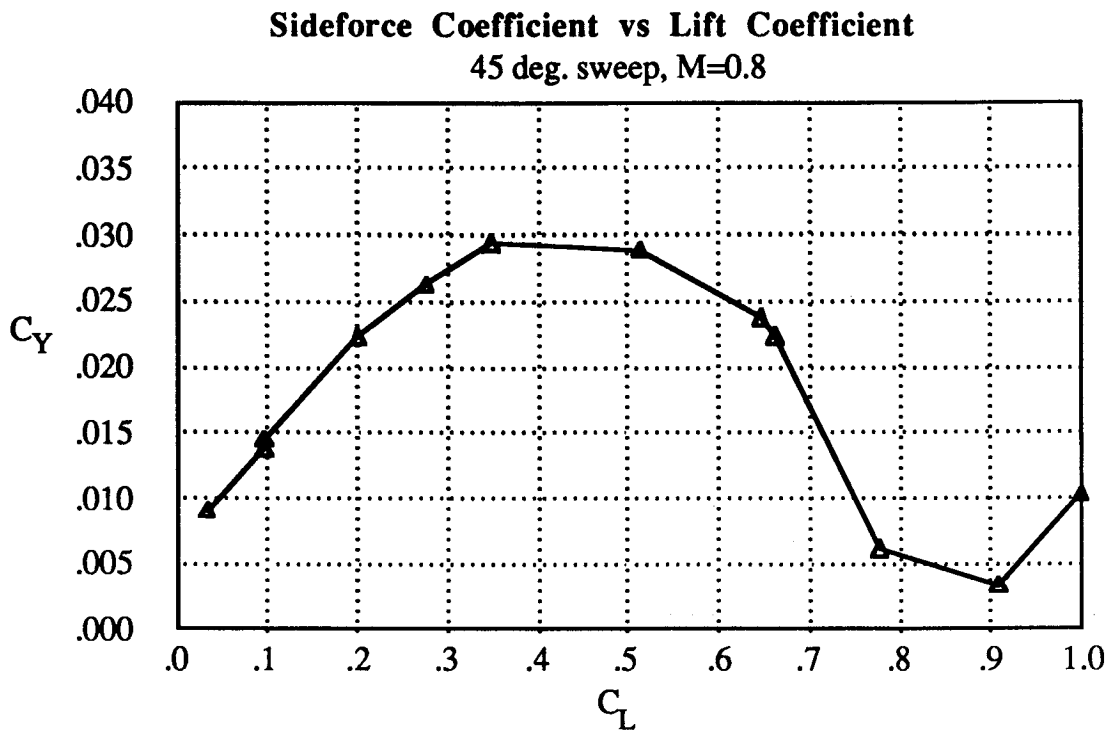
Figure 2.5 sideforce coefficient vs. lift coefficient

Rolling Moment Coefficient vs Lift Coefficient
45 deg. sweep, M=0.8
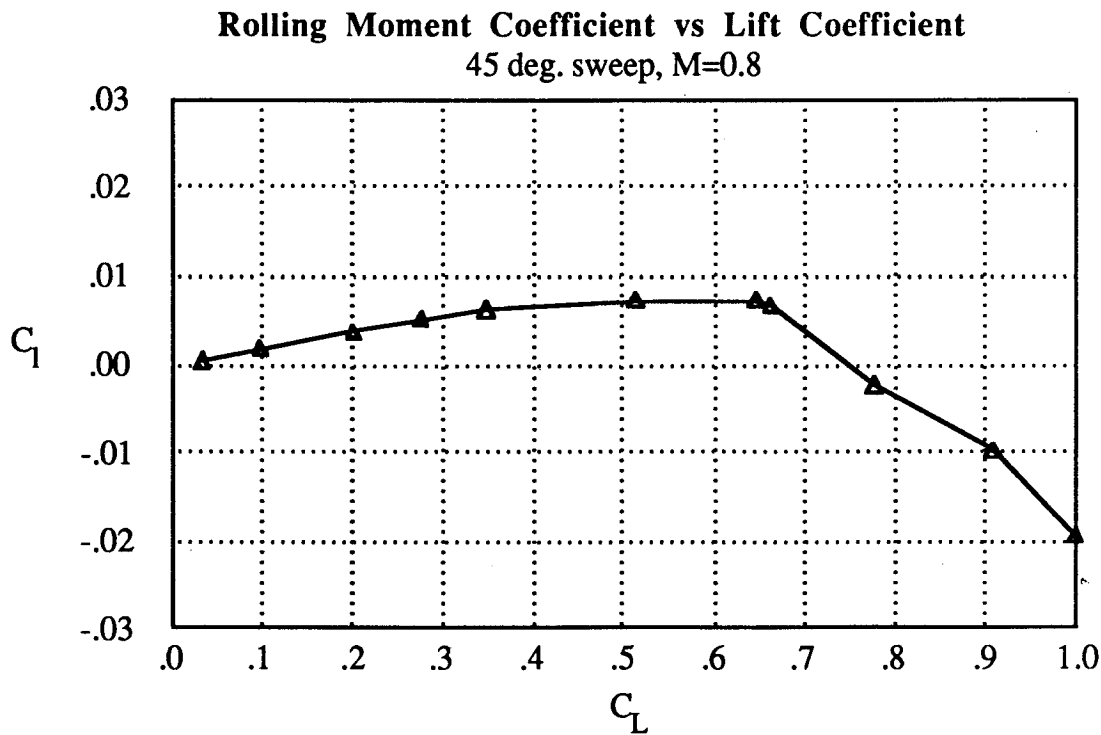
Figure 2.6 roll moment coefficient vs. lift coefficient

Pitching Moment Coefficient vs Lift Coefficient
45 deg. sweep, M=0.8
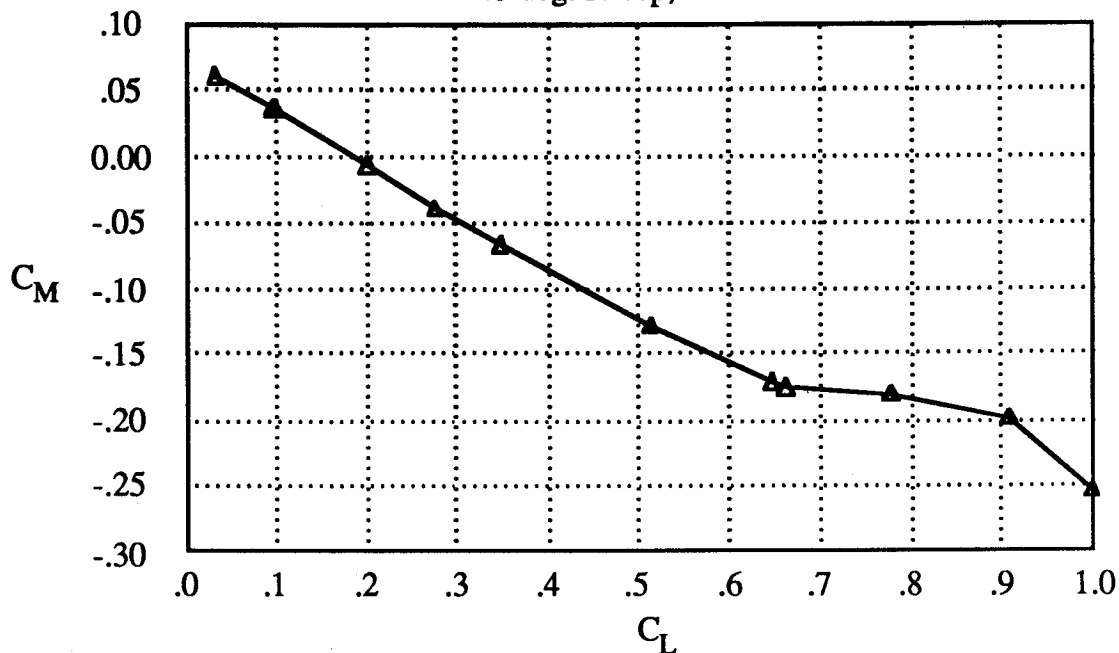
Figure 2.7 pitch moment coefficient vs. lift coefficient

Yawing Moment Coefficient vs Lift Coefficient
45 deg sweep, M=0.8
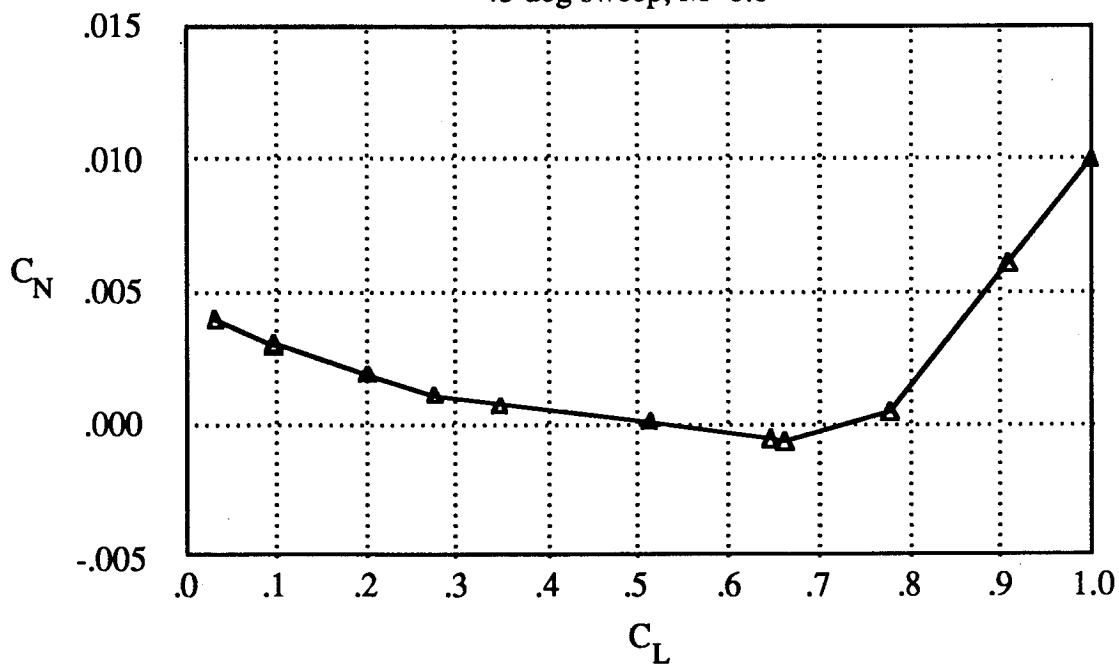
Figure 2.8 yaw moment coefficient vs. lift coefficient

The influence of wing sweep on coupling is more clearly shown in figures 2.9 - 2.14 where C_Y, C_l, and C_N are plotted for sweep angles between 0 and 65 degrees. These results show that significant coupling occurs for oblique wing sweep greater than 30 degrees. The F-8 OWRA is designed to operate at Mach numbers up to 1.6, where the optimal wing sweep for low drag is 65 degrees. At this high speed flight condition the sweep is large enough to insure subsonic leading edges and a subsonic Mach number (0.7) for the flow perpendicular to the quarter chord (i.e. normal Mach number). Because the flow normal to the wing is subsonic and the wing lies inside the Mach cone, the effect of Mach number on the aerodynamic loads is small (except of course for its effect on drag). Wind tunnel data shown in figures 2.15 - 2.20 verifies this claim (at least at low angles of attack), where C_L, C_Y, C_M, C_l, and C_N versus α are plotted for Mach numbers up to 1.6 at 65 degrees sweep. These results justify the use of a subsonic aerodynamics model for numerical estimation of the airloads.

Lift Coefficient vs Angle of Attack
M=0.6
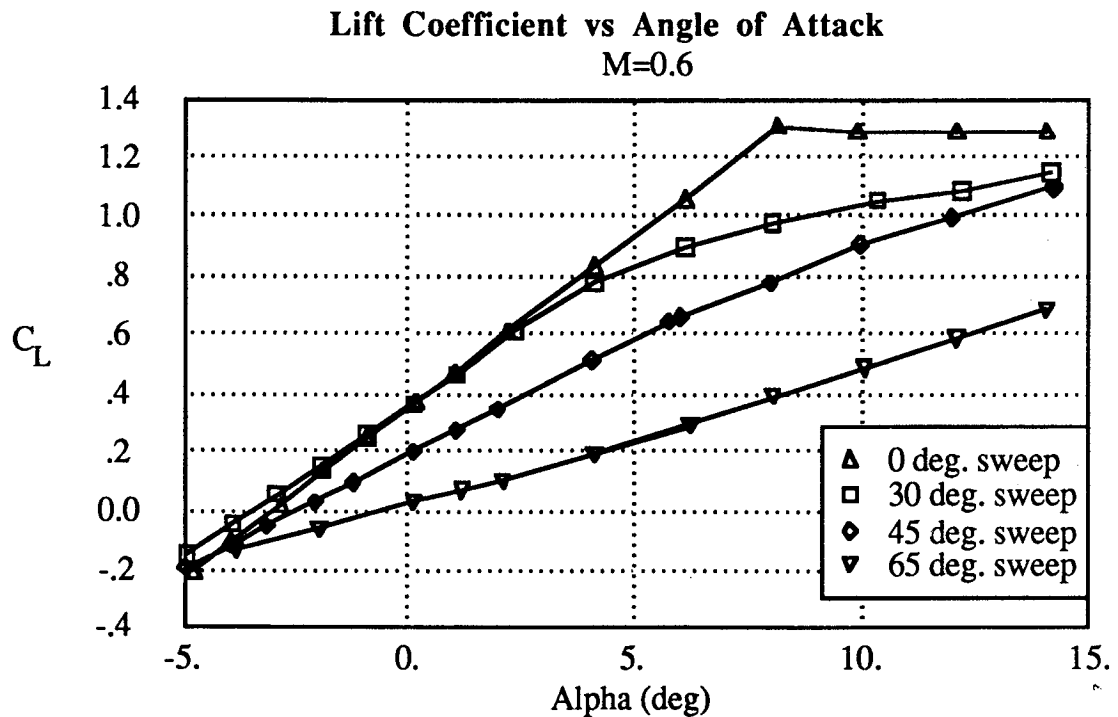
Figure 2.9 lift coefficient vs. angle of attack

14

Drag Coefficient vs Lift Coefficient
M=0.6

Figure 2.10 lift coefficient vs. drag coefficient

Sideforce Coefficient vs Lift Coefficient
M=0.6
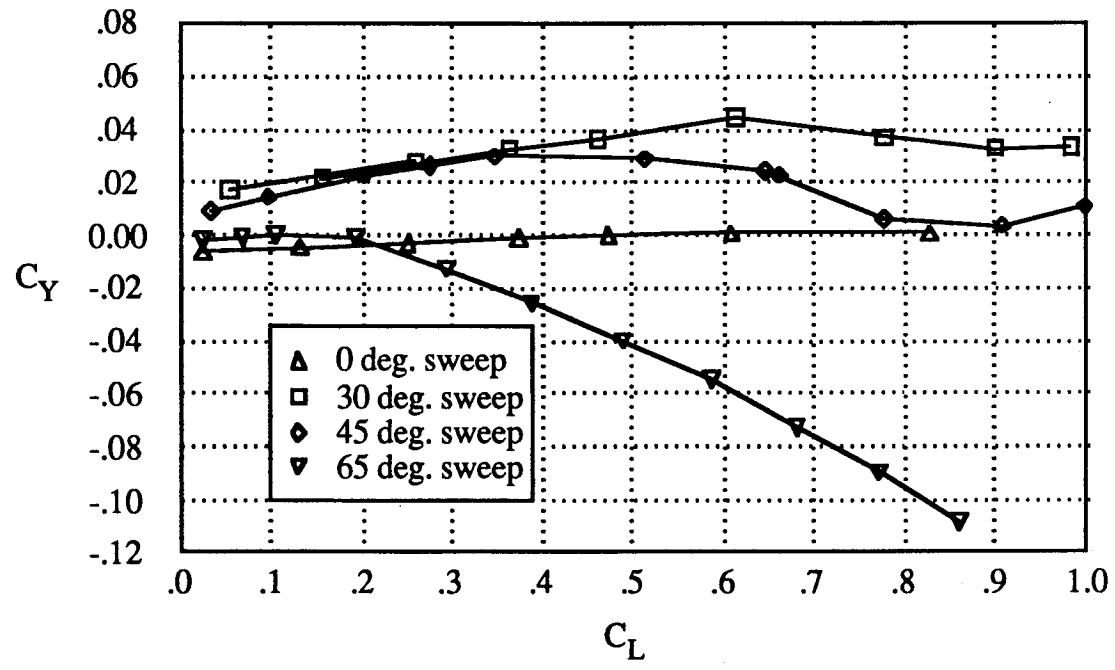
Figure 2.11 sideforce coefficient vs. lift coefficient

15

Rolling Moment Coefficient vs Lift Coefficient
M=0.6
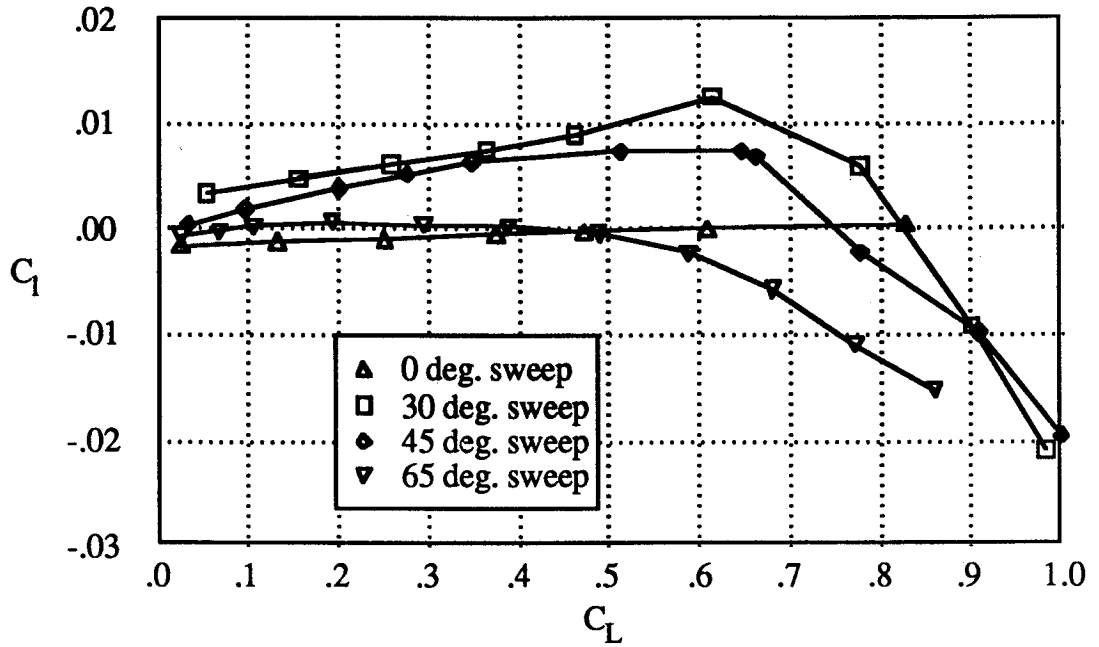
Figure 2.12 roll moment coefficient vs. lift coefficient

Pitching Moment Coefficient vs Lift Coefficient
M=0.6
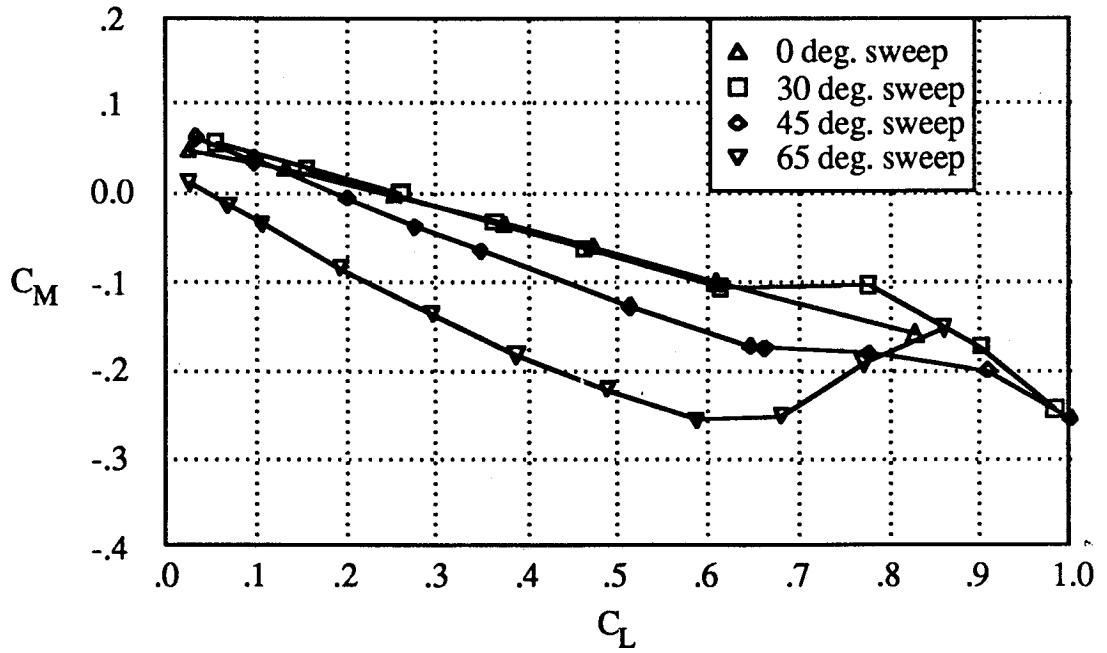
Figure 2.13 pitch moment coefficient vs. lift coefficient

16

Yawing Moment Coefficient vs Lift Coefficient
M=0.6
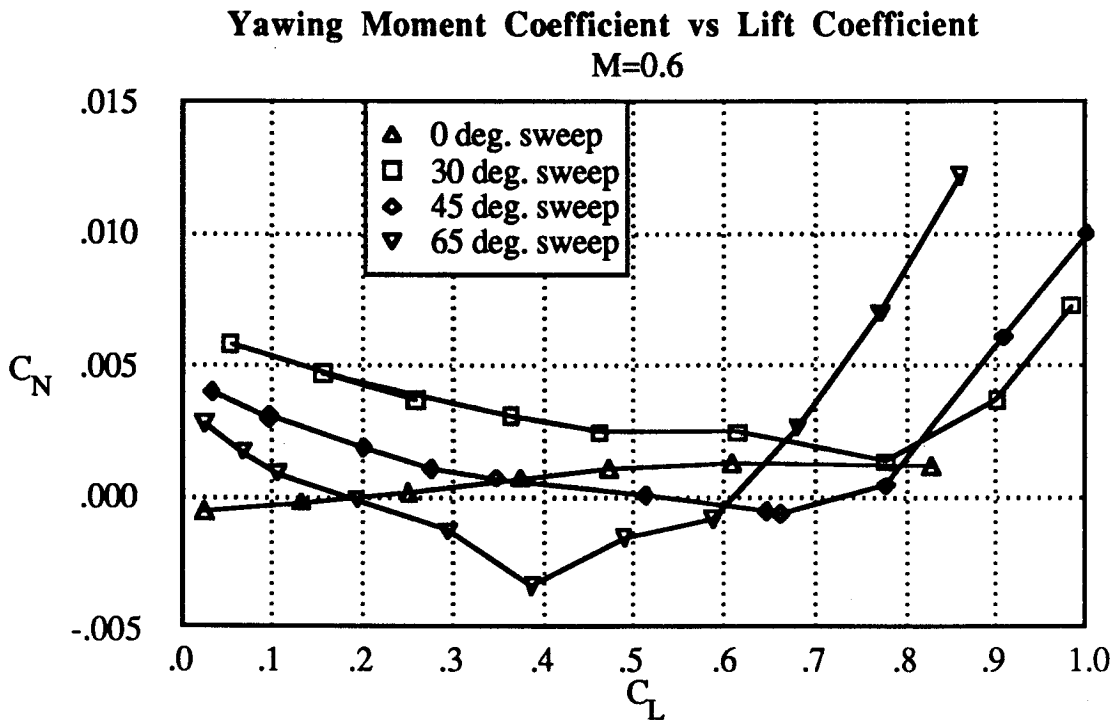
Figure 2.14 yaw moment coefficient vs. lift coefficient

Lift Coefficient vs Angle of Attack
65 deg. sweep
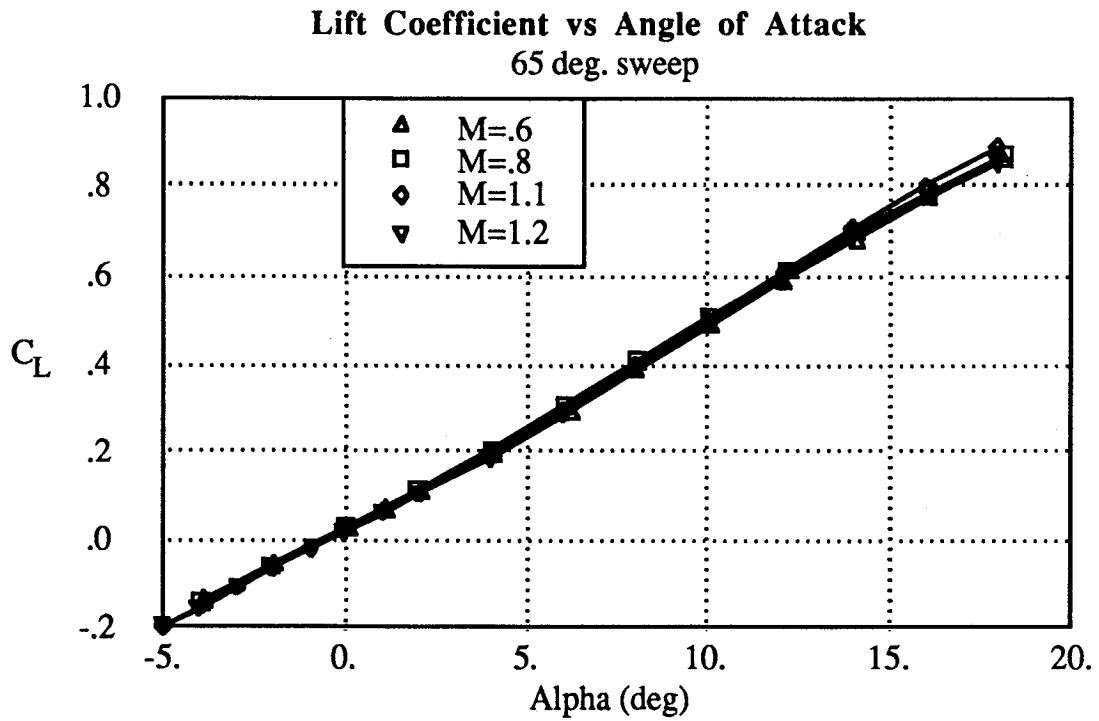
Figure 2.15 lift coefficient vs. angle of attack

17

Drag Coefficient vs Lift Coefficient
65 deg. sweep
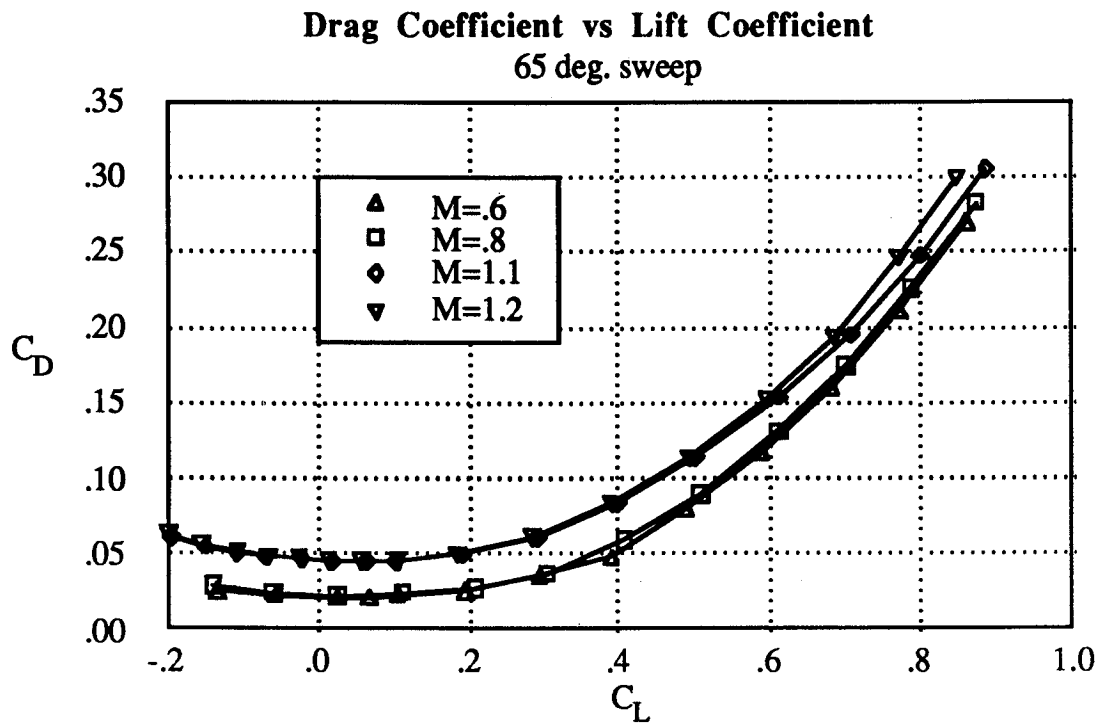
Figure 2.16 drag coefficient vs. lift coefficient

Sideforce Coefficient vs Lift Coefficient
65 deg sweep
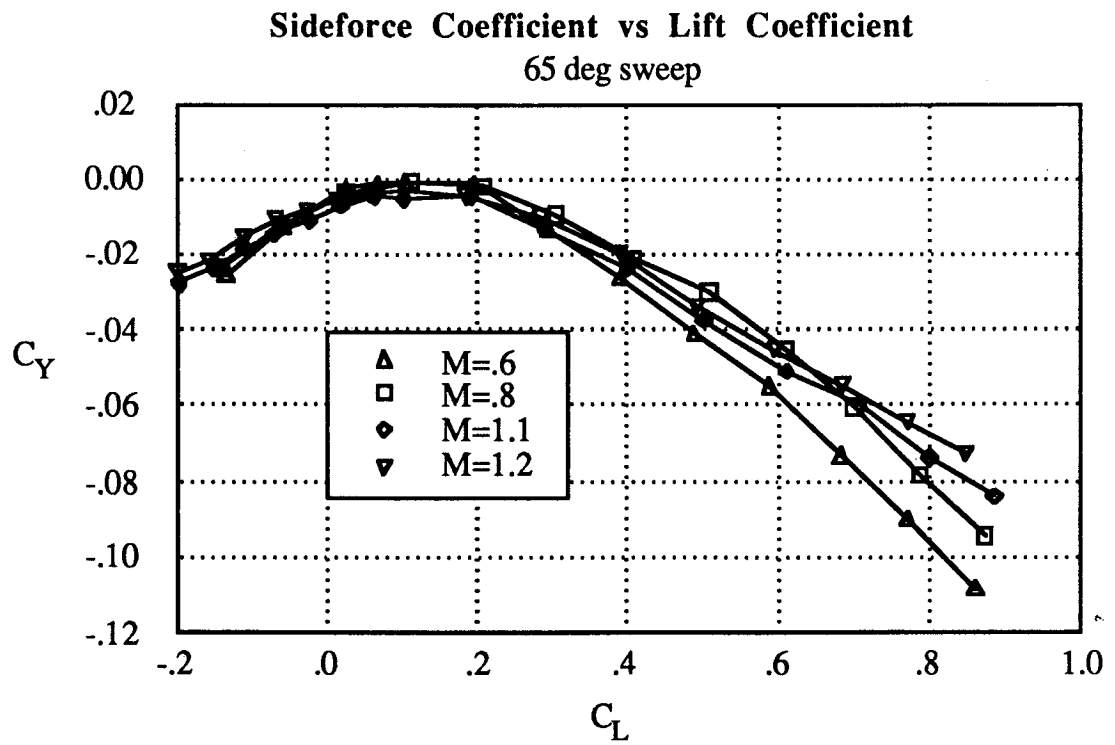
Figure 2.17 sideforce coefficient vs. lift coefficient

18

Rolling Moment Coefficient vs Lift Coefficient
65 deg sweep
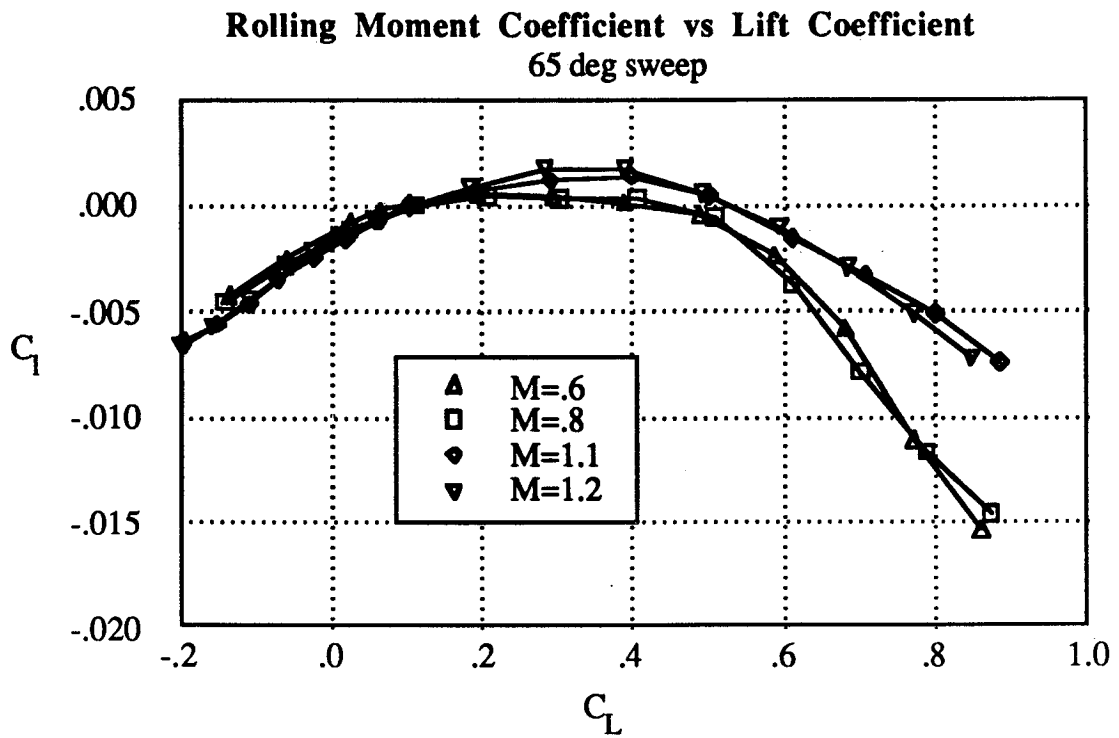
Figure 2.18 roll moment coefficient vs. lift coefficient

Pitching Moment Coefficient vs Lift Coefficient
65 deg. sweep
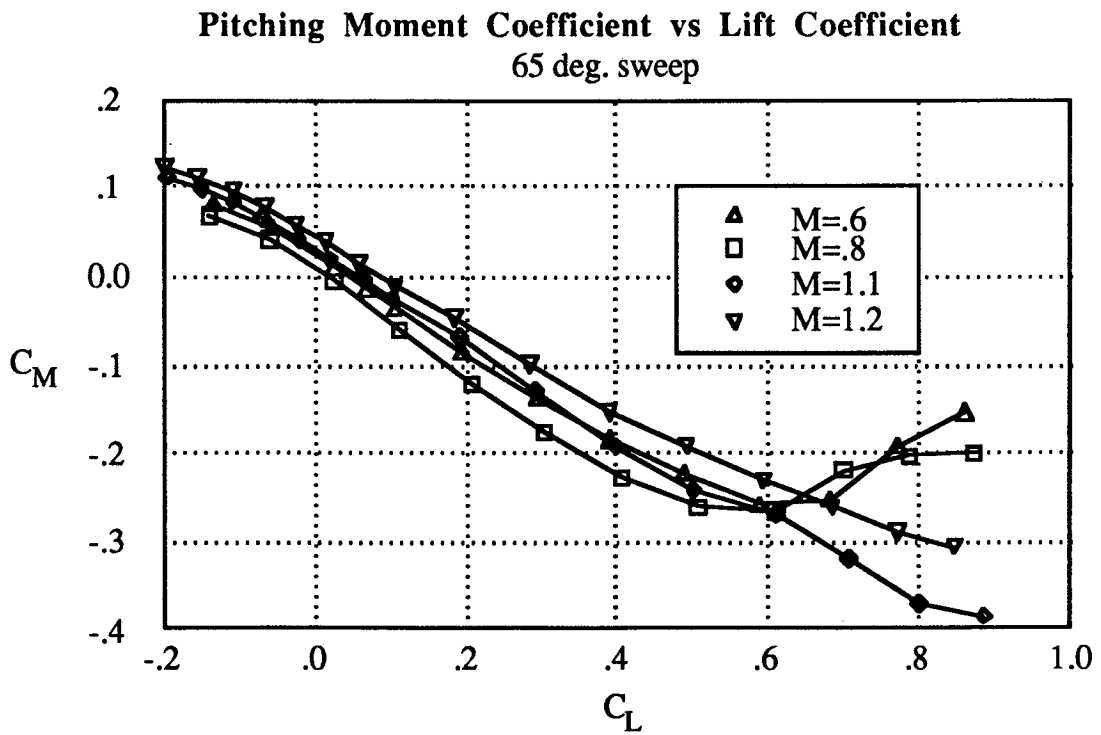
Figure 2.19 pitch moment coefficient vs. lift coefficient

Yawing Moment Coefficient vs Lift Coefficient
65 deg. sweep
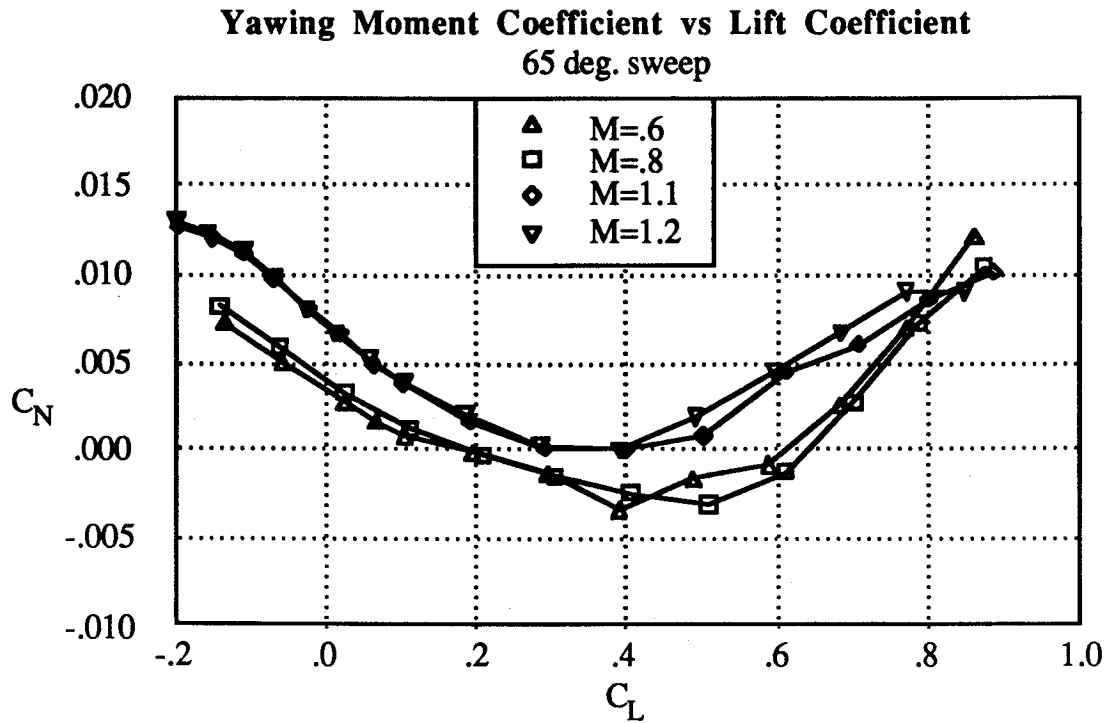
Figure 2.20 yaw moment coefficient vs. lift coefficient

Over most of the operational flight regime the angle of attack is small enough that the flow remains attached to the wing. At higher angles of attack (and oblique sweep greater than 30 degrees) a complicated vortical flow structure occurs as the flow separates from the wing. Figure 2.21 is a photo of the F-8 OWRA in a water tunnel flow visualization test and shows the separated flowfield at 65 degrees sweep and 10 degrees angle of attack. Initially, flow separation occurs on the aft swept wing tip due to increased boundary layer thickness and higher local lift coefficient (both caused by the oblique sweep). At a slightly greater α, a separated vortical flow forms on the leading edge of the forward swept wing panel until it hits the fuselage which acts as a flow fence and forces the vortex into the wake. Flow visualization studies of the wing alone (Fig. 2.22) show that the vortical flow exits near the region of aft tip flow separation when the fuselage is not present.
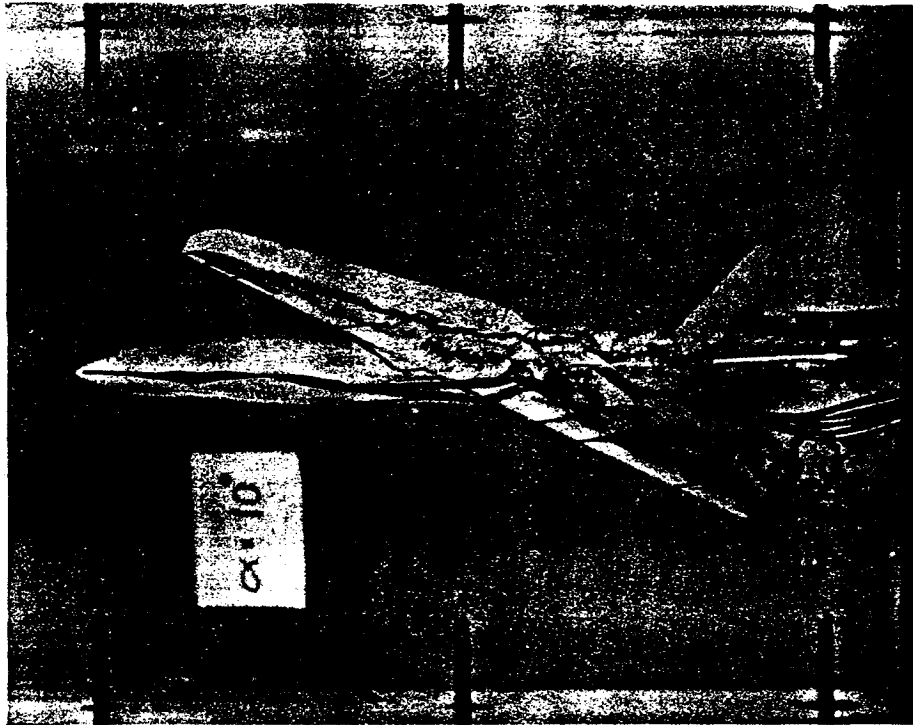
Figure 2.21 water tunnel flow visualization, F-8 OWRA, 65° sweep

Figure 2.22 water tunnel flow visualization, F-8 OWRA, 65° sweep, wing only

21

The leading edge vortex produces nonlinear lift and reduces leading edge suction by the same mechanisms that govern the flow over delta wings at high angles of attack. As a result, the lift coefficient at high angles of attack increases at a rate greater than linear theory predicts, because the nonlinear lift increment from the leading edge vortex exceeds the lift lost from the aft tip flow separation. Figure 2.23 shows this effect for the OWRA with 65 degree wing sweep. Flow separation occurs at 7 degrees angle of attack and the lift coefficient continues to increase (nonlinearly) in the separated flow region.

The influence of flow separation on the aerodynamic coupling terms is to contribute additional nonlinear behavior which is governed by mechanisms different from those in the attached flow regime. This study does not require the ability to predict aerodynamic loads in the separated flow regime because we seek to redesign the aircraft for improved handling qualities in the maneuver and cruise flight conditions where the flow is attached and most of the flying time is spent. Of course, a feasible oblique wing aircraft must remain stable and controllable when flow separation occurs and the flight tests of the AD-1 have shown that this safety issue can easily be achieved in an oblique wing design, although handling qualities may degrade rapidly in this regime. Air combat missions may require extensive operation in the separated flow regime and oblique wing aircraft are less suited for this role due to degraded handling qualities in this flight condition, but for other oblique wing missions the key issue is improved handling in the lower angle of attack flight regimes.
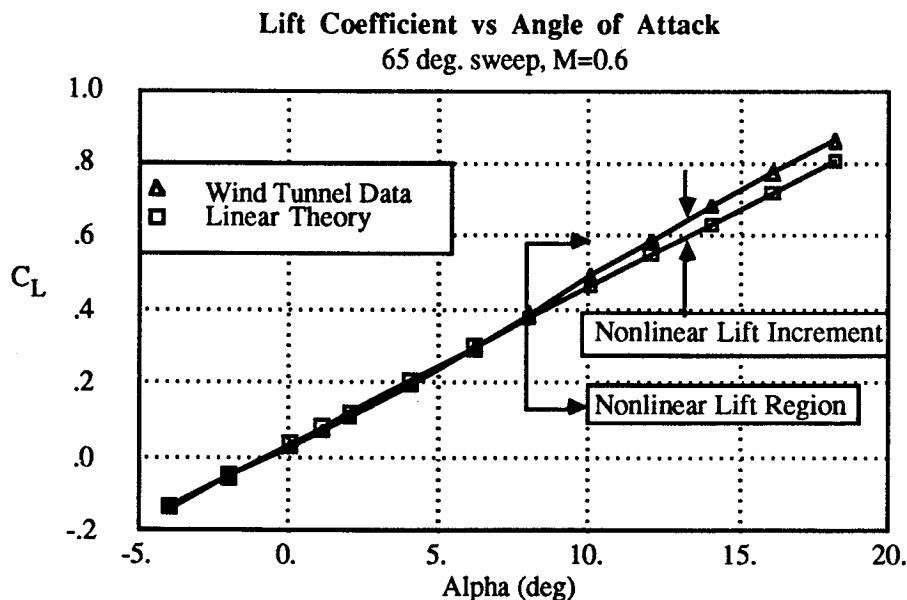
Figure 2.23 nonlinear lift due to leading edge vortex

22

The linear lift shown in figure 2.23 is given by:

(2.2) $\qquad C_L = C_{Lo} + C_{L\alpha}\, \alpha$

and

(2.3) $\qquad C_{L\alpha} = \dfrac{AR \cos(\Lambda)}{AR + 2\cos(\Lambda)}\, 2\pi$

An estimate of the angle of attack at which flow separation first occurs can be obtained from simple sweep theory. If the average wing lift coefficient is C_L then the average lift coefficient for airfoil sections taken normal to the quarter chord ($C_{L\perp}$):

(2.4) $\qquad L = \dfrac{1}{2}\rho V_o^2 C_L S_{ref} \cong \dfrac{1}{2}\rho V_N^2 C_{L\perp} S_{ref}$

and

(2.5) $\qquad V_N = V_o \cos(\Lambda)$

therefore:

(2.6) $\qquad C_{L\perp} \cong \dfrac{C_L}{\cos^2(\Lambda)}$
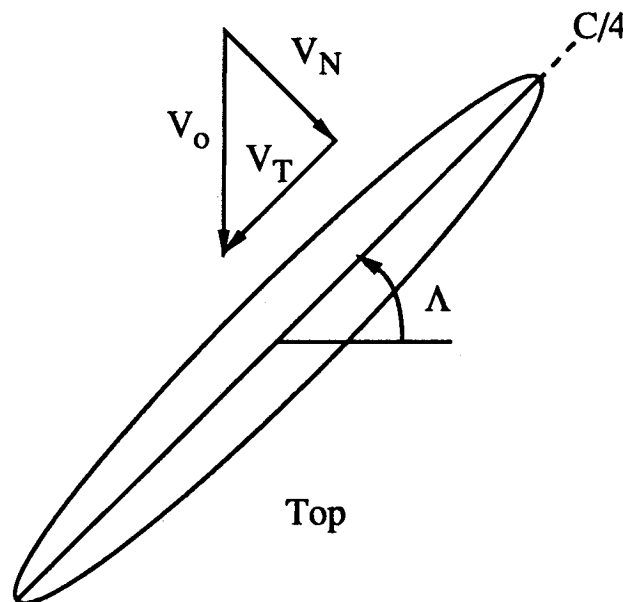
Figure 2.24 normal and streamwise flow directions

23

An estimation of the angle of attack at which local flow separation occurs can be made by comparing the section normal C_l with C_{lmax} for the two dimensional airfoil section normal to the flow. The effect of wing sweep on the C_L where separation first occurs is shown in figure 2.25 (for a 2-D section C_{lmax} of 1.0). This plot shows that at high sweep angles the range of C_L over which the flow is attached is small. For example, at 65 degrees of sweep, flow separation occurs at C_L of 0.18. This simplified study also shows that the design of airfoil sections for oblique wing aircraft requires high lift airfoil sections that have low transonic drag [Ref. 1].

Maximum Lift Coefficient vs Wing Sweep
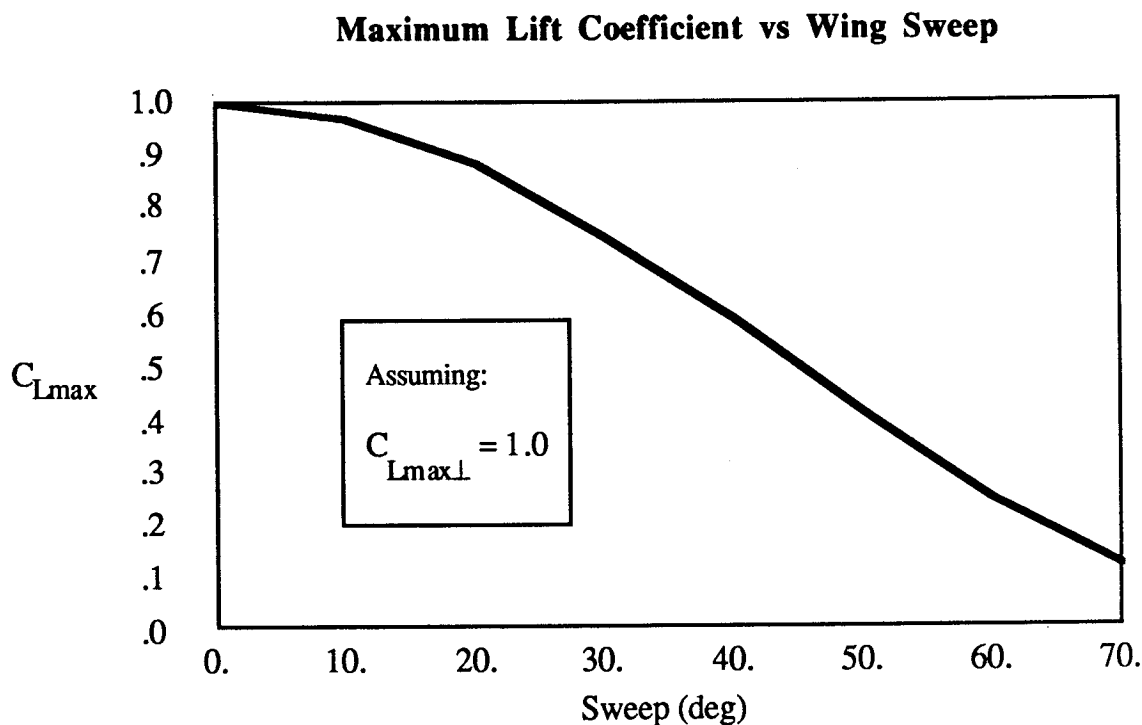
Figure 2.25 maximum lift coefficient for attached flow vs. wing sweep

In the attached flow regime the aerodynamic coupling terms display nonlinear behavior (see Fig. 2.5 - 2.6) which might lead one to conclude that a "linearized" aerodynamic theory will not capture these effects. This conclusion is incorrect because linearized theory can account for induced velocities and nonplanar geometry influences which can produce nonlinear variations in the aerodynamic loads. This section will explain the physical phenomenon contributing to each of the coupling terms and show how the vortex lattice method (presented in the next section) predicts the coupling terms and their nonlinear trends.

The sideforce (C_Y), as angle of attack is varied, is produced by the low pressure region acting along the leading edge of the wing. It is possible to derive a simple expression for C_Y based on the induced drag of the wing and the suction force C_S which acts normal to the leading edge.
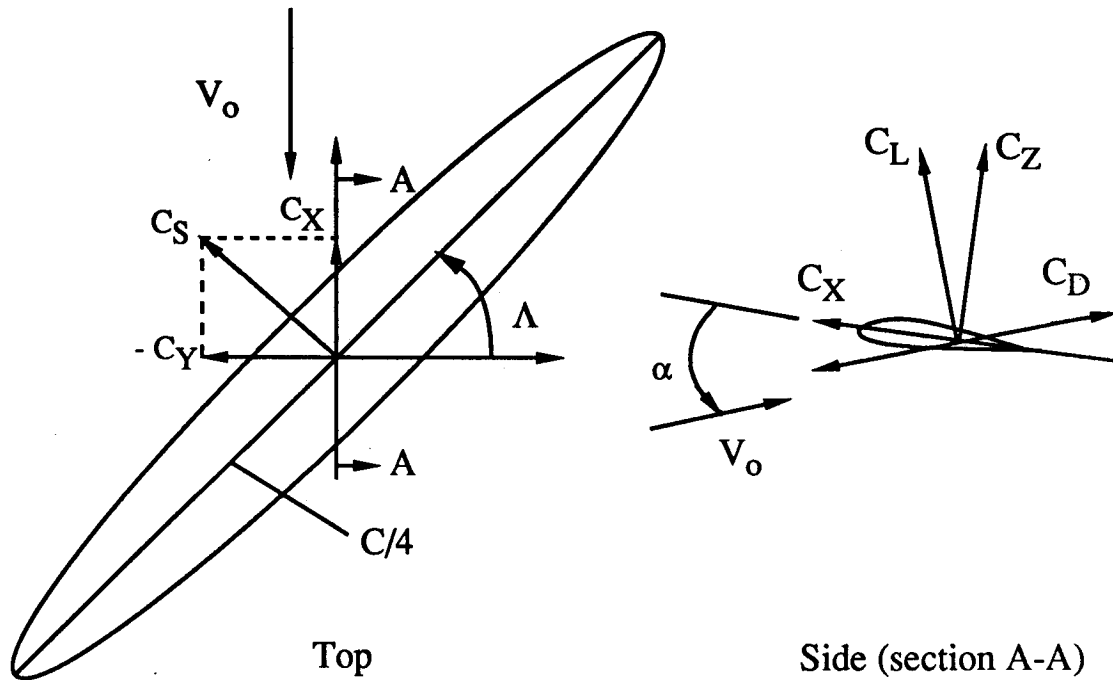
Figure 2.26 sideforce due to leading edge suction

For small α :

$$(2.7) \qquad C_L \approx C_Z$$

$$(2.8) \qquad C_D \approx -C_X + C_L \, \alpha$$

Assuming the drag consists only of induced drag:

$$(2.9) \qquad C_D = C_{Di} = \frac{C_L^2}{\pi \, AR \, e} = -C_X + C_L \, \alpha$$

Solving for C_X:

$$(2.10) \qquad C_X = -\frac{C_L^2}{\pi\,AR\,e} + C_L\alpha$$

The suction and sideforce are related to C_X by:

$$(2.11) \qquad C_S = \frac{C_X}{\cos(\Lambda)}$$

$$(2.12) \qquad C_Y = -C_X\tan(\Lambda)$$

Therefore, the suction force is equal to:

$$(2.13) \qquad C_S = \left(-\frac{C_L^2}{\pi\,AR\,e} + C_L\alpha\right)\frac{1}{\cos(\Lambda)}$$

and the sideforce becomes:

$$(2.14) \qquad C_Y = -\tan(\Lambda)$$

Substituting $C_L = C_{L\alpha}(\alpha + \alpha_o)$

$$(2.15) \qquad C_Y = \tan(\Lambda)\left[-\frac{C_L^2}{\pi\,AR\,e} - \frac{C_L^2}{C_{L\alpha}} + C_L\alpha_o\right]$$

Equation 2.15 shows that the sideforce is quadratic in C_L, based solely upon leading edge suction and induced drag considerations. For a symmetrically swept wing the sideforce produced by the leading edge suction of each panel cancels leaving only the drag force acting in the (-x) direction, whereas oblique wings experience a nonlinear sideforce due to their wing planform asymmetry. It is possible to orient an oblique wing, such that for a given sweep angle and specified lift coefficient, the sideforce at a single flight condition is zero. This is accomplished by requiring that the relative wind axis and the (x) body axis be parallel at the trim condition and that the wing lie in a plane parallel to the x-y plane. If the wing is then rotated about its quarter chord (or long axis) the desired lift can be achieved

26

with zero sideforce. As angle of attack is changed from this trim setting (by gust distur-
bances or maneuvering) the sideforce will not necessarily remain zero and large lateral ac-
celerations may occur. At higher angles of attack, the suction force decreases as flow sep-
aration occurs, and the magnitude of C_Y will also decrease. A comparison between the
simplified theory (Eqn. 2.15) and the experimental value for the sideforce as angle of attack
varies is shown in figure 2.27.

Sideforce vs Lift Coefficient
45 ° sweep
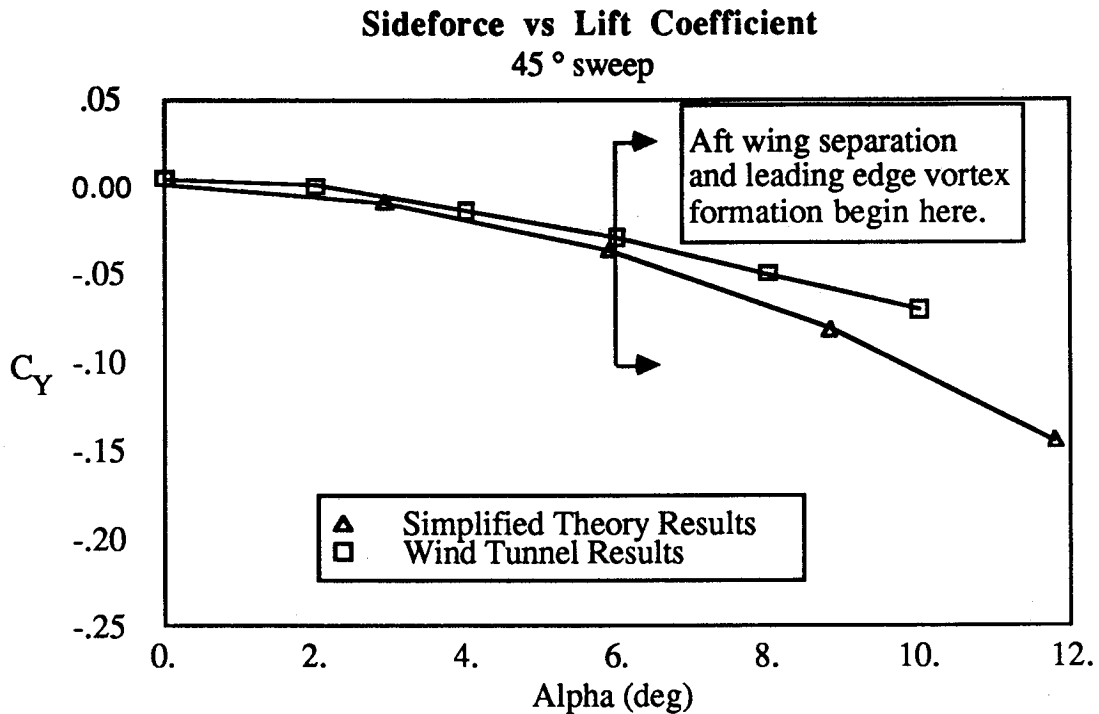
Figure 2.27 sideforce comparison, theory and wind tunnel data

The coupling between rolling moment and angle of attack is caused by induced velocity and
leading edge suction effects. When a planar wing operates with oblique sweep greater than
30 degrees the velocities induced on the wing by the wake cause the aft swept panel to in-
crease in loading more quickly than the forward one for increased angle of attack. For de-
signs with counter clockwise oblique sweep (right wing forward), this induced loading
produces a positive (right) roll moment as angle of attack increases. Figure 2.28 shows the
variation in span loading predicted by a vortex lattice model of a 45 degree obliquely swept
wing at two angles of attack. The difference between the load distributions clearly shows
the increased loading of the aft tip which produces a linear coupling between angle of attack

and rolling moment.

The wing's leading edge suction produces a rolling moment when the aircraft's center of gravity does not lie in the plane of the wing. For the case shown in figure 2.29 the side-force component acting above the center of gravity results in a nonlinear variation in rolling moment which opposes moments produced by induced effects. At higher angles of attack the nonlinear effects dominate and the rolling moment reverses in direction as shown in fig-ure 2.7.

Span Loading at 65 Degree Wing Sweep
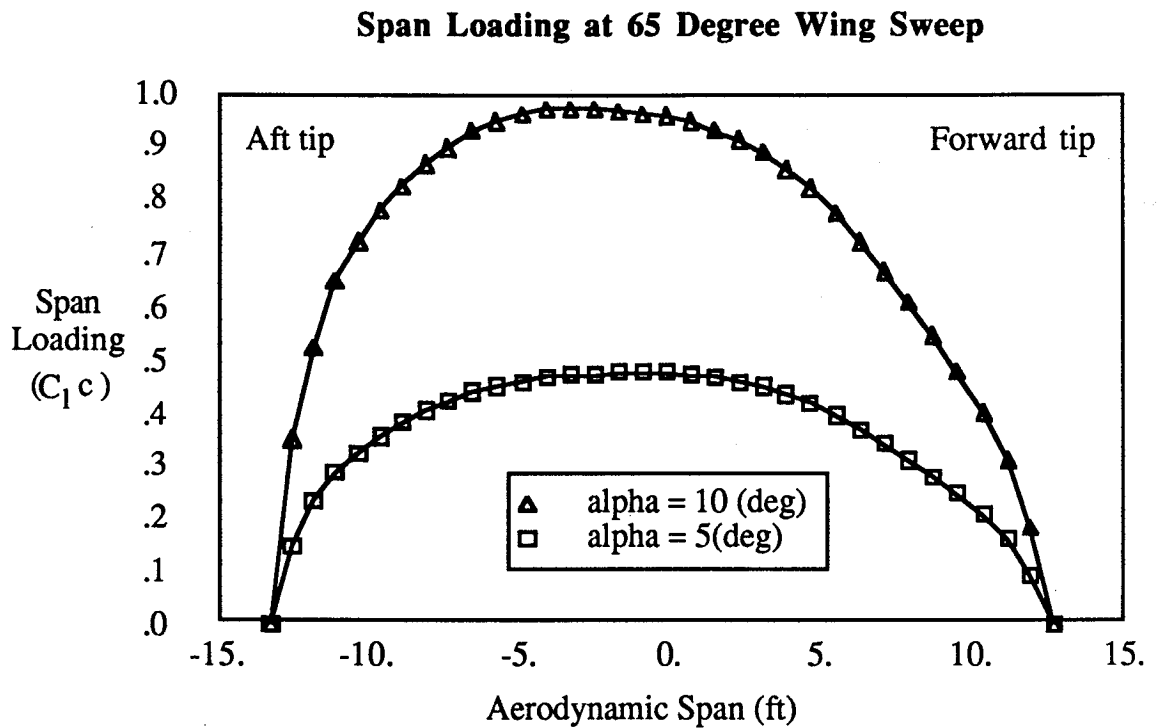
Figure 2.28 rolling moment due to induced asymmetric span loading
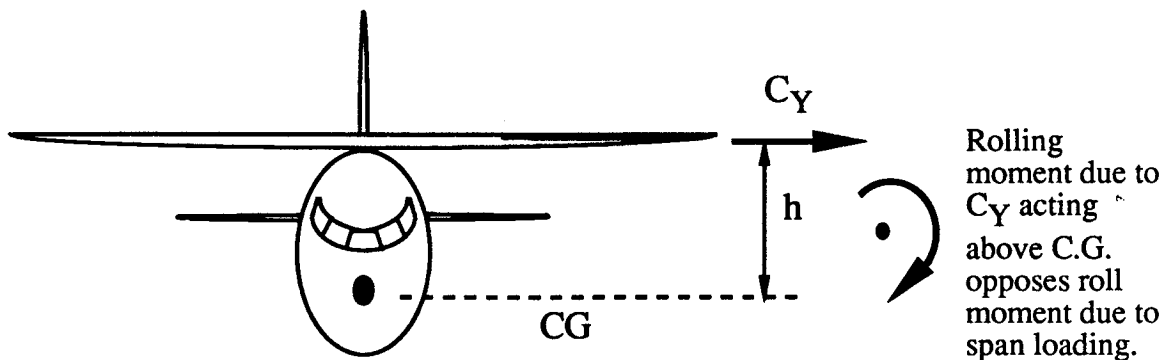
Figure 2.29 rolling moment due to sideforce

28

At high angle of attack, flow separation influences the roll moment coupling by altering the wing's span loading and reducing C_Y. Leading edge vortex formation and flow separation over the aft swept wing tip distort the span loading to produce a negative (left) roll moment for oblique wings with "right-side-forward" sweep. This opposes the roll moment increment due to the loss of leading edge suction (and therefore sideforce, C_Y) which acts above the center of gravity. Wind tunnel results show that the latter effect is stronger and the rolling moment slope becomes more negative at flow separation for the F-8 OWRA configuration (Fig. 2.6).

Yawing moments are produced by the aerodynamic influence of the wing alone and the wing-fuselage interference. The wing alone influence is two-fold. As the angle of attack is increased, The wake induces an asymmetric local angle of attack distribution on the wing which produces a pure yaw couple by altering the distribution of leading edge suction. This couple may be countered by the wing's sideforce component acting ahead of the center of gravity. Interference of the wing and fuselage contributes to yawing moment through lift and thickness-dependent induced effects. The circulation created by the wing to produce lift induces an asymmetric velocity distribution along the fuselage which causes a negative (nose left) yaw moment (Fig. 2.30).

Bound vorticity induces
velocities which cause
suction on the fuselage
in these regions

C_N

Γ
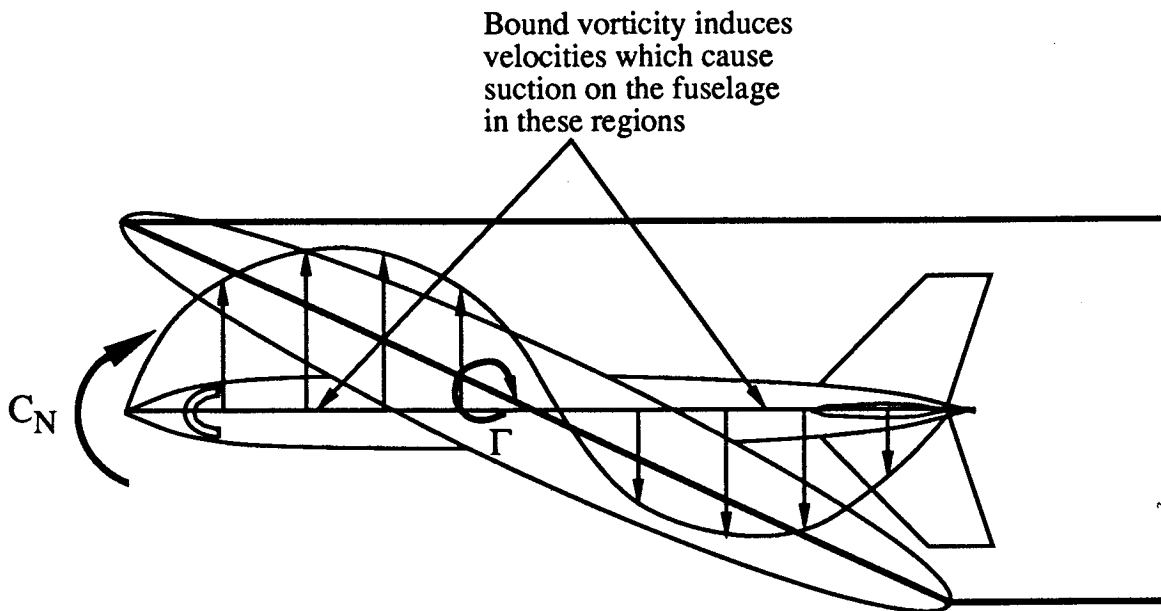
Figure 2.30 yawing moment due to wing-induced fuselage loading

At zero lift the contribution of induced effects to C_N becomes negligible, but the combined influence of the wing and fuselage thickness does not. Wind tunnel results show that at a C_L of zero the value of C_N is nonzero and the slope of C_N vs C_L is distinctly negative in this region (Fig. 2.31). These trends cannot be caused by induced affects (which diminish at low C_L) but instead must be related to an interference of the wing-fuselage thickness distributions. A panel code which models thickness effects (PANAIR [Ref. 15]) was used to study the yawing moment contributions and the results showed that these unusual yawing moment trends could be predicted using this type of panel code. The results also showed that the yawing moment in the low C_L attached flow regime is dominated by wing-fuselage thickness-interference. The displacement of fluid caused by the wing and fuselage thickness (only) produces a low pressure region on the front right side of the F-8 OWRA fuselage at zero C_L (Fig. 2.32) which decreases in strength as angle of attack increases, producing a strong negative C_N slope. If either the wing or fuselage is modeled as a thin surface this effect disappears, indicating the dependence of this phenomenon on thickness. The vortex lattice method used in the design syntheses presented in this work cannot model this thickness interference effect. Therefore, the value of C_N and $C_{N\alpha}$ are estimated from the wind tunnel data (F-8 OWRA) at various sweeps and angles of attack. This necessary approximation for C_N will not significantly affect the design synthesis results because the wind tunnel data shows that these C_N trends are insensitive to wing placement and planform (Fig. 2.34).

Yawing Moment Coefficient vs Lift Coefficient

65 ° sweep, M=0.6
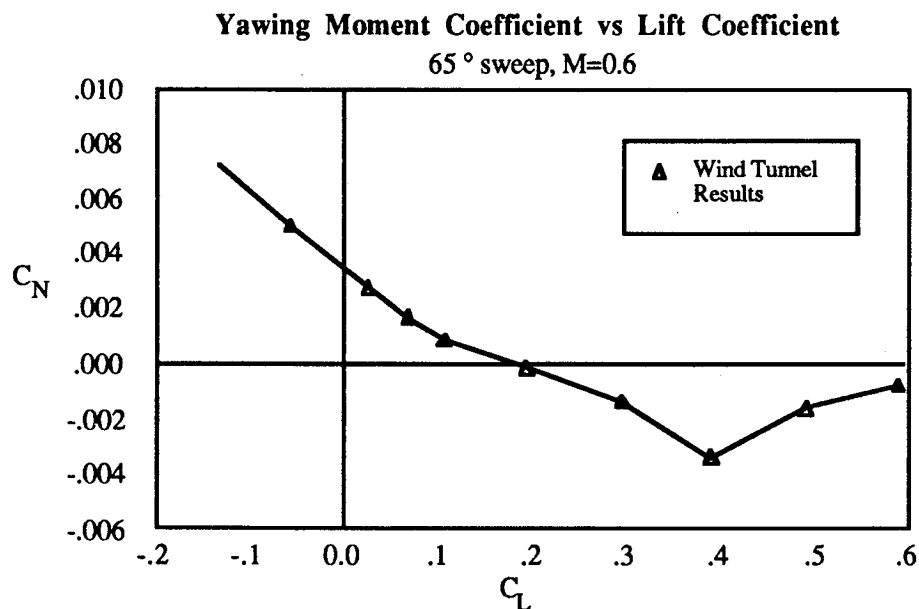
Figure 2.31 yawing moment coefficient vs. lift coefficient

30
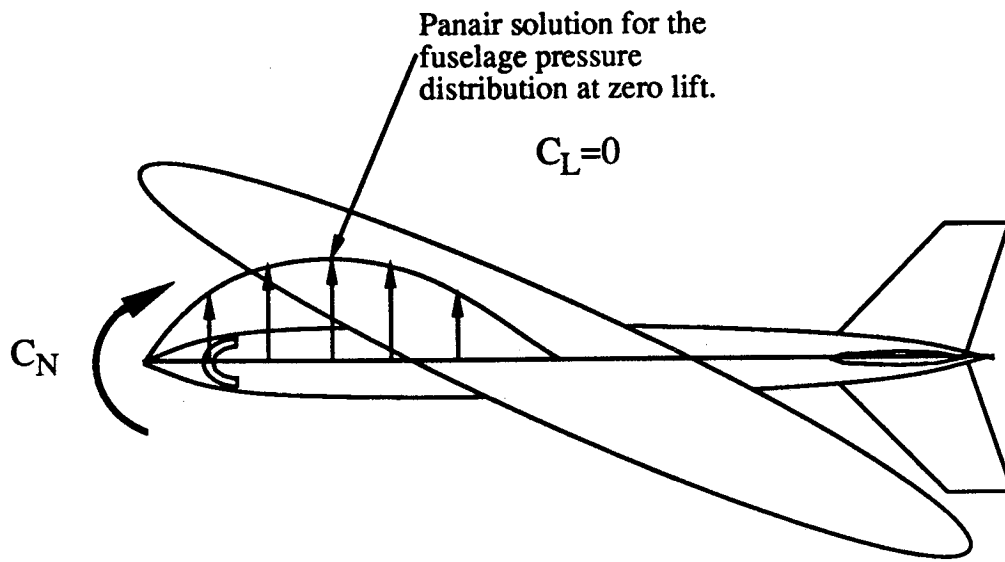
Figure 2.32 yawing moment due to wing-fuselage thickness-interference
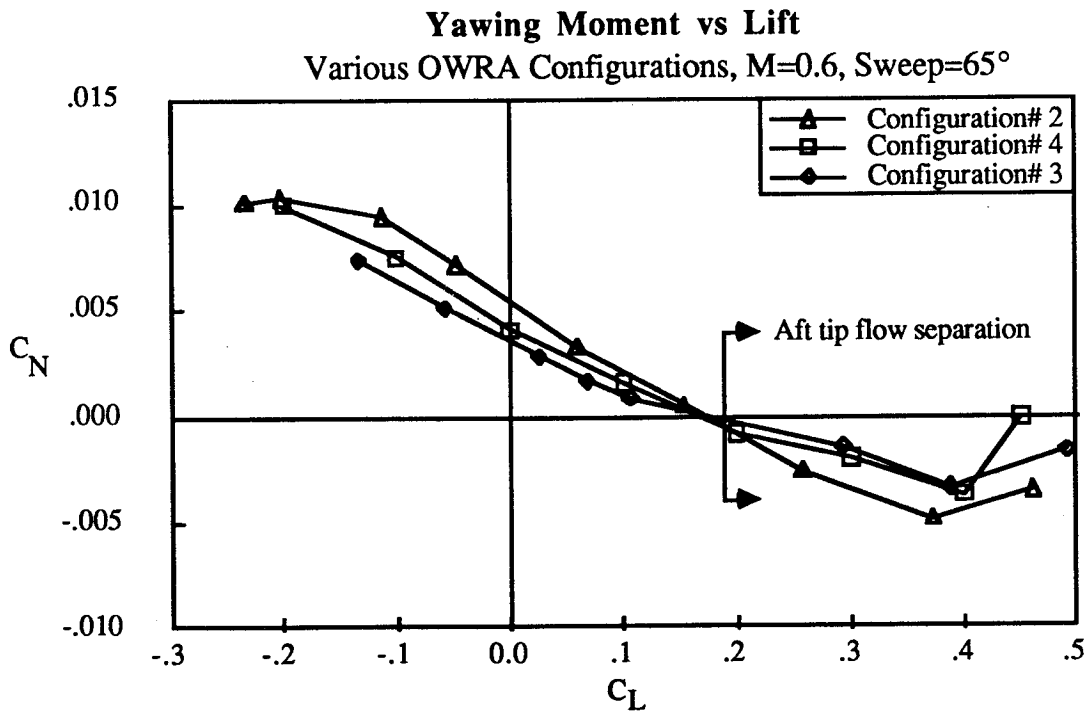
Figure 2.33 yawing moment vs. lift for various OWRA configurations

At higher angles of attack, flow separation produces nonlinear trends in C_N. The leading edge vortex which leaves the wing and trails downstream along the fuselage can strike the vertical tail (Fig. 2.21) producing large variations in C_N that are difficult to predict.

2.2 Vortex Lattice Aerodynamic Model

The aerodynamic coupling loads are predominantly due to the forces and moments generated by the wing. Consequently, the controllability and handling qualities of the aircraft can be influenced by the relative positions of the wing and fuselage. An integrated design synthesis method will be used to investigate this possibility (chapter 4), but a method for efficiently calculating the aerodynamic loads as the wing is repositioned is needed first. Reference [16] describes a vortex lattice method 'LINAIR', by Kroo, which is ideally suited for this task.

For a steady, irrotational flow Laplace's equation for the perturbation velocity potential must be satisfied. Assuming small perturbation velocities (relative to the freestream magnitude) we have:

$$(2.16) \qquad \nabla^2 \, \Phi = 0$$

$$(2.17) \qquad \text{boundary conditions:} \ \vec{V} \cdot \hat{n} = 0$$

$$(2.18) \qquad \text{where} \ \vec{V} = (\, U_o + u \,, v \,, w \,)$$

Vortex singularities placed along the quarter chord of the lifting panel and its wake satisfy Laplace's equation and produce the velocity perturbations required to meet the boundary conditions. Figure 2.34 shows how the vortex filaments are distributed in a 'horseshoe' shape to model a segment of the lifting surface.
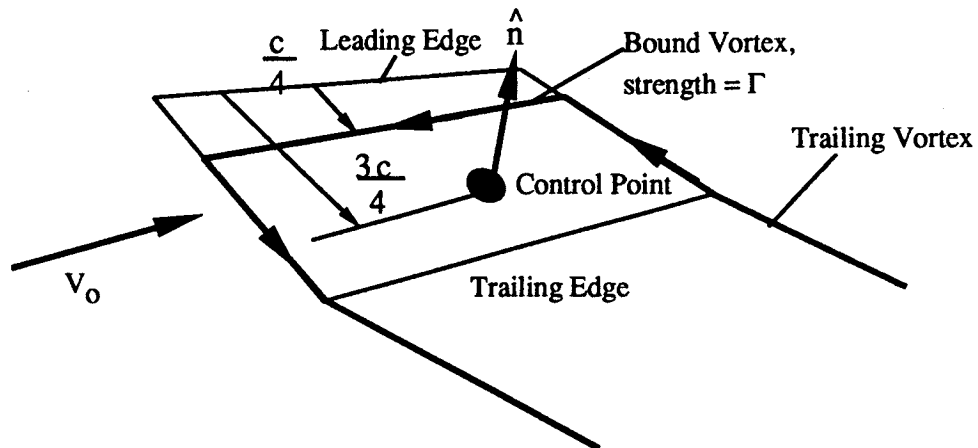
Figure 2.34 typical panel, vortex lattice model

The lifting panels may be any trapezoidal geometry and are not restricted to be in a single plane. The vortex strengths, Γ, are computed by enforcing the boundary conditions. This results in a linear system of equations for Γ.

$$(2.19) \quad [AIC] \{\Gamma\} = \{B\} \quad n = \text{total number of panels}$$
$$n \times n \quad n \times 1 \quad n \times 1$$

where:

$$(2.20) \quad \{B\} = \{\vec{V} \cdot \hat{n} + \vec{\omega} \times \vec{r}\}$$

$$(2.21) \quad \vec{\omega} = \{p, q, r\}$$

The [AIC] matrix is composed of terms representing the influence of the jth vortex at the ith control point, where i and j are indices that span the set of n panels. The vector $\{B\}$ represents the velocity that must be induced at each control point to achieve flow tangency. The first component of $\{B\}$ accounts for the freestream flow and the second term represents the velocities induced by rotational motion of the aircraft.

The vortex strengths (Γ) are obtained by solving the linear system of equations (2.19 - 2.21) above. The forces acting on each panel are:

$$(2.22) \quad \vec{F}_i = \rho \left(\vec{V}_{\frac{c}{4}} \times \vec{\Gamma}_{Bi} \right) \Delta$$

where:

$$(2.23) \quad \vec{V}_{\frac{c}{4}} = \{ [VIC_x] \{\Gamma\}, [VIC_y] \{\Gamma\}, [VIC_z] \{\Gamma\} \}$$

$$\vec{\Gamma}_{Bi} = \text{Bound vorticity on panel (i)}$$

$$\Delta = \text{Bound vortex length}$$

Where the matrices $[VIC_{x,y,z}]$ represent the velocity acting at the center of each panel's quarter chord as a function of the vortex strengths. The VIC influence coefficients are cal-

culated with the bound vortices arranged perpendicular to the longitudinal (x) axis (Fig. 2.35). This prevents the bound vorticity from over-influencing the flow in the vicinity of the quarter chord, which would otherwise occur if the VIC terms were calculated with 'swept' bound vorticity.

Bound vorticity for [AIC]
calculation

Bound vorticity for [VIC]
calculation
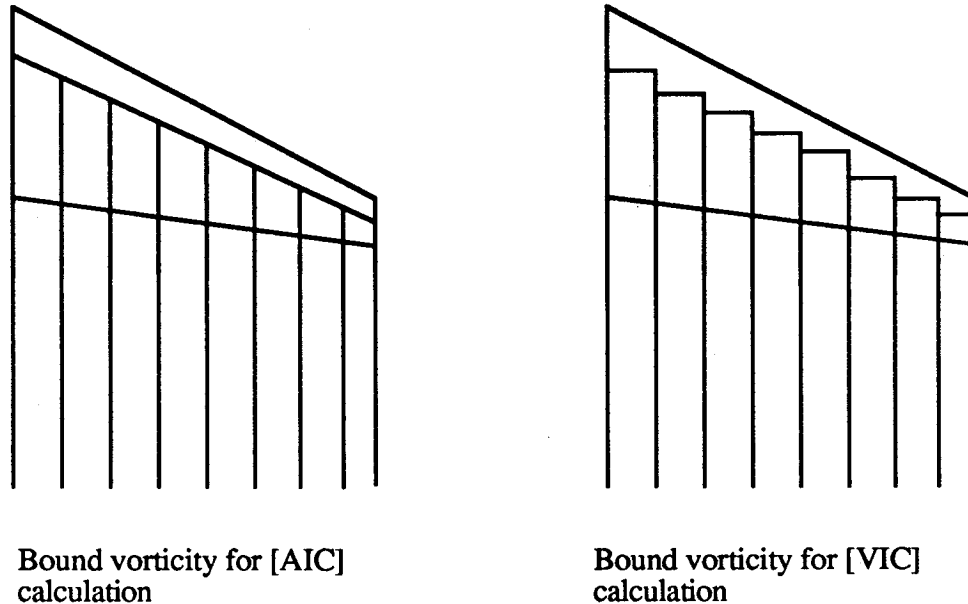
Figure 2.35 bound vorticity placement for near-field velocity estimation

A complete aircraft configuration is modeled by placing trapezoidal lifting elements on the mean surface in an appropriate manner. Several factors determine whether or not a lifting surface model is appropriate. Thin lifting surfaces (such as wings and tails) are best modeled by placing lifting elements along the mean camber line. If control surfaces are present, these are approximated by dividing the lifting surface chordwise at the hingeline into a separate control surface element.

The number of panels required to compute accurate airloads is best determined by a trial and error procedure where the number of panels are increased until the desired accuracy is achieved. Typically, the estimation of drag loads requires significantly more panels than the prediction of other forces and moments. The best results are obtained when the panel spacing does not vary abruptly and the trailing wake vorticity of one element does not pass too close to the control points of another element. Fuselages and other bodies that do not

34

have distinct and sharp trailing edges may be modeled by placing a set of vertical and horizontal lifting panels along the bodies' centerline, where the panels have the same projected shape as the body (Fig. 2.36) . Figure 2.37 shows the results of an analysis where this fuselage model is compared with experimental data [Ref. 18]. This approximation accurately predicts the wing-fuselage interference that reduces $C_{L\alpha}$ and static pitch stability.

Front

Actual Fuselage Geometry

Front

Fuselage Vortex Lattice Model
Fuselage is modeled as two low
aspect ratio lifting surfaces.
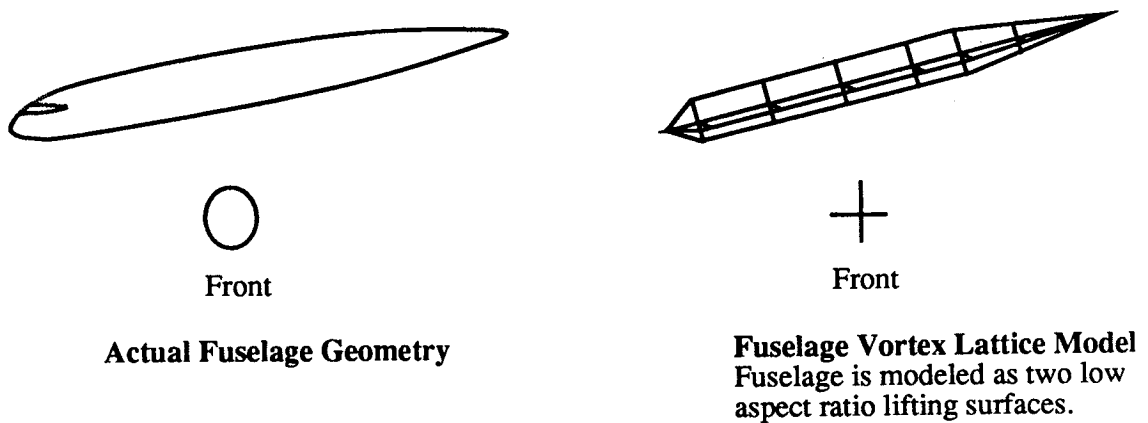
Figure 2.36 fuselage vortex lattice model

Pitching Moment vs Lift Coefficient
Fuselage Vortex Lattice Model
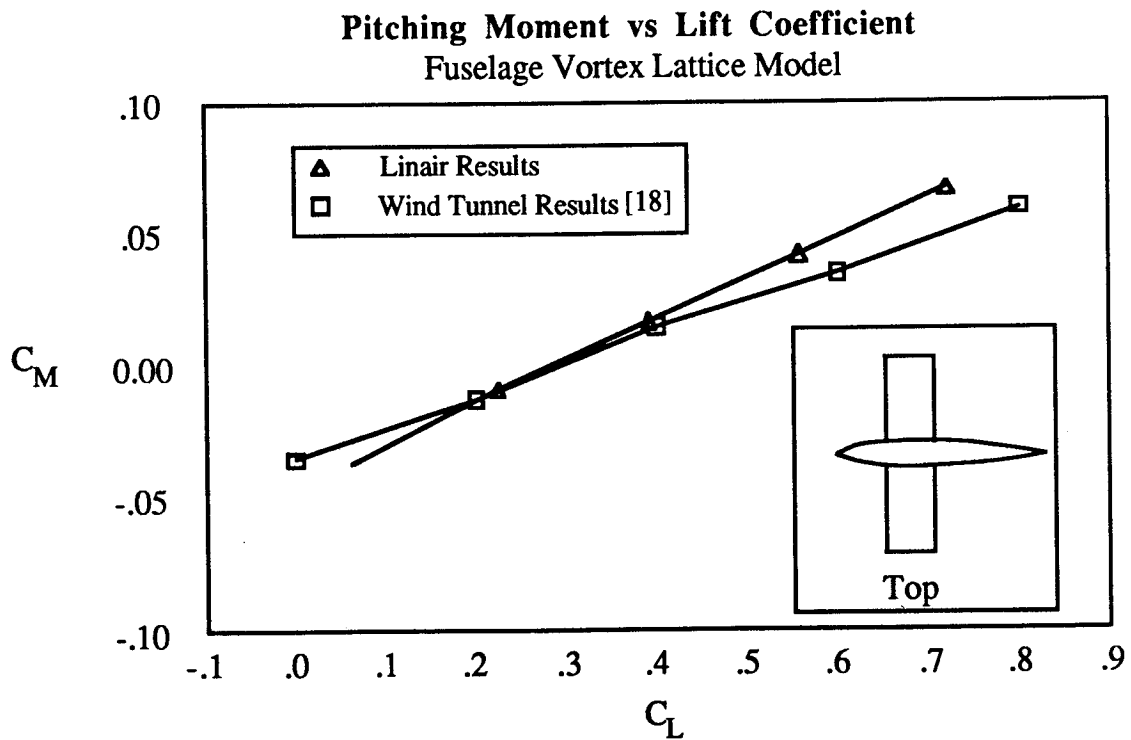
Figure 2.37 fuselage-wing model verification

The vortex lattice model for the F-8 OWRA with 45 degree oblique sweep is shown in figure 2.38. There are 30 spanwise panels along the wing and 48 more panels which comprise the fuselage and tail. One aspect of the wing panelling, which improves the modelling accuracy for oblique wing aircraft, is that the wing's trailing vorticity is parallel to the streamwise direction. This type of panelling is preferred because it places the vorticity closer to its true physical location and the spacing of the wake vorticity remains uniform. Figure 2.39 shows how a wing with a fixed planform is panelled at several oblique sweep angles using streamwise trailing vorticity.

3/4 view

Front   Top

Side
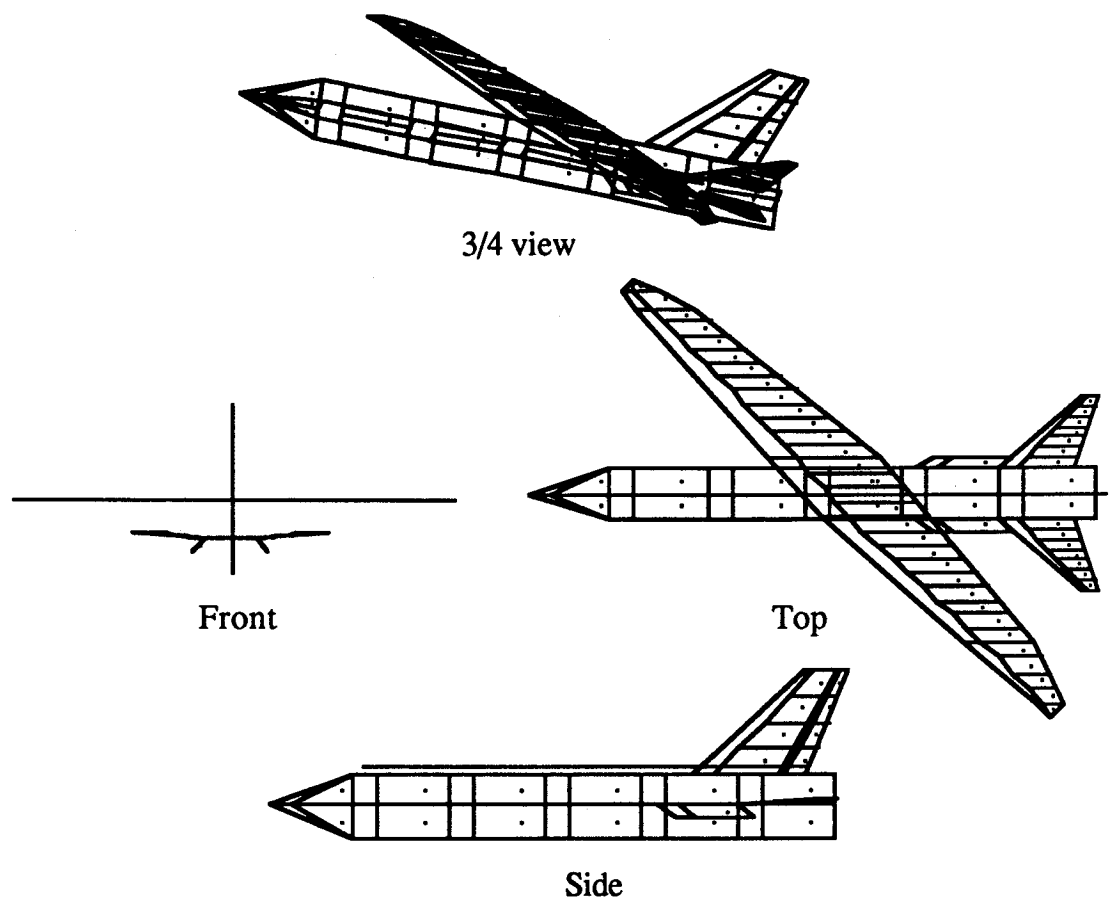
Figure 2.38 F-8 OWRA vortex lattice model, 45° sweep
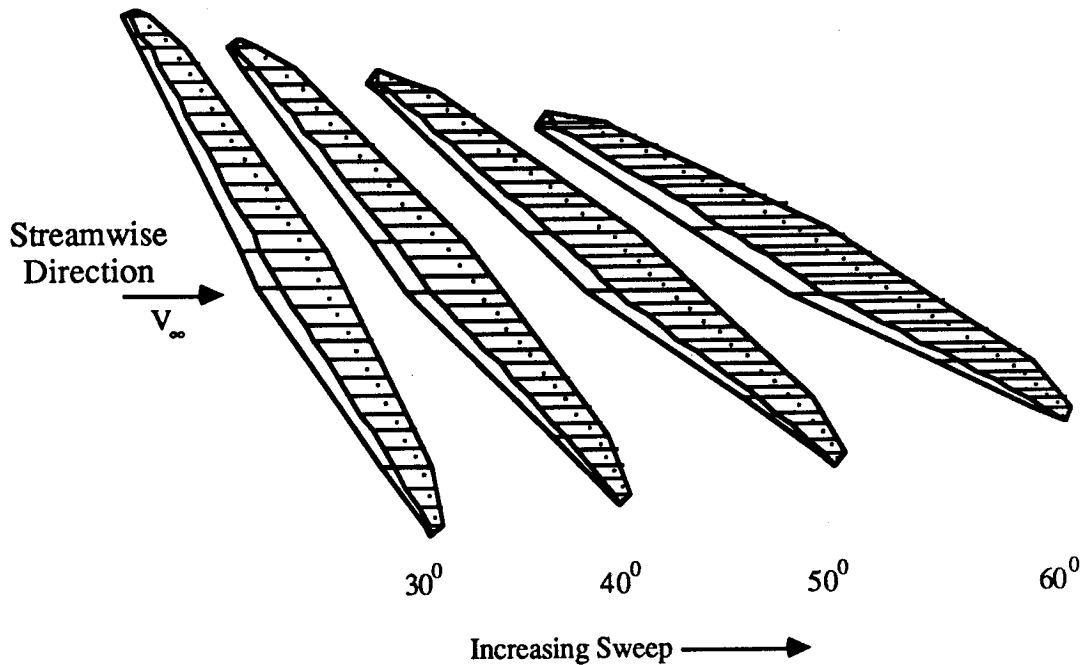
Figure 2.39 streamwise trailing vorticity used for wing vortex lattice model

The accuracy of LINAIR in modelling the F-8 OWRA configuration is shown in figures 2.42 - 2.50 where the results from LINAIR are compared to both PANAIR and wind tunnel results, from references [17] and [13] respectively. The wind tunnel results comparison (Fig. 2.46 - 2.50) are presented for OWRA configuration 3 (Fig. 2.2) and the PANAIR results (Fig. 2.41 - 2.45) are for configuration 2. Figure 2.40 shows the surface panel model used in the PANAIR calculations. Notice that the wind tunnel comparisons include a limiting mark which indicates the largest value of C_L at which attached flow is expected (based upon equation 2.6). The LINAIR prediction for the airloads shows acceptable agreement with both the PANAIR predictions and the wind tunnel results (in the attached flow region) for all forces and moments except yawing moment. As was mentioned previously, the yawing moment is dominated by a fuselage-wing interference effect that depends upon the thickness of both bodies. LINAIR is not capable of modelling this phenomenon because it is a thin lifting surface method. Therefore, the variation of C_N with changing α will be estimated from wind tunnel data in the integrated design synthesis procedure. As was shown in figure 2.33, C_N is relatively insensitive to configuration

37

changes if the sweep angle remains constant, therefore little loss in accuracy is expected from using wind tunnel results to predict C_N trends.
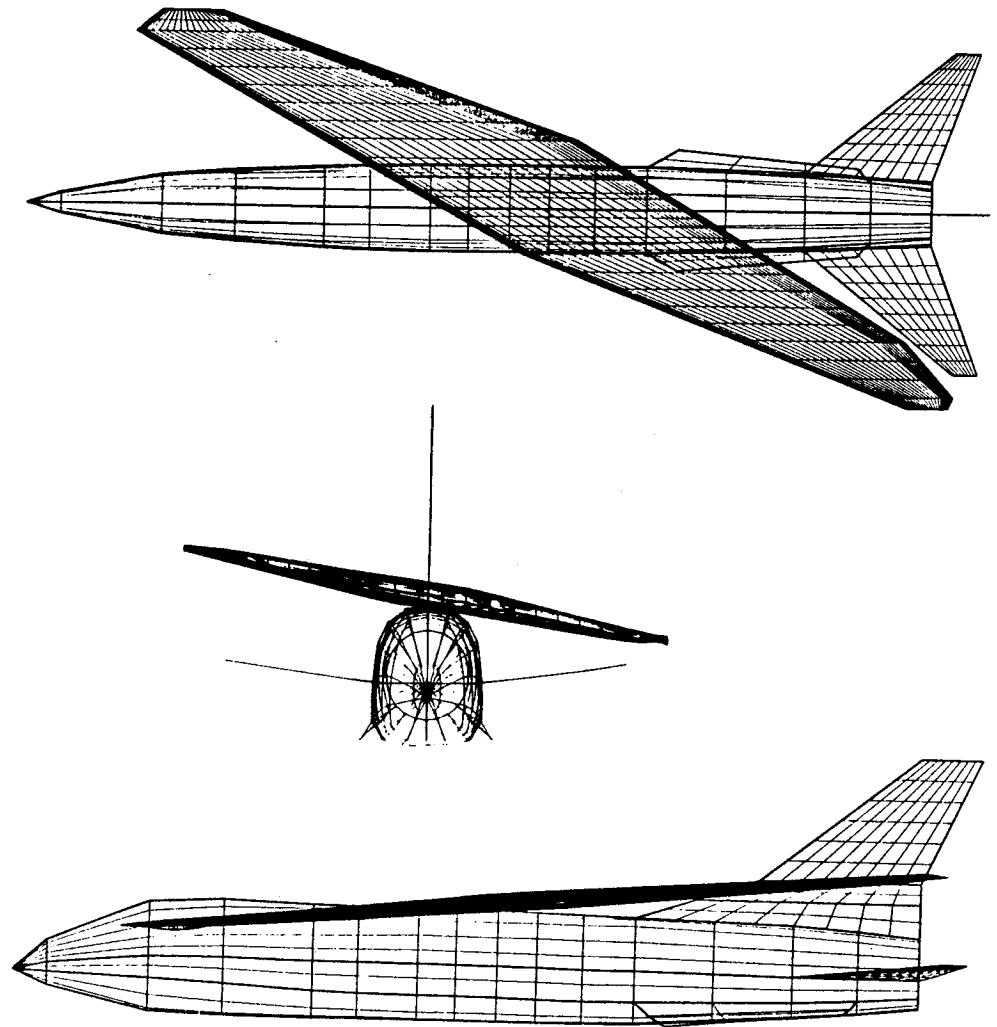
Figure 2.40 PANAIR surface panel model, F-8 OWRA, 45° sweep

Lift Coefficient vs Angle of Attack
65 deg. sweep, M=0.6
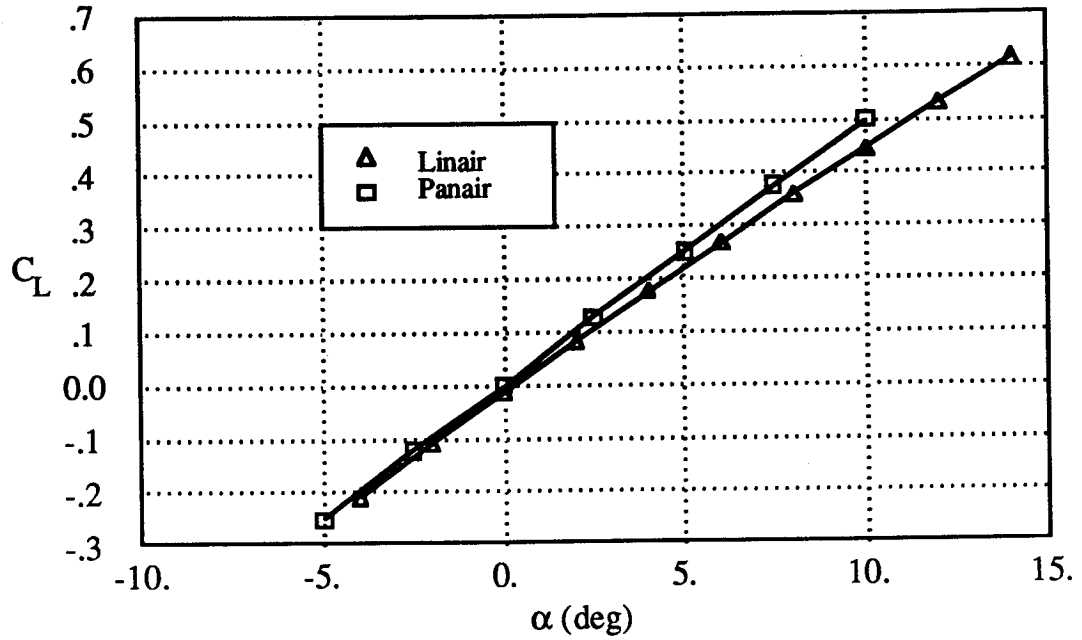
Figure 2.41 lift coefficient vs. angle of attack

Sideforce Coefficient vs Lift Coefficient
65 deg. sweep, M=0.6
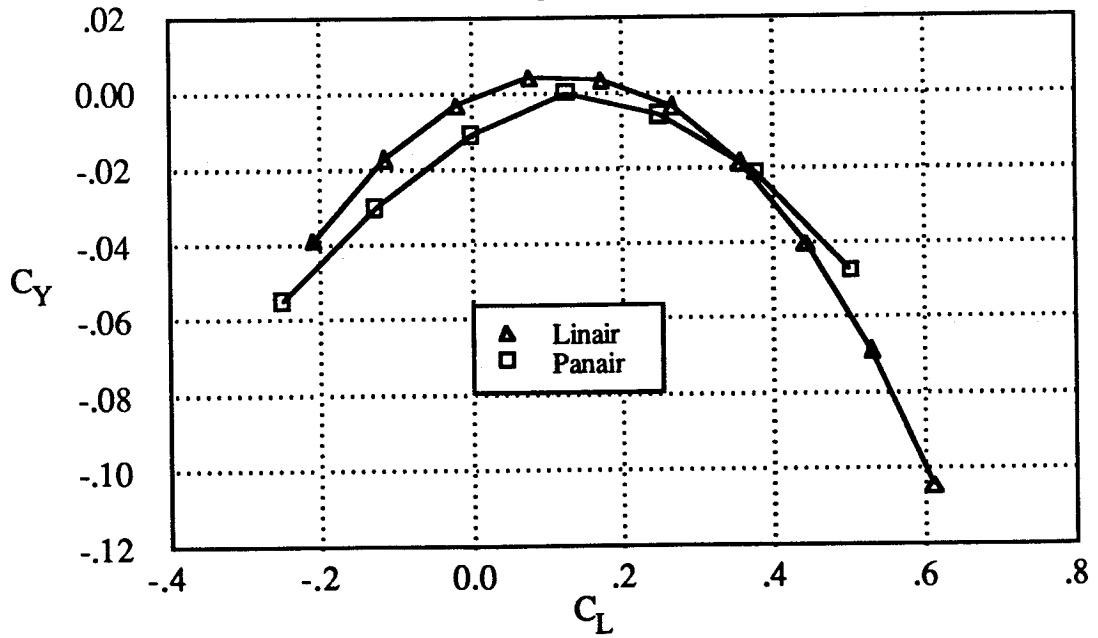
Figure 2.42 sideforce coefficient vs. lift coefficient

39

Rolling Moment Coefficient vs Lift Coefficient
65 deg. sweep, M=0.6
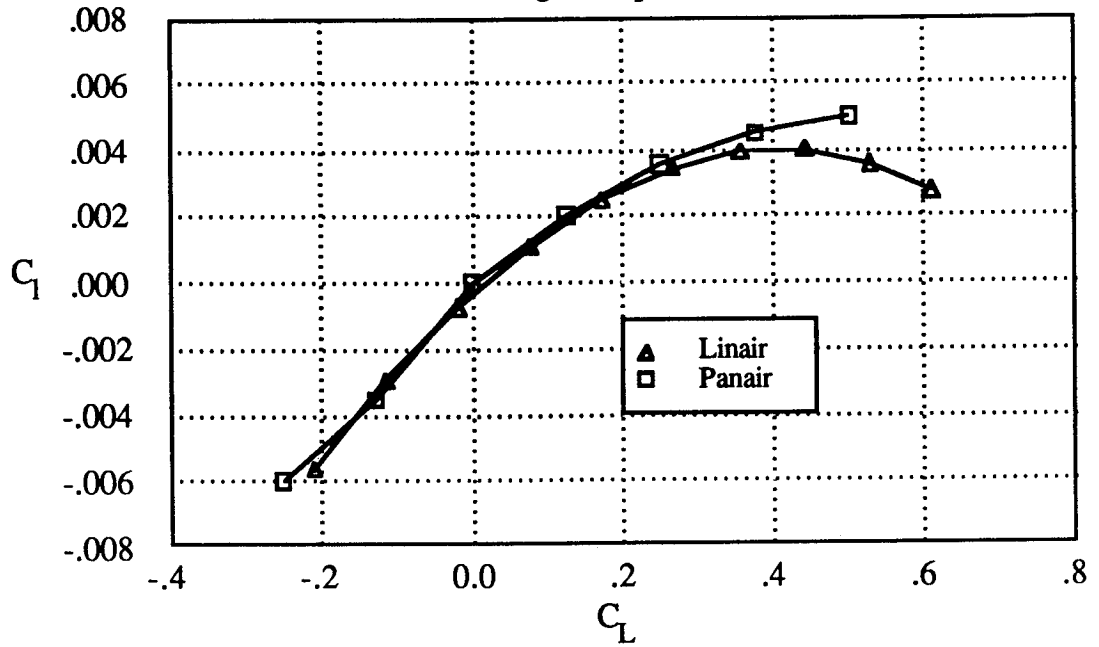
Figure 2.43 rolling moment coefficient vs. lift coefficient

Pitching Moment Coefficient vs Lift Coefficient
65 deg. sweep, M=0.6
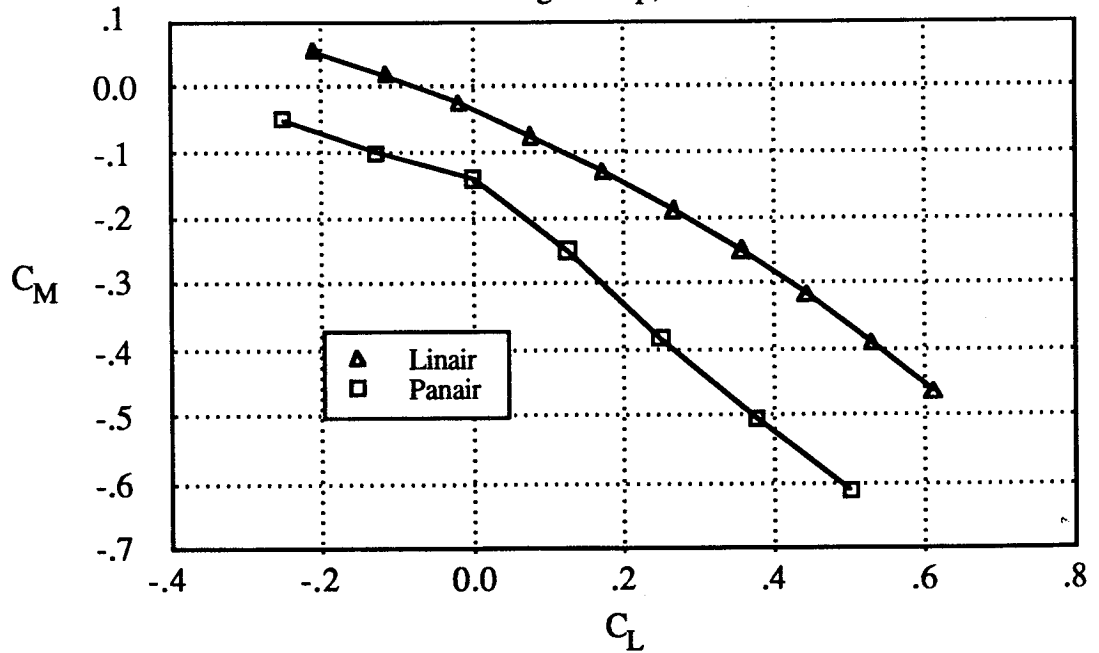
Figure 2.44 pitching moment coefficient vs. lift coefficient

40

Yawing Moment Coefficient vs Lift Coefficient
65 deg. sweep, M=0.6
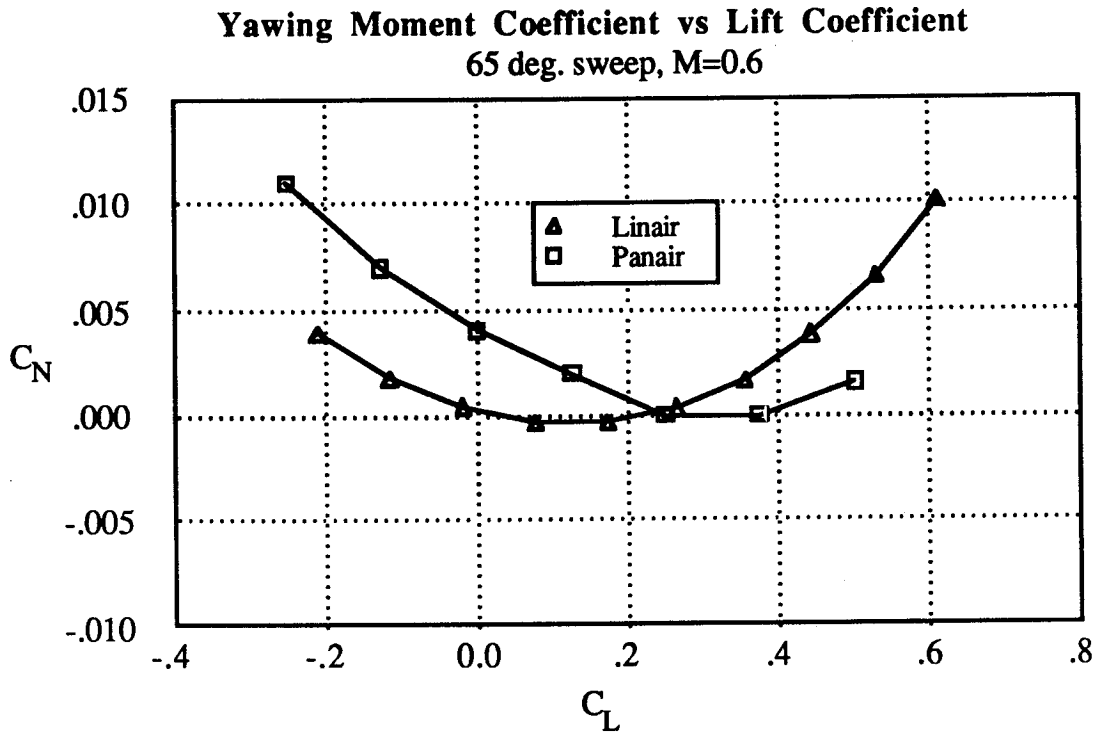
Figure 2.45 yawing moment coefficient vs. lift coefficient

Lift Coefficient vs Angle of Attack
65 deg. sweep, M=0.6
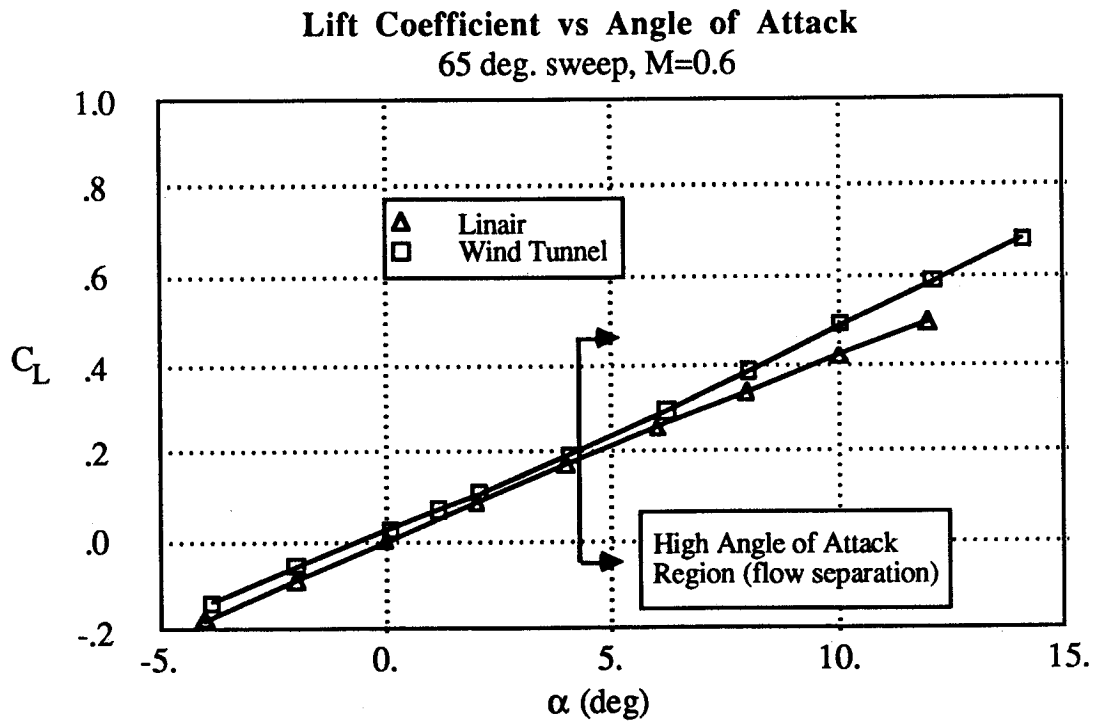
Figure 2.46 lift coefficient vs. angle of attack

41

Sideforce Coefficient vs Lift Coefficient
65 deg. sweep, M=0.6
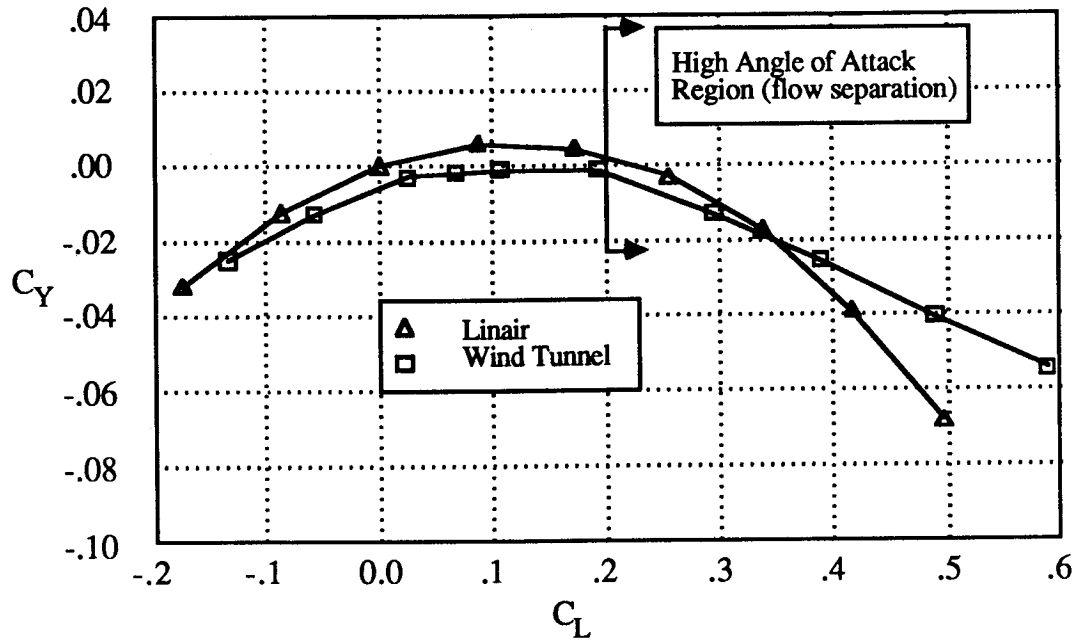
Figure 2.47 sideforce coefficient vs. lift coefficient

Pitching Moment Coefficient vs Lift Coefficient
65 deg. sweep, M=0.6
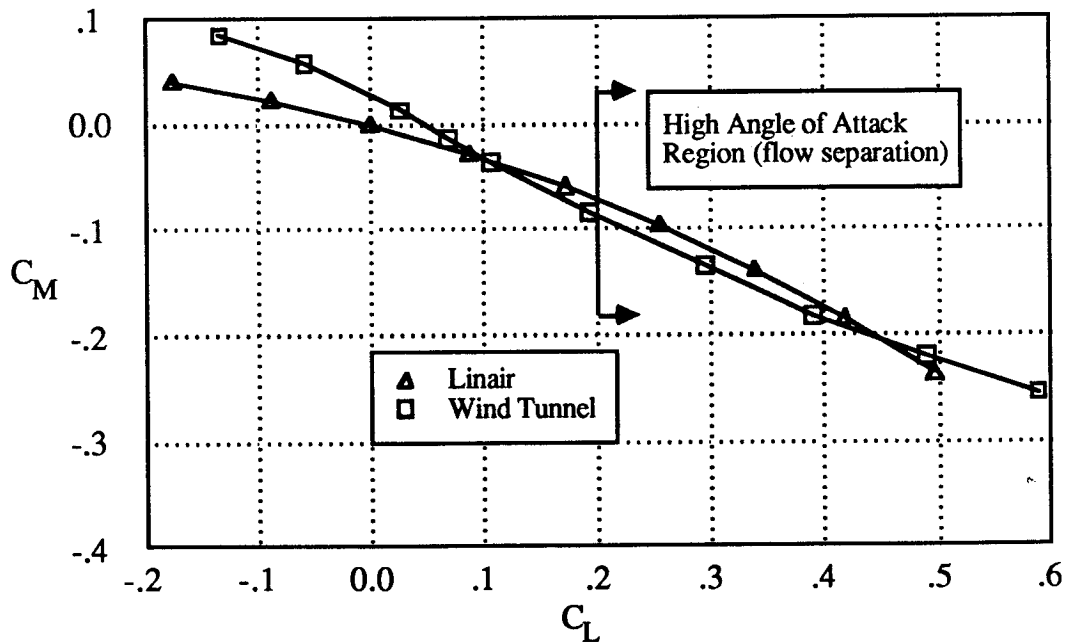
Figure 2.48 pitching moment coefficient vs. lift coefficient

42

Rolling Moment Coefficient vs Lift Coefficient
65 deg. sweep, M=0.6
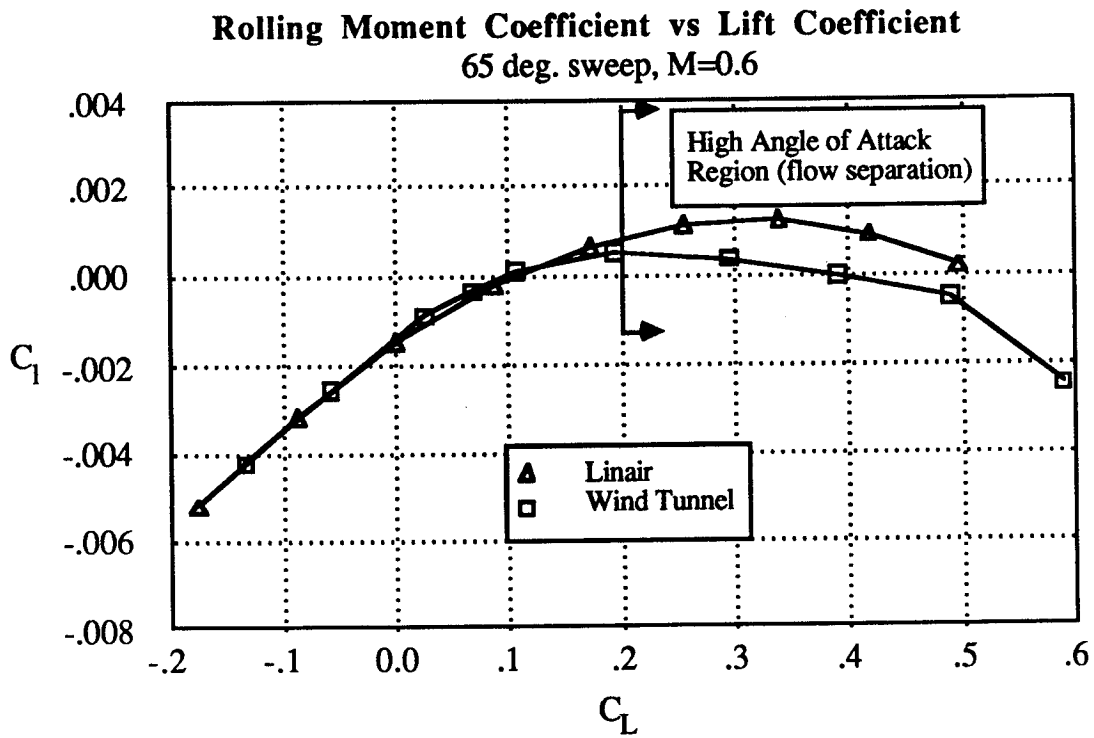
Figure 2.49 rolling moment coefficient vs. lift coefficient

Yawing Moment Coefficient vs Lift Coefficient
65 deg. sweep, M=0.6
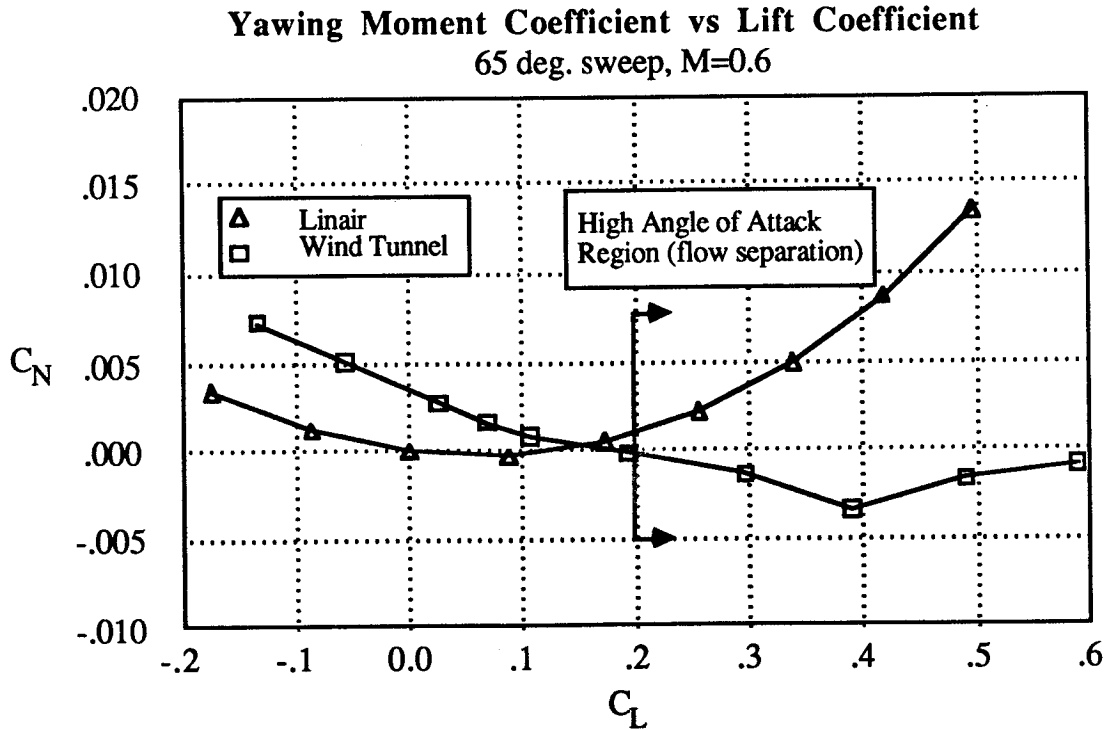
Figure 2.50 yawing moment coefficient vs. lift coefficient

Figures 2.51 - 2.55 display the comparison between Linair and wind tunnel results for the aircraft at (+ & -) 5 degrees sideslip. These plots show that Linair predictions are in good agreement with the wind tunnel results for cases with sideslip. The results for C_N show that the change in yawing moment with sideslip is accurately predicted although the C_N variation with angle of attack must be estimated from wind tunnel results.

Lift Coefficient vs Angle of Attack
65 deg. Sweep, M=0.8

Legend:
- △ Wind Tunnel, Beta=-5 deg.
- □ Wind Tunnel, Beta=5 deg.
- ◆ Linair, Beta=-5 deg.
- ▽ Linair, Beta=5 deg.

High Angle of Attack Region (flow separation)

C_L axis: 1.0, .8, .6, .4, .2, .0, -.2
α (deg) axis: -5., 0., 5., 10., 15., 20.
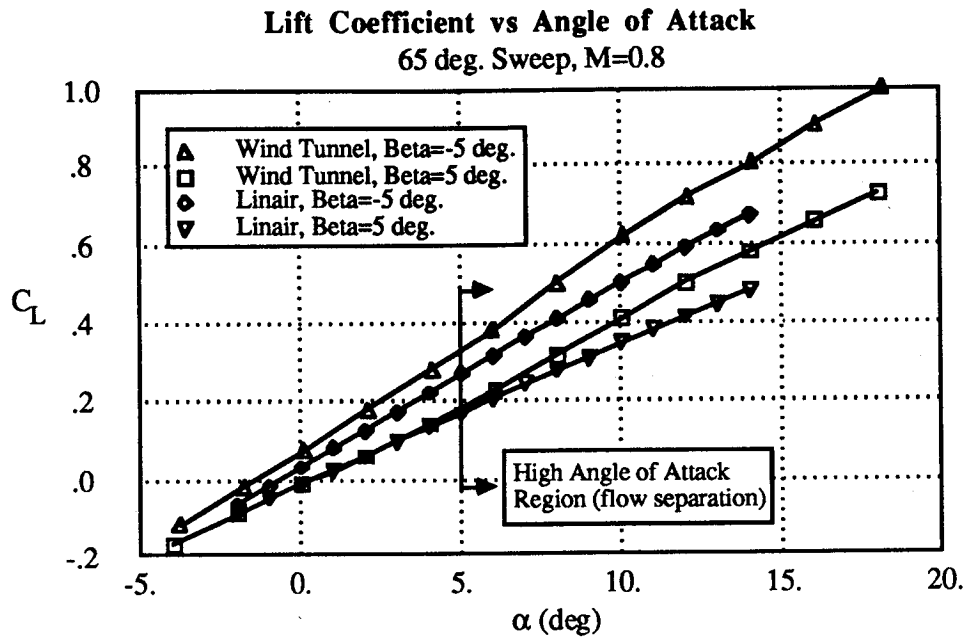
Figure 2.51 lift coefficient vs. angle of attack

Sideforce vs Lift Coefficient
65 deg. Sweep, M=0.8

High Angle of Attack Region (flow separation)

Legend:
- △ Wind Tunnel, Beta=-5 deg.
- □ Wind Tunnel, Beta=5 deg.
- ◆ Linair, Beta=-5 deg.
- ▽ Linair, Beta=5 deg.

C_Y axis: .15, .10, .05, 0.00, -.05, -.10, -.15, -.20, -.25
C_L axis: -.2, .0, .2, .4, .6, .8, 1.0
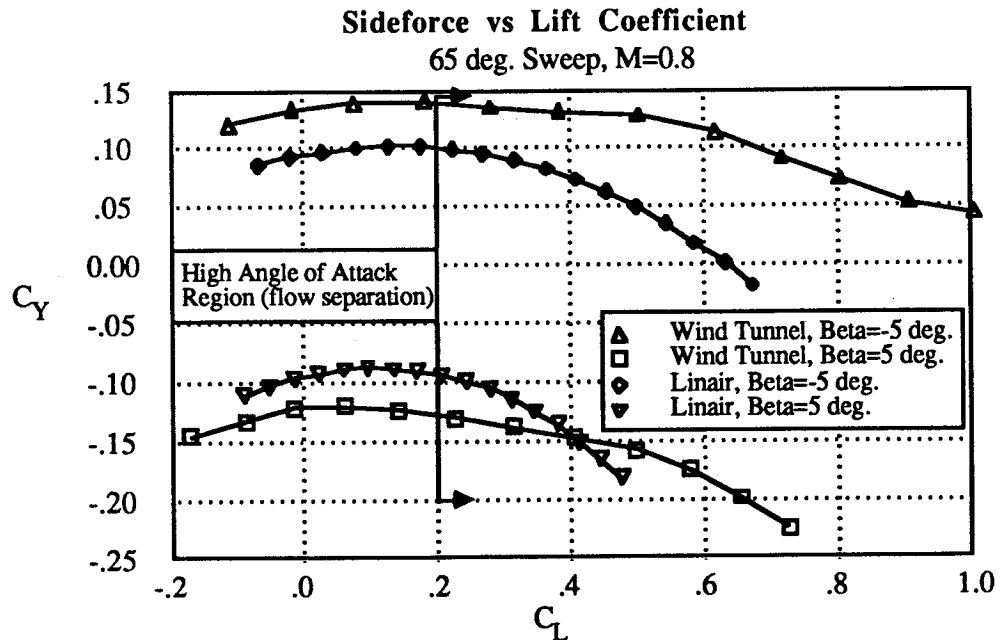
Figure 2.52 sideforce coefficient vs. lift coefficient

44

Rolling Moment Coefficient vs Lift Coefficient
65 deg. Sweep, M=0.8

High Angle of Attack
Region (flow separation)

▲	Wind Tunnel, Beta=-5 deg.
▫	Wind Tunnel, Beta=5 deg.
◆	Linair, Beta=-5 deg.
▽	Linair, Beta=5 deg.

C_l

C_L
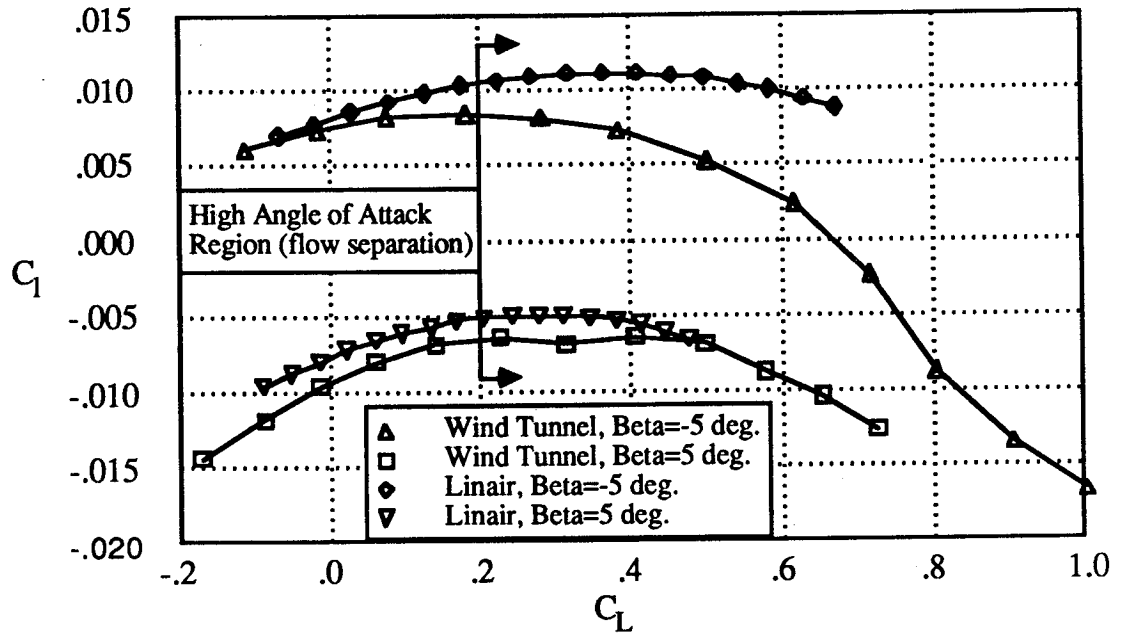
Figure 2.53 rolling moment coefficient vs. lift coefficient

Pitching Moment Coefficient vs Lift Coefficient
65 deg. Sweep, M=0.8

▲	Wind Tunnel, Beta=-5 deg.
▫	Wind Tunnel, Beta=5 deg.
◆	Linair, Beta=-5 deg.
▽	Linair, Beta=5 deg.

C_M

High Angle of Attack
Region (flow separation)

C_L
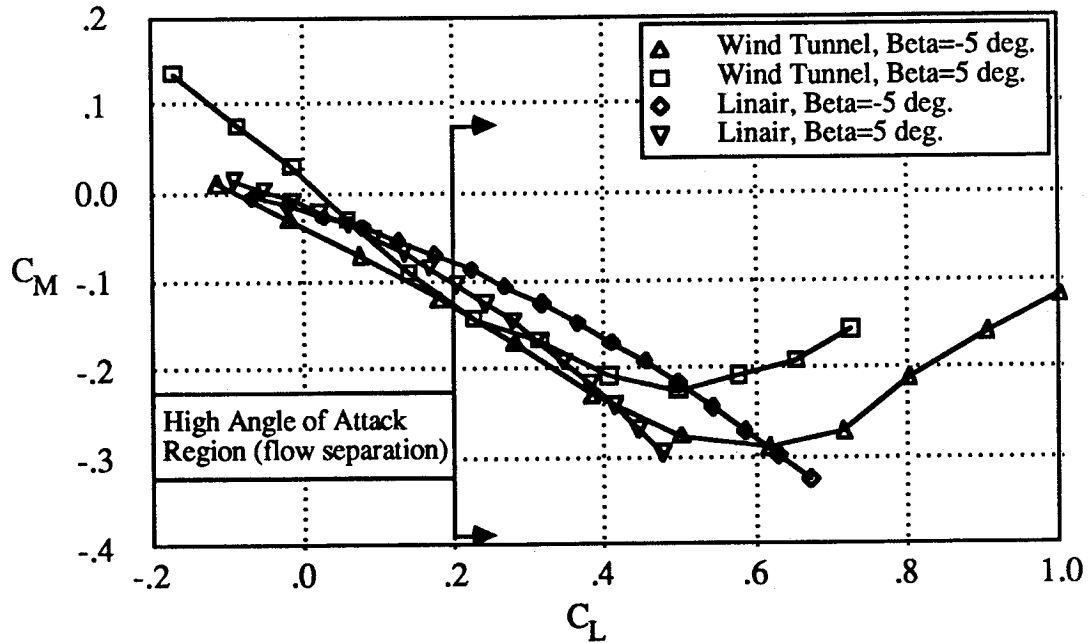
Figure 2.54 pitching moment coefficient vs. lift coefficient

45

Yawing Moment Coefficient vs Lift Coefficient
65 deg. Sweep, M=0.8
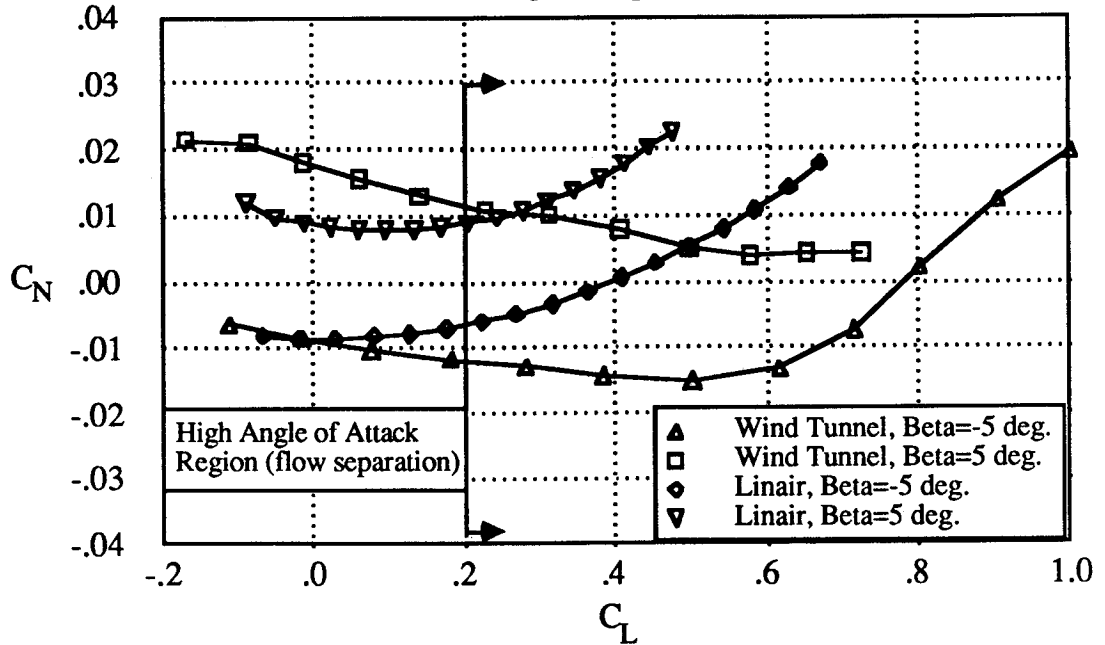
Figure 2.55 Yawing moment coefficient vs. lift coefficient

For each calculation of the airloads, the [AIC] and [VIC] matrices must be evaluated and a linear system with n unknowns (equation 2.19) must be solved. In the integrated design synthesis the airloads must be calculated each time the configuration changes and this may require excessive CPU time for a design with a large number of panels. One method to reduce the amount of numerical calculation is to assume that the [AIC] and [VIC] matrices do not change significantly as the wing is repositioned on the fuselage. Referring to equation 2.19 this implies that only the vector {B}, which represents the flow boundary conditions, changes as the configuration is altered. This assumption is only justifiable if the planform of the wing remains unchanged and the relative position of the wing and fuselage does not change by a 'large' amount. Figures 2.58 - 2.62 compare the airloads calculated using the approximated [AIC] and [VIC] matrices, to those calculated with exact matrices. The results are shown for configurations that have large variations in wing position relative to the fuselage. For the approximated cases, the original [AIC] and [VIC] matrices used correspond to the nominal aircraft shown in figure 2.56. The results clearly show that assuming the [AIC] and [VIC] matrices are constant has only a small effect on the accuracy of the es-

timated airloads, but significantly reduces the required CPU time for repeated aerodynamic calculations.
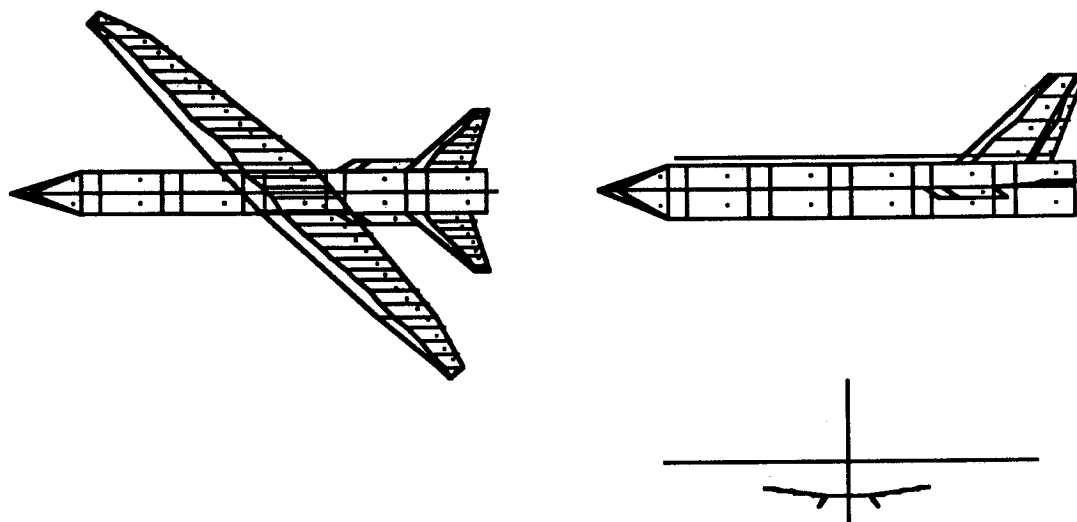
Figure 2.56 nominal configuration (zero wing bank)
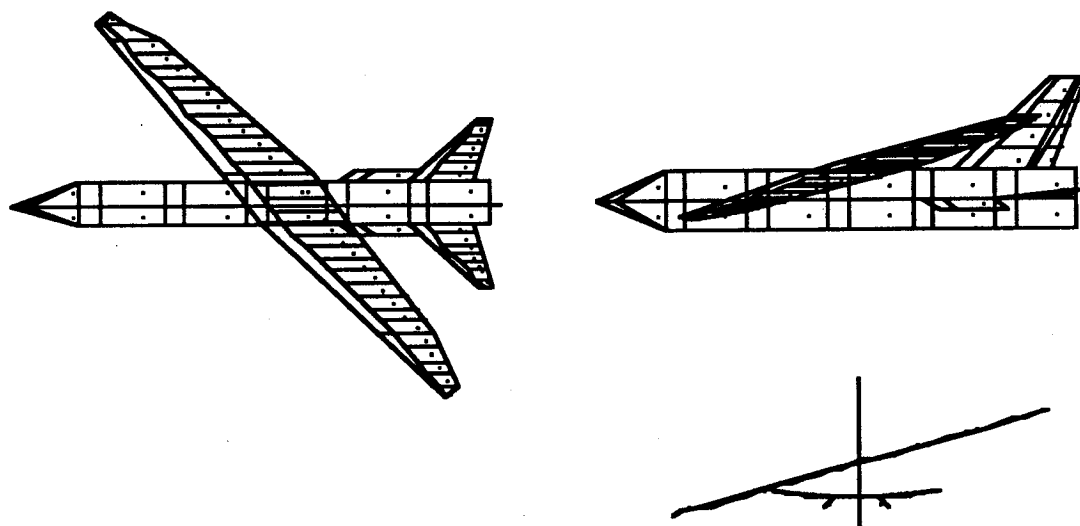
Figure 2.57 modified configuration (15 deg. wing bank)

Lift Coefficient vs Angle of Attack
45 deg. sweep, M=0.6
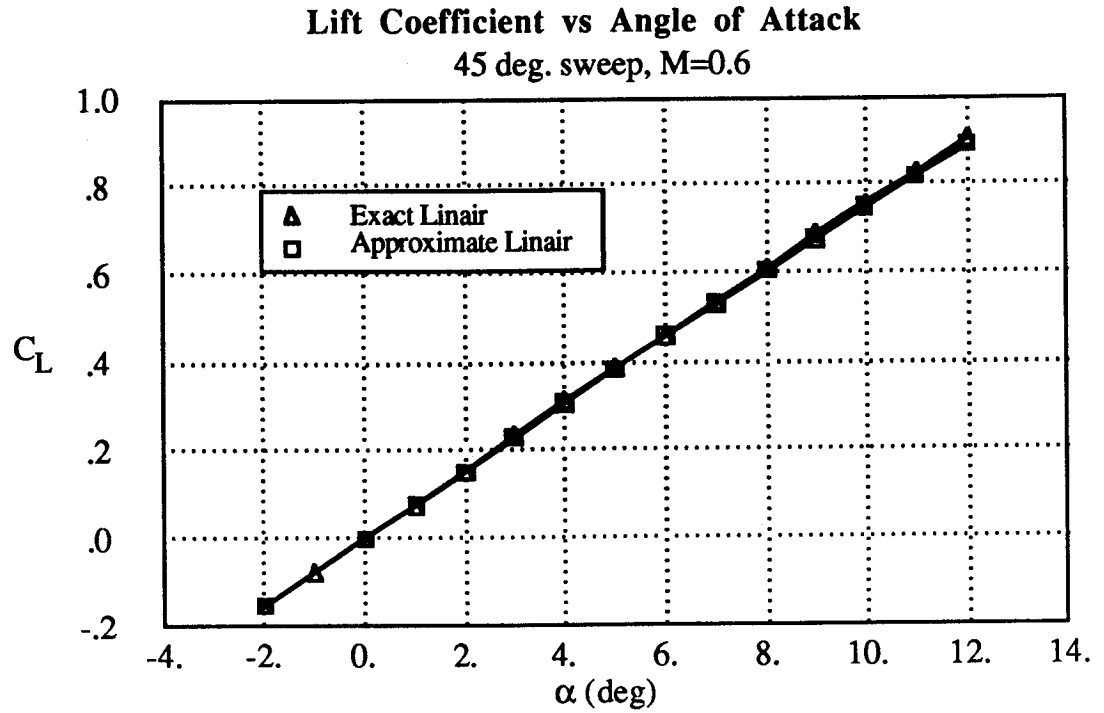
Figure 2.58 lift coefficient vs. angle of attack

Sideforce Coefficient vs Lift Coefficient
45 deg. sweep, M=0.6
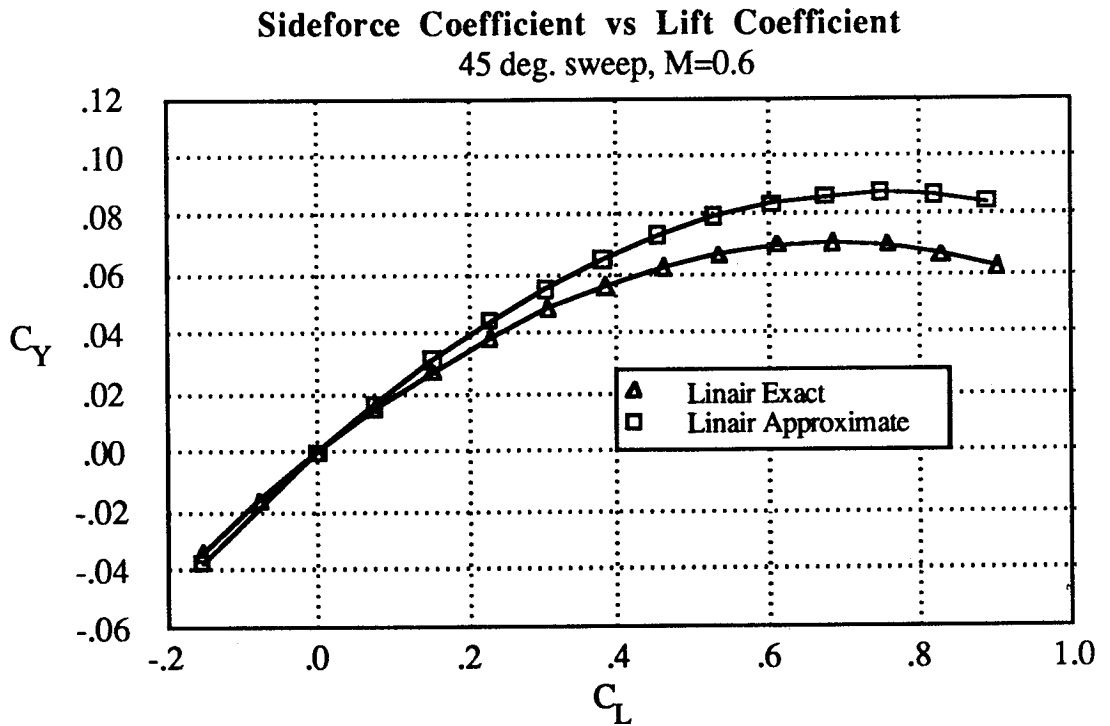
Figure 2.59 sideforce coefficient vs. lift coefficient

48

Pitching Moment Coefficient vs Lift Coefficient
45 deg., sweep M=0.6
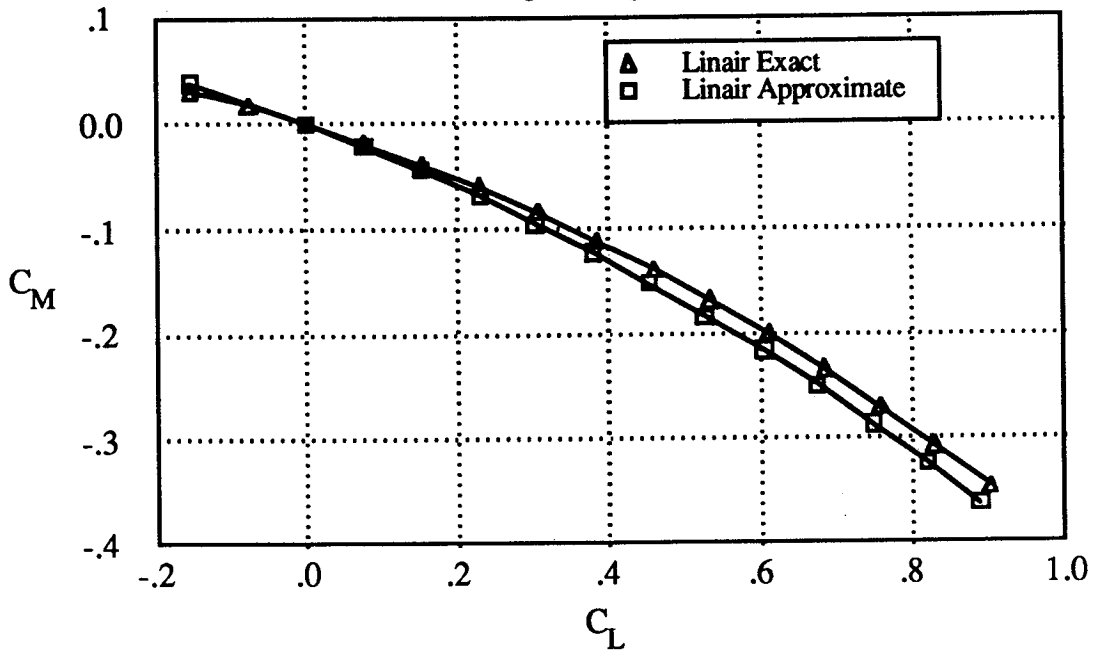
Figure 2.60 pitching moment coefficient vs. lift coefficient

Rolling Moment Coefficient vs Lift Coefficient
45 deg. sweep, M=0.6
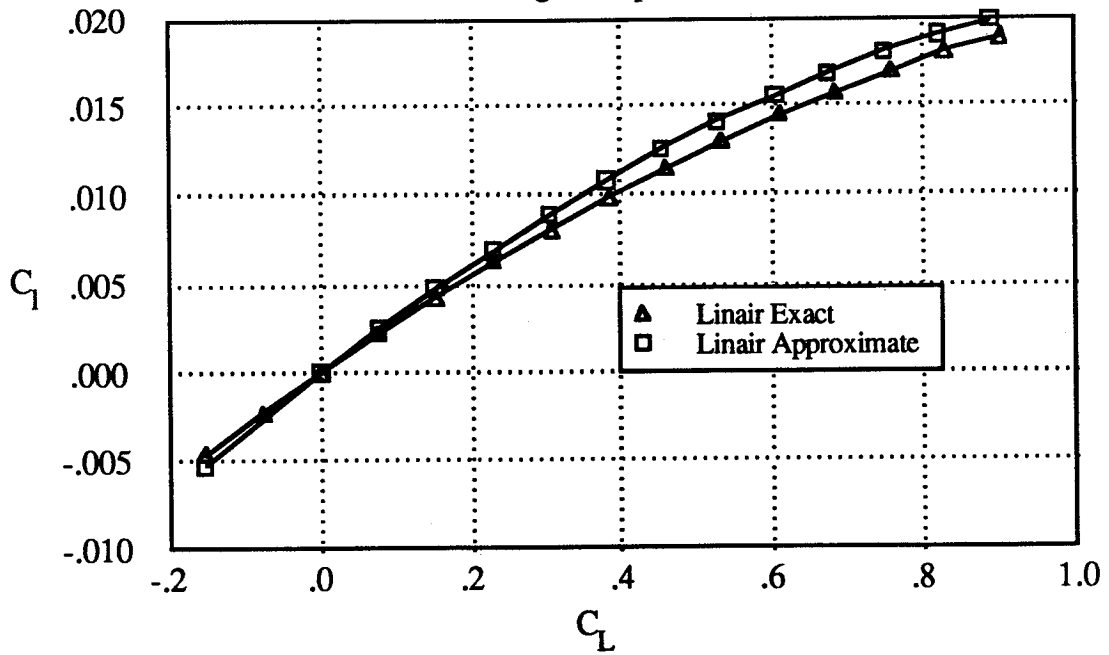
Figure 2.61 rolling moment coefficient vs. lift coefficient

Yawing Moment Coefficient vs Lift Coefficient
45 deg. sweep, M=0.6
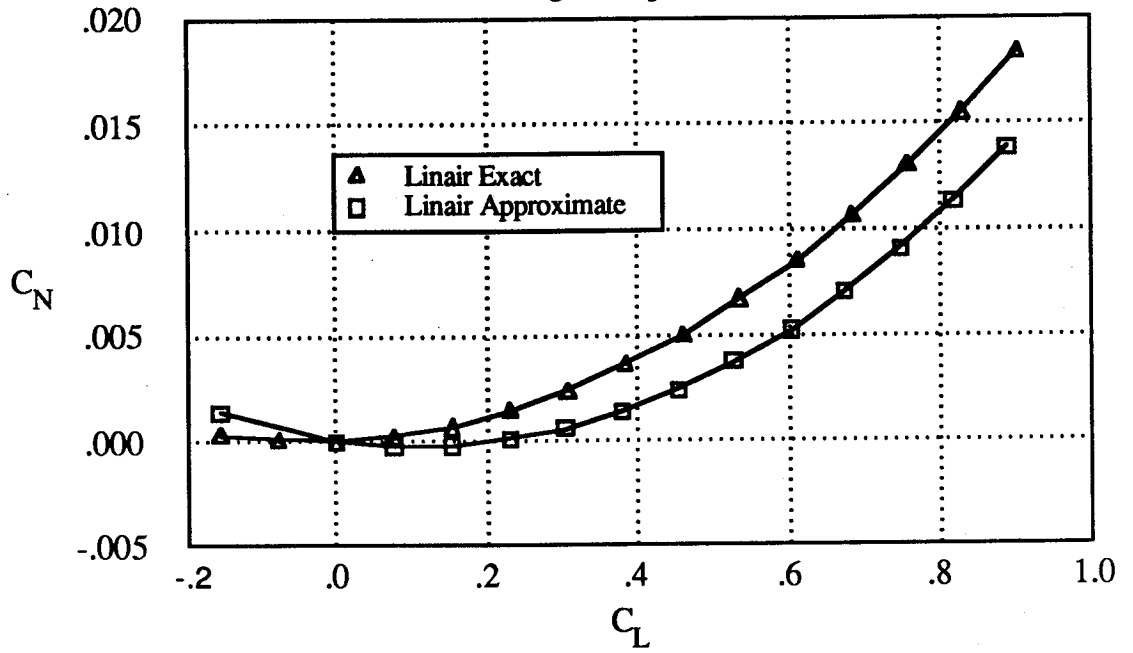
Figure 2.62 yawing moment coefficient vs. lift coefficient

Chapter 3

Dynamic Response
of Oblique Wing Aircraft

The dynamic response of an oblique wing aircraft to control inputs and gust disturbances differs from a conventional aircraft because of aerodynamic and inertial couplings inherent to the asymmetric configuration. In the first section of this chapter the impact of configuration asymmetry on dynamic response and controllability will be investigated using linearized dynamics models of the six degree of freedom aircraft. Aerodynamic stability and control derivatives for the equations of motion are calculated using the vortex lattice method presented in chapter 2. The results obtained by analyzing the equations of motion demonstrate the significance of both aerodynamic and inertia coupling on the degradation of oblique wing aircraft handling qualities. A simple analysis provides explanations for the lack of controllability in some proposed oblique wing configurations. The problem of insufficient dynamic controllability is further investigated in section 3.3 where the OWRA's closed loop response is studied, using several types of controllers. A new model following scheme (reduced order model following) is presented and its advantages for oblique wing control are investigated.

3.1 Linearized 6 D.O.F. Equations of Motion for the Rigid Oblique Wing Aircraft

Figure 3.1 shows the body axis coordinate system (B) in which the equations of motion are derived. Wind axes are also shown to clarify the definition of angles of attack and sideslip. The body axes are aligned with the x axis along the fuselage centerline and the z axis in the vertical plane of symmetry of the fuselage. The origin of the axes lies at the aircraft's mass center.
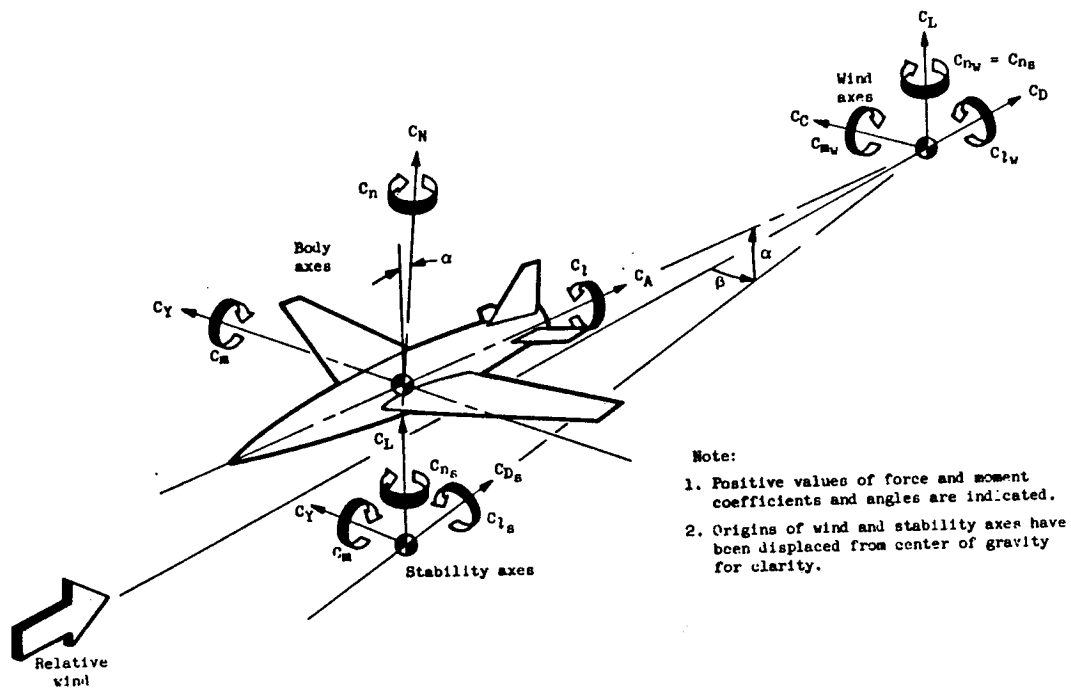
Figure 3.1 axes systems for the rigid aircraft

Newton's laws of motion applied to a rigid body with three translational and three rotational degrees of freedom are:

The right hand side of equations 3.1 and 3.2 can be linearized by defining the following

$$(3.1) \qquad \vec{F} = m \, [\, \frac{\overset{B}{\vec{V}}}{} + \vec{\omega}^{B\text{-}I} \times \vec{V} \,]$$

$$(3.2) \qquad \vec{M} = \bar{\bar{I}} \cdot \frac{\overset{B}{\vec{\omega}^{B\text{-}I}}}{} + \vec{\omega}^{B\text{-}I} \times \bar{\bar{I}} \cdot \vec{\omega}^{B\text{-}I}$$

where:

$\vec{\omega}^{B\text{-}I}$ = Angular velocity with respect to inertial space

$\vec{V}$ = Velocity of the mass center with respect to inertial space

$\dfrac{\overset{B}{\vec{V}}}{}$ = Time derivative of V in the (B) axis system

52

$$\frac{\overset{B}{\dot{\vec{\omega}}^{B\text{-}I}}}{} = \text{Time derivative of w in the (B) axis system}$$

$$\overset{\bullet}{I} = \text{Inertia tensor expressed in (B) axes}$$

$$\overset{\bullet}{I} = \begin{bmatrix} I_{xx} & I_{xy} & I_{xz} \\ & I_{yy} & I_{yz} \\ (\text{SYM}) & & I_{zz} \end{bmatrix}$$

$\vec{F}, \vec{M} = $ Net external force and moment acting on the aircraft

perturbation expressions for V & $\omega^{B\text{-}I}$ (which correspond to 1-g level flight). Where (u, v, w, p, q, r) are perturbation quantities. Substituting for V & $\omega^{B\text{-}I}$ into equa-

$$(3.3, 3.4) \quad \vec{V} = \begin{bmatrix} u_o + u \\ v \\ w_o + w \end{bmatrix} \qquad \vec{w}^{B\text{-}I} = \begin{bmatrix} p \\ q \\ r \end{bmatrix}$$

tions 3.1 and 3.2 and dropping higher order terms:

The net forces and moments consist of aerodynamic, propulsive, and gravity terms:

$$\left[\begin{array}{c} \vec{F} \\ \hline \vec{M} \end{array}\right] = \left[\begin{array}{ccc:ccc} m & & & & & \\ & m & & & 0 & \\ & & m & & & \\ \hdashline & 0 & & & \overset{\bullet}{I} & \end{array}\right] \left[\begin{array}{c} \dot{u} \\ \dot{v} \\ \dot{w} \\ \dot{p} \\ \dot{q} \\ \dot{r} \end{array}\right] + \left[\begin{array}{ccc:ccc} & & & 0 & w_o & 0 \\ & 0 & & -w_o & 0 & u_o \\ & & & 0 & -u_o & 0 \\ \hdashline & 0 & & & 0 & \end{array}\right] \left[\begin{array}{c} u \\ v \\ w \\ p \\ q \\ r \end{array}\right]$$

Equation (3.5)

53

Because the moment reference is at the aircraft mass center, the moments due to gravity

$$(3.6) \qquad \vec{F} = \vec{F}_{aero} + \vec{F}_{grav} + \vec{F}_{prop}$$

$$(3.7) \qquad \vec{M} = \vec{M}_{aero} + \vec{M}_{grav} + \vec{M}_{prop}$$

forces are always zero. The external loads are now linearized using a Taylor Series expansion and dropping all terms with order greater than one:

Where it is assumed that the propulsive forces are appropriate for 1-g level flight trim and

$$(3.8) \qquad \vec{F} = \vec{F}_{aero}^{o} + \vec{F}_{grav}^{o} + \vec{F}_{prop}^{o} + \left[\frac{\delta F_i}{\delta x_j} \right] \vec{x} + \left[\frac{\delta F_i}{\delta d_j} \right] \vec{d}$$

$$(3.9) \qquad \vec{M} = \vec{M}_{aero}^{o} + \left[\frac{\delta M_i}{\delta x_j} \right] \vec{x} + \left[\frac{\delta M_i}{\delta d_j} \right] \vec{d}$$

where:

$$\vec{x} = (u, v, w, p, q, r, \psi, \theta, \phi)$$

$$\vec{d} = (d_{roll}, d_{pitch}, d_{yaw})$$

are not affected by changes in the aircraft's motion. Aircraft trim therefore implies:

The state vector,x, contains three Euler angles which define the aircraft's orientation rela-

$$\vec{M}_{aero}^{o} + \vec{M}_{prop}^{o} = 0$$

$$\vec{F}_{aero}^{o} + \vec{F}_{grav}^{o} + \vec{F}_{prop}^{o} = 0$$

tive to inertial space as a set of successive rotations about non-orthogonal axes. The linearized expression for the gravity forces in terms of the perturbation Euler angle quantities is:

The linear expansion for the aerodynamic forces and moments is explicitly written as:

$$(3.11) \qquad \vec{F}_{grav} = \begin{bmatrix} -(mg)\sin(\theta_o) \\ 0 \\ (mg)\cos(\theta_o) \end{bmatrix} + \begin{bmatrix} 0 & -mg & 0 \\ 0 & 0 & mg \\ 0 & 0 & 0 \end{bmatrix} \begin{bmatrix} \psi \\ \theta \\ \phi \end{bmatrix}$$

54

The control vector (d) consists of generic controls that correspond to deflections of the ap-

$$(3.12) \quad \vec{F}_{aero} = \begin{bmatrix} F_x^o \\ F_y^o \\ F_z^o \end{bmatrix} + \begin{bmatrix} F_{xu} & F_{xv} & \text{------} & F_{xr} \\ F_{yu} & & & \\ F_{zu} & \text{------------} & & F_{zr} \end{bmatrix} \begin{bmatrix} u \\ v \\ w \\ p \\ q \\ r \end{bmatrix}$$

$$+ \begin{bmatrix} F_{x\,droll} & F_{x\,dpitch} & F_{x\,dyaw} \\ F_{y\,droll} & & \\ F_{z\,droll} & \text{--------} & F_{z\,yaw} \end{bmatrix} \begin{bmatrix} d_{roll} \\ d_{pitch} \\ d_{yaw} \end{bmatrix}$$

$$(3.13) \quad \vec{M}_{aero} = \begin{bmatrix} M_{xu} & M_{xv} & \text{--------} & M_{xr} \\ M_{yu} & & & \\ M_{zu} & \text{------------} & & M_{zr} \end{bmatrix} \begin{bmatrix} u \\ v \\ w \\ p \\ q \\ r \end{bmatrix}$$

$$+ \begin{bmatrix} M_{x\,droll} & M_{x\,dpitch} & M_{x\,dyaw} \\ M_{y\,droll} & & \\ M_{z\,droll} & \text{--------} & M_{z\,dyaw} \end{bmatrix} \begin{bmatrix} d_{roll} \\ d_{pitch} \\ d_{yaw} \end{bmatrix}$$

propriate control surfaces to produce roll, pitch , or yaw moments. For the F-8 OWRA roll is caused by antisymmetric elevator deflection, pitch by symmetric elevator deflection, and

55

yaw by rudder deflection. Equations 3.12 - 3.13 are substituted into equation 3.5 to obtain the final form of the linearized equations of motion. Notice that the trim condition has been enforced and that the moments M_x, M_y, M_z, have been re-named L, M, N. Equation 3.14 has the form:

$$
\begin{bmatrix}
m & & & \vdots & & \vdots & \\
& m & & \vdots & 0 & \vdots & 0 \\
& & m & \vdots & & \vdots & \\
\cdots & \cdots & \cdots & \cdots & \cdots & \cdots & \cdots \\
& 0 & & \vdots & \bar{\bar{I}} & \vdots & 0 \\
\cdots & \cdots & \cdots & \cdots & \cdots & \cdots & \cdots \\
& 0 & & \vdots & 0 & \vdots & \begin{matrix} 1 \\ & 1 \\ & & 1 \end{matrix}
\end{bmatrix}
\frac{d}{dt}
\begin{bmatrix} u \\ v \\ w \\ p \\ q \\ r \\ \psi \\ \theta \\ \phi \end{bmatrix}
=
$$

$$
\begin{bmatrix}
F_{xu} & F_{xv} & F_{xw} & F_{xp} & (F_{xq}+w_o) & F_{xr} & 0 & -mg & 0 \\
F_{yu} & \cdots\cdots\cdots & & (F_{yp}-w_o) & F_{yq} & (F_{yr}+u_o) & 0 & 0 & mg \\
F_{zu} & \cdots\cdots\cdots & & F_{zp} & (F_{zq}-u_o) & F_{zr} & \vdots & & 0 \\
L_u & \cdots\cdots\cdots\cdots\cdots\cdots\cdots & & & & L_r & \vdots & & \\
M_u & \cdots\cdots\cdots\cdots\cdots\cdots\cdots & & & & M_r & \vdots & & \\
N_u & \cdots\cdots\cdots\cdots\cdots\cdots\cdots & & & & N_r & \vdots & & 0 \\
0 & \cdots\cdots\cdots & 0 & 0 & \frac{1}{\cos(\theta)} & \vdots & & 0 \\
0 & \cdots\cdots\cdots & 0 & 1 & 0 & \vdots & & 0 \\
0 & 0 & 0 & 1 & 0 & \sec(\theta) & 0 & 0 & 0
\end{bmatrix}
\begin{bmatrix} u \\ v \\ w \\ p \\ q \\ r \\ \psi \\ \theta \\ \phi \end{bmatrix}
$$

$$
+
\begin{bmatrix}
F_{x\delta r} & F_{x\delta p} & F_{x\delta y} \\
F_{y\delta r} & \vdots & \vdots \\
F_{z\delta r} & \vdots & \vdots \\
L_{\delta r} & \vdots & \vdots \\
M_{\delta r} & \vdots & \vdots \\
N_{\delta r} & \cdots\cdots\cdots & N_{\delta y} \\
0 & \cdots\cdots\cdots & 0 \\
0 & \cdots\cdots\cdots & 0 \\
0 & 0 & 0
\end{bmatrix}
\begin{bmatrix} \delta_{roll} \\ \delta_{pitch} \\ \delta_{yaw} \end{bmatrix}
$$

Equation (3.14)

56

Equation 3.15 shows the standard linearized form in which the equations of motion will be

$$[M] \dot{\vec{x}} = [F] \vec{x} + [G] \vec{d}$$

or

(3.15) $$\dot{\vec{x}} = [A] \vec{x} + [B] \vec{d}$$

where:

(3.16) $$[A] = [M]^{-1} [F]$$

(3.17) $$[B] = [M]^{-1} [G]$$

written when studying dynamic response and control. Notice that the matrix [M] is always invertible because it is positive definite and symmetric, by definition of the mass properties.

To evaluate the terms in the matrices [M], [F], and [G] the aircraft's mass properties, flight velocity and altitude, and aerodynamic stability and control derivatives must be known. The aerodynamic model presented in chapter 2 (i.e. LINAIR) can efficiently estimate all of the quasi-steady aerodynamic properties for arbitrary oblique wing configurations. The non-dimensional force and moment coefficient derivatives are calculated by using LINAIR results in a numerical central difference approximation for the derivative.

Where C_{fi} is the ith dimensionless force coefficient, x_j is the jth element of the state vector,

(3.19) $$\frac{\delta C_{fi}}{\delta x_j} \cong \frac{C_{fi} (\vec{x}_o + \vec{\Delta}_j) - C_{fi} (\vec{x}_o - \vec{\Delta}_j)}{2 \Delta_j}$$

Central difference approximation about the $\vec{x}_o$ state.

and Δ_j is the difference interval for x_j. This approximation is accurate to order Δ^2 [Ref. 19]. First order differencing schemes (such as forward or backward differencing) do not provide sufficient accuracy when calculating stability derivatives. For example, first order schemes cannot accurately predict the slope of symmetric functions when the derivative is evaluated at the point of symmetry. This implies that terms such as $F_{x\beta}$, which are nearly symmetric for small sweep angles, are erroneously calculated to have nonzero value when first order schemes are used.

57

3.2 Open Loop Stability and Control

The aerodynamic coefficients from LINAIR are combined with the mass property and flight condition information to form the linearized equations of motion in a FORTRAN subroutine. The dynamic response of the uncompensated (open loop) aircraft is analyzed using numerical simulation and eigensystem analysis of the linear equations of motion. The dynamic coupling of the aircraft's unforced response is shown in figures 3.2 - 3.3 which contain numerical simulation results of the aircraft's motion after being excited by a 50 ft/sec vertical step gust. These results are for the F-8 OWRA with 40 degrees oblique wing sweep and a cruise Mach number of 0.75. For a symmetric aircraft only the longitudinal motion is excited by vertical gusts, but the simulation results show that for large oblique sweep angles, the aerodynamic and inertia coupling of the asymmetric configuration results in excitation of the lateral states β, ψ, θ, ϕ also.

The effect of wing sweep on aerodynamic and inertia coupling is shown in figures 3.4 -

Dynamic Response to a 50 (f/s) Vertical Step Gust
40 (deg) Sweep OWRA
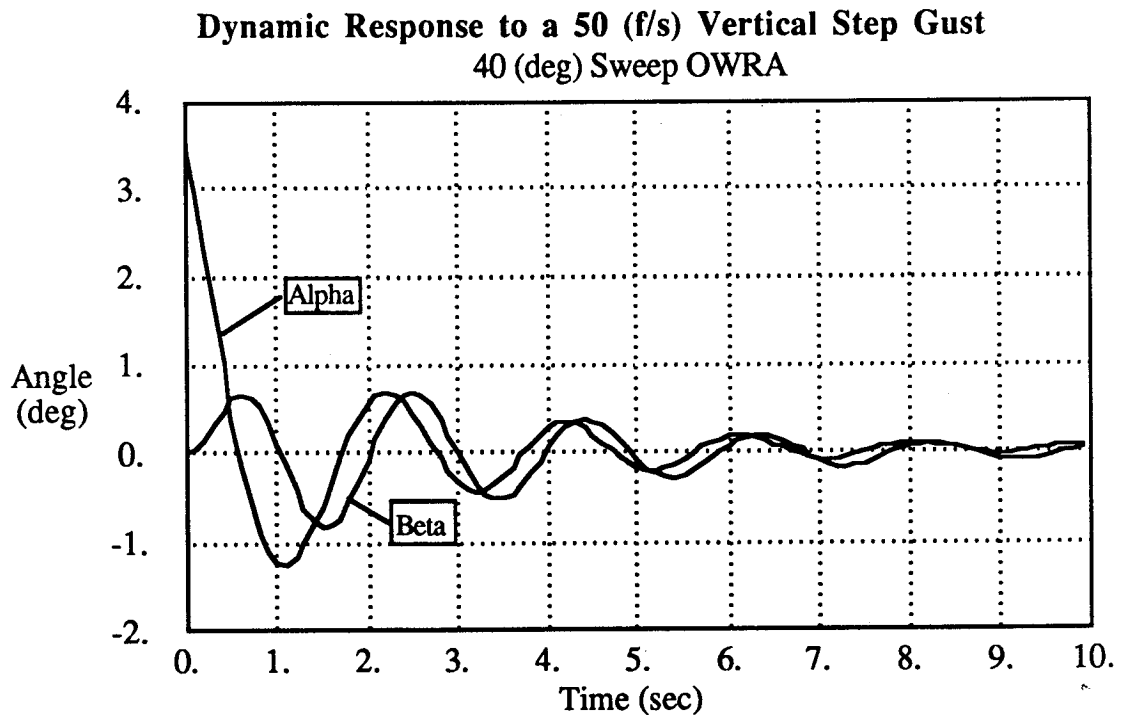
Figure 3.2 OWRA open loop unforced response

58

Dynamic Response to a 50 (f/s) Vertical Step Gust
40 (deg) sweep OWRA
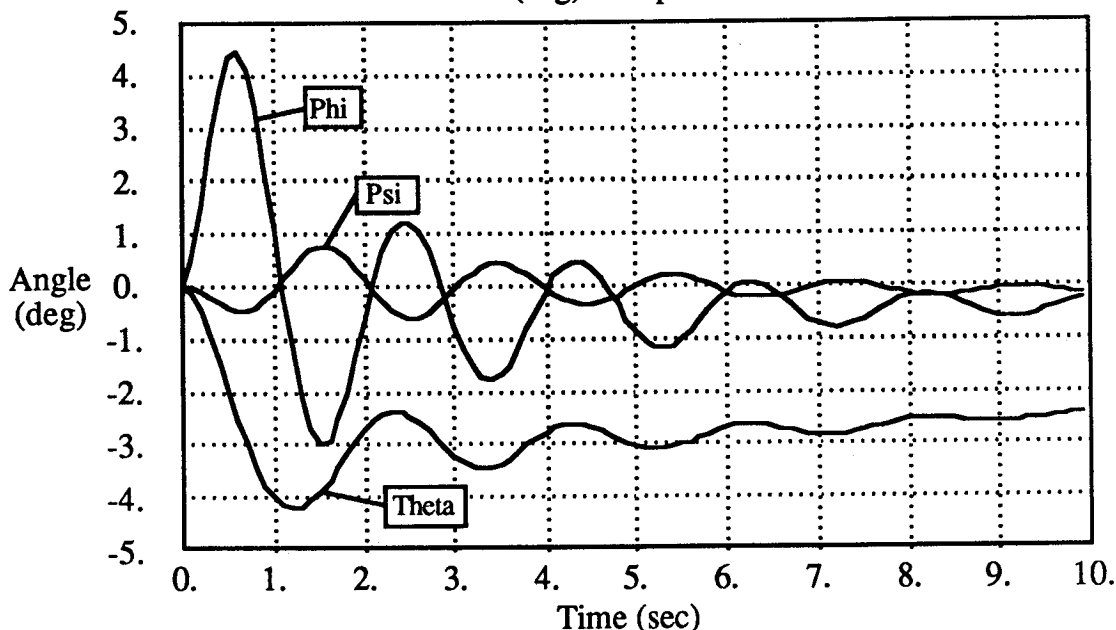
Figure 3.3 OWRA open loop unforced response (continued)

3.6. The variation of the three of the aerodynamic coupling derivatives ($C_{y\alpha}$, $C_{l\alpha}$, and $C_{N\alpha}$) with wing sweep is given in figure 3.4. At zero sweep no aerodynamic coupling exists and as the sweep increases the amount of coupling varies considerably. Figures 3.5 - 3.6 show the effect of wing sweep on the terms in the inertia tensor. As sweep increases, I_{xx} decreases and approaches the value of the fuselage only, where as I_{yy} increases and approaches the value of I_{zz}. The most significant inertia coupling term, I_{xy}, has a maximum value at 45 degrees wing sweep.

The magnitude of the inertia coupling's impact on the dynamic response can be seen from the following example. Consider the aircraft trimmed in 1-g level flight at time = 0, when a pure pitching moment is applied to the aircraft using the control surfaces. For zero inertia coupling this moment should cause only a pitch acceleration, but inertia coupling causes an additional roll acceleration. The magnitude of roll acceleration relative to pitch acceleration is described by equation 3.19.

For the F-8 OWRA I_{xy} / I_{xx} =0.48, which implies that a pure pitch input causes a roll ac-

59

$$(3.19) \qquad \frac{d}{dt}\begin{bmatrix} p \\ q \end{bmatrix} = \frac{I_{xy}}{I_{xx}} \text{ (at time = 0)}$$

celeration of approximately one half the induced pitch acceleration based solely upon consideration of inertia coupling. These results further emphasize the importance of considering both aerodynamic and inertial influences when calculating dynamic response.

The influence of aerodynamic and inertia coupling is not limited to the coupling of the dynamic response, but it also affects the overall dynamic stability of the aircraft. Figure 3.7 is a root locus plot of the open loop aircraft's natural modes for wing sweep ranging from zero to 65 degrees. In each case the aircraft is trimmed in 1-g level flight. The root traces are labelled with the classical names for each dynamic mode as they occur at zero wing sweep. In reality, all of the modes become coupled as wing sweep increases and the labelling of the modes based on the aircraft's motion with zero wing sweep is purely a matter of convenience. These results show that as wing sweep increases the stability of all of the modes (except for the low frequency phugoid and spiral modes) is significantly affected by

Effect of Sweep on Coupling Stability Derivatives
300 sq. ft. wing OWRA, LINAIR Results
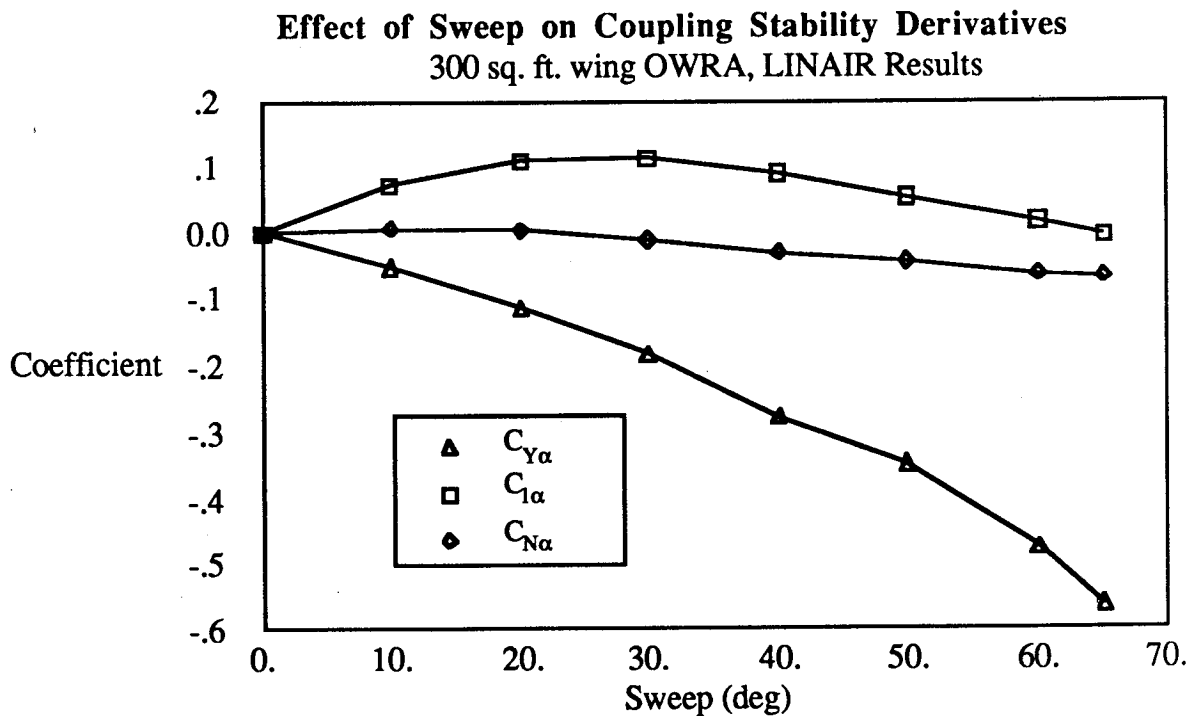
Figure 3.4 effect of oblique sweep on aerodynamic coupling
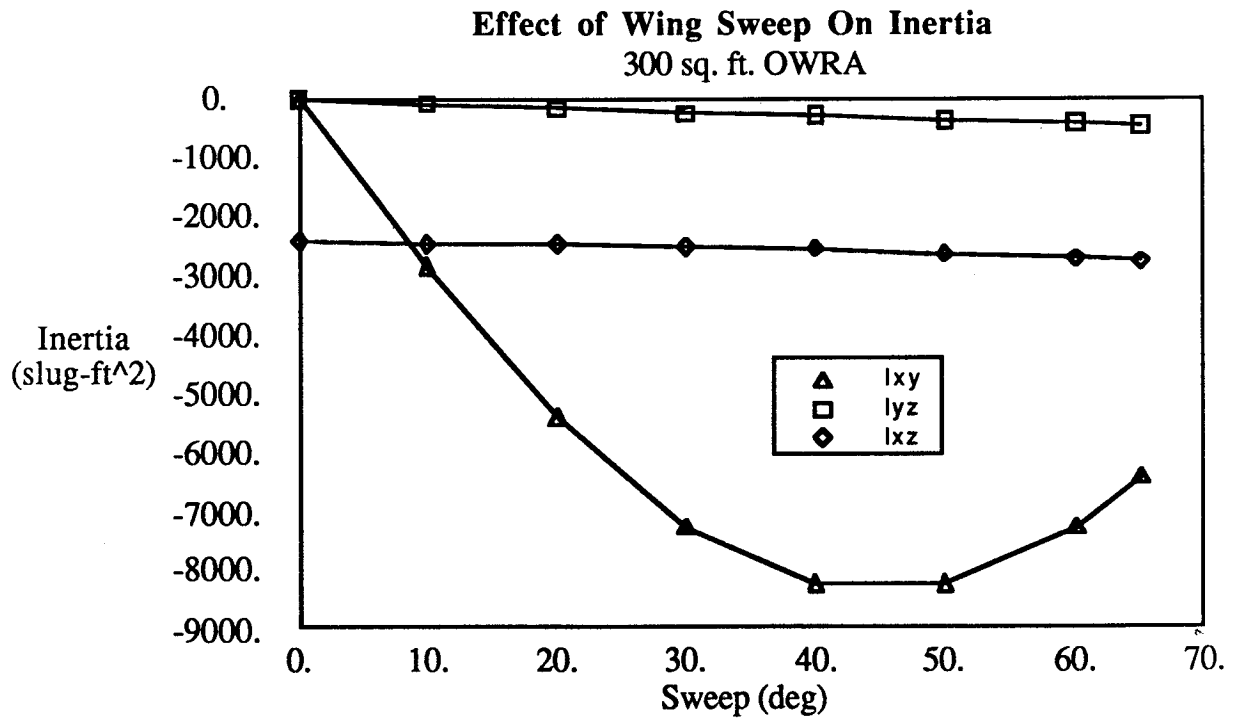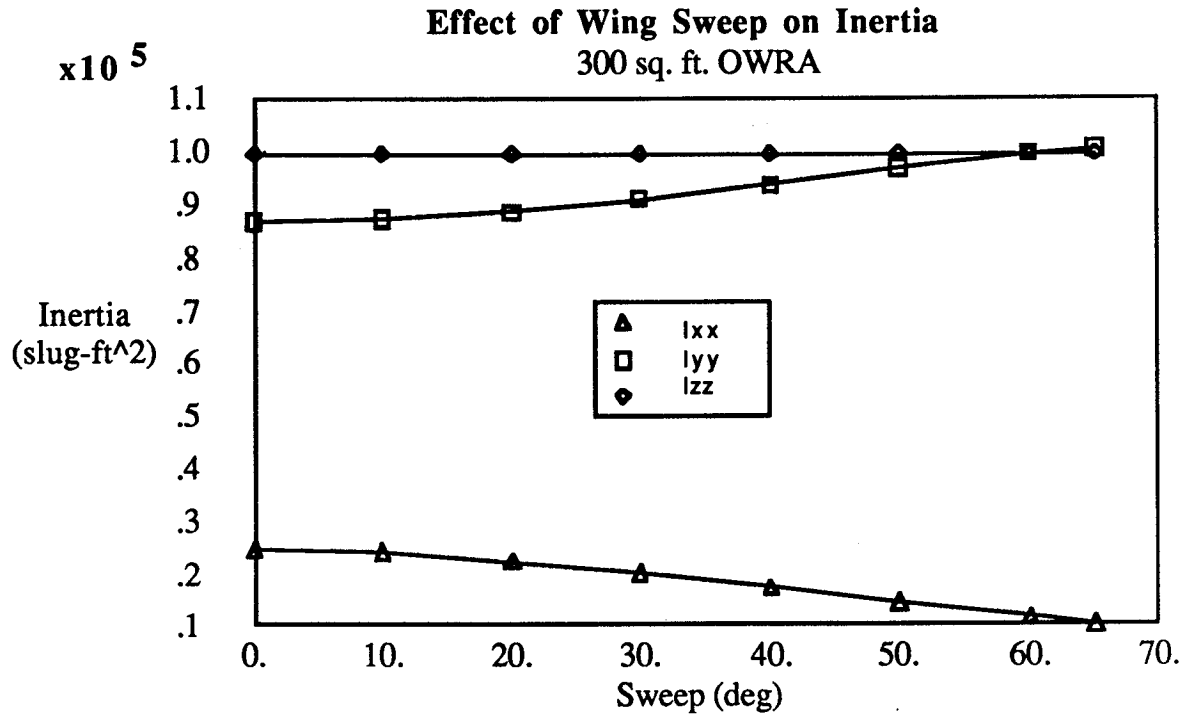
Figure 3.5 effect of oblique sweep on inertia

aircraft asymmetry. A more severe example is the dutch roll mode which becomes unstable at wing sweep greater than 50 degrees.

Root Locus On Wing Sweep
300 ft^2 OWRA, 1-g flight
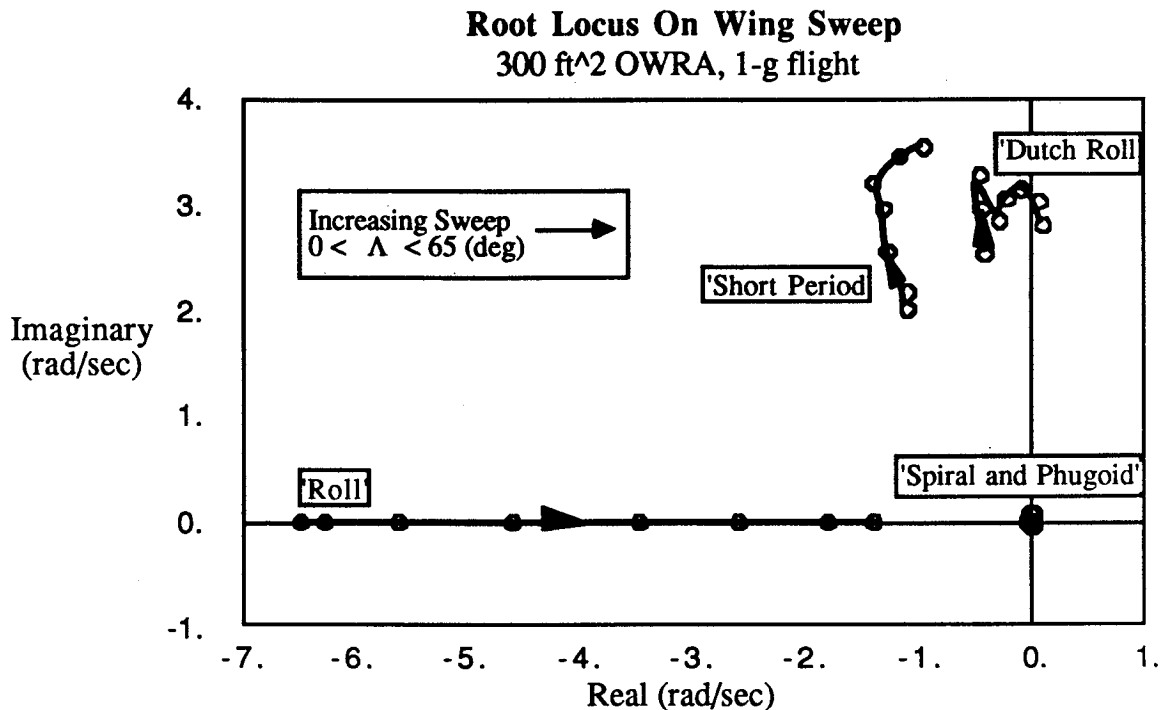
Figure 3.7 effect of oblique sweep on dynamic stability

For the integrated design synthesis it is useful to estimate the key undesirable aspects of the aircraft's dynamic response using the minimum number of state variables. Because of the large frequency separation between the spiral, phugoid and the dutch roll, short period, roll modes it is reasonable to assume that these lower frequency modes, which do not significantly contribute to handling qualities degradation, may be omitted without affecting the response of the higher frequency dynamics. Studies of aircraft handling qualities [Ref. 20] have shown that it is the higher frequency dynamics that most influence handling qualities. Furthermore, the low frequency modes can easily be controlled by the pilot or by a simple controller loop that is designed after the high frequency dynamics have been compensated. Figure 3.8 shows simulation results for the F-8 OWRA response to a gust, with and without the low frequency modes. As is expected, there is negligible difference between the time histories of the two cases for the first five seconds of motion. The results also show that the higher frequency dynamics are unchanged and that the differences that occur be-

yond five seconds are solely due to the contribution of the low frequency modes. For the cases studied in the remainder of this thesis the low frequency spiral and phugoid dynamics will be omitted by eliminating the u, ψ, θ states from the equations of motion. These dynamics will be assumed to be controlled by the pilot or by a low frequency controller which is synthesized in the final design.

Response to a 50 (f/s) Vertical Step Gust
40 deg Sweep OWRA
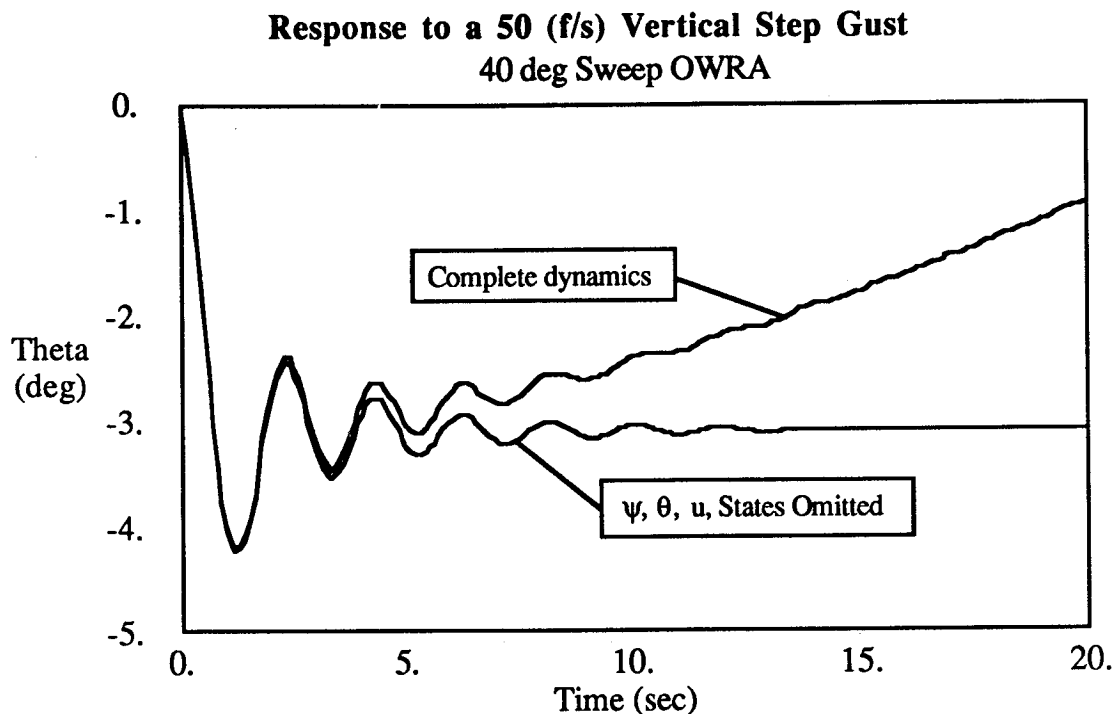
Figure 3.8 open loop response with low frequency modes omitted

Figure 3.9 shows the layout of the proposed aerodynamic control surfaces for the F-8 OWRA. The rudder is used to produce yawing moment, while the full-flying elevator can be deflected symmetrically for pitching moment and asymmetrically for rolling moment. Ailerons produce both rolling and pitching moment when the wing is obliquely swept and loose their effectiveness at high sweep angles due to reduced dynamic pressure in the normal flow direction. Using the tail surfaces to produce rolling moment has the advantage that elevator control effectiveness does not change with wing sweep. However, the elevator deflection may be more likely to saturate during combined pitch and roll commands and applying the rolling moment to the fuselage instead of the wing creates increased structural loads in the fuselage and wing pivot. In previous studies of the F-8 OWRA [Ref. 4] it was assumed that only the elevators are used for roll control, because of the control authority

advantages at high sweep angles and the simplified wing structure that results when ailerons are omitted. In order to be consistent with previous studies, the same assumption will be made in this thesis.

Figure 3.9 also shows the layout of proposed wing tip control surfaces which are effective in producing pitching and rolling moments at high sweep angles. The relative sweep of the hingeline of these control surfaces is small when the wing itself is highly skewed, thus maintaining control effectiveness at high oblique sweep. These control surfaces were tested on wind tunnel models [Ref. 11] but the additional structure and actuators required by wing tip control surfaces have limited the interest shown in these devices.
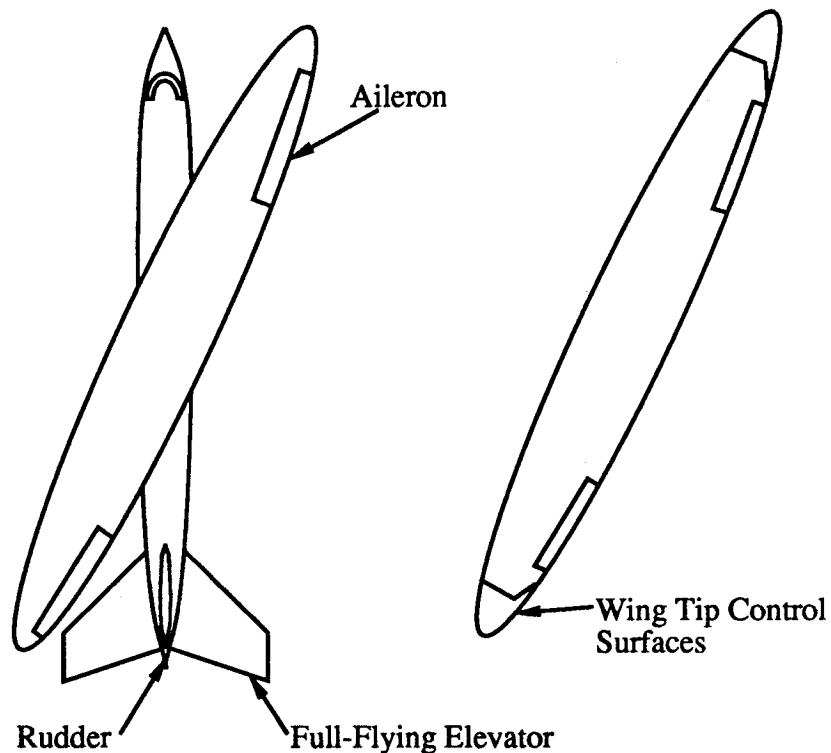
Figure 3.9 oblique wing control surfaces

The dynamically-coupled response of the oblique wing aircraft to control inputs and gusts could easily be solved using a SAS if the aircraft were adequately controllable. Controllability requires that all of the dynamic modes may be influenced using the available controls and that the control authority is adequate to significantly affect these modes without control saturation. It is precisely the lack of controllability inherent to the original OWRA configu-

64

ration that degrades the handling qualities of the closed loop aircraft. The nature of this lack of controllability can be seen when one considers minimizing lateral accelerations and rolling motion during a pitch-up maneuver. For the OWRA with an unbanked wing, the sideforce generated during a pitch maneuver is large enough that excessive sideslip and rudder deflection would be required to trim. Therefore, the aircraft must roll to allow a portion of the aircraft's weight to cancel the sideforce from the wing. In the next section, simulations of the closed loop aircraft (original OWRA configuration) further substantiate these claims. Designing additional direct sideforce control surfaces would be one solution to this problem, but there is a drag and weight penalty associated with these surfaces. A better solution is to re-configure the aircraft so that the SAS can more easily decouple the aircraft's motion. The configuration is changed in ways specifically chosen to not significantly alter the aircraft's weight and drag. The integrated design synthesis method presented in chapter 4 accomplishes this task and is applied to the F-8 OWRA problem in chapters 5 and 6.

3.3 Closed Loop Stability and Control

The undesirable influences of aircraft asymmetry on dynamic response (as demonstrated in the previous section) require that some type of stability augmentation system (SAS) be used to improve aircraft handling qualities. Previous attempts to improve handling qualities through SAS implementation have produced less than satisfactory results because of an inherent lack of controllability in the proposed OWRA design. In this section, criteria for acceptable handling qualities are established and several control law synthesis methods are studied to see how they improve the dynamic response of the nominal OWRA configuration. Handling qualities using the various SAS schemes are compared with each other and with previous studies performed using aircraft motion simulators. The results show how the lack of controllability in the nominal OWRA configuration degrades handling qualities for all SAS designs. Two SAS synthesis schemes are chosen for use in the integrated design synthesis study because of their superior performance and ease of implementation in a numerical optimization procedure.

3.3.1 Oblique Wing Handling Qualities Specifications

Military Specification F-8785-C [Ref. 20] lists criteria which an aircraft must meet in order to have acceptable handling qualities. Specifications are given for different types of aircraft (class I-IV, fighter , bomber, etc.) in various phases of flight (category A-C, takeoff, landing, air-to-air combat, etc.) and for three levels of handling qualities (I-III, acceptable to unacceptable). The specifications are given in terms of the aircraft's natural response and gust response, response to pilot commands for various maneuvers, and stick force characteristics. A successful oblique must meet the Mil-Spec F-8785-C requirements for handling qualities. The F-8 OWRA is a fighter-interceptor aircraft (class IV) which must have acceptable handling qualities (level I) in its most critical flight regimes (category A, air-to-air combat, formation flying , etc.). The handling requirements for a level (I), class (IV), category (A) aircraft are given in table 3.1. Specifications for the stick force gradients are not considered in this study because they are a function of the control surface actuation mechanism which is assumed to be designed separately from the stability augmentation system.

MIL - F - 8785C Handling Quality Requirements
Class IV, Category A, Level 1 (Fighter Aircraft)

Longitudinal Dynamics

Short Period

$3.5 <= \omega_{sp} <= 14$ (rad/sec)

$.35 <= \zeta_{sp} <= 1.3$

Phugoid

$\zeta_{ph} >= 0.04$

Commanded Response

- Must be able to achieve trim without control saturation between -1 'g' and limit load factor in positive 'g'.

Lateral Dynamics

Dutch Roll

$1.0 <= \omega_{dr} <=$ (rad/sec)

$\zeta_{dr} >= 0.4$

Roll

$\tau_r <= 1.0$ (sec)

Spiral

$t_2 >= 12$ (sec)

Commanded Response

- Roll rate oscillations must remain sufficiently small after a step command in roll rate.

- Sideslip excursions for a roll rate step command must be less than 6 degrees when the bank angle changes 60 degrees in 2 seconds.

- Roll authority must be sufficient to achieve 90 degree bank in 1.3 seconds.

Table 3.1 Mil-F-8785C handling quality requirements

One obvious problem in using the Mil.-Spec. criteria to evaluate the handling qualities of oblique wing aircraft is that acceptable limits for the coupling of lateral and longitudinal motions is not specified. This coupling is a significant factor in the degradation of the OWRA's handling qualities and therefore provides a key performance measure for a candidate SAS design. A quantitative measure of how coupling affects handling qualities is given in reference [4] which describes pilot ratings (on a Cooper Harper scale [24]) for the F-8 OWRA (with SAS) as obtained from experiments in NASA's vertical motion simulator (VMS). In this study the F-8 OWRA with a 200 square foot wing (configuration 1) was modelled in the simulator's software using wind tunnel data as the primary aerodynamic database. The simulator has sufficient degrees of freedom to permit rotational motion and longitudinal and lateral accelerations of the cockpit. Acceleration degrees of freedom are a key factor in the results of the VMS study because previous simulation studies (without acceleration capability) yielded much more favorable pilot ratings for the OWRA's handling qualities [Ref. 4]. These erroneous results were due to a lack of motion cues that the pilots would otherwise experience in free flight. The VMS results showed that pilots were most critical of the coupling between pitch motion and lateral acceleration as normal load factor was increased. Criticism was also made of the coupling of pitch and roll motion in high 'g' turns. In general, the handling qualities of the closed loop aircraft were found to degrade with increasing wing sweep and flight dynamic pressure, the worst case being Mach = 1.6 and sweep = 65 degrees. Figure 3.10 [Ref. 4] shows the deterioration of handling quality (Cooper Harper rating) as the ratio of maximum lateral acceleration to achieved normal acceleration increases for a pitch maneuver. The parameter $A(y/n)$ is approximately equal to the ratio of maximum lateral acceleration to achieved normal acceleration.

In order to achieve acceptable handling qualities (i.e. a Cooper-Harper rating of (1-3)) the parameter $A(y/n)$ must be less than 0.05, which implies that the peak lateral acceleration must be less than 1/20th the normal acceleration during a pitch maneuver. The VMS study did not specify acceptable levels of pitch to roll coupling for level flight or in turns, but did indicate that this coupling should be minimized also. Similarly, coupling from the lateral commands to the longitudinal motion was found to be small and had little impact on pilot handling quality ratings. Based upon these results, the criteria for acceptable handling quality is given by the Mil.-Spec. F-8785C requirements with the additional stipulation that

68

lateral and longitudinal commanded response be decoupled; particularly the pitch-to-lateral acceleration and the pitch-to-roll motions.
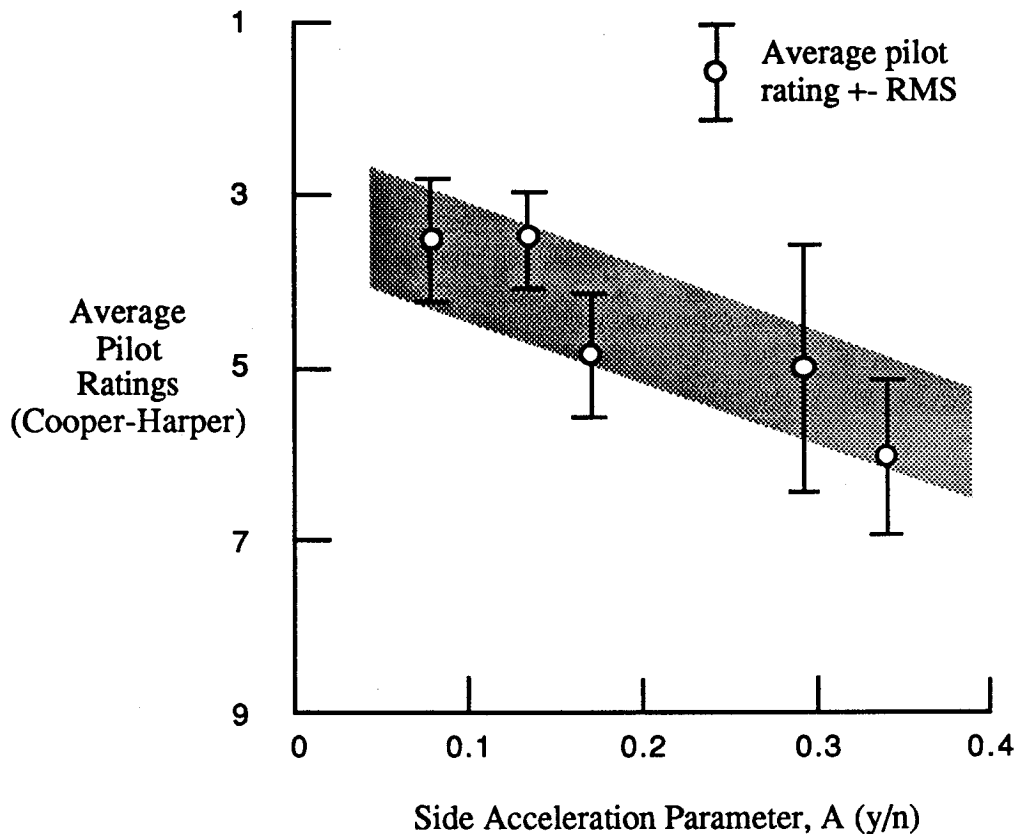
Figure 3.10 Pilot rating vs. lateral acceleration during pitch-up maneuver

The VMS study did not consider the aircraft's response to atmospheric turbulence as part of the handling quality assessment. Mil.-Spec. F- 8785C addresses this issue in terms of frequency and damping requirements for the natural modes, but does specify any requirements for acceptable decoupling of the gust response. For example, an oblique wing aircraft experiences lateral accelerations when excited by a vertical gust. The coupled transients that result may degrade ride quality when compared to an aircraft with decoupled gust response. No data is presently available to verify this claim.

3.3.2 Stability Augmentation System Design

Preliminary design studies of the F-8 OWRA considered two SAS schemes for restoring acceptable handling qualities to the asymmetric aircraft. The first is an Eigenstructure Synthesis technique [Ref. 21] which uses state feedback to drive the OWRA's closed loop ei-

gensystem as close as possible to that of a model case which has decoupled lateral and longitudinal dynamics and meets the Mil.-Spec. F-8785C criteria. The second is a 'Loop Shaping' technique [Ref. 22] which uses state feedback and a precompensator to meet frequency response characteristics obtained from the Mil.-Spec. F-8785C criteria.

Early simulation studies, which used fixed based simulators to evaluate handling qualities, failed to recognize the severe performance degradation caused by pitch to lateral acceleration coupling. As a result, both the loop shaping and eigenstructure synthesis SAS were designed to minimize roll excursions more so than lateral acceleration. The inherent lack of controllability in the original F-8 OWRA configuration makes it impossible to minimize both of these coupling motions simultaneously. When the performance of the two candidate SAS was initially evaluated (fixed base simulation) pilot ratings favored the loop shaping controller, which was then implemented in the VMS simulator trials. A unique SAS was synthesized at five different flight conditions corresponding to 1-g level flight with different Mach numbers, altitudes, and oblique wing sweeps (Table 3.2). Gain scheduling was used during transition between flight flight conditions to define the complete control algorithm.

Trimmed 1-g flight conditions with zero wing bank

No.	Mach	Altitude (ft)	Sweep (deg)	q(lb/ft^2)	Vo(f/s)
1	0.8	20,000	45	436	830
2	1.2	29,000	65	665	1199
3	1.4	29,000	55	905	1399
4	1.6	29,000	65	1181	1599
5	0.9	500	65	1179	1003

Table 3.2 flight conditions investigated in the VMS study

Because the VMS simulator allows the pilot to experience acceleration as well as rotational motion, the degradation in handling qualities during pitch maneuvers was discovered and quantified (Fig. 3.10). Figure 3.11 shows time histories from the VMS study where the closed loop F-8 OWRA is performing pitch maneuvers at flight condition 5. The large coupling between pitch and lateral acceleration is clearly shown.

70

Angle of
attack
α, $\sim$ deg

Lateral
acceleration
a_y, $\sim$ g

Angle of
sideslip
β, deg

Time, sec $\sim$ 1 sec

0   10   20   30   40   50   60

Figure 3.11 closed loop response of the F-8 OWRA performing pitch maneuvers
(from the VMS simulator trials [Ref. 4])

The inability of the SAS to adequately attenuate the roll and lateral acceleration excursions during the pitch maneuver, without saturating the control surfaces or exceeding sideslip limits, is a clear indication of the OWRA's inherent lack of controllability. The closed loop handling qualities of the aircraft will suffer (regardless of what type of SAS is used) unless the configuration is somehow changed to improve controllability. The integrated design procedure (discussed in chapters 4-6) seeks to improve handling qualities by simultaneously reconfiguring the OWRA and its SAS for improved dynamic decoupling. In the remainder of this chapter candidate SAS configurations which are suitable for use in the integrated design synthesis will be presented and studied.

For the purpose of integrated design, a feasible control system scheme is one whose synthesis can easily be incorporated into the numerical design optimization. For example, SAS design methods which require significant ad-hoc restructuring of the controller architecture during the synthesis would not be easy to implement. Both the Loop Shaping and Eigenstructure Synthesis techniques are acceptable, but there are other methods based on optimal

control Linear Quadratic Regulator (LQR) theory which should also be considered. In the next section three types of control systems based on LQR theory are synthesized for the nominal F-8 OWRA configuration . The closed loop dynamic response of the OWRA with each SAS is compared and two of these schemes are chosen for implementation in the integrated design procedure. In these studies controllers are synthesized for one flight condition, although it is assumed that in a final design the SAS gains will be determined at many flight conditions (to account for the aerodynamic nonlinearities) and gain scheduling will be implemented.

3.3.2.1 Explicit Model Following SAS

An Explicit Model Following (EMF) LQR controller causes the outputs of the plant to track the outputs of a model system, when the model system is excited by pilot commands. The controller structure consists of a pre-compensator, which includes the model dynamics, and a feedback compensator which stabilizes the open loop plant and insures adequate bandwidth for the feedback compensated plant to track the model's outputs. A block diagram of the system is shown in figure 3.12.
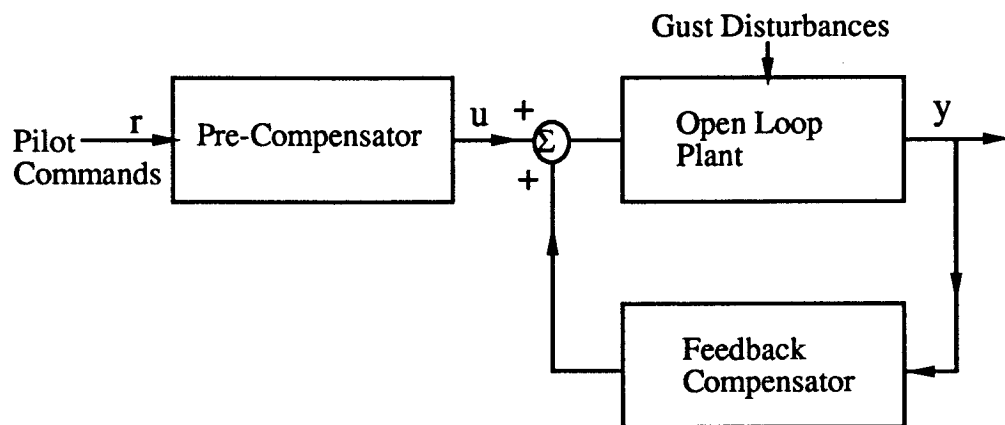
Figure 3.12 Explicit Model Following (EMF) controller block diagram

The EMF controller architecture assumes full-state feedback which implies that the entire state vector is either sensed or estimated from a reduced number of sensed variables (using a Kalman filter). The pre-compensator and feedback gains are determined by solving a single Algebraic Riccatti Equation (ARE) which results in a control law that minimizes the LQR cost function (Ref. [22]). The synthesis of the EMF controller can be stated more explicitly as the following LQR problem:

72

Given:

(3.20) $\dot{y} = [A]\, y + [B]\, u$ y is n x 1   n=number of outputs
                                             u is m x 1   m=number of controls

(3.21) $\dot{y}_m = [A_m]\, y_m + [B_m]\, u_m$

Find [K] where:

(3.22) $u = [K] \begin{bmatrix} y \\ y_m \end{bmatrix}$

such that Jd is minimized

(3.23) $J_d = \int_0^\infty [\, (y\text{-}y_m)^T Q\, (y\text{-}y_m) + u^T R\, u\,]\, dt$

Where [Q] & [R] are positive definite weighting matrices multiplying the model following state error and control effort, respectively. The solution for the controller gains [K] is found by solving the following ARE:

The matrix P is obtained from the following ARE

(3.24) $\bar{A}^T P + P\bar{A} - P\bar{B}\,\bar{R}^{-1}\,\bar{B}^T P + \bar{Q} = 0$

Then K is obtained from:

(3.25) $K = -\bar{R}^{-1}\bar{B}^T P$

where:

(3.26) $\bar{A} = \begin{bmatrix} A & 0 & 0 \\ 0 & A_m & B_m \\ 0 & 0 & D \end{bmatrix}$ (2n+m x 2n+m) $\bar{B} = \begin{bmatrix} B \\ 0 \\ 0 \end{bmatrix}$ (2n+m x 1)

(3.27) $D = \begin{bmatrix} \varepsilon & 0 & 0 \\ 0 & \varepsilon & 0 \\ 0 & 0 & \varepsilon \end{bmatrix}$ (m x m) $\bar{Q} = \begin{bmatrix} Q & -Q & 0 \\ -Q & Q & 0 \\ 0 & 0 & 0 \end{bmatrix}$ (2n+m x 2n+m)

Notice that [K] is (m x 2n) in size and contains both the pre-compensator and feedback gains. The pre-compensator outputs are a function of y_m which implies that the model dynamics must be calculated as part of the control algorithm. The model following controller design requires that the pilot commands be modeled within the augmented system so that these commands may be excited by an appropriately placed initial condition. In this formulation, the pilot commands are modeled as washed-out step commands applied to the model's control inputs. The augmented system [A] contains the additional terms, [D], which are washout filter's pole locations. This approach permits calculation of a feedforward control (from the pilot inputs directly to (u)) while avoiding singularities that would occur in the solution of the ARE if there were rows of zeros in the matrix [A]. The matrix [D] is diagonal with elements that represent the speed of decay for each washed-out step command issued by the pilot. The elements of [D] are chosen to be very small (.001) to model a non-decaying step input. When [D] is large, the pilot commands decay to zero quickly and the influence of steady state errors on the dynamic response performance is reduced. The significance of the [D] matrix will be greatest during the integrated design synthesis where [D] is chosen to appropriately stress the importance of higher frequency dynamics in the overall measure of handling qualities.

The synthesis of an EMF controller for the F-8 OWRA requires an appropriate dynamics model which meets the Mil.-Spec. F-8785C Level 1, Class IV, Category A, handling qualities criteria. The linearized equations of motion given in figure 3.13 meet the Mil.-Spec. requirements for gust and commanded response and are used as the model dynamics in the controller synthesis. Figures 3.14 - 3.18 show the dynamic response of the model to pilot step commands in roll, pitch, yaw and excitation by 50 (f/s) vertical and lateral gusts. The transient and commanded response display the decoupled lateral and longitudinal motions characteristic of a conventional symmetric aircraft.

Mode	Complex Frequency (rad/sec)
short period phugoid	-2.6 ± 4.1j -.007 ± .106j
roll dutch roll spiral	-.95 ± 0.0j -2.03 ± 4.1j -.027 ± 0.0j

Table 3.3 Mil-Spec F-8785-C model eigenvalues

$$\frac{d}{dt}\begin{bmatrix} u \\ v \\ w \\ p \\ q \\ r \\ \psi \\ \theta \\ \phi \end{bmatrix} = \begin{bmatrix} 0.000 & .000 & .284 & 0.000 & -69.317 & .000 \\ 0.000 & -.272 & 0.000 & 69.433 & 0.000 & -789.516 \\ -.230 & 0.000 & -1.535 & 0.000 & 786.091 & 0.000 \\ 0.000 & -.005 & 0.000 & -.905 & 0.000 & .151 \\ .002 & 0.000 & -.021 & 0.000 & -3.606 & 0.000 \\ 0.000 & .025 & 0.000 & -.097 & 0.000 & -3.863 \\ .000 & .000 & .000 & .000 & .000 & 1.000 \\ .000 & .000 & .000 & .000 & 1.000 & .000 \\ .000 & .000 & .000 & 1.000 & .000 & .000 \end{bmatrix}$$

(dynamic matrix continued)

$$\begin{bmatrix} .000 & -32.052 & .000 \\ .000 & .000 & 32.052 \\ .000 & -2.804 & .000 \\ .000 & .000 & .000 \\ .000 & .000 & .000 \\ .000 & .000 & .000 \\ .000 & .000 & .000 \\ .000 & .000 & .000 \end{bmatrix}\begin{bmatrix} u \\ v \\ w \\ p \\ q \\ r \\ \psi \\ \theta \\ \phi \end{bmatrix}$$

$$+ \begin{bmatrix} .000 & .000 & .000 \\ .000 & .000 & -83.000 \\ .000 & 30.000 & .000 \\ 15.000 & .000 & -5.000 \\ .000 & 20.000 & .000 \\ .000 & .000 & 37.000 \\ .000 & .000 & .000 \\ .000 & .000 & .000 \\ .000 & .000 & .000 \end{bmatrix}\begin{bmatrix} droll \\ dpitch \\ dyaw \end{bmatrix}$$

Figure 3.13 Mil.-Spec. F-8785-C model equations of motion (ft-sec-rad)

Pitch Input Dynamic Response, 10 (deg) Elevator Deflection
Mil Spec F-8785-C Model
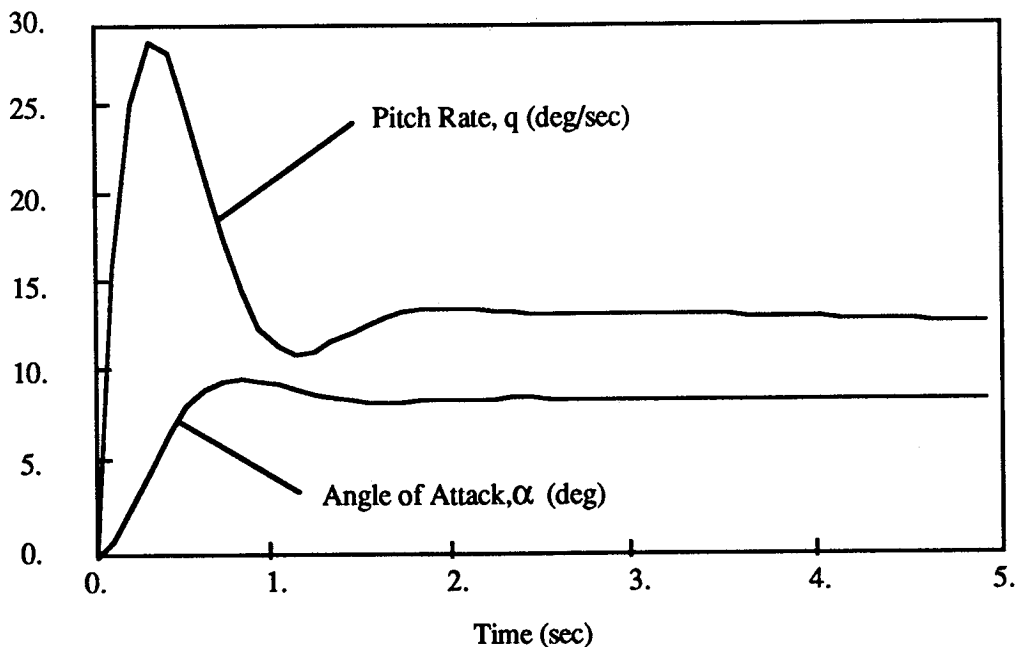
Figure 3.14 model pitch input response

75

Yaw Input Dynamic Response, 5 (deg) Rudder Deflection
Mil Spec F-8785-C Model
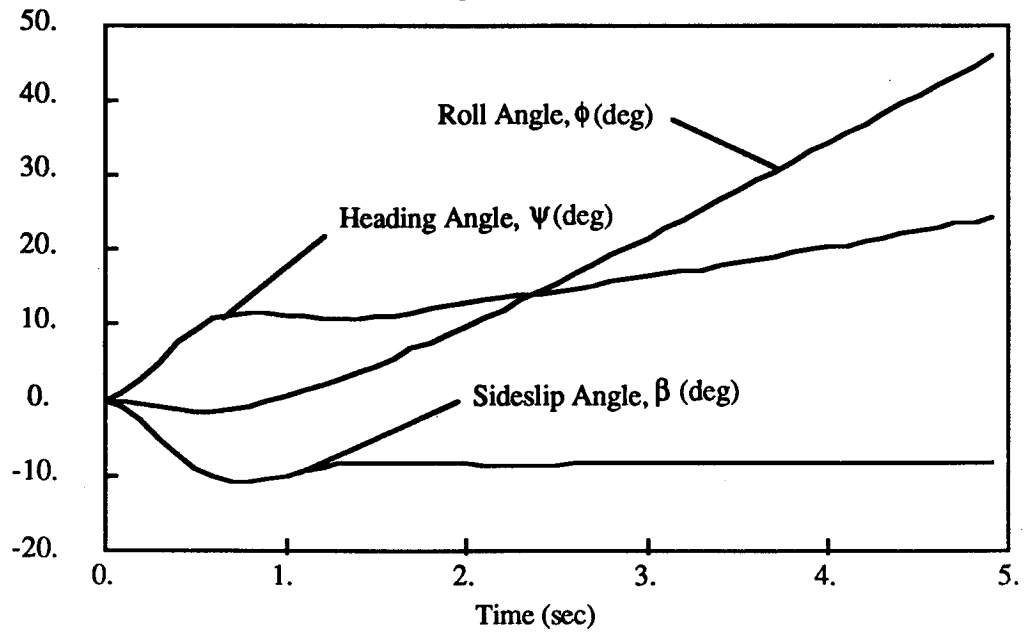
Figure 3.15 model yaw input response

Roll Input Dynamic Response, 10 (deg) Aileron Deflection
Mil Spec F-8785-C Model
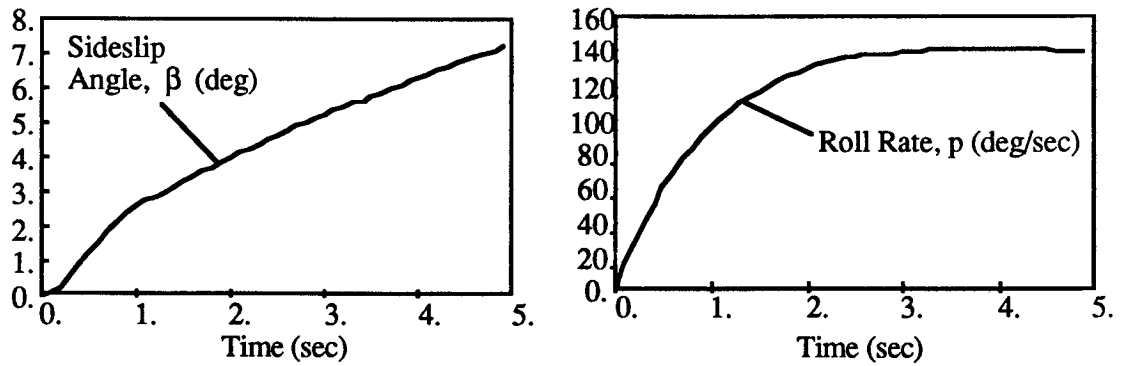
Figure 3.16 model roll input response

76

Dynamic Response, 50 (f/s) Lateral Gust
Mil Spec F-8785-C Model
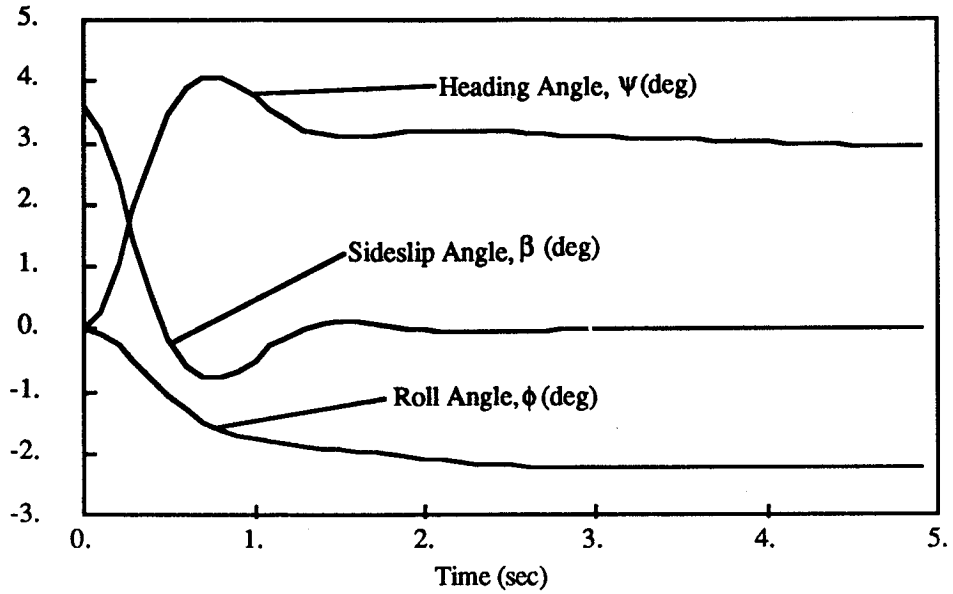
Figure 3.17 model response, lateral gust

Dynamic Response, 50 (f/s) Vertical Gust
Mil Spec F-8785-C Model
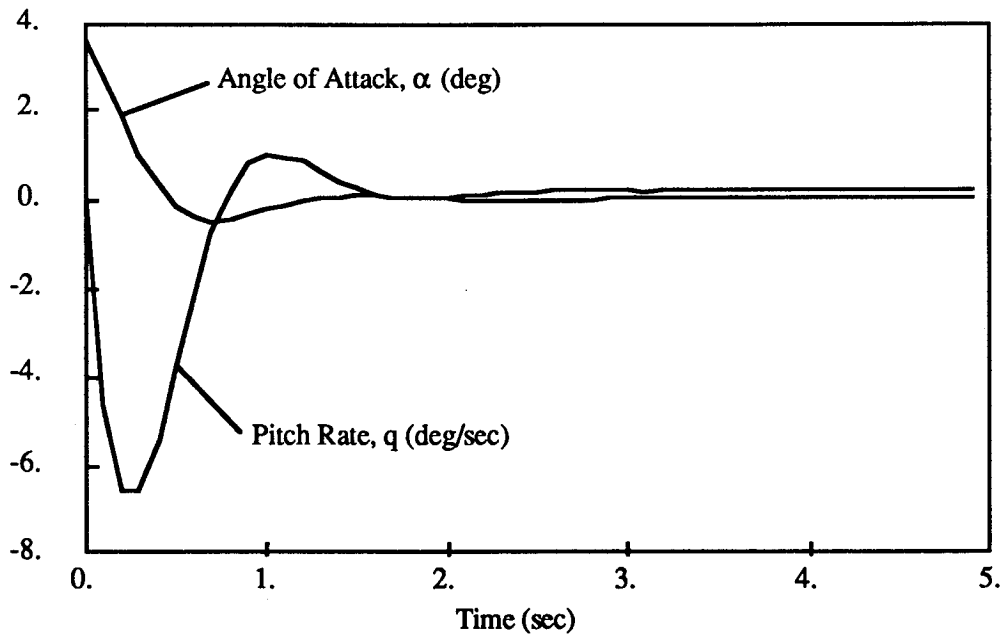
Figure 3.18 model response, vertical gust

77

C-2

The state vector for the model and the open loop OWRA is given by:

(3.28) $\quad \vec{x} = [v, w, p, q, r, \phi]^T$

where the states u, ψ, θ have been omitted to remove the low frequency spiral and phugoid modes from the dynamic response. The regulated (and sensed) variables are:

(3.29) $\quad \vec{y} = [g_y, g_z, p, q, r, \phi]^T$

which includes the outputs to be minimized during the pitch-up maneuver, g_y and ϕ. The state and output vectors (x, y) are augmented to include three additional states corresponding to a first order lag model of the pitch, roll, and yaw actuators. Figure 3.19 shows the actuator dynamics model in block diagram form.

$$\dot{\delta} = (\delta_c - \delta)\, \tau_a$$
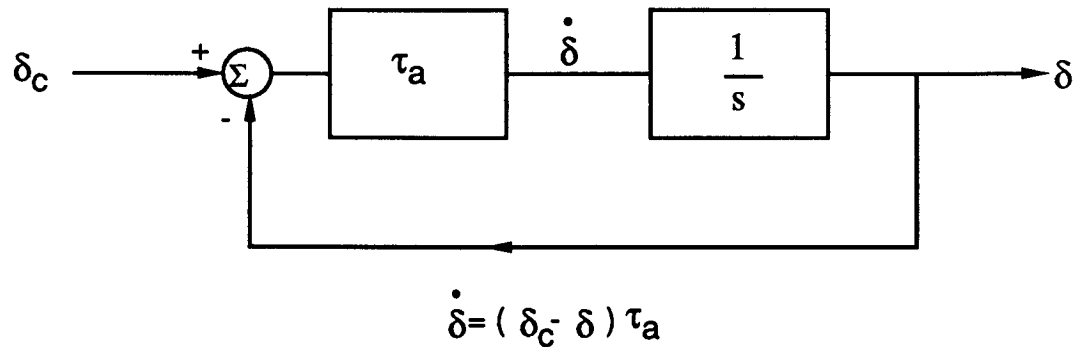
where:

δ_c = actuator commanded position

δ = actuator achieved position

τ_a = actuator pole location

Figure 3.19 first order actuator model

For the EMF design synthesis the actuator poles are placed at s=-23.0 (rad/sec) which sets the actuator bandwidth to 4Hz.

The augmented equations of motion required for an EMF SAS design for the OWRA are obtained as follows:

Let:
n = number of plant states = (6)
m = number of actuators = (3)

78

The state vector (x) is augmented to include the additional actuator states, resulting in the following plant EOM's:

$$(3.30) \qquad \begin{bmatrix} \dot{x} \\ \dot{\delta} \end{bmatrix} = \begin{bmatrix} A & B \\ 0 & F \end{bmatrix} \begin{bmatrix} x \\ \delta \end{bmatrix} + \begin{bmatrix} 0 \\ G \end{bmatrix} \begin{bmatrix} \delta_c \end{bmatrix}$$

$$(n+m) \times (n+m) \qquad (n+m) \times (m)$$

where:

$$x = (v, w, p, q, r, \phi)$$

$$\delta = (\delta_{roll}, \delta_{pitch}, \delta_{yaw})$$

and

$$F = \begin{bmatrix} -\tau_a & 0 & 0 \\ 0 & -\tau_a & 0 \\ 0 & 0 & -\tau_a \end{bmatrix} \qquad G = \begin{bmatrix} \tau_a & 0 & 0 \\ 0 & \tau_a & 0 \\ 0 & 0 & \tau_a \end{bmatrix}$$

These equations may be written in abbreviated notation as:

$$(3.31) \qquad \dot{\bar{x}} = [\bar{A}] \bar{x} + [\bar{B}] \delta_c$$

Similarly the model EOM's may be written:

$$(3.32) \qquad \begin{bmatrix} \dot{x}_m \\ \dot{\delta}_m \end{bmatrix} = \begin{bmatrix} A_m & B_m \\ 0 & F_m \end{bmatrix} \begin{bmatrix} x_m \\ \delta_m \end{bmatrix} + \begin{bmatrix} 0 \\ G_m \end{bmatrix} \begin{bmatrix} \delta_{mc} \end{bmatrix}$$

or in abreviated form:

$$(3.33) \qquad \dot{\bar{x}}_m = [\bar{A}_m] \bar{x}_m + [\bar{B}_m] \delta_{mc}$$

79

where $[F_m]$ and $[G_m]$ are identical to $[F]$ and $[G]$ where τ_a is replaced by τ_{am}. In this study τ_a is assumed equal to τ_{am}.

$\bar{x}$ is now transformed to the output vector of sensed states $\bar{y}$:

$$(3.34) \quad \bar{y} \equiv (g_y, g_z, p, q, r, \phi, \delta_{roll}, \delta_{pitch}, \delta_{yaw})^T$$

The transform between $\bar{x}$ and $\bar{y}$ (i.e.$[\Gamma]$) is given by:

$$\bar{y} = [\Gamma] \bar{x}$$

$$[\Gamma] = \begin{bmatrix} (D\,A+E) & DB \\ 0 & I \end{bmatrix}$$

$$(n+m) \times (n+m)$$

where:

$$D \equiv \begin{bmatrix} \dfrac{1}{g} & 0 & 0 & 0 & 0 & 0 \\ 0 & \dfrac{1}{g} & 0 & 0 & 0 & 0 \\ 0 & 0 & 0 & 0 & 0 & 0 \\ 0 & 0 & 0 & 0 & 0 & 0 \\ 0 & 0 & 0 & 0 & 0 & 0 \\ 0 & 0 & 0 & 0 & 0 & 0 \end{bmatrix} \qquad E \equiv \begin{bmatrix} 0 & 0 & \dfrac{-w_o}{g} & 0 & \dfrac{u_o}{g} & 0 \\ 0 & 0 & 0 & \dfrac{-u_o}{g} & 0 & 0 \\ 0 & 0 & 1 & 0 & 0 & 0 \\ 0 & 0 & 0 & 1 & 0 & 0 \\ 0 & 0 & 0 & 0 & 1 & 0 \\ 0 & 0 & 0 & 0 & 0 & 1 \end{bmatrix}$$

Transforming the plant and model EOM's into the $\bar{y}$ coordinates:

plant

$$(3.36) \quad \bar{y} = \left[\Gamma \, \bar{A} \, \Gamma^{-1} \right] \bar{y} + \left[\Gamma \, \bar{B} \right] \delta_c$$

model

$$(3.37) \quad \bar{y_m} = \left[\Gamma_m \, \bar{A_m} \, \Gamma_m^{-1} \right] \bar{y_m} + \left[\Gamma_m \, \bar{B_m} \right] \delta_{mc}$$

80

Transforming the plant and model EOM's into the $\bar{y}$ coordinates:

plant

(3.36)
$$\dot{\bar{y}} = \left[\Gamma \bar{A} \Gamma^{-1}\right] \bar{y} + \left[\Gamma \bar{B}\right] \delta_c$$

model

(3.37)
$$\dot{\bar{y}_m} = \left[\Gamma_m \bar{A_m} \Gamma_m^{-1}\right] \bar{y_m} + \left[\Gamma_m \bar{B_m}\right] \delta_{mc}$$

The augmented (2n+m x 2n+m) system used for the EMF
SAS design is obtained by combining the plant and model equations:

(3.38)
$$\dot{\xi} = \begin{bmatrix} \Gamma \bar{A} \Gamma^{-1} & 0 & 0 \\ 0 & \Gamma_m \bar{A_m} \Gamma_m^{-1} & \Gamma_m \bar{B_m} \\ 0 & 0 & D \end{bmatrix} \xi + \begin{bmatrix} \Gamma \bar{B} \\ 0 \\ 0 \end{bmatrix} \delta_c$$

or:

(3.39)
$$\dot{\xi} = [\tilde{A}] \xi + [\tilde{B}] \delta_c$$

where [D] is a diagonal matrix which defines the pole
location (washout) for the input excitation:

$$D \equiv \begin{bmatrix} -\varepsilon & & 0 \\ & -\varepsilon & \\ 0 & & -\varepsilon \end{bmatrix} \qquad |\varepsilon| = \text{pole location for the input excitation}$$

The EMF LQR problem may now be written in terms of the augmented
system state vector ξ. The control law is given by the values of δ_c which
minimize the dynamic cost integral:

(3.40)
$$J_d = \int_0^\infty \{\xi^T \tilde{Q} \xi + \delta_c^T R \delta_c\} \, dt$$

81

Where the output error and control effort weighting matrices ([Q] and[R]) are given by:

[R] = (m x m) matrix of control effort weights

$\tilde{[Q]}$ = (2n+m x 2n+m) matrix of output error weights

(3.41) $\tilde{[Q]} = \begin{bmatrix} \overline{Q} & -\overline{Q} & 0 \\ -\overline{Q} & \overline{Q} & 0 \\ 0 & 0 & 0 \end{bmatrix}$

and

$\overline{Q}$ = weighting on the output error ($\overline{y}$ - $\overline{y_m}$)

The solution for δ_c which minimizes J_d is given by : [Ref. 23]

(3.42) $\delta_{copt} = [K]\xi$

Where the full-state feedback gain matrix is determined from:

(3.43) $[K] = -R^{-1}\tilde{B}^T P$

and the matrix [P] is from the solution of the following A.R.E.:

(3.44) $\tilde{A}^T P + P\tilde{A} - P\tilde{B}R^{-1}\tilde{B}^T P + \tilde{Q} = 0$

Note that [K] is (m x 2n+m) and contains all of the gains for the pre-compensator and the feedback compensator :

(3.45) $[K]\xi = [K_{pc}]\overline{y_m} + [K_{fc}]\overline{y} + [K_{ff}]\delta_{mc}$

The SAS synthesized for the F-8 OWRA in this way is shown in a more explicit form in the block diagram of figure 3.20. Notice that the SAS gains are shown as three distinct components; [K_{ff}] - feedforward gains, [K_{pc}] - pre-compensator gains, [K_{fc}] - feedback compensator gains.
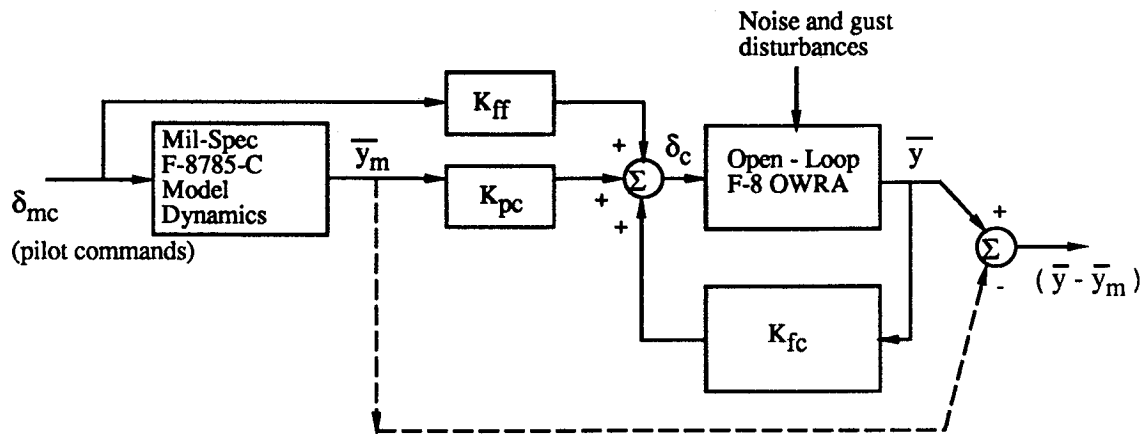
Figure 3.20 F-8 OWRA EMF SAS block diagram

Implementation of the EMF SAS requires that all elements of the {y} vector be sensed (or estimated) including the actuator states. The dynamics of the model must also be simulated as part of the SAS control algorithm in order to generate the required pre-compensator outputs. Figure 3.20 illustrates that the EMF SAS attempts to drive the output error $(y - y_m)$ to zero. A less obvious point is that this statement is only true when the model dynamics are excited by commands from the pilot (δ_{mc}) and not when the aircraft is excited by gusts. Gust disturbances only excite the (y) outputs of the system and the feedback compensator attempts to suppress gust disturbances without any regard to how the model would respond if excited by the same gust. The EMF SAS is therefore only capable of decoupling the commanded response of the aircraft and attenuates gust response instead of decoupling it. If the plant and model experience simultaneous excitation from gust disturbances in the SAS design procedure, then the transient response of the plant will attempt to follow the model's. This possibility, however, is not feasible in the EMF SAS synthesis. The reduced-order model following SAS synthesis will show how commanded and transient response decoupling can be achieved.

An EMF SAS was designed for the F-8 OWRA at the M=0.8, $\Lambda = 45°$ flight condition. Figures 3.21 - 3.22 show the plant and model matrices used in the synthesis. The weighting matrices [Q] and [R] were chosen to maximize dynamic response decoupling without excessive control effort. This is difficult to do because the EMF SAS has the tendency to require excessive feedback bandwidth such that the feedback compensated plant can easily

follow the pre-compensator commands (and therefore track the model's response). As a result, very fast closed loop natural dynamics will occur unless the control effort weighting is large. For the results presented in this work the control effort weighting was chosen to constrain the actuator bandwidth to be no greater than 5Hz. The resulting SAS gains for the F-8 OWRA are shown in figure 3.23. The response of the closed loop aircraft to pilot commands and gusts is shown in figures 3.24 - 3.35.

The model, open, and closed loop OWRA eigenvalues are plotted in figure 3.36. The EMF SAS has increased the amount of damping in all the modes beyond that present in the model. This is typical for an EMF SAS because fast natural response is required in order to track the model's commanded response transients. The fastest eigenvalues (not plotted in figure 3.36) correspond to the actuator states ($s = -33.0 \pm 0j$ rad/sec) whose bandwidth has been "artificially" increased by full-state feedback. Because the actuator position can be fed-back to the servo motor torque, the bandwidth characteristics of the servos can be arbitrarily changed. The control weighting matrix [R] was chosen specifically to limit the bandwidth of these modes to less than 5Hz.

The gust response time histories (Fig. 3.30 - 3.35) show that the transient motion is still coupled (laterally and longitudinally) but highly damped. Therefore, the compensated OWRA has no distinct short period, dutch roll, etc. modes but instead has coupled highly damped transients. The roots plotted in figure 3.36 for the closed loop OWRA are not identified with the classical names because of their coupled nature.

The commanded response time histories (Fig. 3.24 - 3.29) show the model following performance of the closed loop OWRA. For the 4-g pitch-up maneuver, the normal acceleration and pitch rate track the model's almost exactly. The lateral motions are reduced but not completely attenuated by the SAS. The SAS attempts to limit the lateral motions as much as possible for the given control effort weighting but still the excursions in g_y and ϕ are unacceptably large ($A(y/n) = .075$ yields a Cooper-Harper rating of 4 based on Fig. 3.10). From the simulation results it can be seen that the aircraft initially accelerates to the left as the leading edge suction (C_y) increases with angle of attack and then rolls right in an attempt to minimize g_y without excessive sideslip. This behavior reflects the basic lack of

controllability that plagues the nominal OWRA configuration. There are no surfaces that can independently produce significant sideforce and therefore the aircraft must roll (or side-slip) to reduce g_y. The weighting matrices [Q] and [R] (Fig. 3.23) used in the SAS synthesis represent only one reasonable choice for these terms. It is possible to increase the weighting on ϕ (to minimize rolling motion at the expense of β and g_y excursions) and obtain results more like those predicted by the Loop Shaping SAS (Fig. 3.11). Experimentation with various [Q] and [R] values have shown that for all cases the OWRA's controllability deficiency prevents the closed loop handling qualities from being acceptable.

In a final version of the SAS design the low frequency dynamics must also be compensated so that the aircraft trims at the commanded flight condition. The results shown in figures 3.24 - 3.29 clearly show that the trim requirement is not achieved by the proposed EMF controller. Integral feedback of the tracking error $(y-y_m)$ will minimize these steady state errors. This portion of the SAS can be designed after the EMF gains are determined. The dynamic response most crucial to handling qualities occurs in the first few seconds of motion (after a command is issued by the pilot). In this thesis, the initial dynamic response of the aircraft will be studied most carefully because of its strong influence on handling qualities. The design of the low frequency portion of the SAS is not considered in this work, although the integrated design syntheses will ensure adequate control authority to trim at the flight condition studied.

F-8 OWRA Linearized Equations of Motion
45 degree sweep M=0.8

$$\frac{d}{dt}\begin{bmatrix} g_y \\ g_z \\ p \\ q \\ r \\ \phi \\ \delta_{roll} \\ \delta_{pitch} \\ \delta_{yaw} \end{bmatrix} =
\begin{bmatrix}
-.725 & .009 & .680 & -1.664 & 6.561 & .466 & 9.963 & -.711 & 57.843 \\
-.122 & -1.008 & .043 & -24.186 & -1.287 & .172 & .718 & -68.822 & .522 \\
7.885 & -1.674 & -3.101 & 2.242 & .183 & -7.874 & 14.834 & 11.143 & -.975 \\
.499 & .351 & .282 & -1.069 & -.020 & -.499 & -.102 & 12.194 & -1.206 \\
-1.527 & .195 & -.143 & .263 & -.471 & 1.525 & 1.348 & -.282 & 6.899 \\
.000 & .000 & 1.000 & .000 & .000 & .000 & .000 & .000 & .000 \\
.000 & .000 & .000 & .000 & .000 & .000 & -25.000 & .000 & .000 \\
.000 & .000 & .000 & .000 & .000 & .000 & .000 & -25.000 & .000 \\
.000 & .000 & .000 & .000 & .000 & .000 & .000 & .000 & -25.000
\end{bmatrix}
\begin{bmatrix} g_y \\ g_z \\ p \\ q \\ r \\ \phi \\ \delta_{roll} \\ \delta_{pitch} \\ \delta_{yaw} \end{bmatrix}$$

$$+
\begin{bmatrix}
-56.630 & .285 & -10.112 \\
-.309 & 66.085 & -.851 \\
.000 & .000 & .000 \\
.000 & .000 & .000 \\
.000 & .000 & .000 \\
.000 & .000 & .000 \\
.000 & .000 & 25.000 \\
.000 & 25.000 & .000 \\
25.000 & .000 & .000
\end{bmatrix}
\begin{bmatrix} \delta_{roll\ command} \\ \delta_{pitch\ command} \\ \delta_{yaw\ command} \end{bmatrix}$$

Figure 3.21 F-8 OWRA equations of motion 45° sweep, M=0.8 (ft-sec-rad)

F-8 OWRA EMF SAS Weighting Matrices

Model Following Error Weights

$$\bar{Q} = \begin{bmatrix}
1.000 & .000 & .000 & .000 & .000 & .000 & .000 & .000 & .000 \\
.000 & 1.000 & .000 & .000 & .000 & .000 & .000 & .000 & .000 \\
.000 & .000 & 1.000 & .000 & .000 & .000 & .000 & .000 & .000 \\
.000 & .000 & .000 & .100 & .000 & .000 & .000 & .000 & .000 \\
.000 & .000 & .000 & .000 & 1.000 & .000 & .000 & .000 & .000 \\
.000 & .000 & .000 & .000 & .000 & 1.000 & .000 & .000 & .000 \\
.000 & .000 & .000 & .000 & .000 & .000 & 1.000 & .000 & .000 \\
.000 & .000 & .000 & .000 & .000 & .000 & .000 & 1.000 & .000 \\
.000 & .000 & .000 & .000 & .000 & .000 & .000 & .000 & .000
\end{bmatrix}$$

Control Effort Weights

$$R = \begin{bmatrix}
30.000 & .000 & .000 \\
.000 & 30.000 & .000 \\
.000 & .000 & 30.000
\end{bmatrix}$$

F-8 OWRA EMF SAS Optimal Gains

Feed-Forward

$$K_{ff} = \begin{bmatrix}
-.376 & .323 & -.169 \\
-.190 & -1.483 & -.045 \\
-.462 & .628 & -.485
\end{bmatrix}$$

Precompensator

$$K_{pf} = \begin{bmatrix}
-.019 & .001 & -.151 & .054 & -.040 & -.168 & -.085 & .049 & -.097 \\
-.001 & .065 & -.066 & -.718 & -.008 & -.067 & -.037 & -.637 & -.005 \\
-.014 & -.011 & -.084 & .130 & -.118 & -.133 & -.054 & .116 & -.277
\end{bmatrix}$$

Feedback

$$K_{fb} = \begin{bmatrix}
.131 & -.019 & .084 & .025 & .264 & .051 & .112 & .076 & .353 \\
.108 & -.107 & .053 & .798 & .200 & -.047 & .068 & .747 & .223 \\
.084 & .013 & .007 & -.064 & .513 & .051 & .092 & -.057 & .461
\end{bmatrix}$$

Figure 3.23 EMF SAS weighting matrices and optimal gains

88

Lateral Acceleration vs Time

EMF SAS, 45° Sweep OWRA
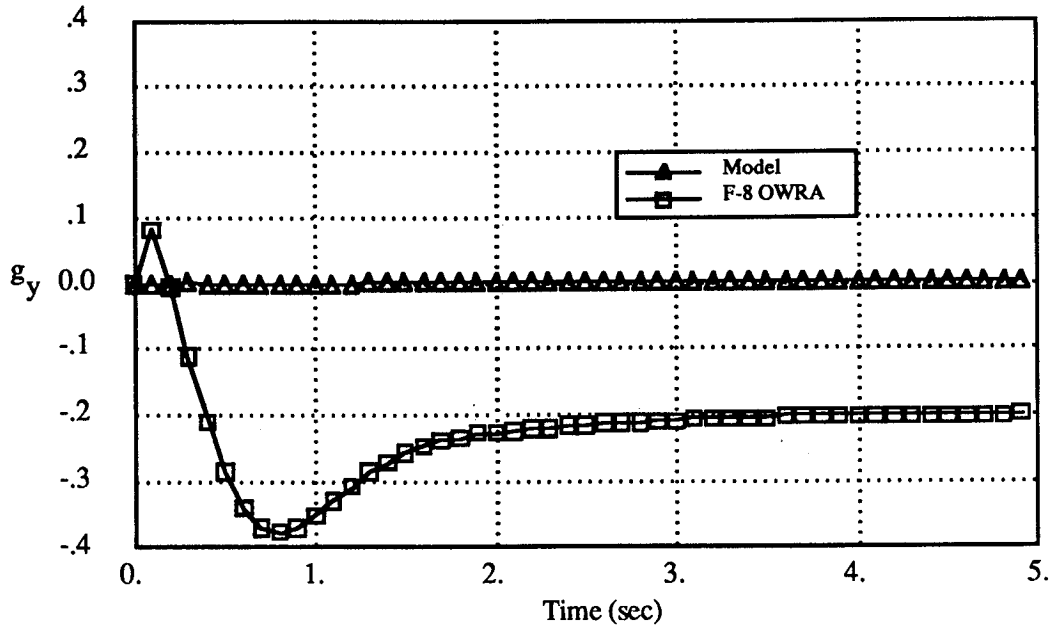
Figure 3.24 lateral acceleration vs time

Normal Acceleration vs Time

EMF SAS, 45° Sweep OWRA
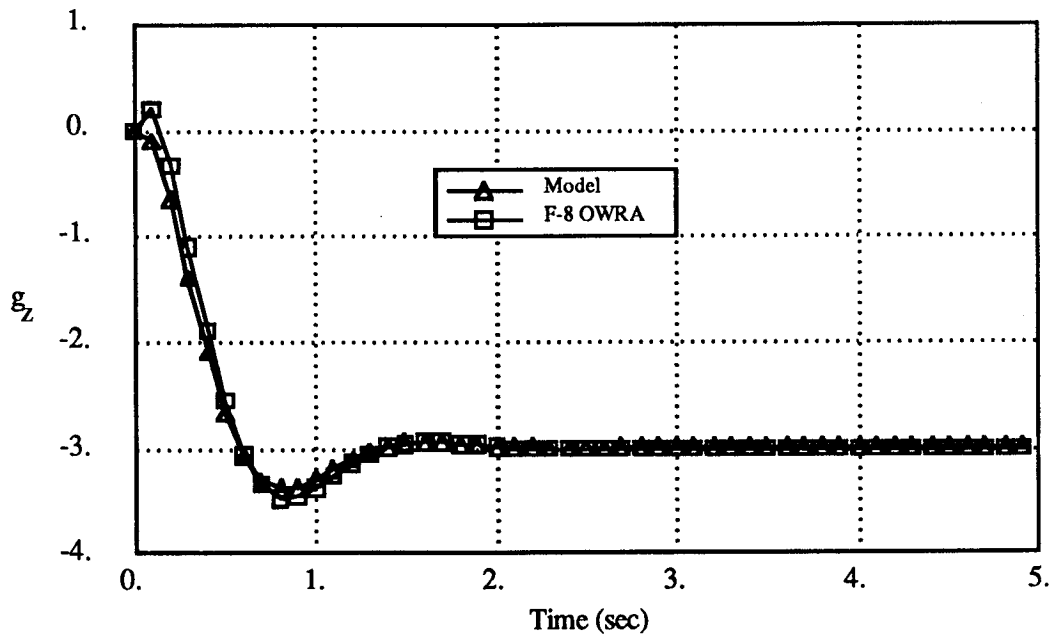
Figure 3.25 normal acceleration vs time

89

Pitch Rate vs Time
EMF SAS, 45° Sweep OWRA
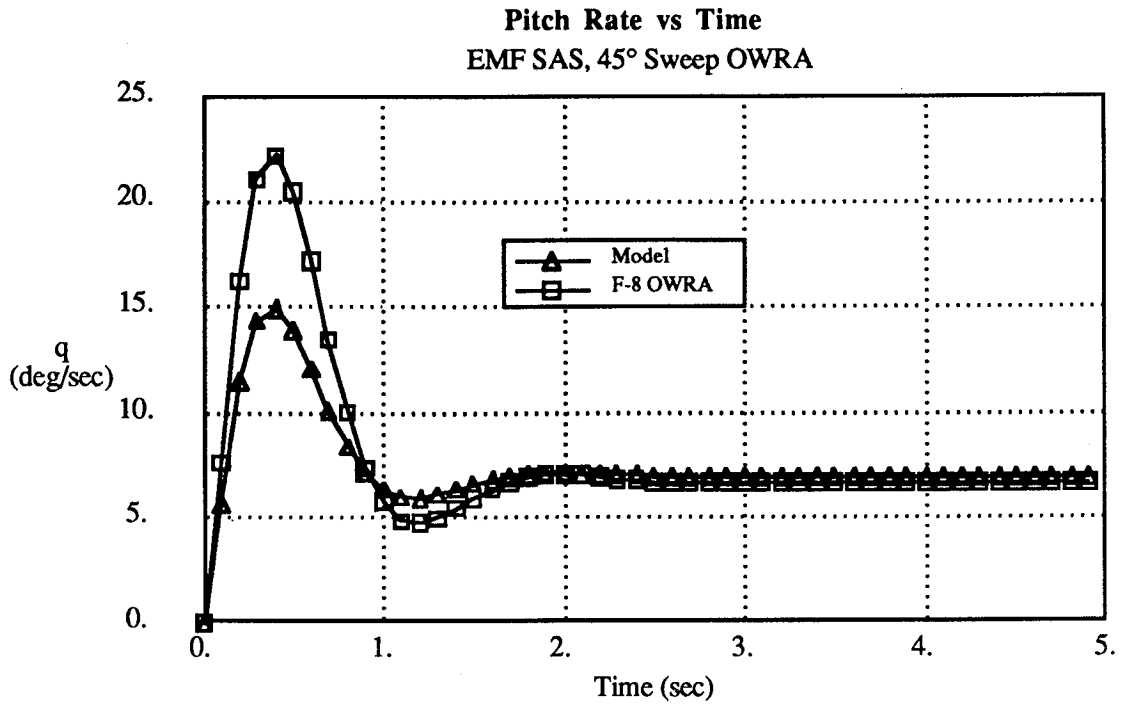
Figure 3.28 pitch rate vs time

Yaw Rate vs Time
EMF SAS, 45° Sweep OWRA
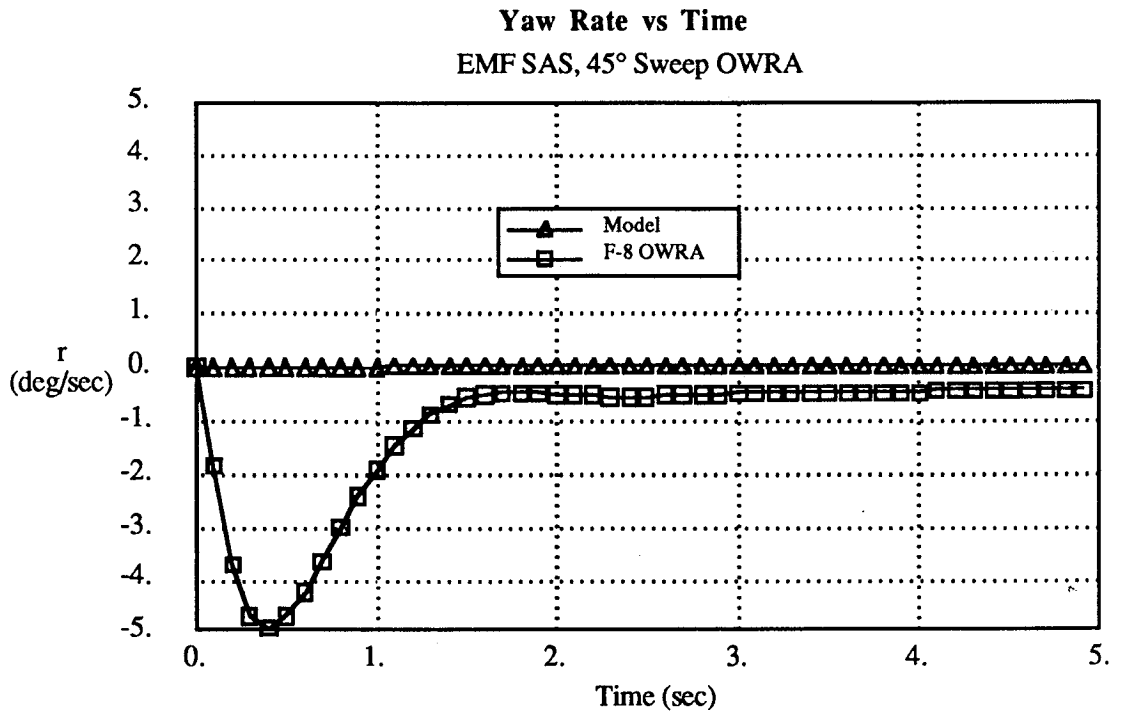
Figure 3.29 yaw rate vs time

Roll Angle vs Time
EMF SAS, 45° Sweep OWRA
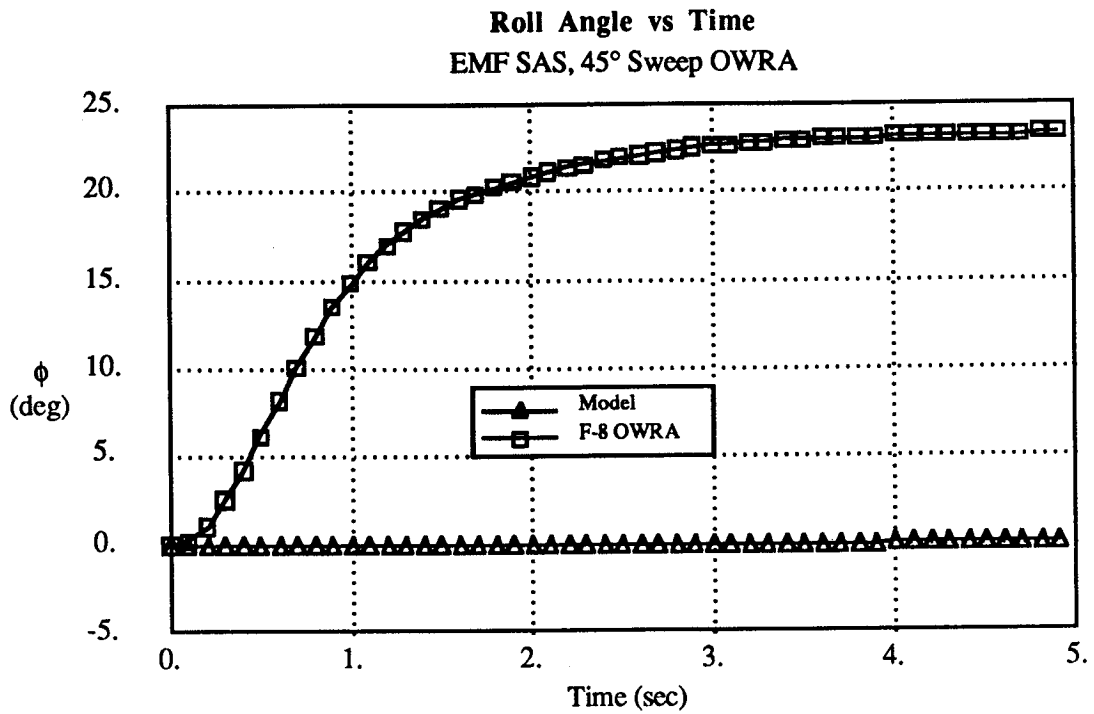
Figure 3.28 roll angle vs time

Control Surface Deflection vs Time
EMF SAS, 45° Sweep OWRA
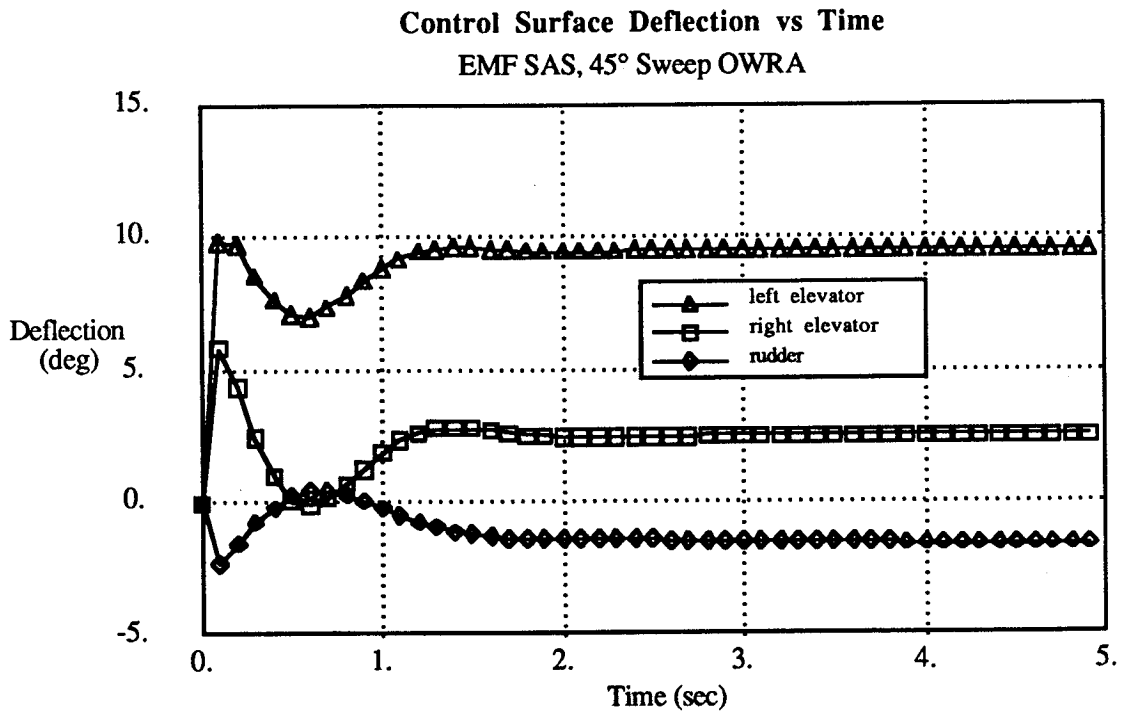
Figure 3.29 control surface deflection vs time

91

Lateral Acceleration vs Time

EMF SAS, 1-g Vertical Gust, 45° Sweep OWRA
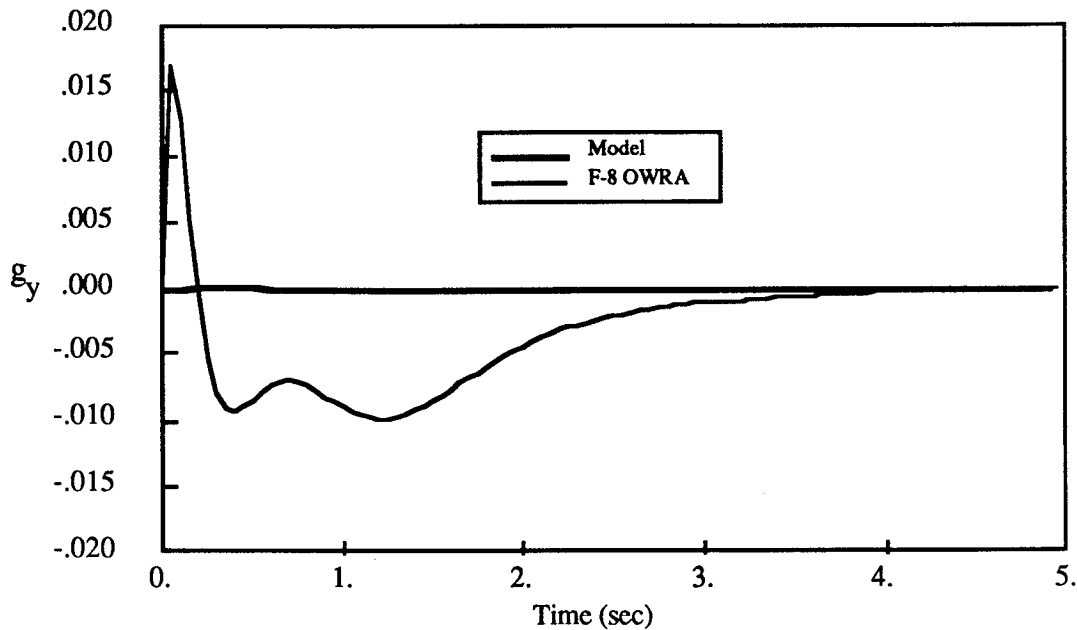
Figure 3.30 lateral acceleration vs time

Normal Acceleration vs Time

EMF SAS, 1-g Vertical Gust, 45° Sweep OWRA
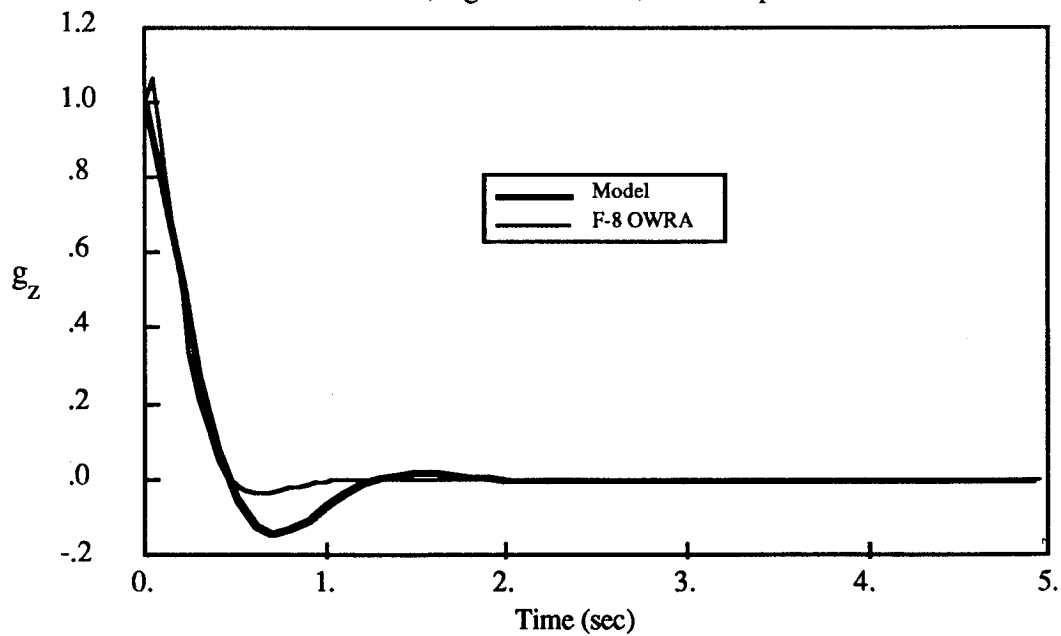
Figure 3.31 normal acceleration vs time

Pitch Rate vs Time

EMF SAS, 1-g Vertical Gust, 45° Sweep OWRA
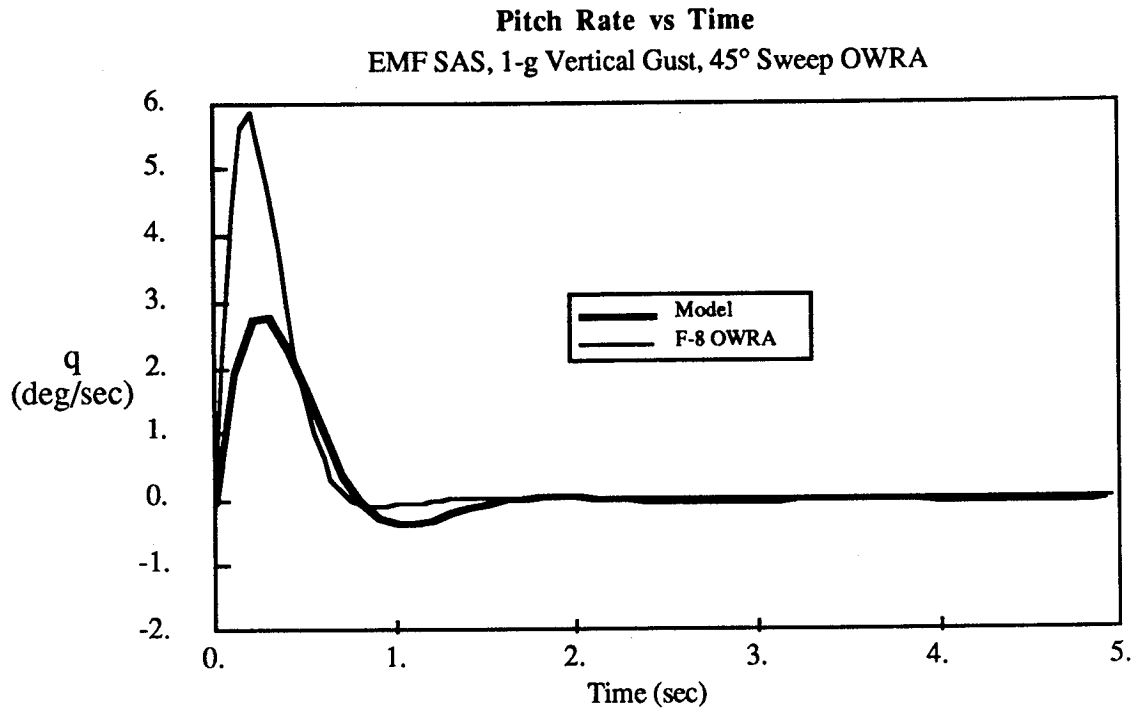
Figure 3.32 pitch rate vs time

Yaw Rate vs Time

EMF SAS, 1-g Vertical Gust, 45° Sweep OWRA
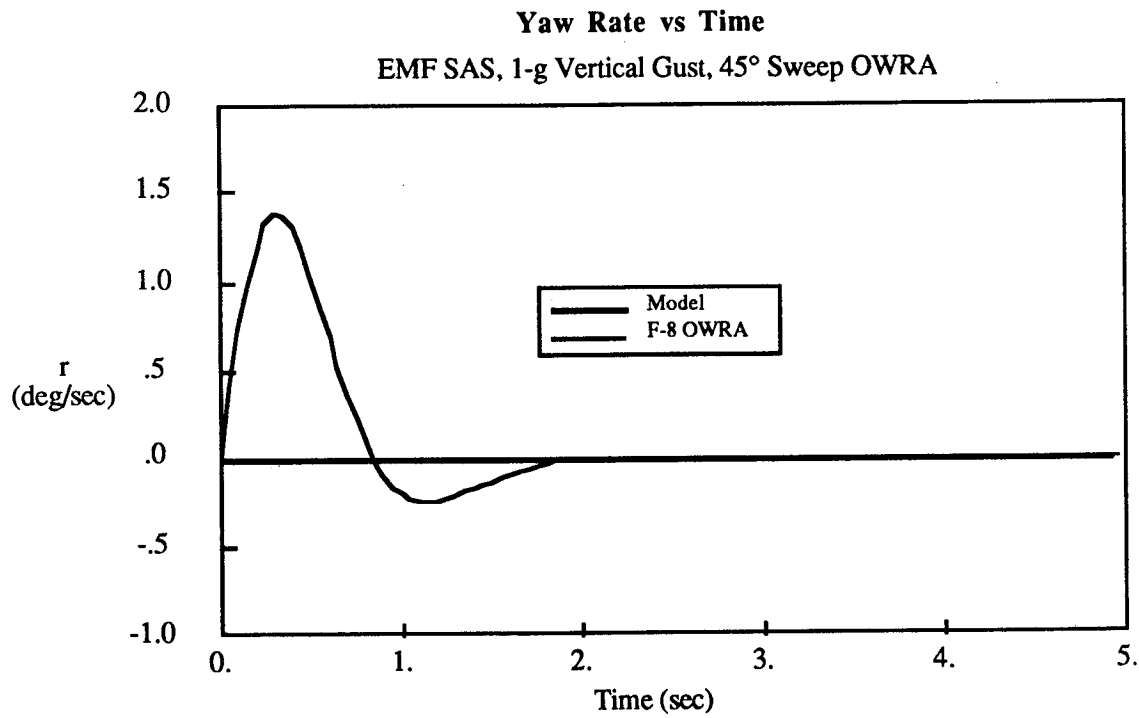
Figure 3.33 yaw rate vs time

Roll Angle vs Time

EMF SAS, 1-g Vertical Gust, 45° Sweep OWRA
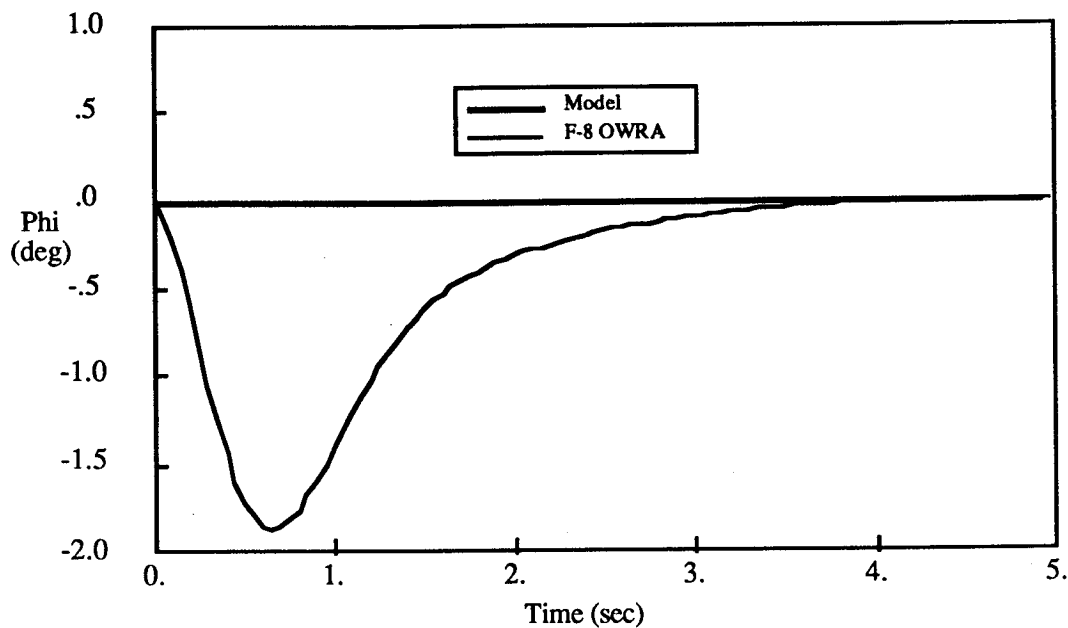
Figure 3.34 roll angle vs time

Control Surface Deflection vs Time

EMF SAS, 1-g Vertical Gust, 45° Sweep OWRA
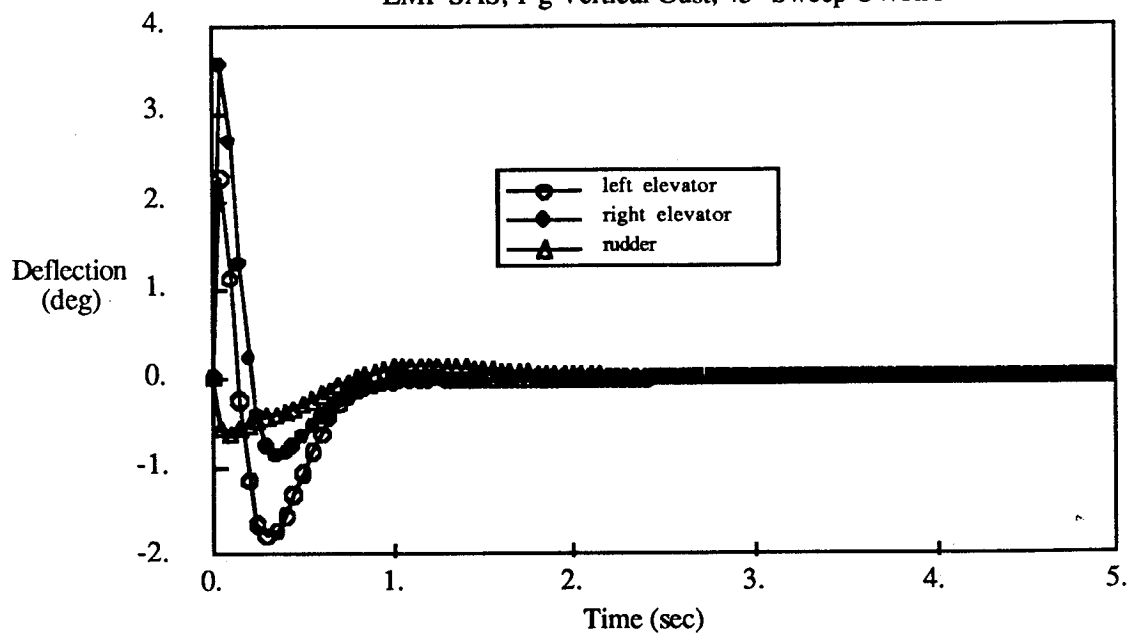
Figure 3.35 control surface deflection vs time

94

EMF SAS Closed Loop Natural Modes

45 (deg) Sweep OWRA
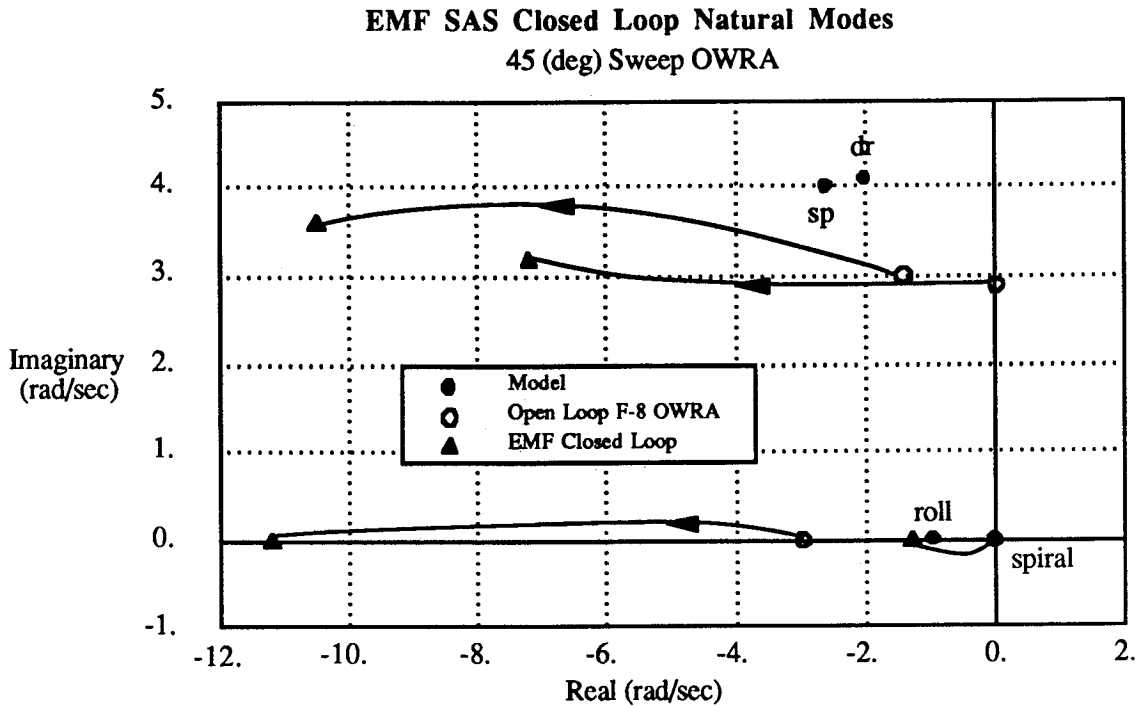
Figure 3.36 natural modes, OWRA with EMF SAS

3.3.2.2 Implicit Model Following SAS

Neglecting the inherent lack of controllability of the F-8 OWRA, the EMF SAS properly attempts to decouple the commanded response of the aircraft. The principle disadvantages of the EMF controller are:

1) The closed loop aircraft has natural dynamic modes significantly faster than the model's (for good tracking accuracy). The EMF SAS may therefore require high-speed, expensive actuators. Excessive bandwidth in the feedback path may make the system overly sensitive to unmodeled high frequency dynamic modes (such as structural flexibility modes) and noise disturbances.

2) The natural (unforced) response does not display the decoupling present in the model's response.

3) Full-state feedback (or an estimator) is required.

The disadvantage of high bandwidth actuators and coupled transient response may be alleviated by designing the feedback path of the EMF SAS so that it attempts to match the transient response of the closed loop aircraft to that of the model. Reference [23] explains that the feedback path of the EMF SAS may be designed by techniques other than minimizing

95

the quadratic dynamic cost integral (equation 3.23) if specific constraints on the transient response are to be met. Implicit Model Following (IMF) [Ref. 22] is a type of model following controller that attempts to match the transient response of the closed loop plant to the model's through use of full-state feedback. The IMF method minimizes a quadratic cost integral that contains an "implicit" representation of the model tracking error. Because the model following error is minimized through the feedback path, the resulting SAS will have unforced dynamics similar to the model's. The pre-compensator and feedforward gains of the SAS must still be designed using the EMF technique and the solution for the IMF feedback gains is obtained by solving a single ARE. Figure 3.37 shows the feedback portion of the IMF SAS in block diagram form.
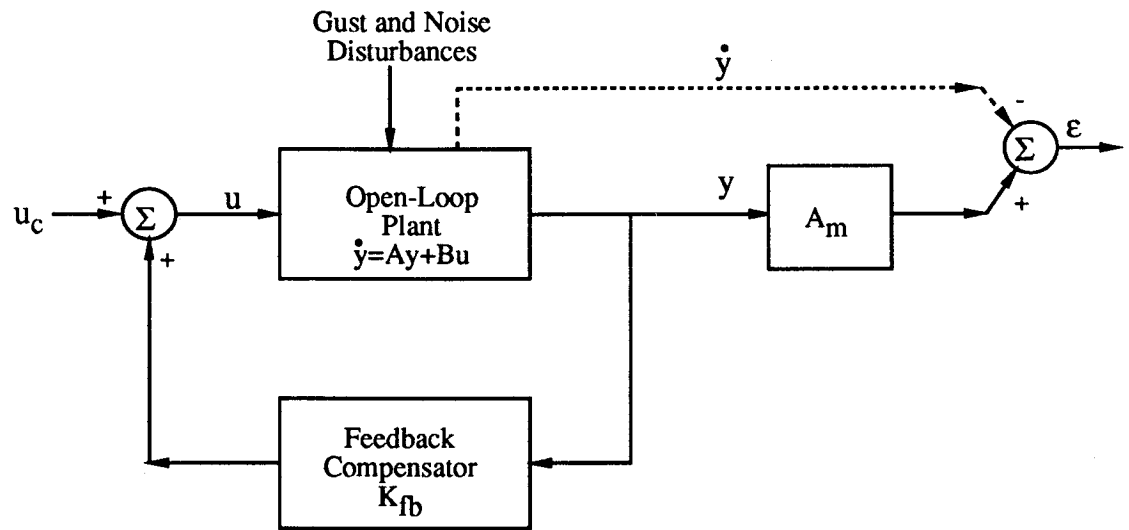
IMF SAS minimizes (J):

$$J = \int_0 (\varepsilon^T Q \varepsilon + u^T R u) \, dt$$

Figure 3.37 IMF SAS block diagram

The following mathematical description of the IMF SAS synthesis explains "implicit" model tracking and shows how the feedback gains are determined.

Given:

Plant

$$\dot{y} = [A] y + [B] u$$

Model

$$\dot{y}_m = [A_m] y_m + [B_m] u_m$$

Find (u) that minimizes (J) where the dynamic cost (J) is given by:

$$(3.46) \quad J = \int_0^\infty \left\{ (\dot{y} - [A_m] y)^T [Q] (\dot{y} - [A_m] y) + u^T [R] u \right\} dt$$

Note that ($\dot{y} - [A_m] y$) is approximately equal to ($\dot{y} - \dot{y}_m$)
(i.e. if $y \cong y_m$ then $[A_m] y \cong [A_m] y_m$).

Minimization of ($\dot{y} - [A_m] y$)^T [Q] ($\dot{y} - [A_m] y$) is implicitly related to
minimization of {($y - y_m$)^T [Q] ($y - y_m$)} which explicitly defines the model
following performance.

The solution for {u} is given in reference [23] as:

$$(3.47) \quad u_{opt} = [K_{fb}] y$$

where:

$$(3.48) \quad [K_{fb}] = -\hat{R}^{-1} (\hat{S} + B^T P)$$

[P] is obtained from the solution of the following A.R.E.:

$$(3.49) \quad (A - B \hat{R}^{-1} \hat{S})^T P + P (A - B \hat{R}^{-1} \hat{S}) - P B \hat{R}^{-1} B^T P + \hat{Q} - \hat{S}^T \hat{R}^{-1} \hat{S} = 0$$

where the matrices $\hat{Q}$, $\hat{R}$, $\hat{S}$ are given by:

$$(3.50) \quad \hat{Q} = (A - A_m)^T Q (A - A_m)$$

$$(3.51) \quad \hat{R} = R + B^T Q B$$

$$(3.52) \quad \hat{S} = B^T Q (A - A_m)$$

It is essential to note that the IMF synthesis **assumes** that ($y \cong y_m$) and that the minimization of the implicit dynamic cost integral:

$$(3.53) \quad J_d = \int_0^\infty (\dot{y}_m - \dot{y})^T Q (\dot{y}_m - \dot{y}) dt$$

will produce the same effect as the minimization of the explicit dynamic cost integral:

$$(3.54) \quad J_d = \int_0^\infty (y_m - y)^T Q (y_m - y) dt$$

97

For linear systems with reduced controllability it may not be possible to force {y} to be sufficiently close to {y_m} such that the previous assumption is true. As a result, the IMF designed SAS may produce inferior closed loop performance.

A simple linear system which demonstrates how an IMF controller produces model following transient response is given by the two degree of freedom torsion disc system shown in figure 3.38.
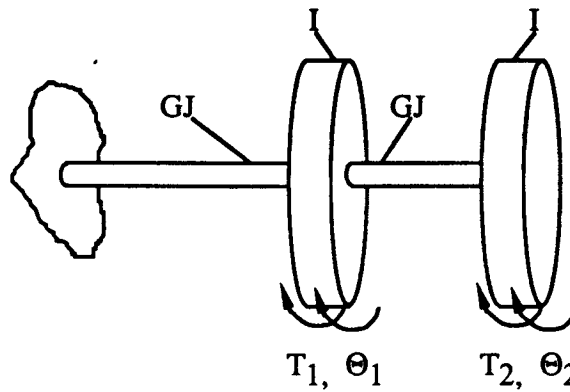
I = Disc Iinertia
GJ = Torsional stiffness
T = External torque acting on disc
Θ = Rotational angle of disc

Figure 3.38 2-disc torsional vibration dynamic system

The linearized equations of motion for the 2-disc torsion system are:

$$(3.58) \quad \begin{bmatrix} \ddot{\Theta}_1 \\ \ddot{\Theta}_2 \\ \dot{\Theta}_1 \\ \dot{\Theta}_2 \end{bmatrix} = \begin{bmatrix} -\tau & 0 & -2k & k \\ 0 & -\tau & k & -k \\ 1 & 0 & 0 & 0 \\ 0 & 1 & 0 & 0 \end{bmatrix} \begin{bmatrix} \dot{\Theta}_1 \\ \dot{\Theta}_2 \\ \Theta_1 \\ \Theta_2 \end{bmatrix} + \begin{bmatrix} \frac{1}{I} & 0 \\ 0 & \frac{1}{I} \\ 0 & 0 \\ 0 & 0 \end{bmatrix} \begin{bmatrix} T_1 \\ T_2 \end{bmatrix}$$

The linearized equations of motion may be written in the form:

$$\dot{x} = [A]\,x + [B]\,u$$

98

where:

$$x = (\dot{\Theta}_1, \dot{\Theta}_2, \Theta_1, \Theta_2)^T$$

$$k = \frac{\text{Torsional Stiffness}}{\text{Disc Inertia}} = \frac{GJ}{I}$$

$$\tau = \text{Damping Coefficient} = \frac{C}{I}$$

and the assumed values of the parameters are:

$$I = 1.0 \ (\text{slug-ft}^2)$$

$$k = 2.0 \ (\frac{\text{lbf}}{\text{slug-ft}})$$

$$\tau = 0.5 \ (\frac{\text{lbf-sec}}{\text{slug-ft}^2})$$

For this example a model system, whose dynamic response is decoupled in θ_1 and θ_2, will be used to specify the desired transient response.

Model System Equations of Motion

$$(3.56) \quad
\begin{bmatrix} \ddot{\Theta}_1 \\ \ddot{\Theta}_2 \\ \dot{\Theta}_1 \\ \dot{\Theta}_2 \end{bmatrix} =
\begin{bmatrix} -1 & 0 & -1 & 0 \\ 0 & -1 & 0 & -1 \\ 1 & 0 & 0 & 0 \\ 0 & 1 & 0 & 0 \end{bmatrix}
\begin{bmatrix} \dot{\Theta}_1 \\ \dot{\Theta}_2 \\ \Theta_1 \\ \Theta_2 \end{bmatrix}$$

An IMF SAS of the form $\{u\} = [K]\{x\}$ (where [K] is a full-state feedback gain matrix) is designed assuming $[Q] = [1]$ and $[R] = \sigma[1]$. Control systems are designed for several values of the control effort weighting parameter σ and a root locus of each closed loop system's eigenvalues is shown in figure 3.39.

2-Disc Root Locus, IMF SAS

Root Trajectories Indicate Increasing Control Effort Weighting
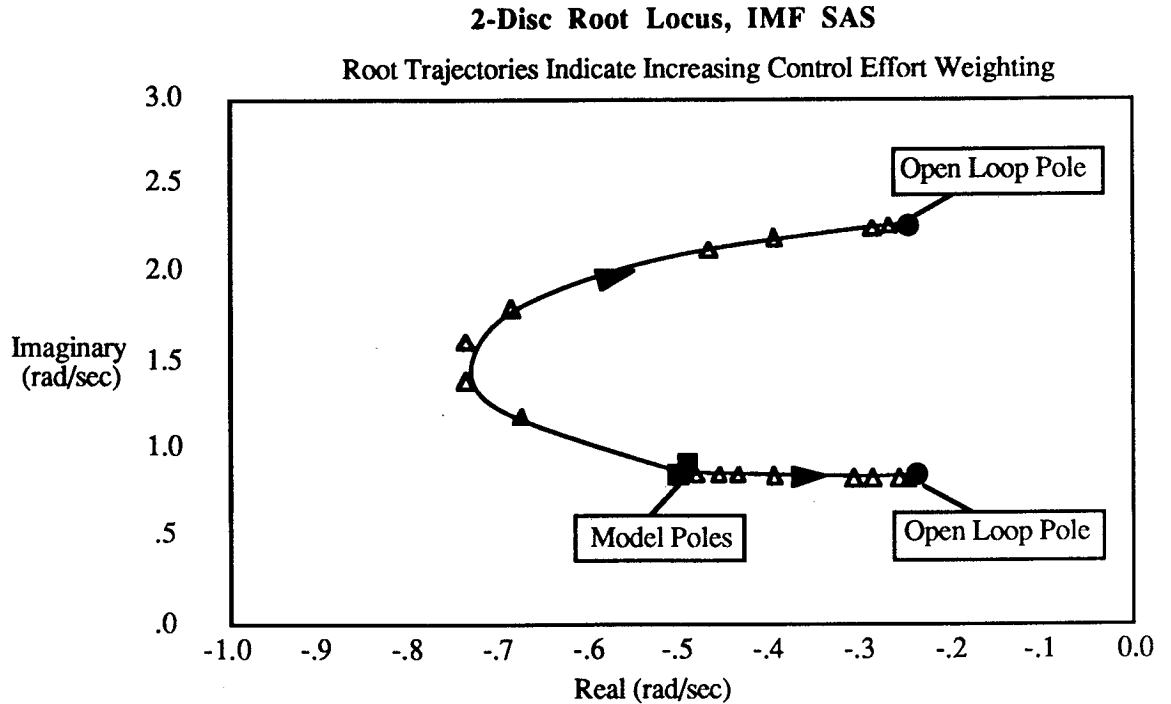
Figure 3.39 2-disc closed loop natural modes, IMF SAS

For σ = 0 (no control effort weight) the closed loop eigenvalues match the model's exactly. Furthermore, the closed loop system matrix is identical to the model's indicating that the transient response of the closed loop plant will also match the model's exactly. As control effort weight is increased the response reverts to the coupled transients of the open loop system. In this example the IMF SAS is able to match the model's eigensystem exactly because the system is sufficiently controllable.

Now consider the synthesis of an IMF SAS for the feedback compensation of the F-8 OWRA. The goal of the feedback controller is to force the transient response of the closed loop aircraft to be most like that of the Mil.-Spec. F-8785C model. A pre-compensator SAS which decouples the commanded response can then be designed after the feedback compensator is known. The system matrices for the open loop OWRA at 45 degree oblique sweep, M=0.8 and the model were previously given in figures 3.21 and 3.22. Initially the weighting matrices are chosen to be:

$$[Q] = I \qquad\qquad [R] = .001[I]$$

This choice of [Q] and [R] ensures a SAS design which attempts to decouple the response as much as possible, with little regard to the control effort required. Applying the IMF

SAS procedure (equations 3.46 - 3.52) the following full-state feedback controller gains are obtained:

$$F\text{-8 OWRA, } 45° \text{ sweep, } M=0.8, Q = I, R = 0$$

$$
K_{fb} = \begin{array}{ccccccc}
 & g_y & g_z & p & q & r & \phi \\
\left[\begin{array}{c} \\ \\ \\ \end{array}\right. & \begin{array}{c} 39.780 \\ .454 \\ -7.072 \end{array} & \begin{array}{c} -12.136 \\ -.152 \\ 2.163 \end{array} & \begin{array}{c} -15.618 \\ -.184 \\ 2.795 \end{array} & \begin{array}{c} 12.071 \\ -.057 \\ -2.178 \end{array} & \begin{array}{c} -40.027 \\ -.497 \\ 7.060 \end{array} & \left.\begin{array}{c} -38.937 \\ -.444 \\ 6.925 \end{array}\right]
\end{array}
$$

(matrix continued)

$$
\begin{array}{ccc}
\delta_{roll} & \delta_{pitch} & \delta_{yaw} \\
-21.981 & 69.547 & 171.461 \\
-.284 & 1.380 & 2.002 \\
4.090 & -12.405 & -30.913
\end{array}
$$

Figure 3.40 IMF SAS feedback gain solution for the F-8 OWRA

The transient response of the closed loop system to an initial condition of a 1 "g" vertical acceleration is plotted in figures 3.41 - 3.45 along with the response of the model to the same initial condition. This excitation is similar to a vertical gust disturbance which produces a phugoid and short period motion in a decoupled aircraft.

Lateral Acceleration vs Time
45 (deg) sweep OWRA, 1- g Vertical Gust
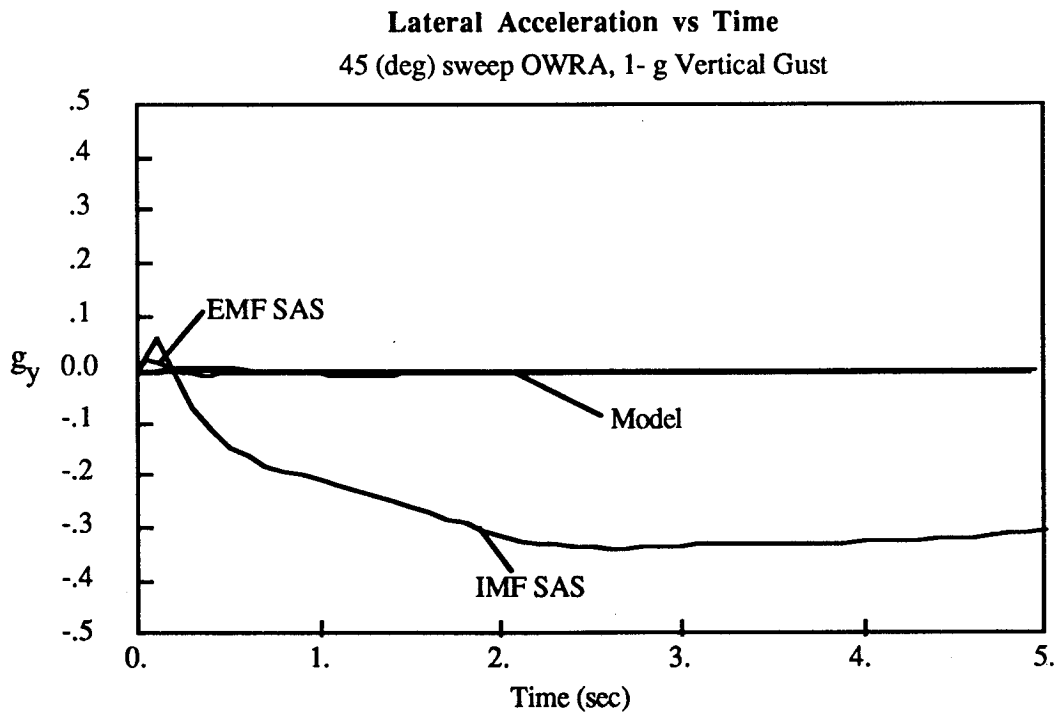
Figure 3.41 lateral acceleration vs time

Normal Acceleration vs Time
45 (deg) Sweep OWRA, 1-g Vertical Gust
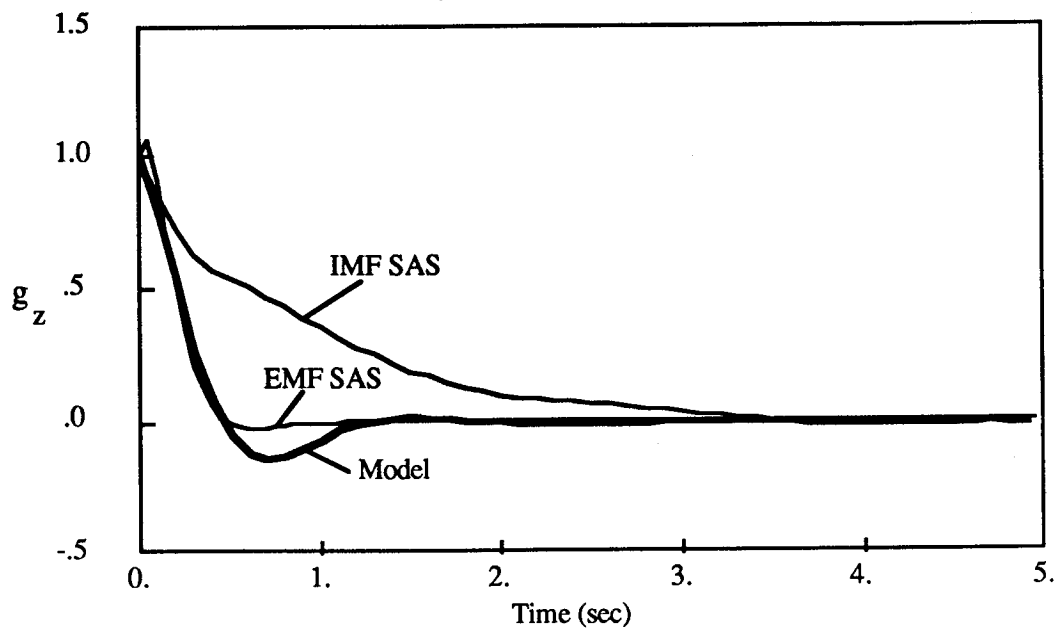
Figure 3.42 normal acceleration vs time

Pitch Rate vs Time
45 (deg) Sweep OWRA, 1-g Vertical Gust
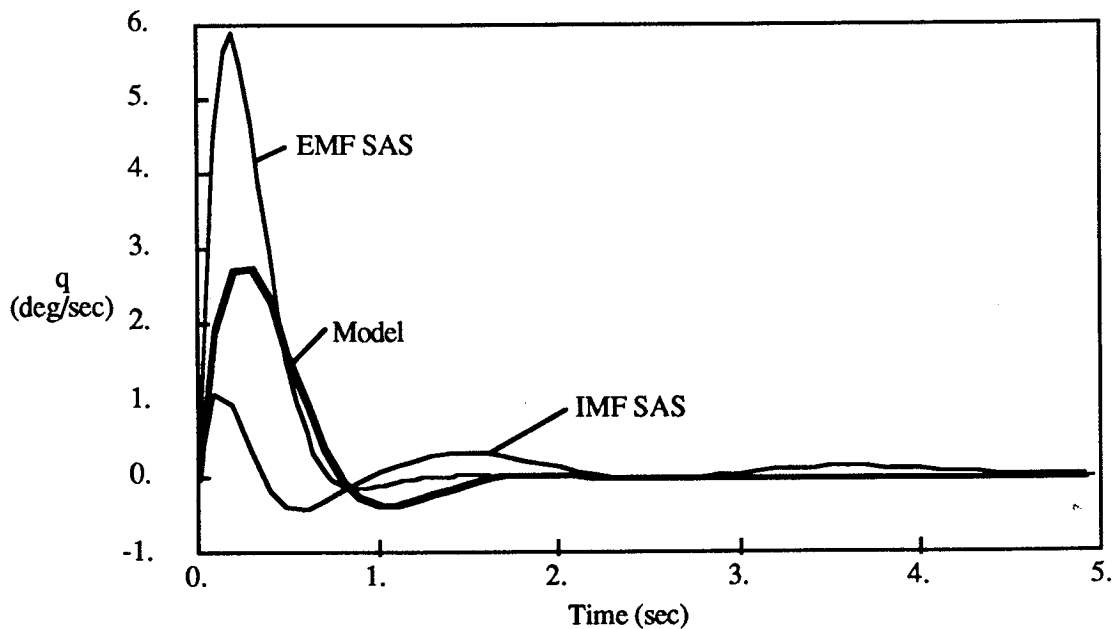
Figure 3.43 pitch rate vs time

Yaw Rate vs Time

45 (deg) Sweep OWRA, 1-g Vertical Gust
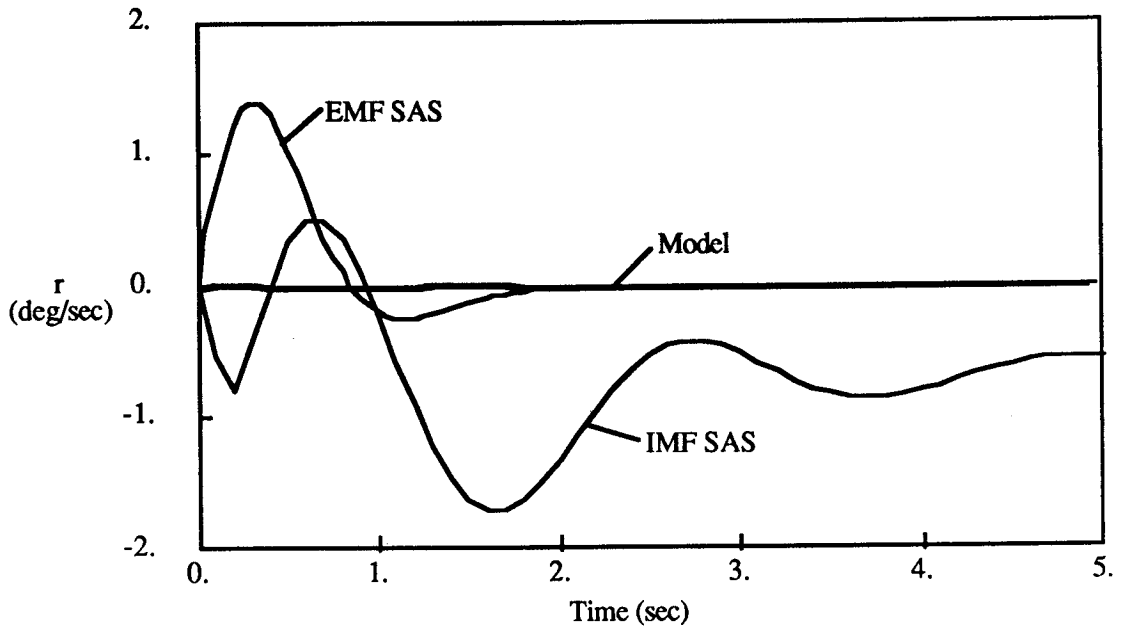
Figure 3.44 yaw rate vs time

Roll Angle vs Time

45 (deg) Sweep OWRA, 1-g Vertical Gust
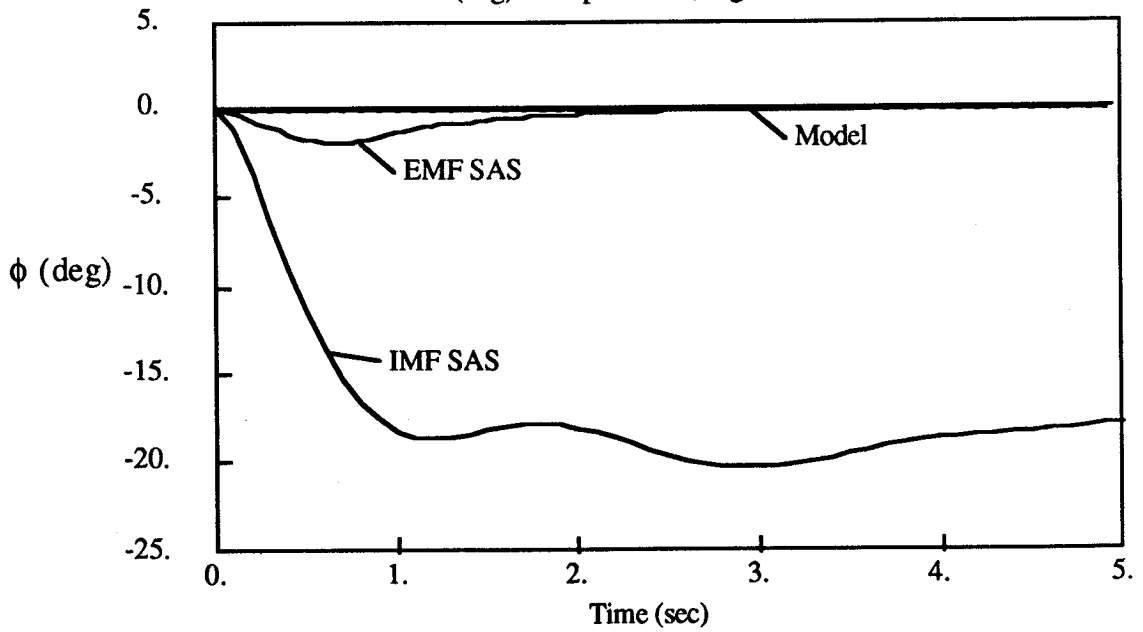
Figure 3.45 roll angle vs time

103

The time histories of the closed loop transient response show that substantial coupling of the lateral and longitudinal motions still exists. The longitudinal response (g_z, q) appears to be following the model, but not very closely. The response of the same aircraft with the previously designed EMF SAS is also plotted in figures 3.41 - 3.45 and although the longitudinal response is not following the model any better than the IMF SAS, the coupling to the lateral motions (g_y, ϕ) is substantially less. This is not to say that the EMF SAS is actually decoupling the transient response (it is not) but that the IMF SAS, which should have shown improved decoupling over the EMF SAS, has failed to do so. The reason for the poor performance of the IMF compensated aircraft is that for dynamic systems with reduced controllability (such as the OWRA) the assumption that:

$$(3.57) \qquad J = \int_0^\infty \left\{ (\dot{y} - [A_m] \, y)^T [Q] \, (\dot{y} - [A_m] \, y) + u^T [R] \, u \right\} dt$$

is similar to:

$$(3.58) \qquad J = \int_0^\infty \left\{ (y - y_m)^T [Q] \, (y - y_m) + u^T [R] \, u \right\} dt$$

is no longer valid! As a result the IMF SAS solution for systems with reduced controllability may be unacceptable regardless of the choice of [Q] and [R]. In the next section a new SAS design method will be presented which solves the problem of achieving model following transient and commanded response.

3.3.2.3 Reduced Order Model Following SAS

The previous sections have shown that both the IMF and EMF SAS have performance deficiencies when attempting to decouple the natural and forced response of an oblique wing aircraft. In this section a new type of SAS synthesis will be presented which decouples the commanded and unforced response, does not require excessive actuator bandwidth, and does not assume full-state feedback. The synthesis of this SAS is based on robust, reduced order controller design techniques presented by Ly in reference 23. The SAS gains are found by minimizing a quadratic dynamic cost function using a nonlinear numerical optimization procedure. This requires significantly greater computation time than solving a single ARE (i.e. EMF or IMF SAS design) but the advantages of improved closed loop performance and increased flexibility in the controller architecture justify this cost.

Ly [Ref. 23] presents a controller synthesis method that provides robustness to plant uncertainties with a controller that does not require full-state feedback. Because the gains are found using a numerical optimizer, the controller architecture can have any linear form. Ly shows how to analytically evaluate the gradient of the dynamic cost function (J) with respect to the controller gains and does this for infinite and finite time integrals of the cost function. In this thesis, some of the basic ideas in Ly's method will be incorporated into a SAS synthesis scheme where the objective function and the SAS architecture are carefully chosen to produce the desired model following controller. Controllers synthesized using this new method will be called Reduced order Model Following SAS or RMF SAS. The synthesis of an RMF SAS is as follows:

Given the plant and model dynamic systems:

Plant

$$\dot{x} = [A] x + [B] u$$

$$y = [Z] x$$

Model

$$\dot{x}_m = [A_m] x_m + [B_m] u_m$$

$$y_m = [Z_m] x_m$$

n = number of outputs (y)
m = number of inputs (u)

Consider the augmented dynamic systems:

(3.57) $$\dot{\tilde{y}} = \begin{bmatrix} Z A Z^{-1} & 0 & 0 \\ 0 & Z_m A_m Z_m^{-1} & Z_m B_m \\ 0 & 0 & \varepsilon \end{bmatrix} \tilde{y} + \begin{bmatrix} Z B \\ 0 \\ 0 \end{bmatrix} u$$

(2n+m x 2n+m)   (2n+m x m)

(3.58) $$\dot{\tilde{y}}_m = \begin{bmatrix} Z_m A_m Z_m^{-1} & 0 & Z_m B_m \\ 0 & \varepsilon & 0 \\ 0 & 0 & \varepsilon \end{bmatrix} \tilde{y}_m$$

(2n+m x 2n+m)

105

Where:

$$\tilde{y} \equiv \left[\, y, y_m, u_m \, \right]^T$$

$$\tilde{y}_m \equiv \left[\, y_m, \text{arbitrary}, u_m \, \right]^T$$

The dynamic cost function, which includes terms related to the model following error and required control effort, is defined as follows:

$$(3.59) \qquad J = \int_0^\infty \left\{ (\tilde{y} - \tilde{y}_m)^T \tilde{Q} \, (\tilde{y} - \tilde{y}_m) + u^T R \, u \right\} dt$$

where:

$$(3.60) \qquad \tilde{Q} \equiv \begin{bmatrix} Q & 0 & 0 \\ 0 & 0 & 0 \\ 0 & 0 & 0 \end{bmatrix}$$

[Q] is the weighting on the model following error { $y - y_m$ } and (J) represents a quadratic cost proportional to the weighted model following error where only the differences between { $y - y_m$ } contribute. It is important to note that this choice of { $y - y_m$ } guarantees that initial conditions that excite the plant (y_o) will also excite the model transients if it is assumed that $y_o = y_{mo}$. This produces a true model following error when the plant is excited by any initial condition, i.e. those representing pilot inputs and those representing gusts. The {y_m} outputs are included in the {y} vector so that the model outputs are available for the pre-compensator portion of the SAS. This method distinguishes between the model states implemented in the SAS pre-compensator and the additional model states which are excited by the same disturbances (gusts and pilot commands) as the closed loop aircraft. This distinction is of key importance if the total response is to be decoupled. The resulting RMF SAS architecture can be expressed as:

$$(3.61) \qquad u = [K] \, \tilde{y}$$

Where any term in [K] may be arbitrarily held at zero to reduce the order of the controller from that of full-state feedback. For example, in the OWRA synthesis, the actuator states have zero feedback gain associated with them so that these states are not required by the feedback and pre-compensator SAS segments. By carefully choosing {y} and [K] it is

possible to model any desired linear feedback control architecture in the RMF SAS synthesis.

The solution for the nonzero terms in [K] is obtained by minimizing (J) using a numerical optimization scheme. The successive evaluation of (J) necessary for this type of solution is accomplished by solving the following system of Lyapunov matrix equations [Ref. 25]:

$$(3.62) \qquad (\tilde{A} + \tilde{B} K)^T P_1 + P_1 (\tilde{A} + \tilde{B} K) + (\tilde{Q} + K^T R K) = 0$$

$$(3.63) \qquad (\tilde{A} + \tilde{B} K)^T P_2 + P_2 (\tilde{A}_m) + (\tilde{Q}) = 0$$

$$(3.64) \qquad (\tilde{A}_m^T) P_3 + P_3 (\tilde{A}_m) + (\tilde{Q}) = 0$$

$$(3.65) \qquad P \equiv \left[P_1 - P_2 - P_2^T + P_3 \right]$$

The dynamic cost (J) is given by:

$$(3.66) \qquad J = \tilde{y}_o^T P \tilde{y}_o$$

Notice that the value of the initial condition $\{y_o\}$ is required to evaluate (J). Full state feedback LQR controllers have the same solution for the optimal controller gains regardless of the initial conditions considered. The design of reduced order LQR controllers depends on the initial conditions which excite the plant because full state feedback is not assumed. Typically, more than one initial condition is critical to performance, therefore, a sum of the dynamic cost for various initial conditions is used to calculate the total dynamic cost function:

$$(3.67) \qquad J_d = \sum_{i=1}^{N_{ic}} \tilde{y}_{o_i}^T P \tilde{y}_{o_i} \qquad N_{ic} = \text{Number of ic's considered}$$

The solution of each Lyapunov equation (equations 3.62 - 3.64) represents an integral of a portion of the dynamic cost from time equal to zero to infinity. If the solution to the Lyapunov equations is to be bounded, the closed loop system must be dynamically stable.

Dynamic stability requires that:

$$R_e(\sigma_i) \leq -\xi \qquad \text{for } i = 1 \text{ to } 2n+m, \; \xi \text{ is assumed positive}$$

where σ_i is the ith eigenvalue of the closed loop system and ξ is a minimum damping requirement based on the feasibility of numerically solving the Lyapunov equations. This stability constraint is enforced by appending a penalty function to (J_d) that becomes active when the closed loop damping drops below the specified limit:

$$(3.68) \qquad J_d = \sum_{i=1}^{N_{ic}} y_{o_i}^T P \, y_{o_i} + \begin{cases} 0 & \text{if Re}(\sigma_i) \leq -\xi \\ k_i \left(\left| \text{Re}(\sigma_i) \right| - \xi \right)^2 & \text{if Re}(\sigma_i) > -\xi \end{cases}$$

where k_i is a penalty function weight.

Equation 3.68 is the complete form of the objective function (J_d) to be minimized. In reference [23] Ly avoids the problem of enforcing a stability constraint by evaluating the dynamic cost over a finite time interval.

Finite time dynamic cost function may be implemented:

$$J_d = \int_0^{T_f} (y^T Q \, y + u^T R \, u) \, dt$$

instead of:

$$J_d = \int_0^{\infty} (y^T Q \, y + u^T R \, u) \, dt$$

The optimization procedure to minimize J_d is then repeated for increasing values T_f until the value of J) converges to a minimum. This approach permits initial guesses for [K] which may produce an unstable plant, where as the infinite time integral approach requires a stable initial guess. Ly's finite time method is more robust to stability constraints but requires significantly more computation effort due to repeated minimization of J_d at various T_f. In the case of a SAS design for an oblique wing aircraft, it is easy to produce initial guesses for [K] that yield a stable closed loop system. Therefore, the infinite time formulation of the dynamic cost integral will be used in this work.

An RMF SAS is synthesized by using a Quasi-Newton (or Variable Metric) numerical opti-
mizer [Ref. 19] to find the gains [K] which minimize J_d. This optimization procedure
searches for a minimum along descent directions which improve in accuracy (based upon a
second order model of the objective function) as the optimization progresses. The Quasi-
Newton method is used in this work because it represents a satisfactory compromise be-
tween the high computation costs of second order methods and the poor convergence speed
of first order schemes. Gradient calculations are obtained from a numerical derivative ap-
proximation (central difference) for the derivative of J_d with respect to the control gains.
Analytical expressions for the gradient given by Ly [23] could be implemented to minimize
computation costs and this option is recommended for future work.

A block diagram of the RMF controller is shown in figure 3.46.
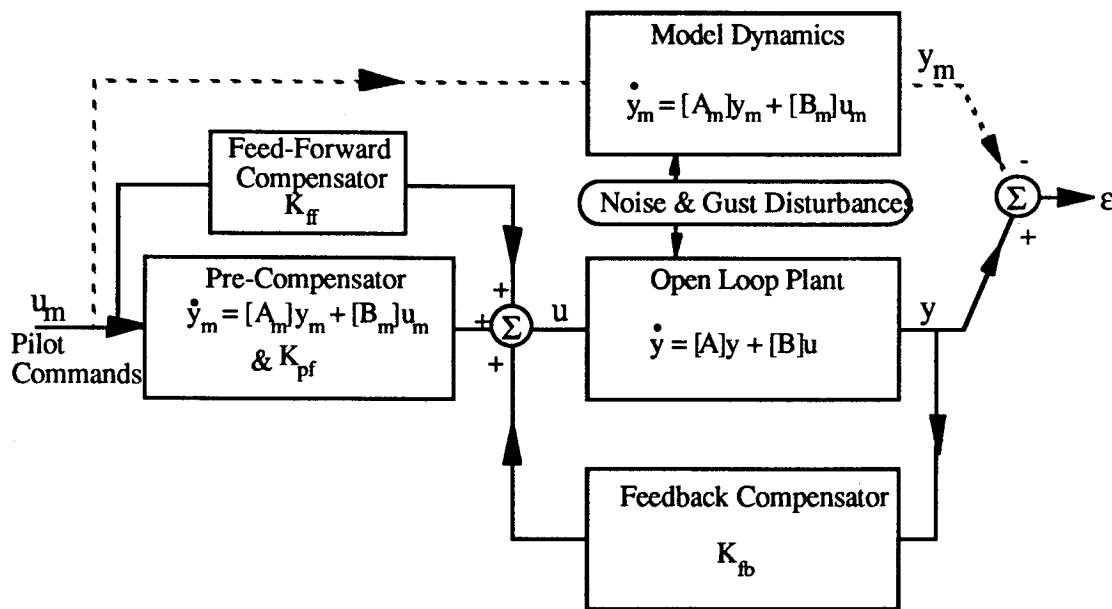
Figure 3.46 RMF controller block diagram

The model dynamics appear twice, first in the pre-compensator to facilitate commanded re-
sponse decoupling, and then in the formulation of $\varepsilon = \{ y - y_m \}$ so that the plant and model
experience the same noise excitation for transient response decoupling.

To better understand how the RMF SAS performs and is synthesized, a controller for the
2-disc torsion system presented in section 3.3.2.2 is synthesized and the results compared
with the IMF controller performance for the same system. Two cases are considered, the

first having a torque actuator on each disk, and the second having an actuator only on the first disc for reduced controllability.

Case 1
(2) Torque Actuators

Case 2
(1) Torque Actuator
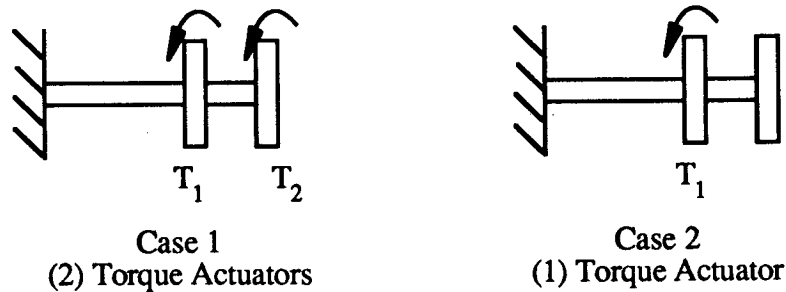
Figure 3.47 2-disc torsion dynamic system

The plant and model dynamic matrices are:

Plant

$$\dot{y} = [A]\, y + [B]\, u$$

$$y = (\dot{\Theta}_1, \dot{\Theta}_2, \Theta_1, \Theta_2)^T$$

$$[A] = \begin{bmatrix} -.5 & 0 & -4 & 2 \\ 0 & -.5 & 2 & -2 \\ 1 & 0 & 0 & 0 \\ 0 & 1 & 0 & 0 \end{bmatrix}$$

Case 1
$$[B] = \begin{bmatrix} 1 & 0 \\ 0 & 1 \\ 0 & 0 \\ 0 & 0 \end{bmatrix}$$

Case 2
$$[B] = \begin{bmatrix} 1 \\ 0 \\ 0 \\ 0 \end{bmatrix}$$

Model

$$\dot{y}_m = [A_m]\, y_m$$

$$[A_m] = \begin{bmatrix} -1 & 0 & -1 & 0 \\ 0 & -1 & 0 & -1 \\ 1 & 0 & 0 & 0 \\ 0 & 1 & 0 & 0 \end{bmatrix}$$

In order to maintain simplicity, only feedback compensation will be considered for the 2-disc controller. The goal of the control system is identical to that of the IMF example, to force the transient response of the closed loop plant to approach that of the model's.

The RMF controller dynamic performance is calculated as follows:

Plant $\qquad \dot{y} = [A]\,y + [B]\,u$

Model $\qquad \dot{y}_m = [A_m]\,y_m$

Control Law $\quad u = [K]\,y$

Dynamic Cost

$$J_d = \int_0^\infty (\varepsilon^T Q\,\varepsilon + u^T R\,u)\,dt + \text{Penalty Function for Stability Constraint}$$

where:

$$\varepsilon = (y - y_m)$$

J_d is computed by solving three Lyapunov equations

1) $(A + B K)^T P_1 + P_1 (A + B K) + (Q + K^T R K) = 0$

2) $(A + B K)^T P_2 + P_2 (A_m) + (Q) = 0$

3) $(A_m)^T P_3 + P_3 (A_m) + (Q) = 0$

$$P \equiv \left[P_1 - P_2 - P_2^T + P_3 \right]$$

$$J_d = \sum_{i=1}^{N_{ic}} y_{o_i}^T P\, y_{o_i} + \text{P.F. (stability)}$$

Full state feedback is assumed in this example, so that the results may be compared directly with those for the IMF SAS. The initial conditions used in the RMF synthesis are:

2 Disc RMF SAS initial conditions

$y_{01} = 1 \quad 0 \quad 0 \quad 0$

$y_{02} = 0 \quad 1 \quad 0 \quad 0$

$y_{03} = 0 \quad 0 \quad 1 \quad 0$

$y_{04} = 0 \quad 0 \quad 0 \quad 1$

Using these initial conditions, the total dynamic cost is simply:

$$J_d = \text{Trace } [P] + \text{penalty functions on dynamic stability}$$

111

Case 1 Results

Figure 3.48 is a root locus plot for the closed loop plant as the control effort weighting is increased. As in the case of the IMF SAS, the roots move from the open loop plant values at high control effort weight to those of the model at low control effort weight. Because the system is controllable, the closed loop dynamics can exactly match the model's when the control effort weight is small. It is important to note that although both methods yield the same dynamic response at the extreme range of the root locus, the root traces themselves are different indicating that the dynamic performance is not identical for all values of control effort weight.

2-Disc System Natural Modes

Root Traces Indicate Direction of Increasing Control Effort Weighting
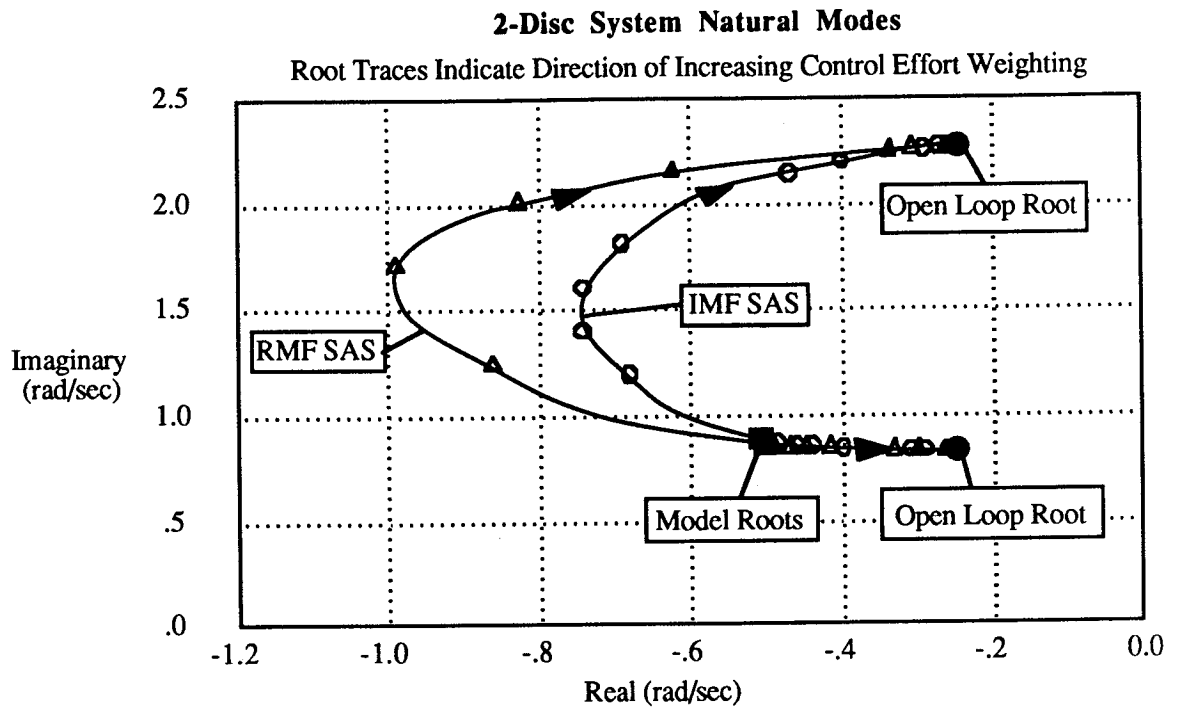
Figure 3.48 2-disc system closed loop natural modes

Case 2 Results

In case 2 there is only one torque actuator available and it is therefore impossible to completely match the dynamic response the model because of the closed loop system's inherent lack of controllability. Feedback controllers synthesized using IMF and RMF techniques show different performance for cases with reduced controllability. For the case where the control effort weighting is zero, the solution for the full-state feedback gain matrices and the closed loop eigenvalues are given in figure 3.49. Simulated time histories of the closed

loop system response to the initial condition $\{y\} = \{1\ 0\ 0\ 0\ \}^T$ are given in figures 3.50 - 3.53 for both the RMF and IMF SAS solutions.

$$B = [1, 0, 0, 0]^T \qquad Q = [I] \qquad R = 0$$

<u>IMF</u>   <u>RMF</u>

$K = [-1.38, .34, 1.731, -1.15]$ $K = [-3.96, -.20, -4.20, 1.48]$

Closed Loop Eigenvalues   Closed Loop Eigenvalues

$S_{1,2} = -0.5 \pm 0.87\,j$ $S_{1,2} = -1.86 \pm 1.69\,j$

$S_{3,4} = -0.69 \pm 1.53\,j$ $S_{3,4} = -0.62 \pm 1.05\,j$

Figure 3.49 controller gains for case #2, 2-disc controller

y1 vs Time
2-Disc System yo=[1 0 0 0]T

Figure 3.50 y1 vs time

y2 vs Time
2-Disc System yo=[1 0 0 0]T

Figure 3.51 y2 vs time

y3 vs Time
2- Disc System, yo=[1 0 0 0]T

Figure 3.52 y3 vs time

114
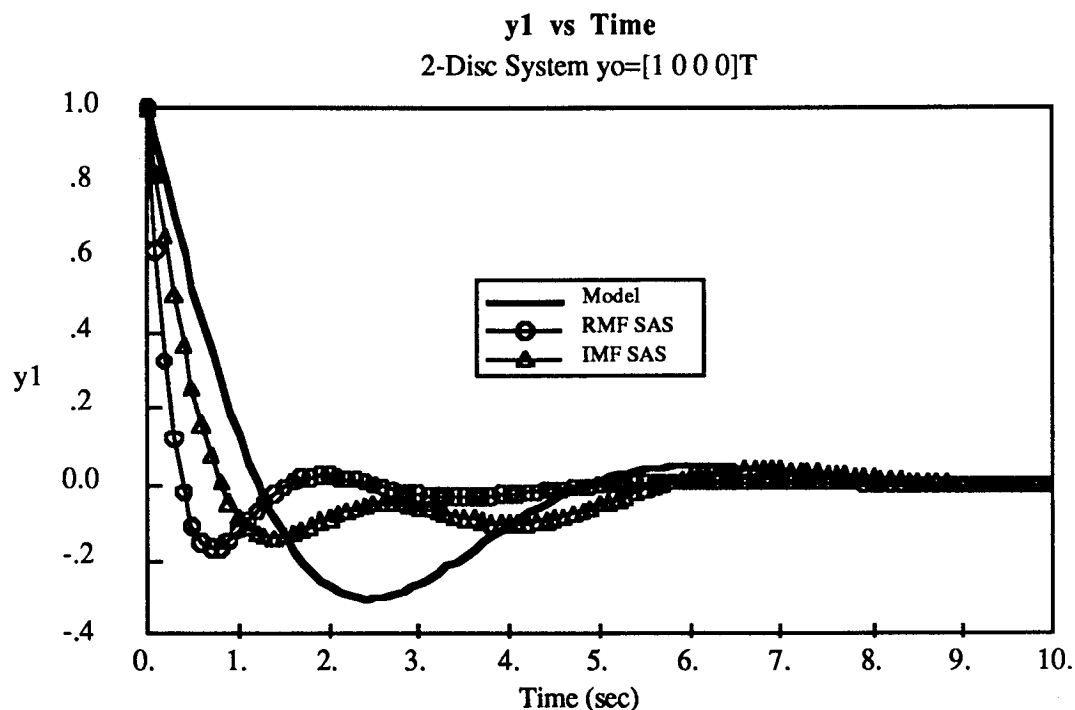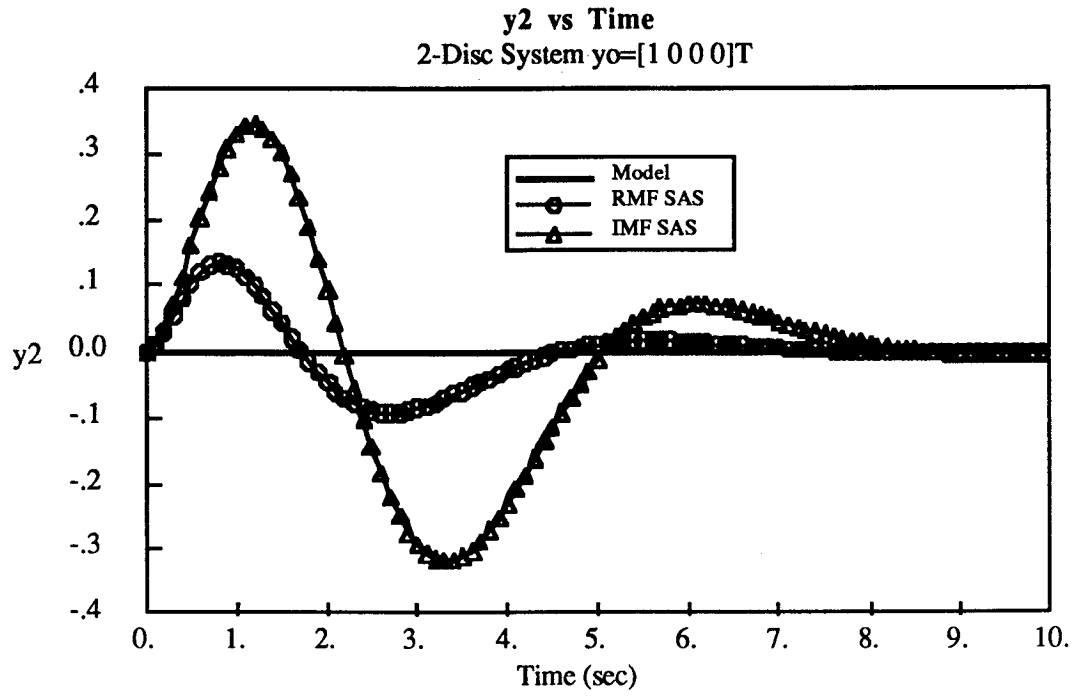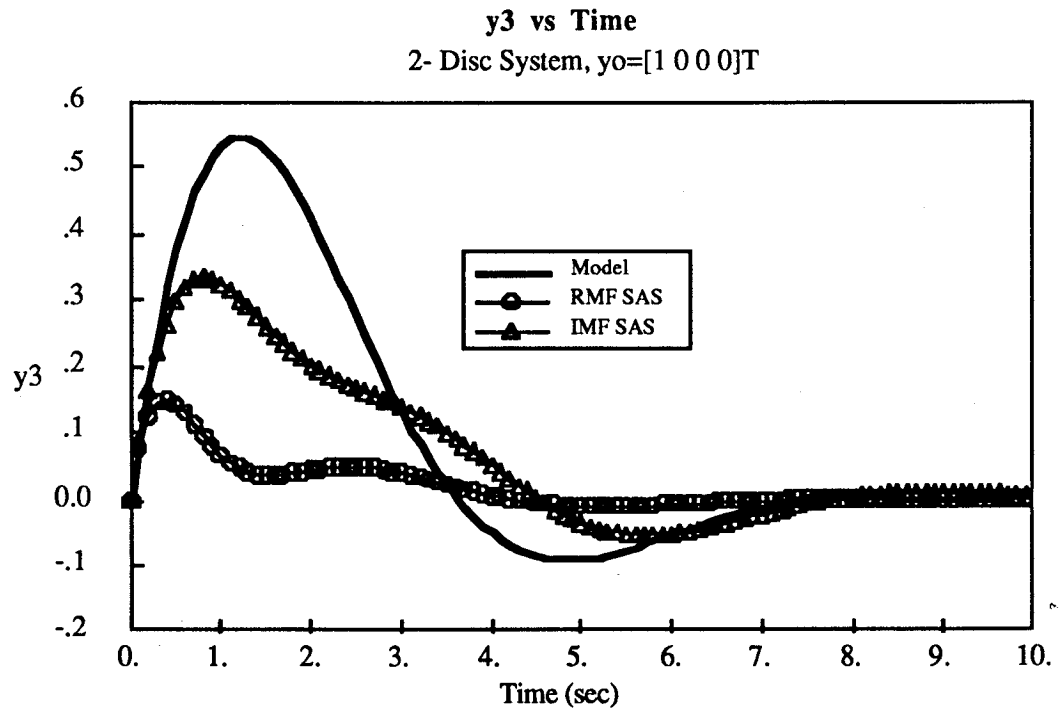
y4 vs Time
2- Disc System, yo=[1 0 0 0]T
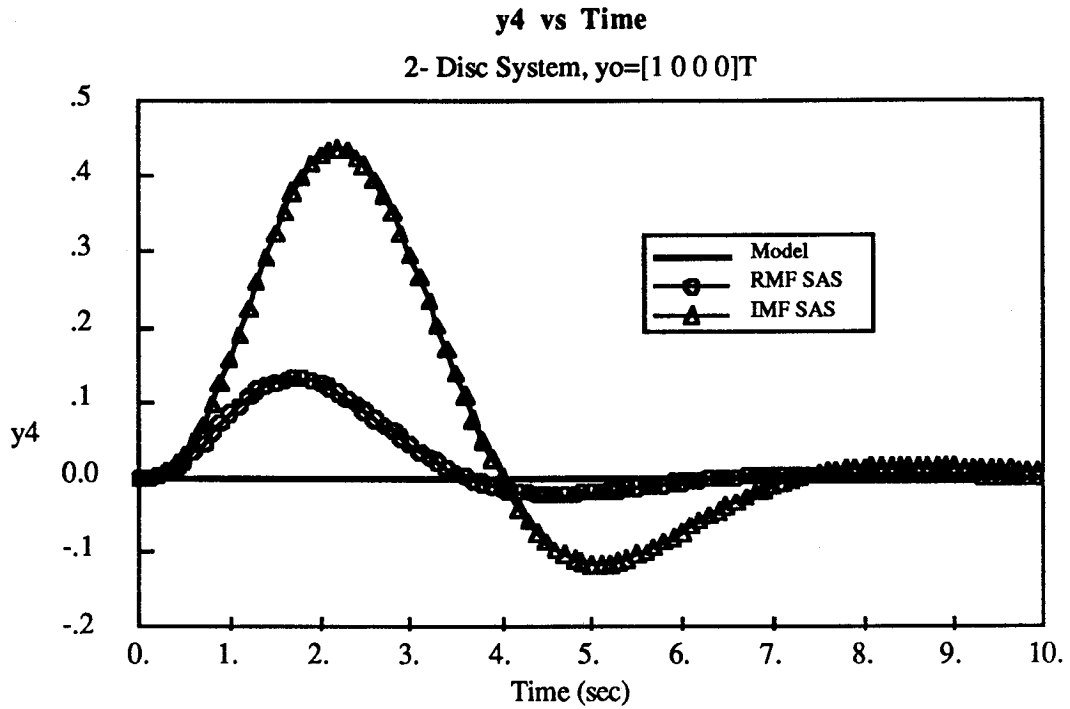
Figure 3.53 y4 vs time

Inspection of figures 3.50 - 3.53 shows that the RMF SAS displays improved decoupling of the y_2 and y_4 states where as the IMF SAS shows slightly better model following performance of the y_1 and y_3 states. A quantitative measure of the closed loop performance for each case can be obtained by evaluating the dynamic cost integral:

$$J_d = \int_0^\infty (\epsilon^T [Q] \epsilon) \, dt \quad \text{(for zero control effort weight)}$$

Equations 3.62 - 3.64 describe how this is done and the results are given in figure 3.54 for the IMF and RMF controllers.

$$J_d = \int_0^\infty \left\{ (y\text{-}y_m)^T Q (y\text{-}y_m) + u^T R u \right\} dt$$

$$Q = [I]$$
$$R = [0]$$
$$y_0 = [1\ 0\ 0\ 0]^T, [0\ 1\ 0\ 0]^T, [0\ 0\ 1\ 0]^T, [0\ 0\ 0\ 1]^T$$

IMF: $J_d = 5.30$
RMF: $J_d = 3.97$

RMF SAS has 25% better performance than IMF SAS

Figure 3.54 SAS performance - RMF and IMF

115

The results show that the RMF SAS performance exceeds that of the IMF SAS by 25%. This is because the RMF controller minimizes the cost function :

$$J_d = \int_0^\infty \varepsilon^T [Q] \, \varepsilon \, dt$$

where as the IMF controller minimizes the implicit form of this cost function:

$$J_d = \int_0^\infty (\dot{y} - [A_m] \, y)^T [Q] \, (\dot{y} - [A_m] \, y) \, dt$$

As was noted in the IMF SAS results, the implicit formulation of the cost function can yield inferior SAS performance for systems with reduced controllability. The RMF SAS design uses the explicit formulation of the dynamic cost and therefore achieves superior performance in dynamic response, even in this extreme example where the control authority weighting is zero.

The 2-disc elastic system example shows how an RMF SAS can achieve improved model following transient response (when compared with other SAS designs) in problems with reduced controllability. In the next section an RMF SAS will be synthesized for the F-8 OWRA. The goal of the control system is to provide model following response in both the commanded and unforced response of the aircraft. The controller architecture will be reduced order (i.e. not full-state feedback) so that the actuator bandwidth limitations will be preserved in the final closed loop design. The resulting closed loop OWRA's response to pilot commands and gusts will be compared to the OWRA's response with the previously designed EMF SAS.

The linear dynamics models used in the RMF SAS synthesis (F-8 OWRA with 45° oblique sweep and the Mil.-Spec. F-8785C model) are the same as those given in figure 3.22. The state and output vectors are assumed to be:

(3.69) $x = [v, w, p, q, r, \phi, \delta_{roll}, \delta_{pitch}, \delta_{yaw}]^T$

(3.70) $x_m = [v_m, w_m, p_m, q_m, r_m, \phi_m, \delta_{mroll}, \delta_{mpitch}, \delta_{myaw}]^T$

(3.71) $y = [g_y, g_z, p, q, r, \phi, \delta_{roll}, \delta_{pitch}, \delta_{yaw}]^T$

(3.71) $y = [g_y, g_z, p, q, r, \phi, \delta_{roll}, \delta_{pitch}, \delta_{yaw}]^T$

(3.72) $y_m = [g_{ym}, g_{zm}, p_m, q_m, r_m, \phi_m, \delta_{mroll}, \delta_{mpitch}, \delta_{myaw}]^T$

The control inputs are:

(3.73) $u_c = [\delta_{croll}, \delta_{cpitch}, \delta_{cyaw}]^T$

The Pilot Inputs Are:

(3.74) $u_{mc} = [\delta_{mcroll}, \delta_{mcpitch}, \delta_{mcyaw}]^T$

All of the outputs are assumed to be sensed and available to the controller excepting the actuator states:

$$\delta_{roll}, \delta_{pitch}, \delta_{yaw}, \delta_{mroll}, \delta_{mpitch}, \delta_{myaw}$$

This insures that the SAS will not artificially increase the actuator's bandwidth by feeding back actuator position to the actuator input command. The sensed quantities are thus:

$y_{sensed} = \{ g_y, g_z, p, q, r, \phi, \delta_{mcroll}, \delta_{mcyaw}, \delta_{mcpitch} \}^T$. Figure 3.55 shows the RMF SAS for the F-8 OWRA in block diagram form.

The controller uses 9 pieces of sensed information (y_{sensed} and u_{mc}), has 6 internal states (y_m), and affects 3 controls ($\delta_{croll}, \delta_{cpitch}, \delta_{cyaw}$). This implies that there are 45 control gains to compute in the RMF SAS.

The augmented system equations (Eqn. 3.57 - 3.58) are formed from the plant and model dynamics matrices. Also required is the value of the pilot command washout parameter, (ε), which is used to stress the importance of high bandwidth dynamics relative to low frequency and steady state response. ε is also used to define the eigenvalues of the arbitrary states included in the augmented model dynamics matrix (Eqn. 3.58). These arbitrary states are an artifact of the requirement that y and y_m have the same dimension and in no way do they affect the SAS design or the dynamic performance. For the RMF SAS synthesis, the actuator bandwidth is chosen to be 1.6 Hz. This fixes the actuator pole locations at s = -10.0 (1/sec). A bandwidth of 2 Hz or less reflects a more realistic model of the actu-

117

ators and is substantially lower than the 5Hz bandwidth assumed in the EMF SAS design.
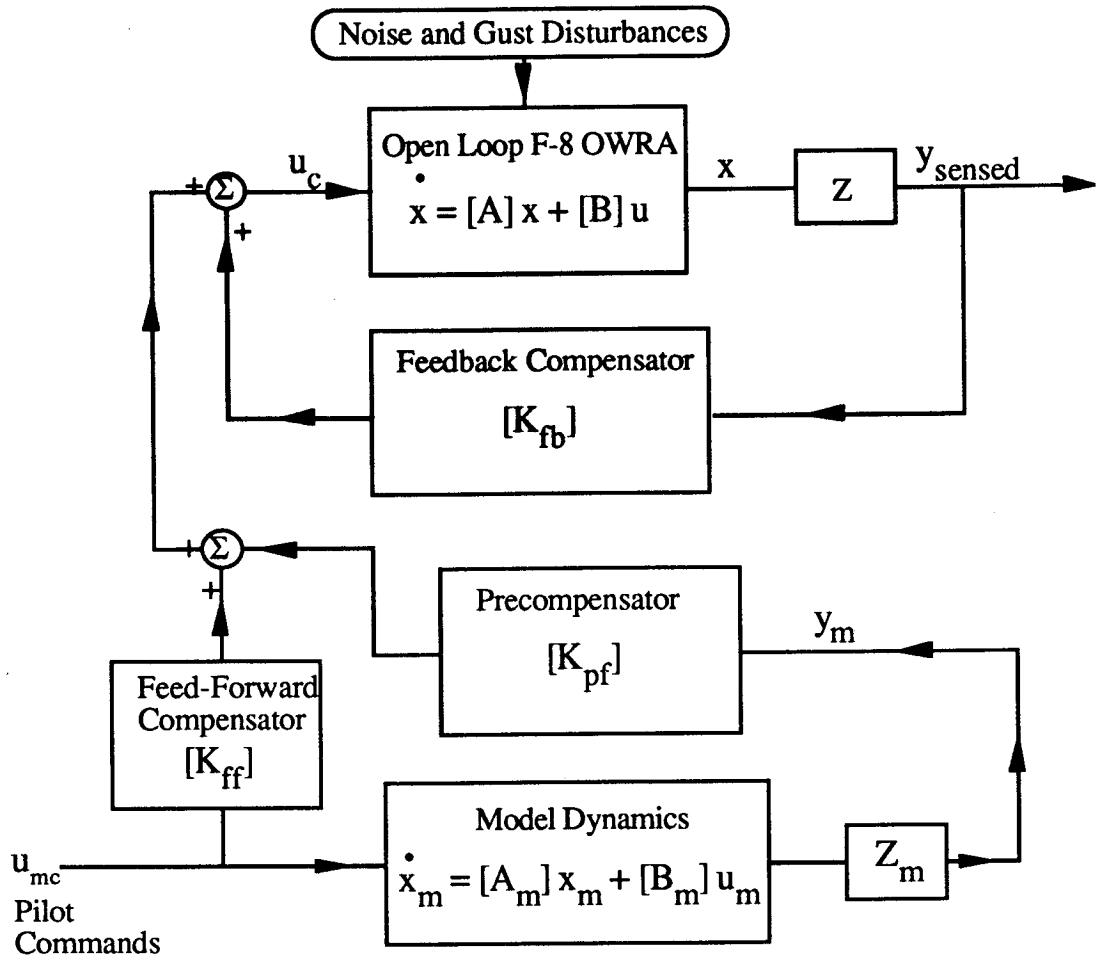
Figure 3.55 RMF SAS for the F-8 OWRA

The weighting matrices [Q] and [R] are chosen to produce the best possible closed loop response without excessive control effort. For the results presented in this section the following values were used:

Output error weighting

$$[Q] = diag [\overset{g_y\ g_z\ p\ q\ r\ \phi}{10, 5, 1, 1, 1, 10}]$$

Control effort weighting

$$[R] = diag [\overset{\delta_{roll}\ \delta_{pitch}\ \delta_{yaw}}{100, 100, 100}]$$

Pilot command washout filter pole location

$\varepsilon = 2.0$

Actuator pole location

s = 10.0 (1.6 Hz B.W.)

Figure 3.56 RMF SAS synthesis input parameters

Unlike the EMF and IMF SAS's, the RMF SAS design is sensitive to the initial conditions used to evaluate J_d. Ideally, the initial conditions should reflect the type of excitation that the aircraft will experience in flight (i.e. pilot commands and gusts). Figure 3.57 lists the initial conditions assumed for the RMF SAS design.

vertical gust $\quad \mathbf{y}_o = [\, 0, 0.5, 0, 0, 0, 0, 0, 0, 0, \,]^T$

lateral gust $\quad \mathbf{y}_o = [\, 0.5, 0, 0, 0, 0, 0, 0, 0, 0 \,]^T$

roll input $\quad \tilde{\mathbf{y}}_o = [\, 0, 0, 0, 0, 0, 0, 0.5, 0, 0, \,]^T$

pitch input $\quad \tilde{\mathbf{y}}_o = [\, 0, 0, 0, 0, 0, 0, 0, 1.0, 0 \,]^T$

yaw input $\quad \tilde{\mathbf{y}}_o = [\, 0, 0, 0, 0, 0, 0, 0, 0, 0.5 \,]^T$

Figure 3.57 RMF SAS initial conditions

If the dynamic response to initial disturbances of each state variable were instead used to calculate J_d (i.e. J_d =Trace[P]), then the closed loop performance with respect to the subset of physical initial conditions would be reduced.

The RMF SAS synthesis is carried out using the Quasi-Newton numerical optimization procedure to solve for the 45 control gains which minimize J_d. In this example, 2000 objective function evaluations and 30 line searches were required to converge to a solution, when the initial guess for the gains was zero. This computation cost includes all of the objective function evaluations necessary to numerically estimate the gradient of J_d with respect to the 45 SAS gains.

The closed loop performance of the F-8 OWRA with the RMF SAS is shown in figures 3.58 - 3.68. Response to gust disturbances and pilot command inputs are presented along with similar results for the OWRA with an EMF SAS.

The simulation results show that the RMF and EMF SAS have nearly identical performance in decoupling the commanded response of the OWRA. For the 4-g pitch up maneuver, both SAS designs produce a 20 degree bank and a 0.3 g lateral acceleration. These large excursions in lateral motion are due to a lack of independent sideforce control, as was pre-

119

viously described in the EMF SAS section. The response to vertical gust initial conditions shows that the RMF SAS attempts to decouple the gust response, but it is not obvious that its performance is any better than the EMF SAS which merely attenuates the gust response. In reality, there is a significant difference in the natural response of these two cases. The difference is most clearly seen in figure 3.69 where the eigenvalues corresponding to the four rigid body dynamic modes of the closed loop aircraft are plotted. Figure 3.69 clearly shows that the RMF SAS has eigenvalues that very closely approximate those of the model in both frequency and damping, where as the EMF SAS eigenvalues are all substantially faster than the models. The "closeness" of the RMF eigenvalues to the model's indicates that the RMF SAS produces an unforced response that attempts to follow that of the model and is not merely a very fast, attenuated response as in the case of the EMF SAS.

Not shown in figure 3.69 are the eigenvalues corresponding to the actuator states. The EMF SAS actuators have more than twice the bandwidth of the RMF SAS (i.e. 5 Hz vs 1.6 Hz). Nonetheless, the RMF SAS is still capable of decoupling the commanded response as well as the EMF SAS. This is because the eigenvalues of the RMF closed loop system are very close to those of the model and the commanded response transients are generated naturally in the feedback path and need not be generated in the pre-compensator (EMF SAS) as commands to be tracked. Overall, the RMF SAS appears to be an ideal controller for oblique wing aircraft because it decouples both the commanded and unforced response of the aircraft without excessive requirements in actuator performance.

Lateral Acceleration vs Time

45 (deg) Sweep OWRA, 4-g Pitch-Up
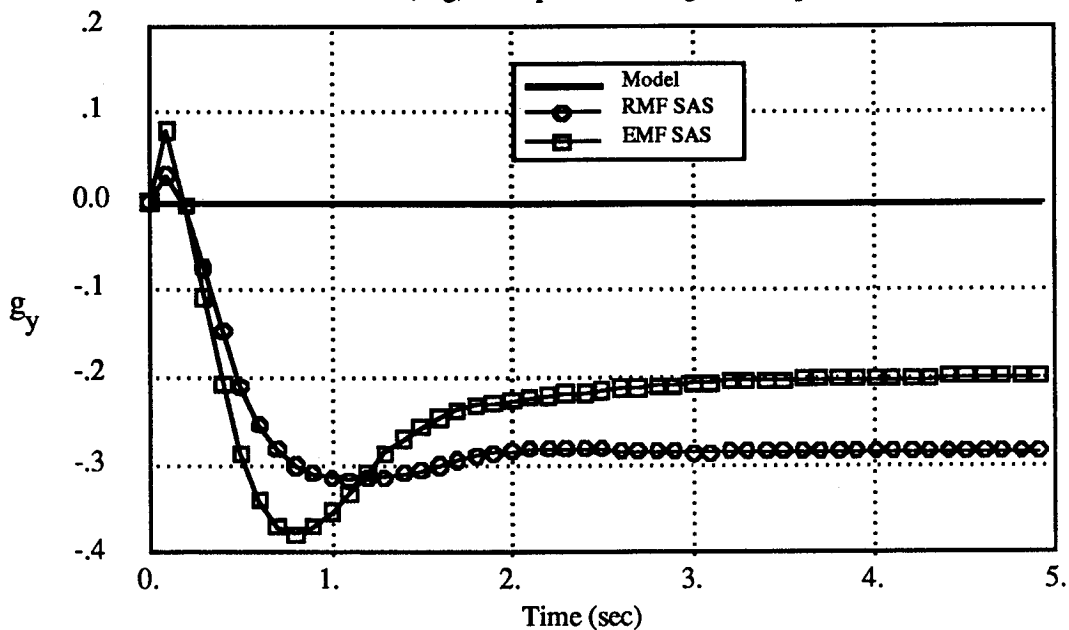
Figure 3.58 lateral acceleration vs time

Normal Acceleration vs Time

45 (deg) Sweep OWRA, 4-g Pitch-Up
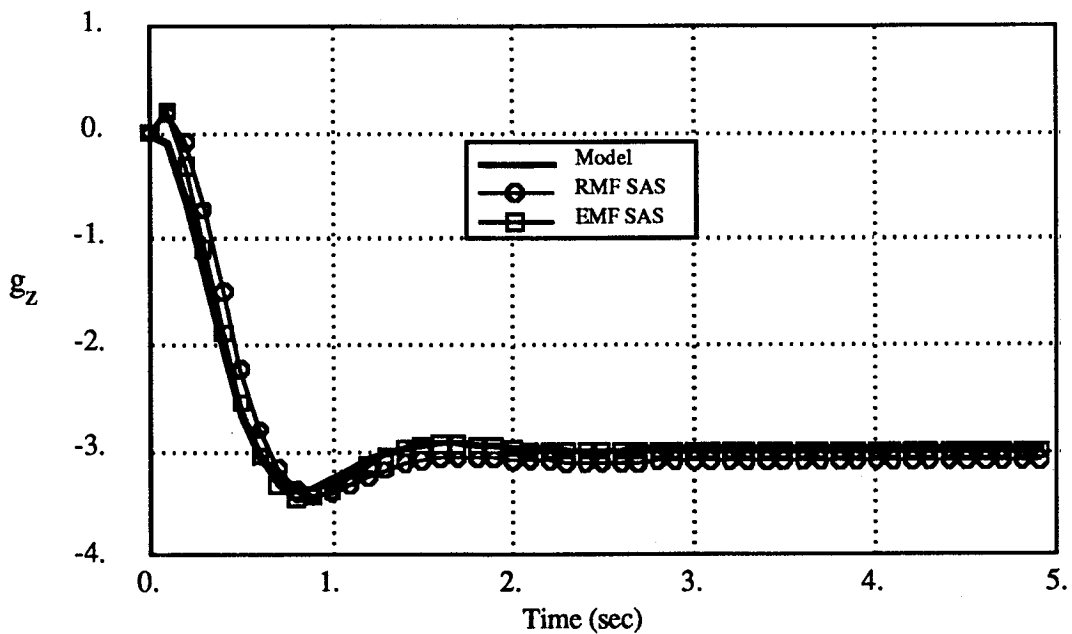
Figure 3.59 normal acceleration vs time

121

Pitch Rate vs Time

45 (deg) Sweep OWRA, 4-g Pitch-Up
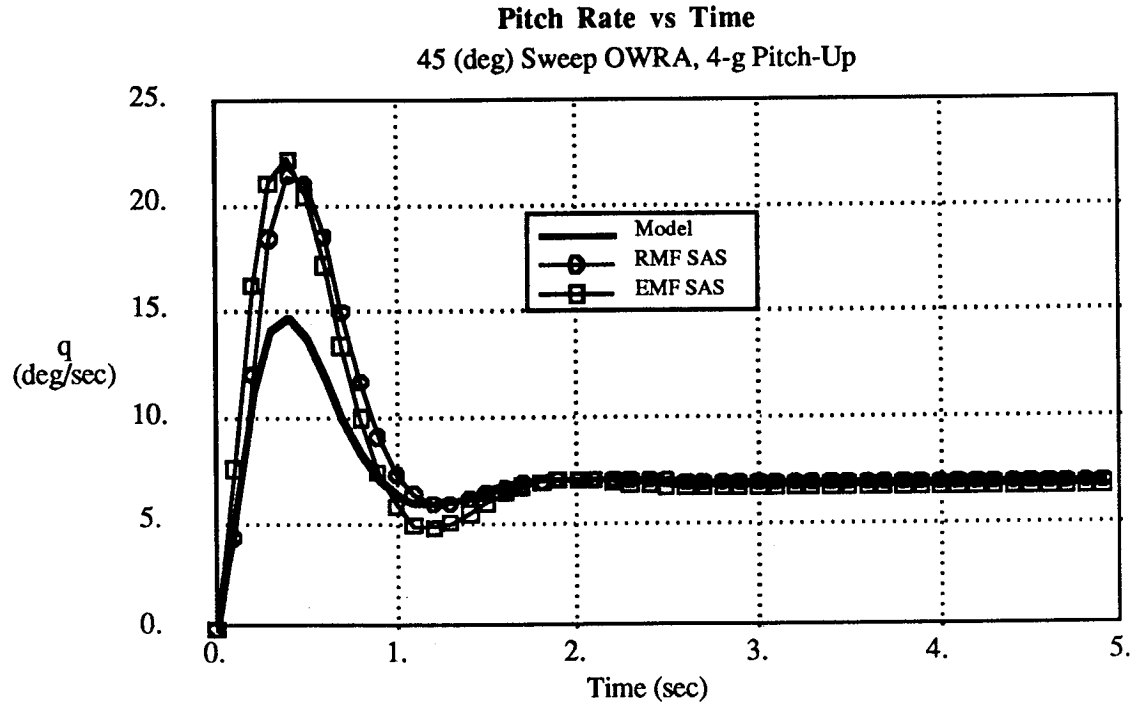
Figure 3.60 pitch rate vs time

Yaw Rate vs Time

45 (deg) Sweep OWRA, 4-g Pitch-Up
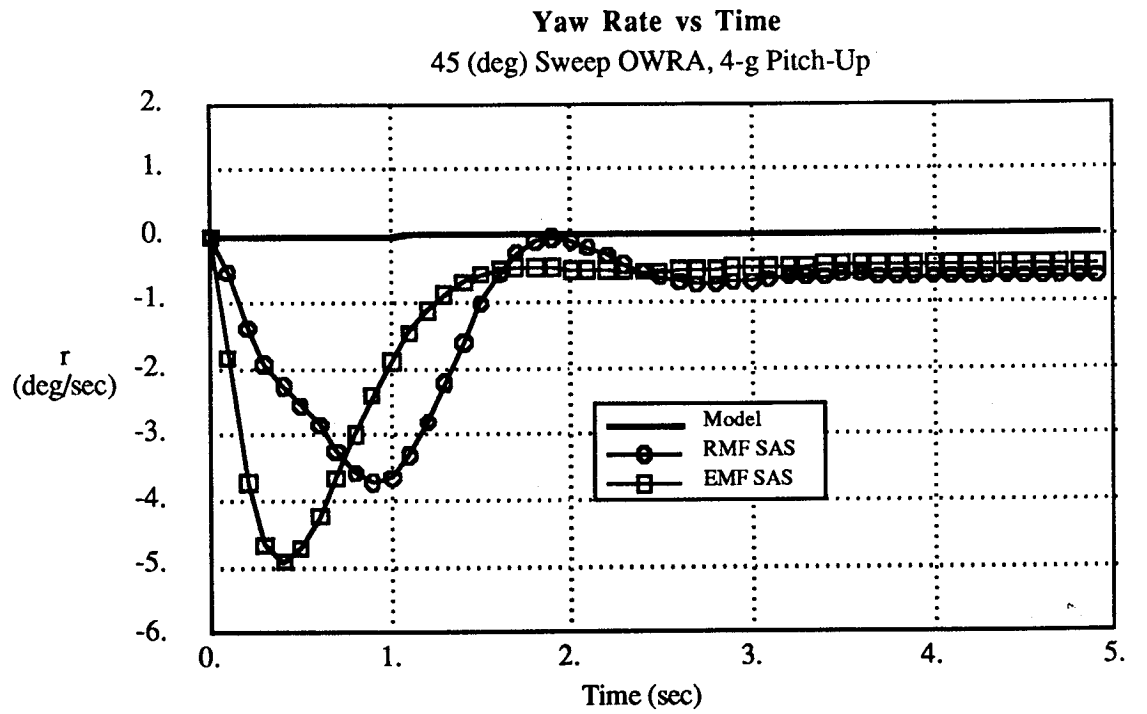
Figure 3.61 yaw rate vs time

Roll Angle vs Time
45 (deg) Sweep OWRA, 4-g Pitch-Up
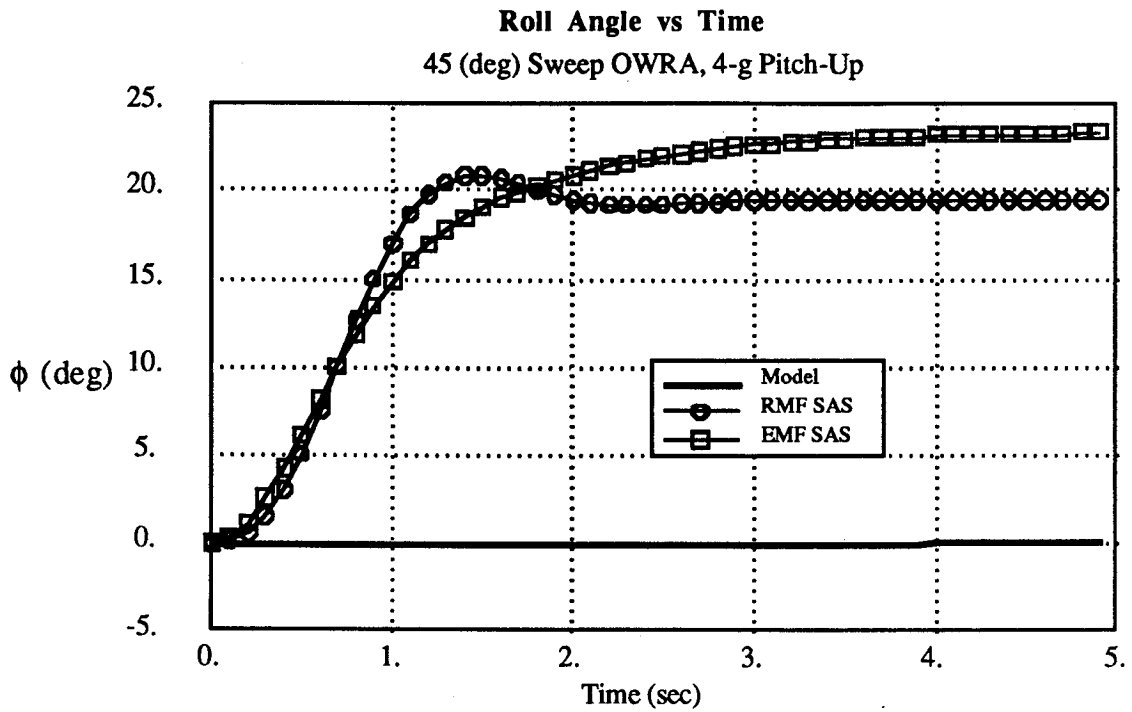
Figure 3.62 roll angle vs time

Control Deflection vs Time
45 (deg) Sweep OWRA, 4-g Pitch-Up
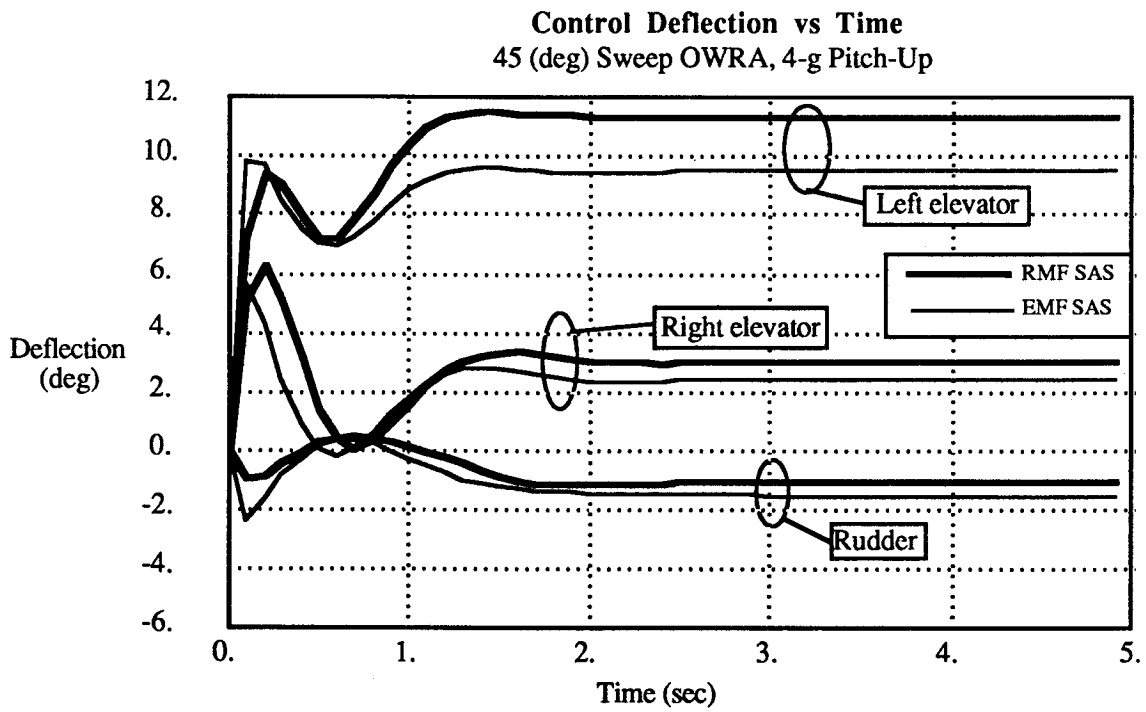
Figure 3.63 control surface deflection vs time

Lateral Acceleration vs Time
45 (deg) Sweep OWRA, 1-g Vertical Gust
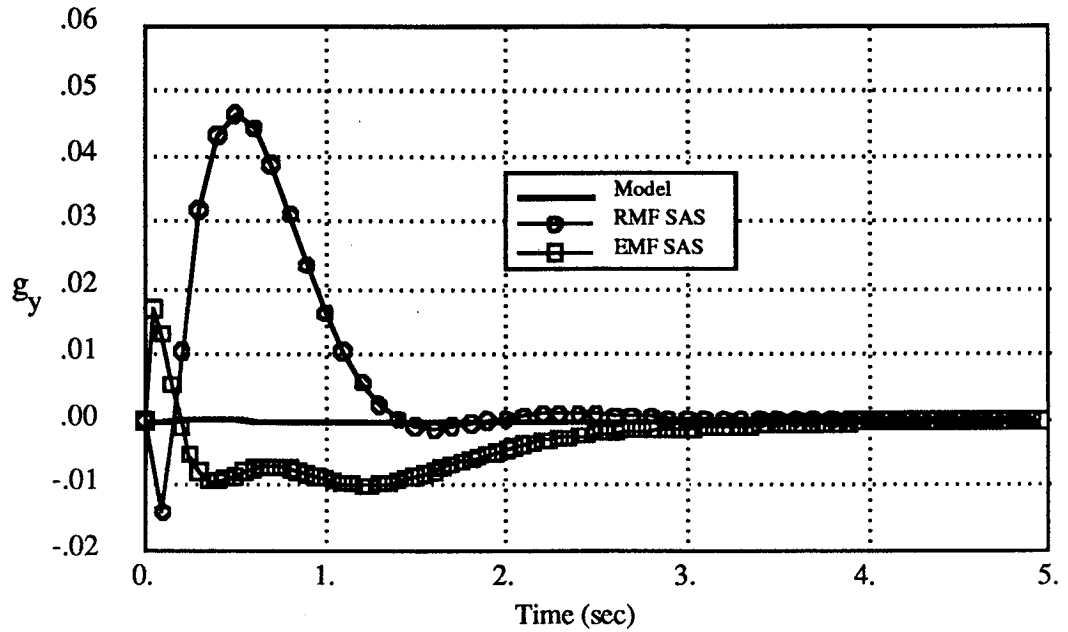
Figure 3.64 lateral acceleration vs time

Normal Acceleration vs Time
45 (deg) Sweep OWRA, 1-g Vertical Gust
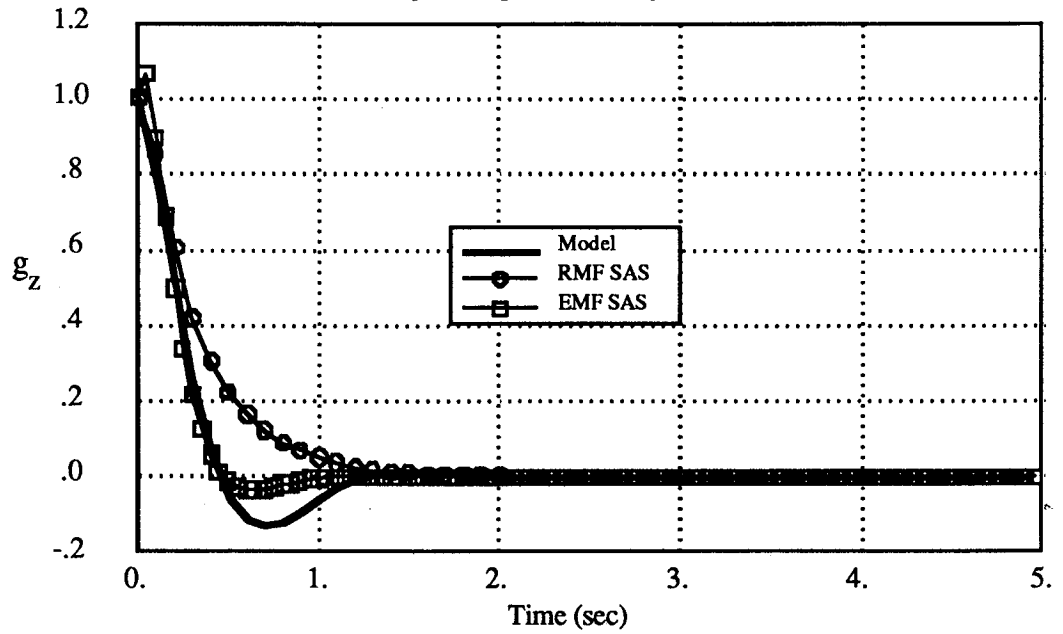
Figure 3.65 normal acceleration vs time

Pitch Rate vs Time

45 (deg) Sweep OWRA, 1-g Vertical Gust
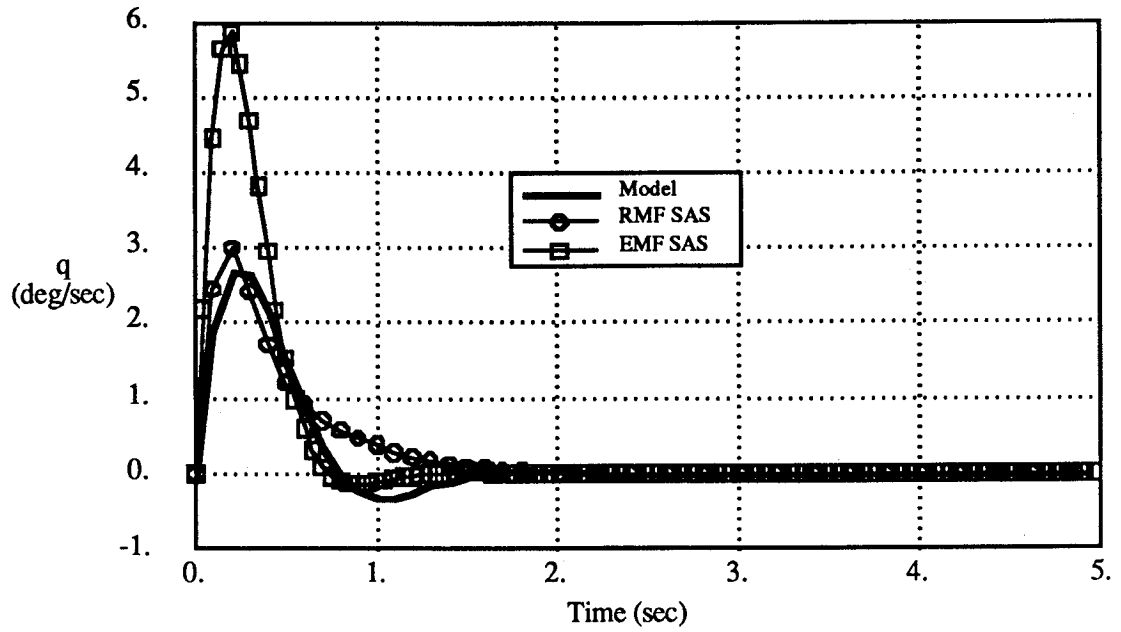
Figure 3.66 pitch rate vs time

Yaw Rate vs Time

45 (deg) Sweep OWRA, 1-g Vertical Gust
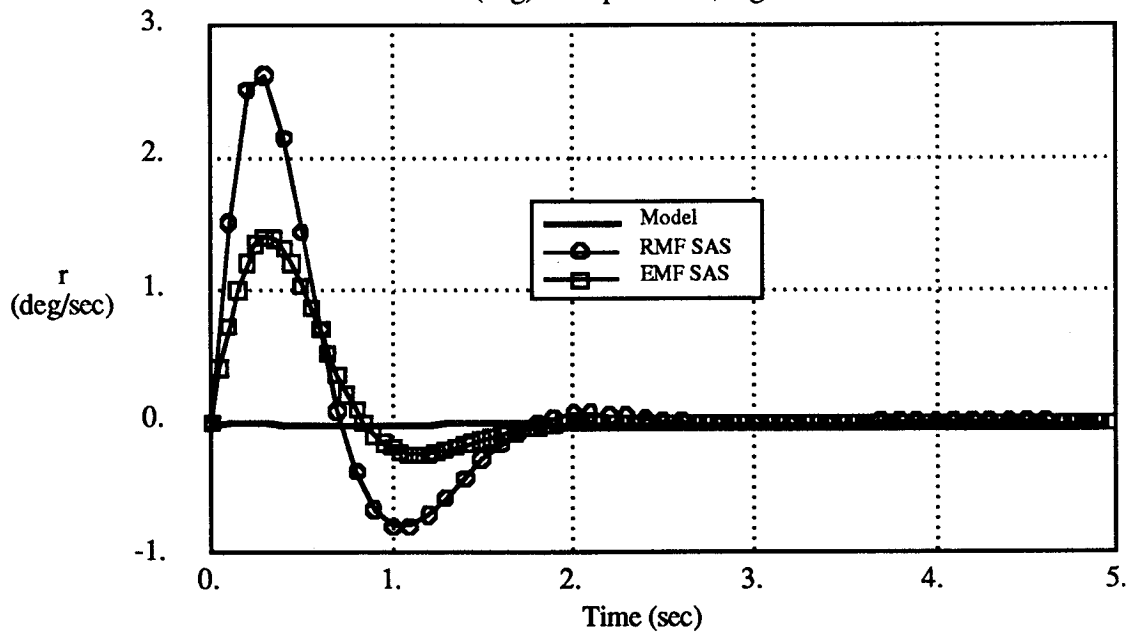
Figure 3.67 yaw rate vs time

125

Roll Angle vs Time
45 (deg) Sweep, 1-g Vertical Gust
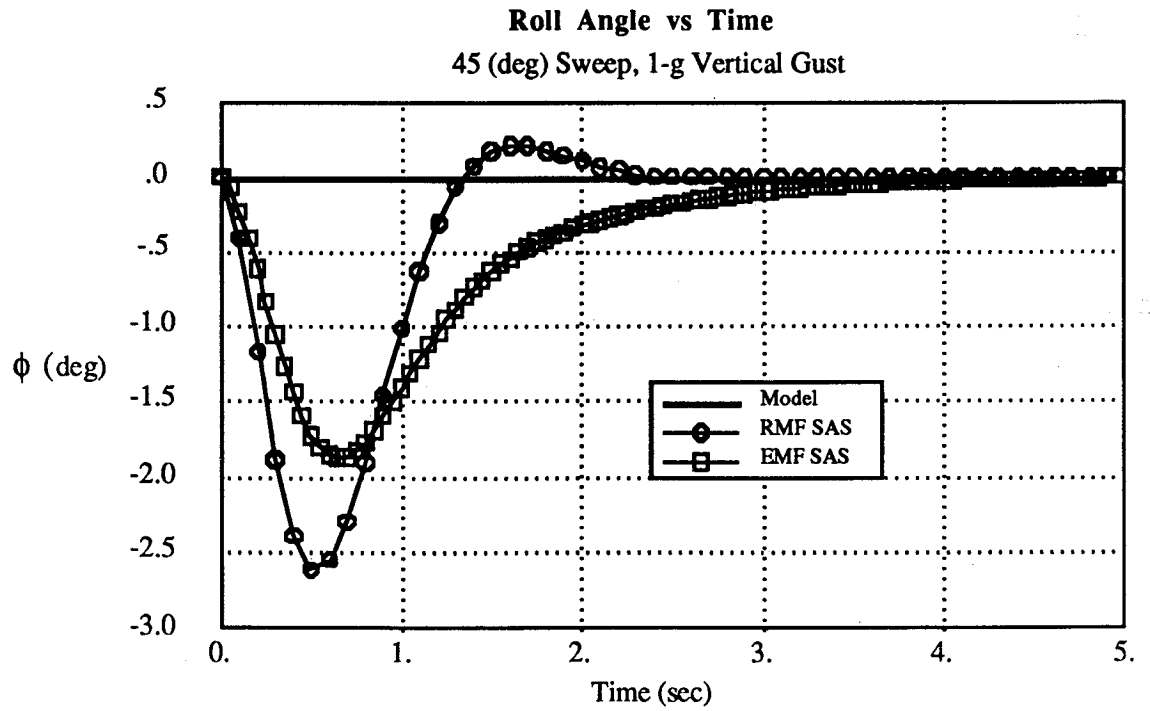
Figure 3.68 roll angle vs time

RMF SAS Natural Modes
45 (deg) Sweep OWRA
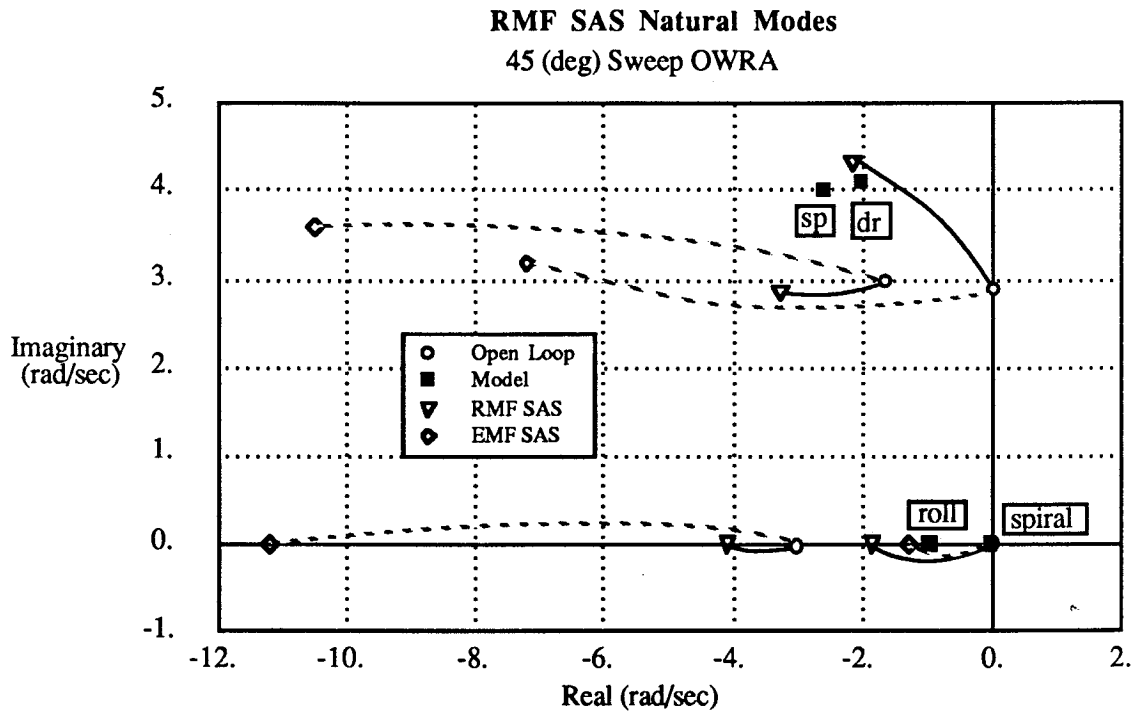
Figure 3.69 RMF SAS natural modes

3.4 SAS Choices for Integrated Design Synthesis

The integrated design synthesis method, which will be presented in the next chapter, attempts to improve the OWRA's handling qualities by simultaneously synthesizing the aircraft's configuration and its SAS. A numerical optimization procedure, similar to that used in the RMF SAS synthesis, is used to solve for the optimal configuration and SAS gains. The numerical solution technique requires that feasible SAS architectures be automatable in the numerical solution for the dynamic performance. Both the EMF and RMF controllers fulfill this requirement and have been shown to produce closed loop performance representative of what is achievable given the reduced controllability of the nominal F-8 OWRA configuration. In the initial integrated OWRA design syntheses, the EMF controller will be implemented, because it simplifies the optimization procedure substantially by solving for all of the control gains in a single A.R.E. solution. After the capability of the integrated design method has been demonstrated with EMF controllers, RMF controllers will then be synthesized to show how more realistic, practical, and efficient control may be accomplished in the integrated synthesis.

Chapter 4

Integrated Design Synthesis Method (MIDSM)

The closed loop handling qualities of the F-8 OWRA do not meet the desired Mil.-Spec. level I requirements due to an inherent lack of controllability in the proposed design. A possible solution to this problem involves adding control surfaces that will provide the aircraft with independent sideforce control. This course of action is undesirable because the additional weight, drag, and complexity of these surfaces will decrease the performance of the oblique wing configuration considerably. A more desirable solution is to somehow re-configure the existing aircraft such that the weight and drag are essentially unchanged, but the controllability is substantially improved. In this asymmetric design more than others, configuration design changes that might improve controllability are not obvious because of the strong aerodynamic and inertial coupling that affects the dynamic response. An integrated design technique which can simultaneously account for the influence of configuration and SAS changes on the closed loop handling qualities is required to synthesize an in improved design. In this chapter a multidisciplinary, integrated, design synthesis method (MIDSM) will be presented which is capable of re-configuring the F-8 OWRA for improved flying qualities. Although the original motivation for creating MIDSM came from the need to improve oblique wing handling qualities, the method is extended to include performance measures from other disciplines (structures aerodynamics, aeroelastics, etc.) so that the trade-off between handling qualities and more conventional measures of performance (drag, weight, etc.) may be studied. In this chapter the integrated design method MIDSM is presented and is used to solve two example problems: tail sizing for minimum trimmed drag with longitudinal handling qualities constraints and tailless aircraft wing weight minimization with aeroelastic constraints. Chapters 5 and 6 will present the results for the integrated OWRA synthesis.

4.1 Introduction to MIDSM

The dynamic response of an aircraft is often an important aspect of its performance; yet the analysis of handling qualities and control system design are often performed after the major aerodynamic and structural properties have been established. In many cases, this sequential approach to multidisciplinary design leads to suboptimal results. The method presented here (MIDSM) integrates the design of the aircraft and its control system in order to obtain better mission performance than could be achieved in a sequential design procedure. By minimizing a cost function consisting of both conventional performance criteria and a measure of aircraft handling qualities, a design with maximum performance for a specified level of handling can be achieved. Handling qualities are measured using a quadratic cost function similar to that used in the design of optimal feedback control systems. This function is proportional to the difference between the dynamic response of the aircraft and a "model" case with dynamics that are considered acceptable. The variables to be optimized may include both aircraft configuration parameters (e.g. span, tail area, skin thickness) and control system feedback gains. The design variables are determined by an unconstrained numerical optimization procedure, using penalty functions to enforce both explicit and implicit constraints. The method is most useful in the simultaneous synthesis of airframe and flight control systems to achieve improved handling or improve performance with a specified level of handling quality. In certain cases results obtained by this integrated synthesis procedure are substantially better than those obtained by the usual sequential design methods.

Previous research on the integrated synthesis of dynamic systems and full state feedback controllers is described in references 8 and 9. Sakawi et. al [Ref. 9] optimized the wing and tail geometry of an actively-controlled aircraft excited by gust disturbances. The synthesis assumed a full state feedback control architecture and used a random search procedure to solve for the global minimum. In reference 8, Zeiler and Weisshaar describe the integrated design of a four degree-of-freedom aeroservoelastic system. The design variables consisted of the elastic axis location and the full state feedback control gains. A multi-level linear decomposition scheme was used to solve for the optimal system variables.

In the work presented here, an integrated synthesis procedure is extended to handle any lin-

ear control system architecture including reduced-order controllers and passive (no controller) designs. The procedure is used to optimize the system's commanded response as well as its unforced response. Multidisciplinary performance indices are considered, illustrating the trade-offs between handling qualities and other measures of performance.

Two examples are used to demonstrate the method. Reduced-order controllers and multidisciplinary performance indices are first introduced in the synthesis of an aft-tail aircraft. The proposed method is used to find the tail size and static margin that produce acceptable handling qualities with minimum drag. When the control system gains are included as design variables, the procedure automatically synthesizes statically unstable configurations and an appropriate reduced order control system.

The minimum weight aeroservoelastic design of a free flying aircraft represents a highly integrated structural and control design. The second example considers this problem by synthesizing a tailless aircraft which experiences a coupled short-period/wing-bending flutter mode. The synthesis procedure determines the spar cap thickness (as a function of span) for minimum wing weight with acceptable handling qualities. In some cases a reduced order control system is also designed. This synthesis differs from conventional flutter suppression studies because not only must the flutter mode be stable, but the phugoid and short period dynamics must meet specified handling quality criterion.

In some cases, handling qualities may be the only performance measure that the designer wishes to improve. This type of problem is solved in chapters 5 and 6, where an oblique wing aircraft is designed for improved handling qualities by simultaneously optimizing the wing geometry and control system gains. The integrated synthesis procedure uses configuration variables to enhance the controllability of the closed loop system. This produces an aircraft with handling qualities superior to those achievable in a sequential design procedure.

The basic approach is outlined in figure 4.1. The design method is an unconstrained optimization procedure which minimizes a composite objective function, J, consisting of three terms: the non-dynamic performance measure, J_{nd}, the weighted dynamic performance,

J_d, and the constraint violation penalty function, J_{pen}:

$$(4.1) \qquad J = K_d J_d + J_{nd} + J_{pen}$$
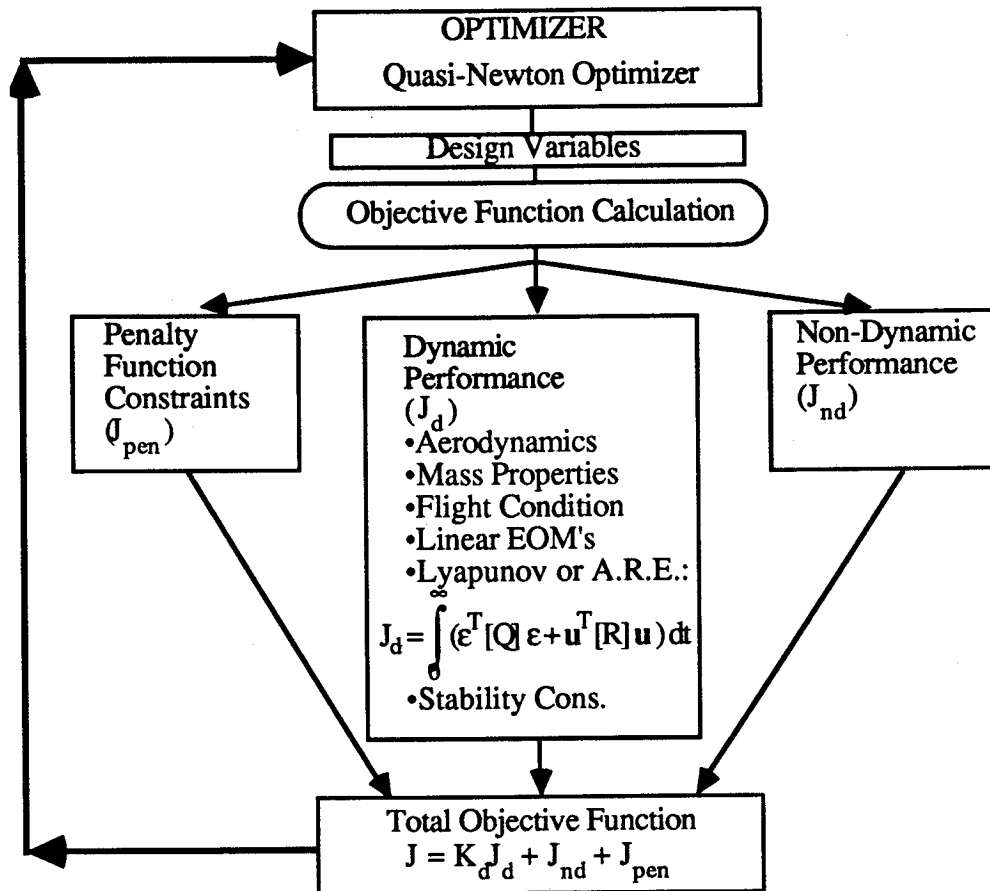
Figure 4.1 MIDSM flowchart

The non-dynamic performance measure describes the mission performance that is not directly related to handling qualities. Typically, this function is the structural weight, drag, or direct operating cost, etc., of the aircraft. The content of this term is problem-specific and will be discussed further within each design example, but for cases in which only the handling qualities are to be improved, this term is excluded.

The dynamic performance, J_d, provides a measure of the aircraft's handling qualities and its computation was described in chapter 3 for both EMF and RMF SAS's. It is calculated from a quadratic cost function identical to that used in the design of optimal control systems; but the control system architecture is not restricted to full state feedback when a RMF SAS is assumed. Dynamic performance is related to the difference between the aircraft's

response and a model case chosen for its desirable handling qualities. In general, the control gains are included as design variables in the synthesis. This permits the designer to choose any control linear system structure: reduced order, full state feedback, or a passive design with no controller at all. Control systems can be synthesized which tailor the forced and/or the unforced response of the aircraft (as was shown in chapter 3). In the composite objective function, J_d is weighted by a constant, K_d, which is used to specify the relative importance of handling qualities in the design synthesis. As K_d is varied from zero to a very large number, the optimal solution moves from one in which dynamics are not considered, to one which is required to achieve acceptable handling qualities at the expense of all other types of performance. Configuration design variables affect the handling qualities (and therefore J_d) by altering the aerodynamic, flexibility, and mass properties of the design being considered. Particular designs may require a complete aerodynamic analysis of an unusual aircraft configuration whose geometry is changed during the synthesis. An aerodynamic analysis method that can accurately predict the aircraft's forces and moments with little CPU time is desired. The vortex lattice method (LINAIR) described in chapter 2 fulfills these requirements for designs in which a thin lifting surface model is appropriate.

The third term of the objective function, J_{pen}, consists of penalty functions which are used to enforce any explicit and implicit constraints in the synthesis.

A numerical optimizer based on the Quasi-Newton or Variable Metric Gradient Method is used to solve for the design variables that minimize J. This optimizer searches for a minimum along descent directions which improve in accuracy (based on a second order model of the objective function) as the optimization progresses [Ref. 19]. This optimization procedure was chosen because it represents a satisfactory compromise between the high computation costs of second order methods and the poor convergence speed of first order schemes. Other optimizers may be better suited for particular problems. For example, if the non-dynamic performance index is known to have local minima, a more robust optimizer may be required. The examples presented here demonstrate that a variety of interesting problems may be formulated such that local minima are avoided, thus eliminating the need for such robust, but inefficient, optimizers.

132

4.2 Calculation of the Dynamic Performance Index

Calculation of the dynamic performance index is identical to the method shown in chapter 3 for the RMF SAS. J_d is a scalar equal to the weighted integral over time of the difference between the state vectors of the aircraft being synthesized and a model system whose dynamic response is considered ideal. An additional term representing the control surface activity is also included.

Interpretation of J_d

J_d is a scalar measure of the aircraft's handling qualities. Because there is no way to relate this number directly to a Cooper-Harper rating or a Mil. Spec. F-8785-C classification, additional analysis of the synthesized design (simulations, frequency response, etc.) must be performed to determine the adequacy of a design's handling qualities. The formulation of J_d does, however, guarantee that for fixed [Q] and [R] matrices the handling qualities will improve as J_d decreases. It is this fact that enables this synthesis method to improve the handling qualities in each optimization iteration and allows the designer a means of trading dynamic performance for non-dynamic performance.

The dynamic performance index calculation requires that the linearized equations of motion for the aircraft be created as a function of the design variables at each objective function evaluation. This portion of the synthesis can be the most costly in terms of CPU time, particularly if the aerodynamic stability derivatives must be re-evaluated. The overall utility of this method relies on the careful choice of the analysis routines which evaluate the [A] and [B] matrices. Methods which capture the essential physical phenomena and minimize computation time are desired.

4.3 Example Applications

4.3.1 Aft-Tail Design for Minimum Trimmed Drag

Two examples are presented to illustrate the use of this method. The first of these, and the simplest, is the design of a wing and tail system. The configuration is required to trim at a selected lift coefficient while minimizing drag and retaining adequate longitudinal handling

qualities and control authority. The design variables include horizontal tail area and wing location; in some of the designs a reduced order controller (consisting of angle of attack feedback to the elevator) is also synthesized.
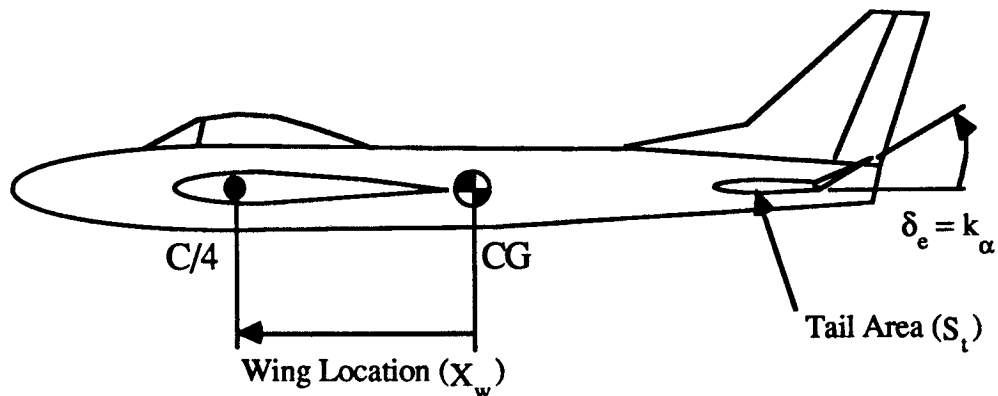
Goal: Minimize Trimmed Drag With a Given Level of Handling Quality

Design Variables: Tail Area, Wing Location, Angle of Attack Feedback (optional)

Figure 4.2 aft tail design for minimum trimmed drag with handling quality constraints

Dynamic Performance

The dynamic performance J_d is computed based on a model case with wing location and tail area sized to provide Mil. Spec. 8785C level 1 response in the short period and phugoid dynamics. The longitudinal dynamics are modeled using axial velocity, u, plunge velocity, w, pitch rate, q, and pitch angle, θ, as states. The design variables are horizontal tail area, S_t, wing position (relative to the c.g.), X_w, and a feedback gain, K_α, from sensed angle of attack to elevator deflection for the cases with a reduced-order control system. J_d is calculated from the difference between the model and subject aircraft's dynamic response to the same initial disturbances. This guarantees that as J_d is minimized the short period and phugoid dynamics of the aircraft will approach those of the model case.

Non-Dynamic Performance

The size of the horizontal tail and static margin required for acceptable handling qualities may result in a design with excessive trimmed drag. The drag coefficient is used as the non-dynamic performance measure so that trade-offs between handling qualities and drag may be studied. The drag coefficient is calculated analytically assuming elliptic loading on the wing and tail:

134

$$J_{nd} = C_D = (\frac{1}{\pi AR_w} + C_{D2w}) C_{Lw}^2 + C_{Dow}$$

$$+ (\frac{1}{\pi AR_T} + C_{D2T}) C_{LT}^2 + C_{DoT}$$

$$+ 2 (\frac{1}{\pi AR_w}) C_{Lw} C_{LT}$$

This formulation accounts for parasite drag, lift dependent viscous drag, and the vortex drag associated with the interfering lifting surfaces (under the assumption that they are coplanar).

Constraints

Three constraints are enforced during the design synthesis:

1) Pitch trim at a specified lift coefficient

2) Trim at maximum lift without tail stall

3) Dynamic stability

Dynamic stability implies that the largest real part of any eigenvalue must be less than zero. This constraint must be enforced explicitly because the Lyapunov equation solution for J_d is only valid if the system is dynamically stable.

Aft -Tail Design Results

Figure 4.3 shows the trade-off between trimmed drag and the handling quality parameter for the aft tail design synthesis. Curves are shown for designs with and without a feedback control system. Each point on the curves represents a unique design that is optimal for a fixed weighting of handling qualities. As the weighting on handling is increased, J_d decreases and the dynamic response of the aircraft approaches that of the model case. Note also that the trimmed drag increases with improved handling quality. This occurs because the optimal tail size and static margin increase as J_d decreases, with a subsequent increase in parasite and trim drag. Designs with feedback control show reduced trimmed drag for a fixed level of handling compared to designs without control systems. The synthesis method has recognized that relaxed static stability and smaller tail size can reduce trimmed drag, while feedback control can ensure adequate handling qualities by providing artificial stabili-

135

ty. As a result, designs that are statically unstable and have optimally designed reduced order controllers to provide stability are automatically synthesized. The values of J_d for which the longitudinal dynamics meet the Mil. Spec. 8785C level 1 handling quality requirements are marked on each curve.

Aft Tail Design Results
Trim Drag vs Handling Quality
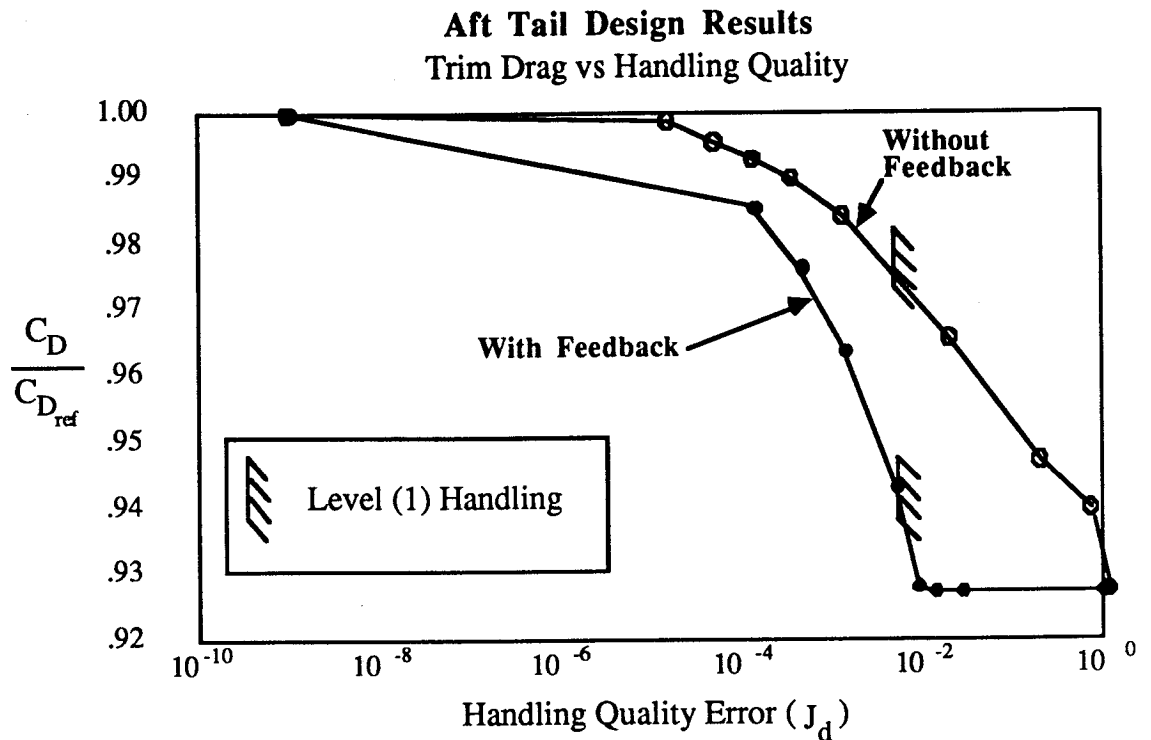
Figure 4.3 aft tail drag vs handling quality

Because the selected control system does not provide rate feedback, adequate damping requires some tail area; thus it is not possible to eliminate the tail completely. Even if large values of J_d (poor handling) are accepted, trim constraints still yield a non-zero tail area when the wing pitching moment at zero lift is not zero. This leads to the flat part of the curve with feedback at higher values of J_d.

The static margin and tail volume of the optimal aft tail designs are plotted in figures 4.4 and 4.5 as a function of dynamic cost weighting. Designs with negative static margin are inherently unstable and rely on the active control system to provide stability. The design with the smallest tail (and consequently the lowest drag) which meets the level 1 handling quality criteria is shown in figure 4.4 to be an inherently unstable design.

Figure 4.6 shows the eigenvalues of each optimal design as the handling qualities weight-

ing factor K_d is increased. When the weighting is large, the eigenvalues associated with both the short period and phugoid modes are driven to those of the model case. This eigenvalue analysis is one means of assigning a physical interpretation to the handling qualities parameter, J_d. Another way of determining the handling qualities of a given design is to study the time history of its dynamic motion. Figure 4.7 shows the dynamic response of two aft tail designs, with and without feedback, to a vertical gust disturbance. Both designs meet the Mil. Spec. level 1 handling quality criteria because their short period response is adequately similar to that of the model's.

Static Margin vs Dynamic Cost Weighting
Optimal Aft Tail Designs
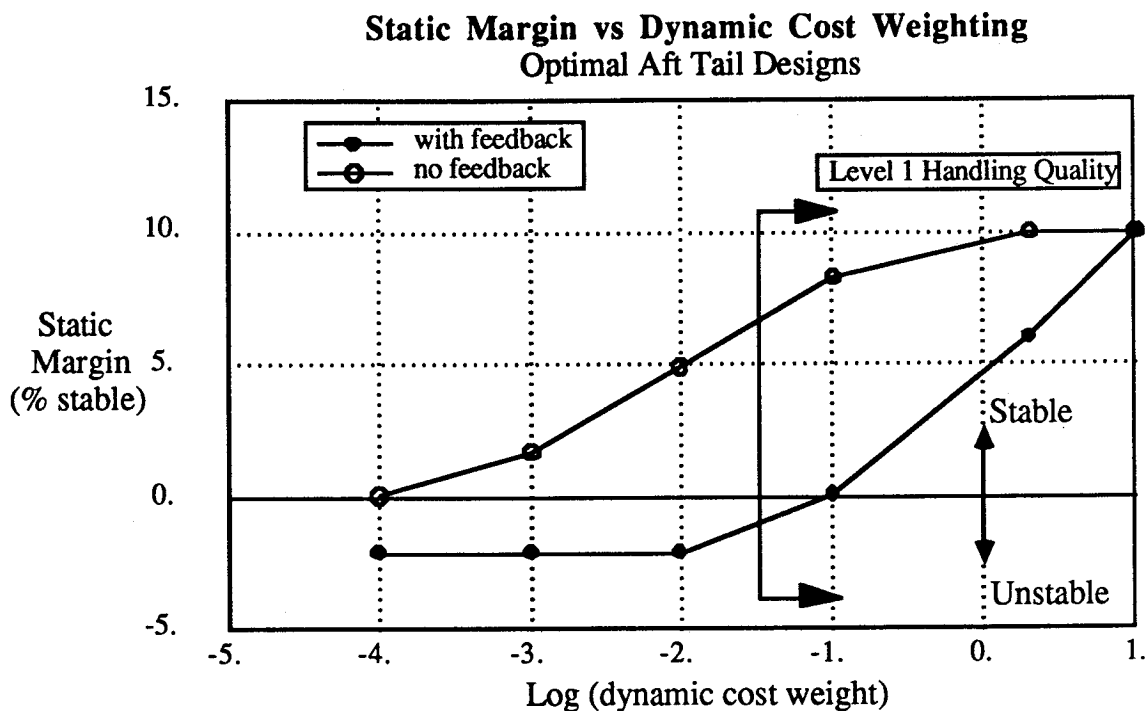
Figure 4.4 static margin vs handling quality

Tail Volume vs Dynamic Cost weighting
Optimal Aft Tail Designs
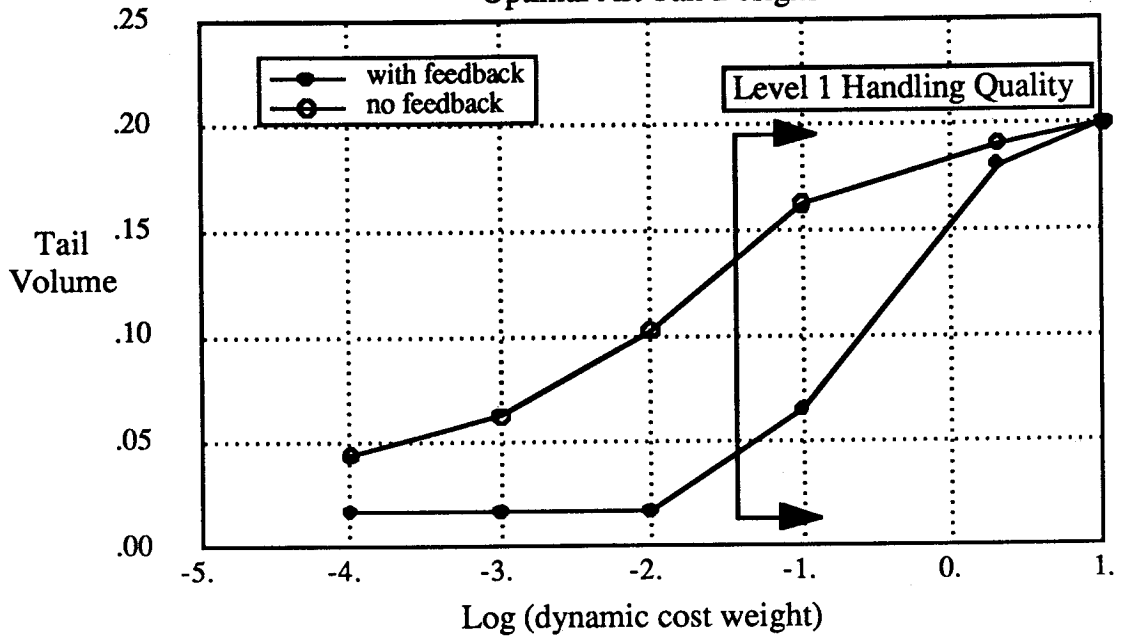
Figure 4.5 tail volume vs handling quality

Optimal Design Root Locus
Aft Tail Synthesis
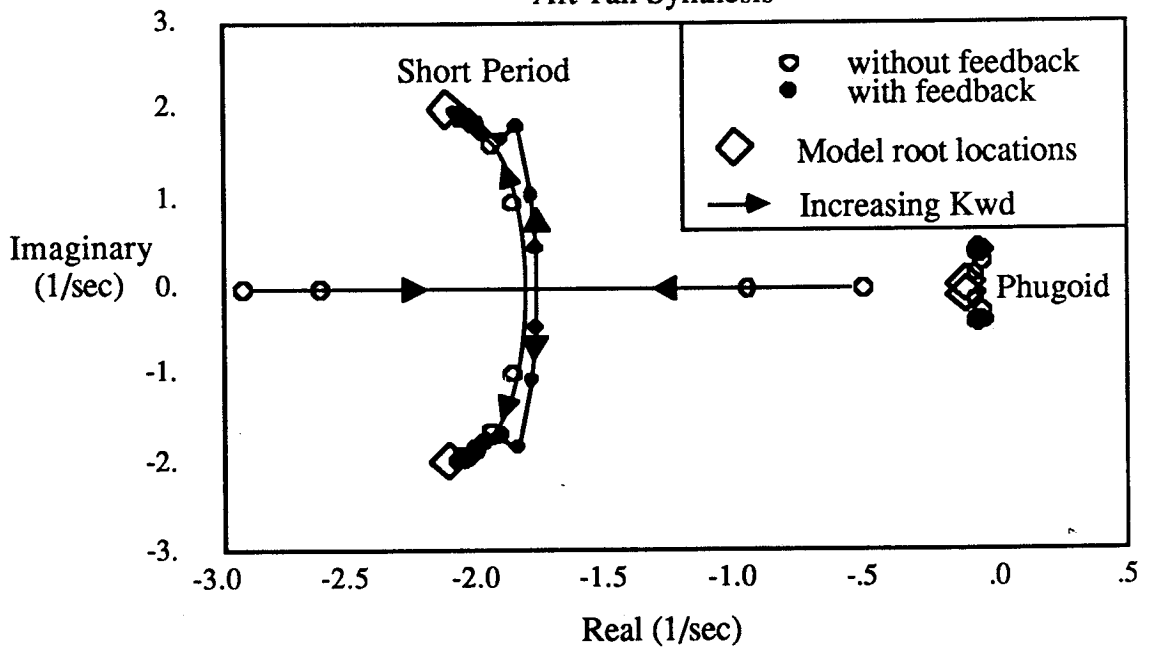
Figure 4.6 aft tail handling quality root locus

Pitch Angle vs Time

Optimal Aft Tail Designs, Vertical Gust Step Response
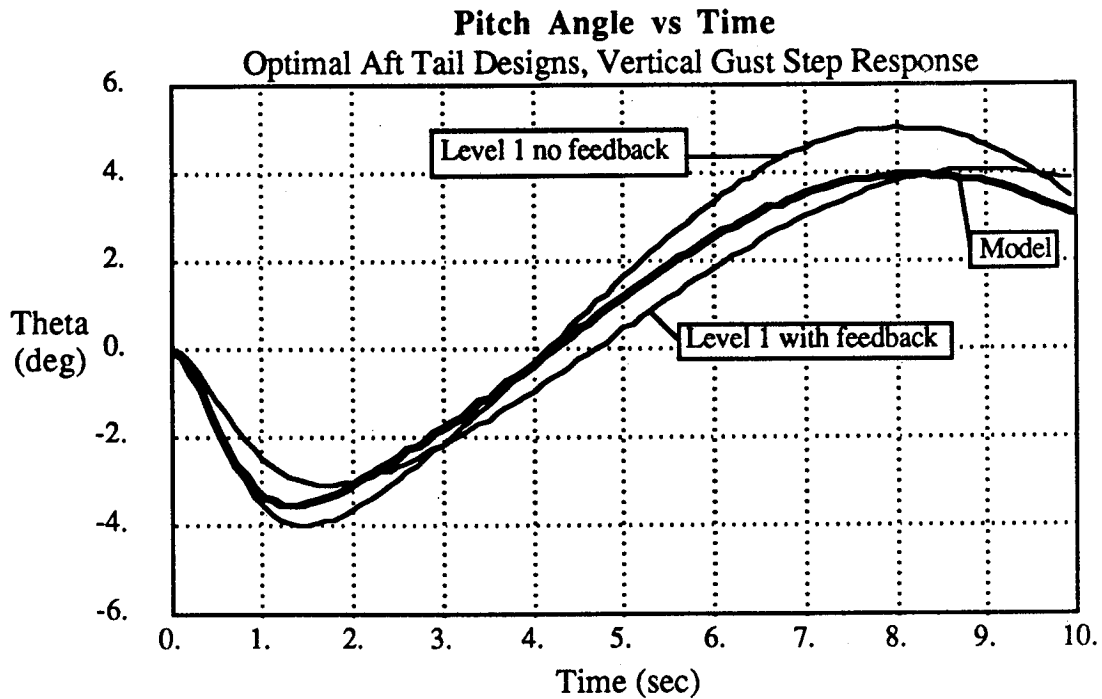
Figure 4.7 optimal aft tail gust response

4.3.2 Tailless Aircraft Flutter Suppression

The second example deals with a tailless aircraft designed for minimum wing weight and an acceptable level of handling quality. Tailless aircraft with swept wings may exhibit a unique flutter mode, characterized by a coupling of the short period dynamics with the wing bending modes. The frequency of this flutter mode is slow (typically 1-2Hz) and corresponds to the wing bending and short period frequencies. Reference 26 describes a high performance tailless sailplane (the SB-13, figure 4.8) for which this flutter mode was the critical factor in the structural design.
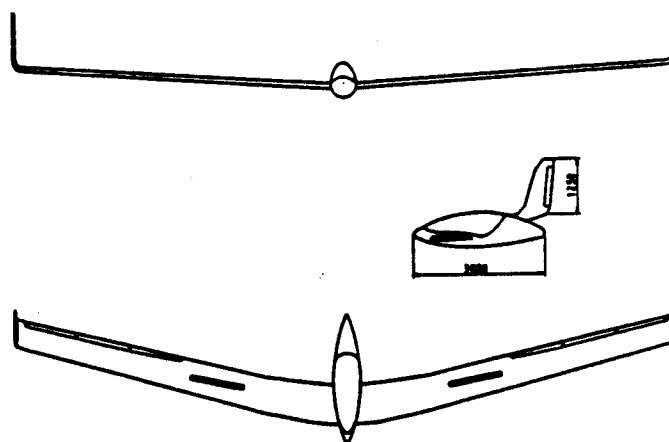
Figure 4.8 SB-13 sailplane 3-view

139

Using the design procedure presented in this paper, a swept-wing tailless aircraft, operating in a flight regime where flutter is critical, is designed for minimum structural weight with specified longitudinal handling quality. The spar cap thickness at various stations along the span are used as design variables. Some designs include a feedback control system with elevons deflected in proportion to the wing tip deflection to help control the flutter. The design synthesis involves solving for the skin thickness distribution (and elevon feedback gain for cases with active control) that yield a stable aircraft with distinct short period and phugoid modes while using the least amount of structural material in the wings. The integrated design procedure improves the handling by simultaneously suppressing the flutter and driving the unrestrained dynamic modes to be most like that of a rigid aircraft. This differs from conventional flutter suppression techniques which only guarantee flutter stability and do not attempt to restore acceptable handling qualities to the unrestrained modes of the free flying aircraft.

Bending structure model is upper and lower spar caps

Active control of elevons (optional)

$$\delta_e = K_\delta \delta_{bt}$$

Vortex lattice aerodynamics model

δ_{bt}

Goal: Minimize structural weight with acceptable longitudinal handling qualities

Design variables: Spar cap thickness (at 20 spanwise stations), optional active control of elevons
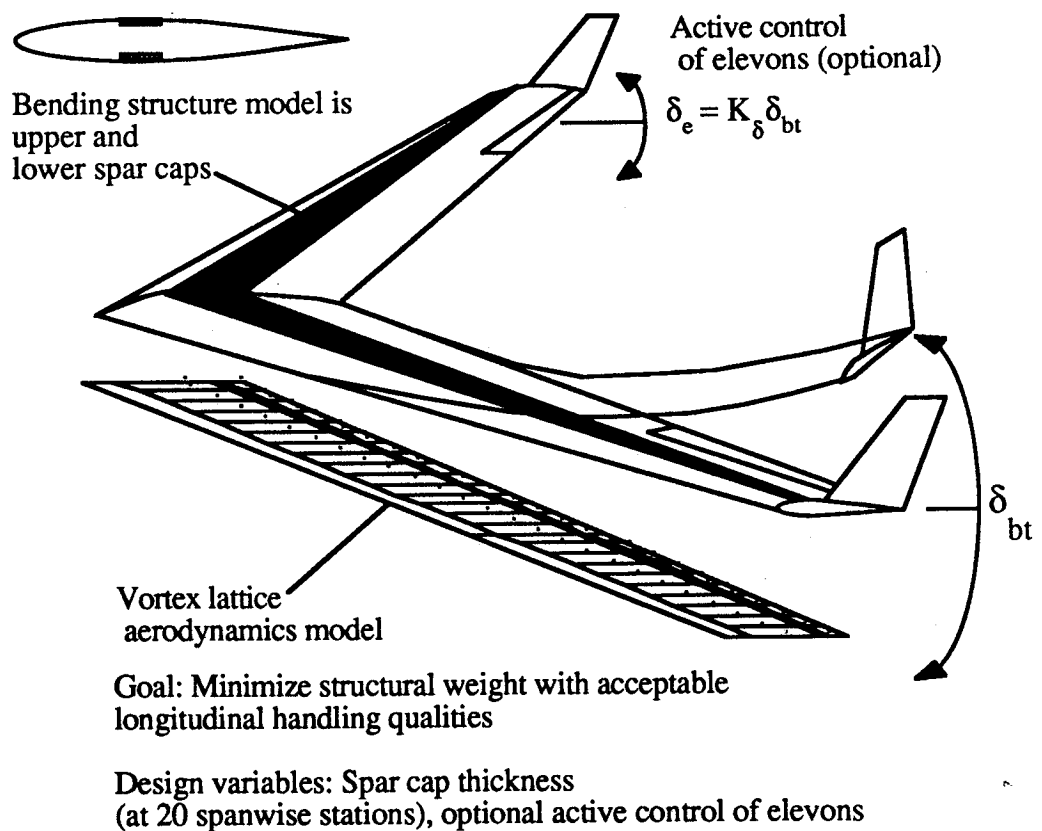
Figure 4.9 tailless aeroelastic design synthesis

Figure 4.10 shows the layout of the swept wing tailless aircraft whose structure (and possibly control system) are to be synthesized. The design flight speed is chosen so that a wing sized to support the static structural loads will not be stiff enough to avoid flutter. This choice of trimmed flight condition ensures that the dynamic response will be dominated by aeroelastic phenomenon. The root locus shown in figure 4.11 indicates that the short period mode and the lowest frequency wing bending mode become coupled as airspeed increases, ultimately resulting in flutter at 200 (f/s) airspeed.
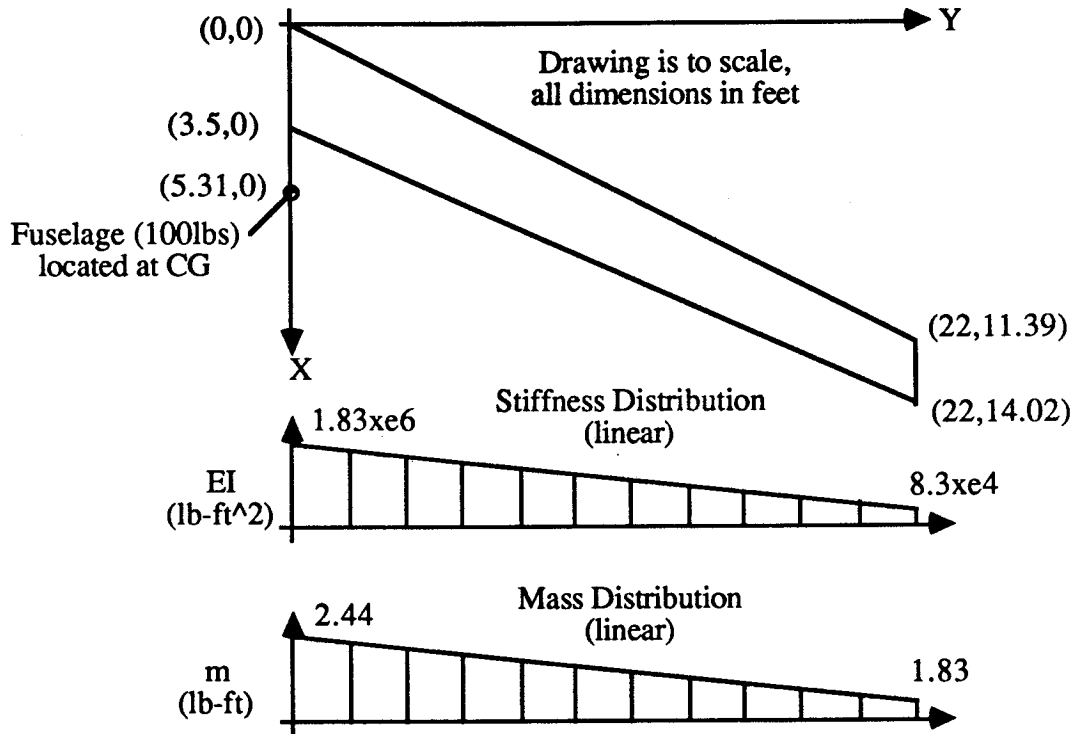
Figure 4.10 tailless aircraft planform and structure
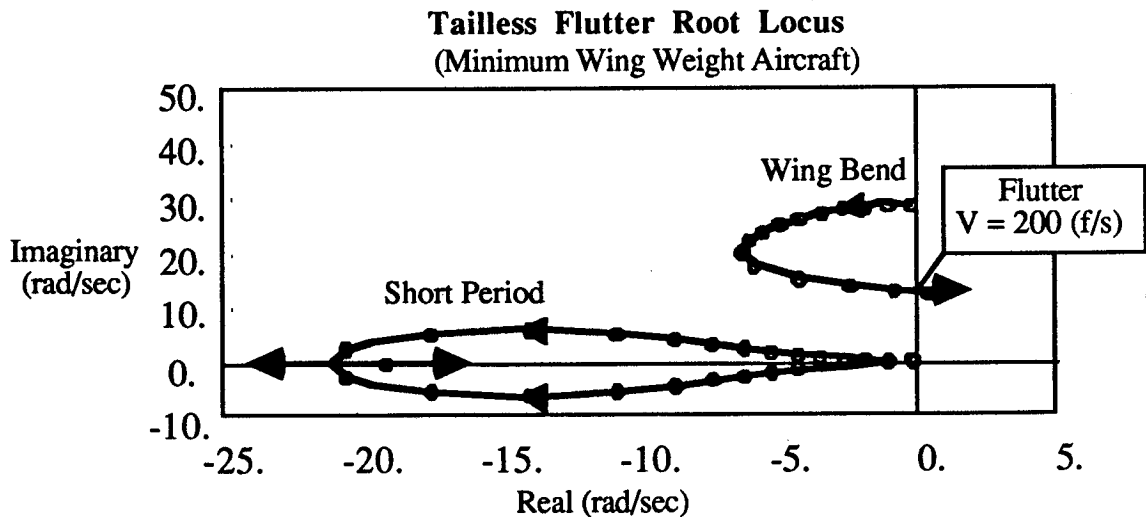
Figure 4.11 tailless aircraft flutter root locus

141

Dynamic Performance

A flutter problem of this type is unusual because acceptable handling qualities requires not only that the flutter be suppressed, but also that the short period and phugoid dynamics be acceptable. To achieve these results, a rigid aircraft with longitudinal dynamics meeting Mil. Spec. F-8785-C level 1 requirements is used as the model for the design synthesis. As J_d is minimized, the tailless aircraft's response will approach that of the rigid model case, ensuring a suppressed flutter mode and acceptable short period and phugoid response.

In reference 8 it is suggested that the present definition of J_d is not a sufficient measure of handling qualities for the flutter suppression problem. If the design synthesis considers only one flight condition, it is possible that the optimized design will be unstable at velocities below the design value. This situation can be avoided, however, by including in the dynamic performance index, the sum of J_d's evaluated at several flight velocities, up to and including the design flight condition. Designs synthesized using this composite J_d will be dynamically stable *and* have acceptable handling qualities over the entire flight envelope. In this example problem only one flight condition will be considered.

The linearized equations of motion (E.O.M.) for an unrestrained elastic flight vehicle must be formed to evaluate J_d. Lagrange's method is used to derive the E.O.M. (see chapter 6) assuming two wing bending modes ($\eta1,\eta2$) and all longitudinal degrees of freedom (u,w,q,θ). Linearization with a finite state model is possible because the wing bending is modeled using two assumed modes and the aerodynamics model is quasi-steady. This formulation of the E.O.M. has the advantage that the rigid aircraft dynamics are separable from aeroelastic effects, permitting the designer to see the influence of structural flexibility explicitly in the E.O.M.. Figure 4.12 shows the linearized EOM for the tailless aircraft with wing flexibility (assuming a typical wing mass and stiffness distribution) and the rigid wing model. In some cases a reduced order controller is also designed with feedback of the sensed wing tip deflection to elevon deflection. Aerodynamic stability and control derivatives are predicted by a quasi-steady vortex lattice method, appropriate because of the low reduced frequency of this flutter mode. Wing mass and stiffness properties are recomputed as the skin thickness is varied during the optimization.

Model (Rigid) Aircraft Equations of Motion

$$\frac{d}{dt}\begin{bmatrix} u \\ w \\ q \\ \theta \end{bmatrix} = \begin{bmatrix} 0.0000 & 1.3888 & -12.9932 & -32.1740 \\ -.7860 & -11.2360 & 182.3281 & .0000 \\ .0184 & -.2628 & -6.9880 & .0000 \\ .0000 & .0000 & 1.0000 & .0000 \end{bmatrix}\begin{bmatrix} u \\ w \\ q \\ \theta \end{bmatrix}$$

Elastic Tailless Aircraft Equations of Motion

$$\frac{d}{dt}\begin{bmatrix} u \\ w \\ q \\ \theta \\ \dot{\eta}_1 \\ \eta_1 \\ \dot{\eta}_2 \\ \eta_2 \end{bmatrix} = \begin{bmatrix} 0.0000 & 1.1765 & -13.1397 & -32.1740 & -.3906 & -1.7572 & -.2510 & -1.6781 \\ -.0524 & -1.4962 & 200.0665 & .0000 & .2483 & -77.3003 & .4664 & 237.3482 \\ .4214 & 4.5216 & 3.3457 & .0000 & -1.5768 & -73.8694 & -1.2652 & -130.1258 \\ .0000 & .0000 & 1.0000 & .0000 & .0000 & .0000 & .0000 & .0000 \\ 5.1798 & 69.1944 & -195.8978 & .0000 & 28.2246 & -324.6815 & 55.2096 & 14236.6300 \\ .0000 & .0000 & .0000 & .0000 & 1.0000 & .0000 & .0000 & .0000 \\ 4.2281 & 52.4027 & 747.7197 & .0000 & -126.6376 & -2017.6450 & -149.1517 & -23579.5110 \\ .0000 & .0000 & .0000 & .0000 & .0000 & .0000 & 1.0000 & .0000 \end{bmatrix}\begin{bmatrix} u \\ w \\ q \\ \theta \\ \dot{\eta}_1 \\ \eta_1 \\ \dot{\eta}_2 \\ \eta_2 \end{bmatrix}$$

Figure 4.12 equations of motion for the elastic tailless aircraft and model (ft-sec-rad)

143

Non-Dynamic Performance

In theory, design problems associated with aircraft flexibility and flutter can always be solved by adding more material to the structure to increase its stiffness. The designer's goal is to add the material intelligently so that the aircraft's structural weight will remain a minimum. By choosing wing bending weight as the non-dynamic performance in this example, designs are synthesized with minimum structural weight consistent with a specific level of handling quality. Wing bending weight is calculated by integrating the weight of the material in the spar caps at 20 stations along the span.

Constraints

Penalty function constraints are imposed to limit the maximum stress in the spar caps at a 3-g load factor; a minimum skin gauge is also imposed. Maximum skin stresses are calculated using a static aeroelastic analysis that accounts for inertia relief and the effect of wing deformation on the spanwise loading. A third penalty function is used to ensure dynamic stability of the system. This is identical to the constraint implemented in the aft tail design synthesis. The combination of these three constraints ensures that all designs will be strong enough to meet the static load requirements and be aeroelastically stable.

Tailless Flutter Design Results

Results for the tailless aircraft design example are shown in figure 4.13. As in the previous case, each point on the curves represents an optimal design with a specific value of handling quality weighting. Smaller values of J_d indicate improved handling, and increased values of weight ratio correspond to increased wing weight. The regions in which handling quality becomes acceptable lie to the left of the "level 1" limiting marks. Designs with feedback control show reduced wing weight since elevon deflection can provide artificial stiffness without additional material in the skins.

In a sequential design procedure the wing structure is first sized for minimum weight based on static aeroelastic loading and minimum gauge requirements. The reduced order control

system is then designed for the best handling quality with a fixed wing design. The resulting sequentially-designed aircraft has a stable flutter mode but its short period and phugoid dynamics are still highly coupled to the wing bending mode giving poor handling qualities. This design is represented by the point marked with an asterisk in figure 4.13.

Tailless Flutter Design Results
Wing Weight vs Handling Quality
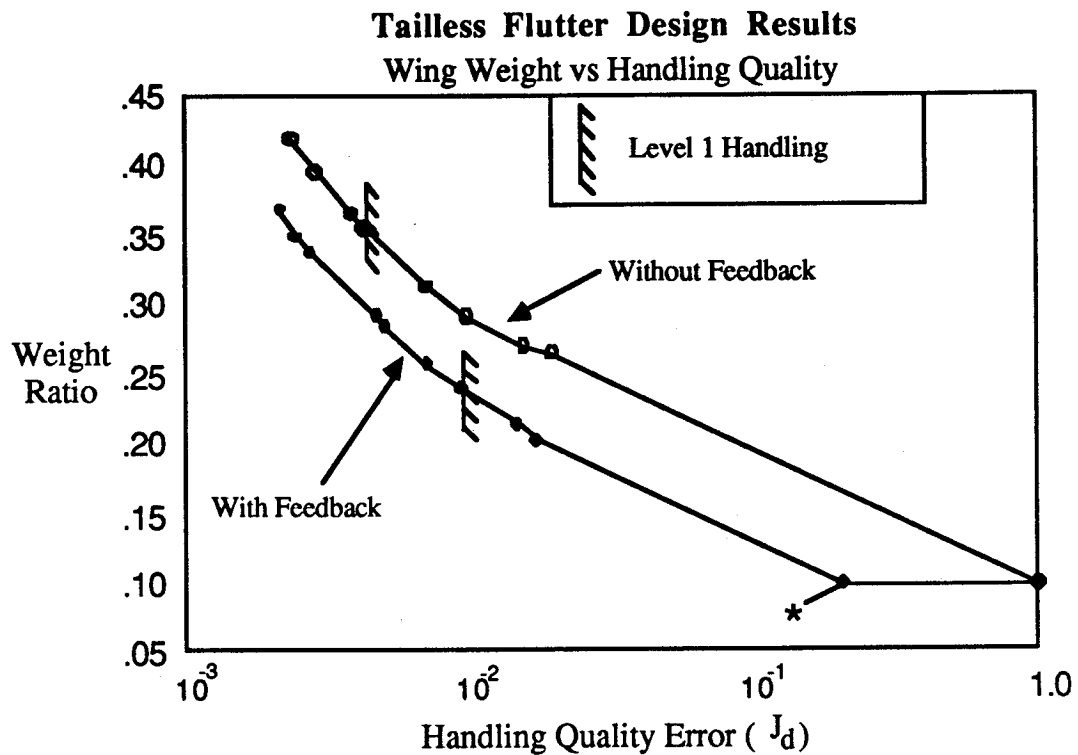
Figure 4.13 tailless flutter results, wing weight vs. handling quality

By contrast, the integrated design procedure achieves a stable flutter mode with acceptable rigid body dynamics and does so with the least penalty in wing weight. The eigenvalues and eigenvectors approach those of the model case as the handling quality weighting is increased. This is important to note, because the handling qualities for this example only become acceptable when the short period, phugoid, and wing bending modes are distinct and properly damped. Figures 4.14 - 4.16 show the response of the Level 1 design with feedback and the best sequential design to a step vertical gust. The phugoid mode of the sequentially designed aircraft has lower damping and shows distinct coupling to the wing bend and short period dynamics. The level 1 integrated design, however, displays dynamic response more like that of the model's and does so with substantially less control effort from the elevons.

145

(u) Velocity vs Time
Tailless Aircraft, Vo=200 (f/s), Step Vertical Gust
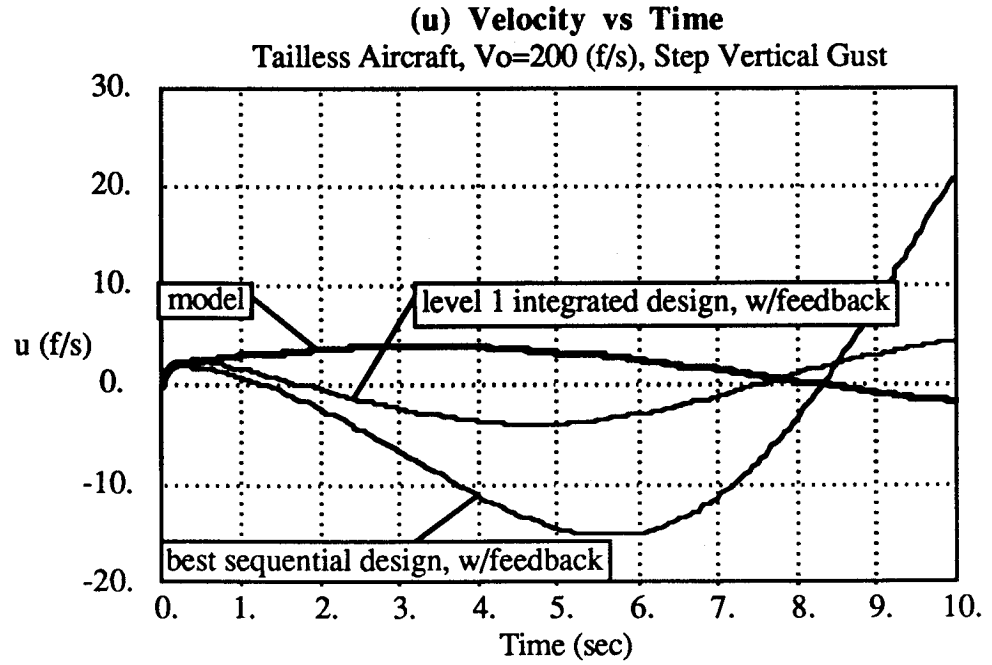
Figure 4.14 (u) velocity vs time

Angle of Attack vs Time
Tailless Aircraft, Vo=200 (f/s), Step Vertical Gust
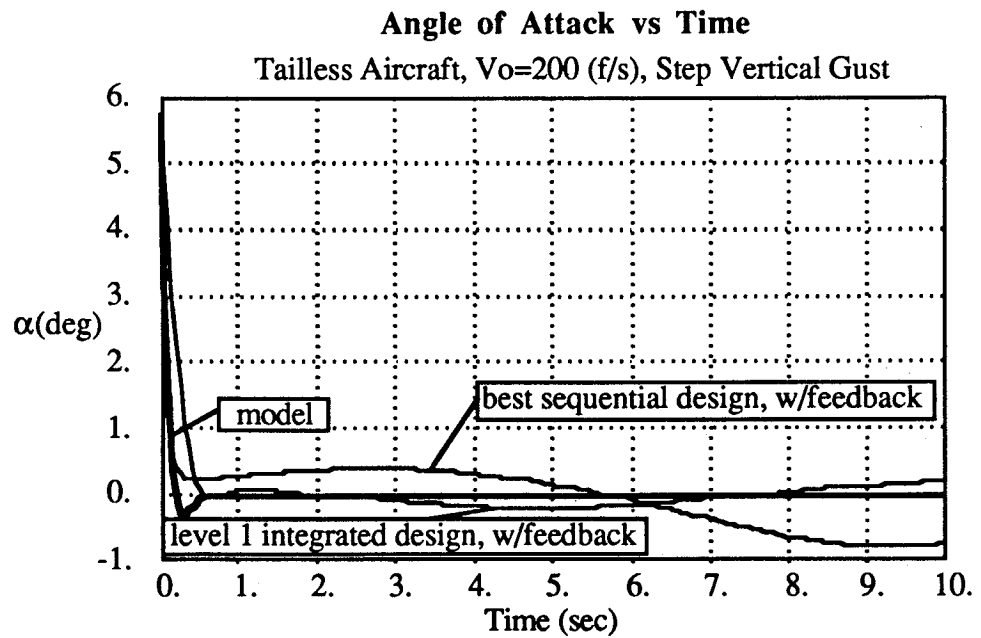
Figure 4.15 angle of attack vs time

146

Wing Tip Deflection vs Time
Tailless Aircraft, Vo=200 (f/s), Step Vertical Gust
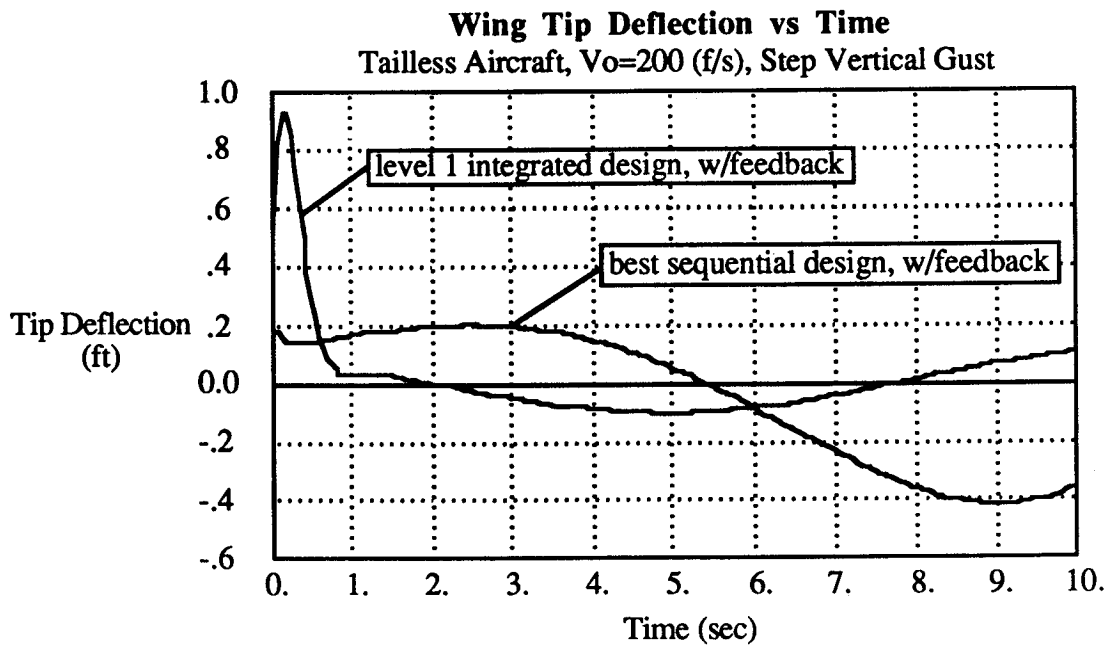
Figure 4.16 wing tip deflection vs time

Optimal Spar Cap Thickness Distribution
Spar Cap Thickness vs Semi-Span Fraction
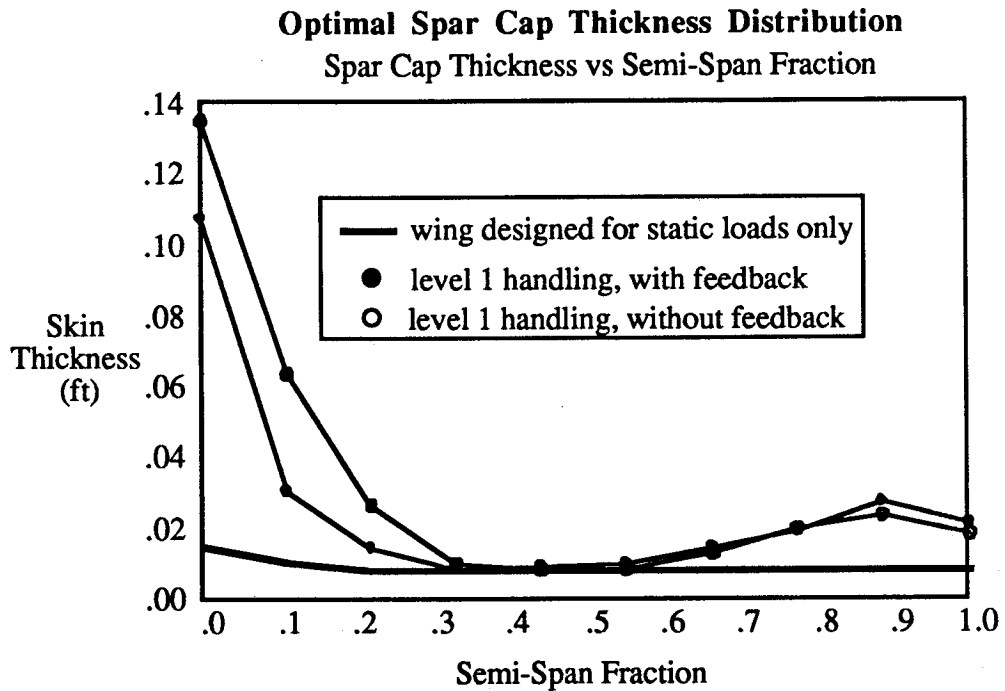
Figure 4.17 optimal spar cap thickness vs semi-span

The optimal solutions for the skin thickness as a function of semi-span are shown in figure 4.17. Aeroelastic stability requires that the skin thickness be increased at the wing root, with greater thickness required for cases without a feedback controller. Interestingly, the results also show increased skin thickness at the wing tip. The presence of this additional

147

mass further separates the frequencies of wing bending and short period dynamic modes and is a significant factor in the achieving flutter stability.

4.4 Summary

The method described here for aircraft design optimization with dynamic response considerations provides an inexpensive means of integrating dynamics into aircraft preliminary design. By defining a dynamic performance index that can be added to a conventional objective function, a designer can investigate the trade-off between performance and handling. The procedure is formulated to permit the use of control system gains as design variables, but does not require full-state feedback. The examples discussed here show how such an approach can lead to significant improvements in the design when compared with the more common sequential design of system and control law.

This integrated design procedure is most useful for studying problems in which handling qualities and other types of mission performance are highly coupled. Many problems of current interest fall into this category:

1) Aeroservoelastic design of flexible aircraft

2) Aeroelastic tailoring of aircraft with composite structures

3) Design of unstable aircraft for minimum trimmed drag

Problems in which only the handling qualities are to be improved are also readily solved by this method. Examples of this type of problem include the design of unstable aircraft for super-maneuverability and the integrated synthesis of oblique wing aircraft for improved controllability.

Chapters 5 and 6 will show how the MIDSM method is used to re-design the F-8 OWRA and its SAS for improved handling qualities. Initially, aircraft with an EMF SAS will be considered at single and then multiple flight conditions. The RMF SAS will then be implemented and the influence of wing flexibility will be included in the synthesis.

Chapter 5

Integrated Design of Oblique Wing Aircraft

In this chapter the integrated design synthesis method, MIDSM, is used to simultaneously re-configure the F-8 OWRA and re-design its controller to obtain handling qualities which exceed those achieved by the closed loop nominal configuration. Five configuration design variables, that determine the location and orientation of the wing relative to the fuselage, are considered (along with the SAS gains) in the MIDSM synthesis to further decouple the OWRA's dynamic response. Because most of the aerodynamic coupling (which significantly affects handling qualities) is caused by the airloads acting on the wing, optimization of the configuration variables which determine the wing placement provides a rational approach for improving the dynamic response without significantly affecting drag and weight. Constraints are placed on the range of the wing displacement to ensure that the configuration is feasible from a structural standpoint and so that drag is not significantly effected. Trim in 1-g level flight is guaranteed by placing constraints on the maximum control surface deflections and sideslip angle required to trim. The dynamic performance is measured using the same quadratic dynamic cost integrals described in chapter 3 for the EMF and RMF SAS designs. The MIDSM OWRA synthesis is very much like the OWRA SAS design problem considered in chapter 3, except that now there are configuration variables which provide additional degrees of freedom with which to further drive the OWRA's dynamic response toward that of the Mil.-Spec. F-8785C model.

Several types of MIDSM syntheses are performed in this chapter. First, the OWRA with an EMF SAS is synthesized for improved handling qualities at a single flight condition. This example demonstrates that MIDSM is capable of significantly improving the OWRA's handling qualities and shows the details of how the synthesis is carried out. In the second example a single OWRA design with an EMF SAS is synthesized for improved handling qualities at several flight conditions. Although the control gains in the SAS may be changed as flight condition varies, the configuration of the aircraft remains fixed after it is

built and must therefore be optimal for performance over a range of flight conditions. These multiple flight condition syntheses demonstrate that MIDSM is capable of 'robust' configuration synthesis. The last example in this chapter synthesizes the OWRA with an RMF SAS instead of an EMF SAS. This requires that the optimizer search through a design space that includes all of the controller gains (45) and the configuration design variables (4). The results of this example demonstrate that the configuration changes which improve the OWRA's controllability are independent of the SAS architectures considered. This analysis is continued in chapter 6, where the influence of wing flexibility on dynamic performance and the optimal MIDSM OWRA configuration is studied.

5.1 Aerodynamics and Dynamics Models

Chapters 2 and 3 described how the aerodynamic loads and the dynamic response of an oblique wing aircraft are accurately predicted with a minimum computational cost by using a vortex lattice aerodynamic analysis and linearized equations of motion. Figure 5.1 is a block diagram which illustrates how the components of the LINAIR vortex lattice analysis are incorporated into the MIDSM synthesis. In chapter 2 it was shown that for relatively large changes in the wing's position relative to the fuselage, the assumption that the [AIC] and [VIC] matrices remain constant during these configuration changes is quite good. This assumption is therefore implemented in all of the F-8 OWRA MIDSM synthesis studies presented in this work. The [AIC] and [VIC] matrices are computed once for the initial guess configuration and as the optimizer re-positions the aircraft's wing, only the boundary conditions are updated in the solution for the airloads. Omitting the re-calculation of these matrices substantially reduces the computation cost of the aerodynamics calculations. It is important to note that the validity of this approximation is strongly dependent on a choice of design variables which only alter the wing's position and orientation. If the wing planform or sweep were to be changed, the assumption that the[AIC] and [VIC] matrices are not significantly affected would be in gross error. In all of the cases presented in this work, the final MIDSM configuration performance results are predicted using [AIC] and [VIC] matrices calculated for the actual configuration (and not those of the initial guess).

The stability and control derivatives are estimated by perturbing the states $\{\alpha, \beta, p, q, r\}$ and the control surface deflections to numerically calculate the required derivatives. As was mentioned in chapter 2, LINAIR provides accurate predictions of all of the aerodynamic
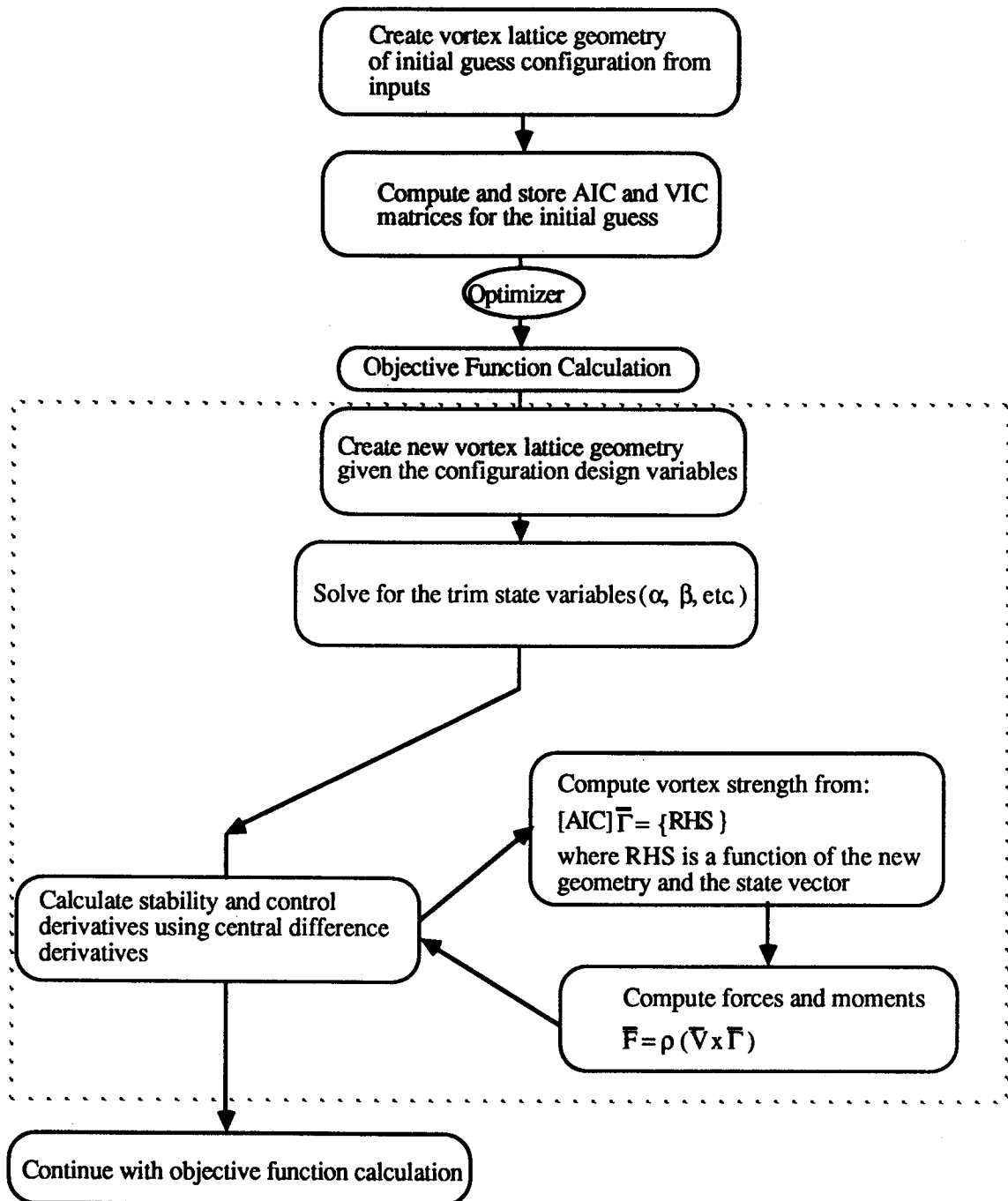
Figure 5.1 aerodynamic loads calculation in MIDSM

loads except for yawing moment (C_N). The unusual interference which occurs between the wing and fuselage (due to thickness) cannot be predicted by a thin surface aerodynamics model. Fortunately, the influence of the wing's position relative to the fuselage has little effect on the pitch-yaw coupling (for a fixed wing sweep - see figure 2.33). Therefore, the wind tunnel data for C_N as a function of wing sweep and angle of attack may be

151

used to predict the yawing moment for all of the configurations considered in this work.

As the wing is re-positioned on the fuselage the aircraft's inertia properties are changed. The importance of inertial coupling on handling qualities dictates that this effect be included in the design synthesis. Given the wing and fuselage mass properties (relative to their own mass centers) the following relations describe the total aircraft inertia for any wing position and orientation:

Inertia Tensor Calculation

$$(5.1) \quad \bar{I}_{total} = \bar{I}_{f\&t} + \Lambda \, [\bar{I}_w] \, \Lambda^T + \begin{bmatrix} d_2^2 + d_3^2 & -d_1 \, d_2 & -d_1 \, d_3 \\ \uparrow & d_1^2 + d_3^2 & -d_2 \, d_3 \\ SYM \rightarrow & & d_1^2 + d_2^2 \end{bmatrix} m_w$$

where:

$\bar{I}_w$ = wing inertia tensor about the wing C.G., expressed in wing coordinates

$\bar{I}_{f\&t}$ = fuselage and tail inertia tensor about the aircraft C.G. expressed in body ax

$\bar{I}_{total}$ = total aircraft inertia about the aircraft C.G., expressed in body axes

$\bar{d}$ = vector from the aircraft C.G. to the wing C.G. in body axes

m_w = wing mass

Λ = transform from wing local axes to body axes

The linearized equations of motion for a proposed OWRA configuration are obtained by substituting the aerodynamic stability and control derivatives, flight condition, and mass property data into equations 3.14 - 3.17. The CPU time required to form the EOM is very small in comparison to that required to evaluate the airloads.

In all of the MIDSM OWRA syntheses the following constraints are enforced by appending the appropriate penalty functions to the dynamic cost:
1) Trim at 1-g level flight with small control surface deflections and sideslip angle.
2) Dynamic stability

152

3) Explicit limits on the feasible range of each configuration design variable.

The trim constraint is enforced by computing the control deflections and sideslip angle required to yield no sideforce or moment about the C.G. and a specified lift coefficient. If the deflections exceed specified limits then a penalty is added to the objective function. The following system of linear equations is used to find the aircraft's trim deflections:

Linearized Trim State Solution

$$(5.2) \quad \begin{bmatrix} C_{y\alpha} & C_{y\beta} & C_{y\delta roll} & C_{y\delta pitch} & C_{y\delta yaw} \\ C_{z\alpha} & & & & \\ C_{l\alpha} & & & & \\ C_{m\alpha} & & & & \\ C_{n\alpha} & & & & C_{n\delta yaw} \end{bmatrix} \begin{bmatrix} \Delta\alpha \\ \beta \\ \delta_{roll} \\ \delta_{pitch} \\ \delta_{yaw} \end{bmatrix} = \begin{bmatrix} 0 \\ C_z \\ 0 \\ 0 \\ 0 \end{bmatrix}$$

Because the angle of attack (α) is computed as part of the trim solution it cannot be known in advance for appropriately linearizing the aerodynamic derivatives. Therefore, an iterative solution is required, stopping when the angle of attack value converges. Typically, this takes less than three iterations. The final computed value for the trimmed angle of attack is used as the condition for linearizing the stability and control derivatives for the dynamics analysis. Table 5.1 list the maximum acceptable deflections for the trim variables.

Trim state	Maximum value (absolute)
β	2 (deg)
δ_{roll}	5 (deg)
δ_{pitch}	5 (deg)
δ_{yaw}	5 (deg)

Table 5.1 1-g level flight trim constraints

5.2 Application of MIDSM to the F-8 OWRA

Because the loads acting on the wing contribute most to the aerodynamic coupling, it is reasonable to try to improve the handling qualities by re-positioning the wing relative to the fuselage so that the aerodynamic coupling is favorably altered (without significantly affecting drag and structural weight). Five configuration design variables are chosen which determine the relative position and orientation of the wing and fuselage, along with the wing's symmetric dihedral. Figure 5.2 defines these variables. The location of the wing pivot along the fuselage (X_{pf}) determines the wing's placement relative to the C.G. and therefore significantly affects static pitch stability. The chordwise location of the wing pivot (X_{pw}) influences the amount of wing area projected on either side of the fuselage as the wing sweeps obliquely. Small changes in this variable can strongly influence the roll-pitch and pitch-roll coupling. If the wing pivot axis is not parallel to the z body axis, then the wing's orientation relative to the fuselage will change as sweep varies (Fig. 5.13). In all cases studied, it is assumed that the plane of the wing is parallel to the x-y body axis plane when the wing is unswept. This assumption forces the configuration to remain symmetric at zero wing sweep. Pivot axis tilt and wing banking most significantly influence the pitch to sideforce and the pitch to roll coupling of the aircraft by tilting the resultant aerodynamic force vector as the wing banks.

The presence of a skewed pivot axis introduces some ambiguity in the definition of wing sweep because the wing does not rotate about the z body axis. In this study, sweep is defined as a rotation about the wing pivot axis. This produces differences in sweep (between the wing pivot and the z body axis) of less than 1 degree at 65 degrees sweep for a wing bank angle of 15 degrees. Wing incidence (at zero wing sweep) is the only variable that needs to be defined to completely describe the wing's orientation relative to the fuselage. This parameter is not considered as a design variable because it merely defines the decalage between the wing and tail, which can be arbitrarily changed by a symmetric elevator deflection of the full-flying elevators. The final design variable is the symmetric dihedral built into the wing (assumed parabolic). Dihedral affects the pitching and rolling moments required to trim and also influences dynamic stability. The dimensionless wing tip deflection (η) fixes the amount of dihedral in a given design.

Pivot Axis Orientation

Parabolic Dihedral

Wing Tip
Deflection

η= wing tip
deflection / reference
span

Pivot Location Relative to the Fuselage

Pivot Location Relative to the Wing Root Chord
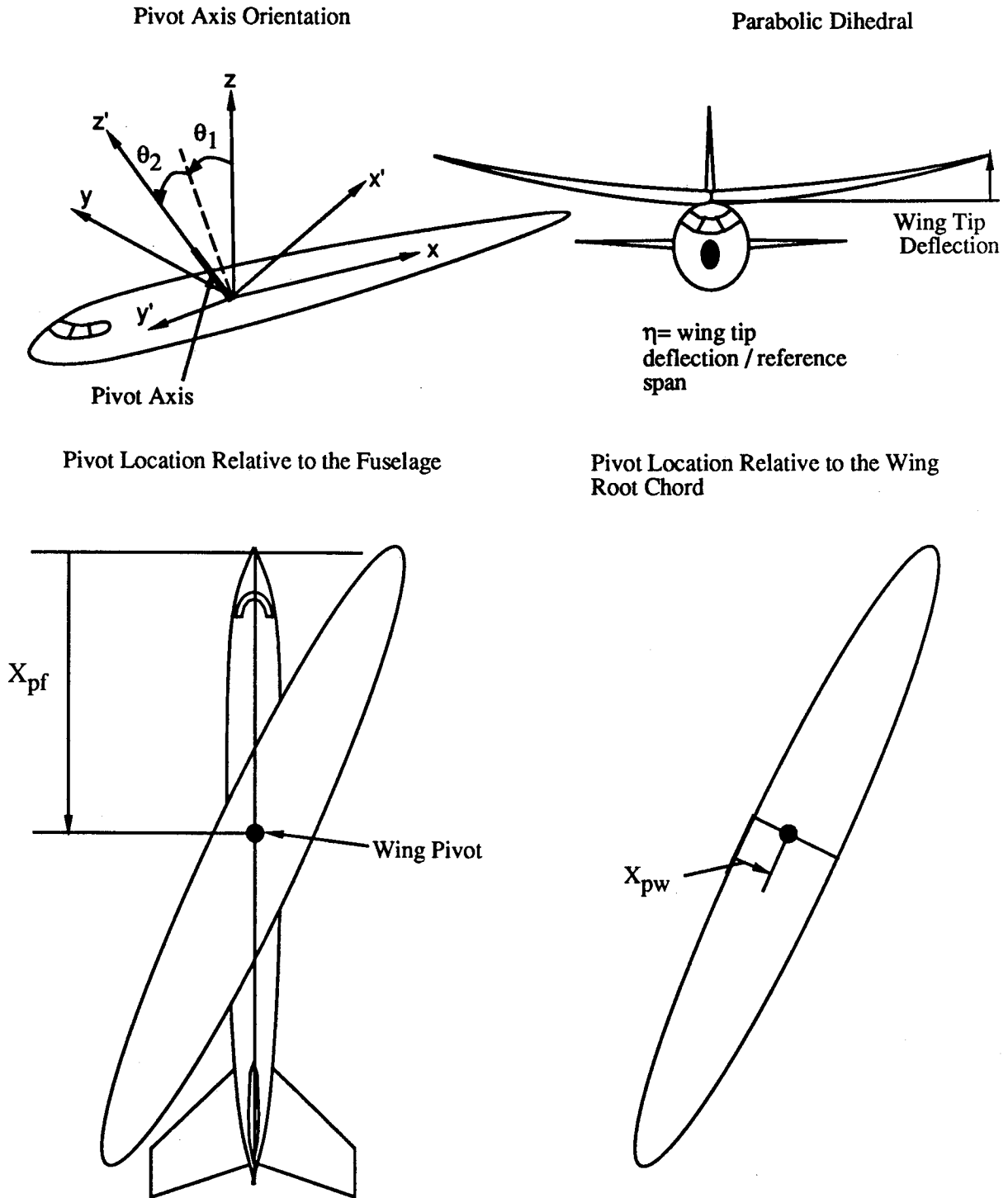
Figure 5.2 configuration design variables
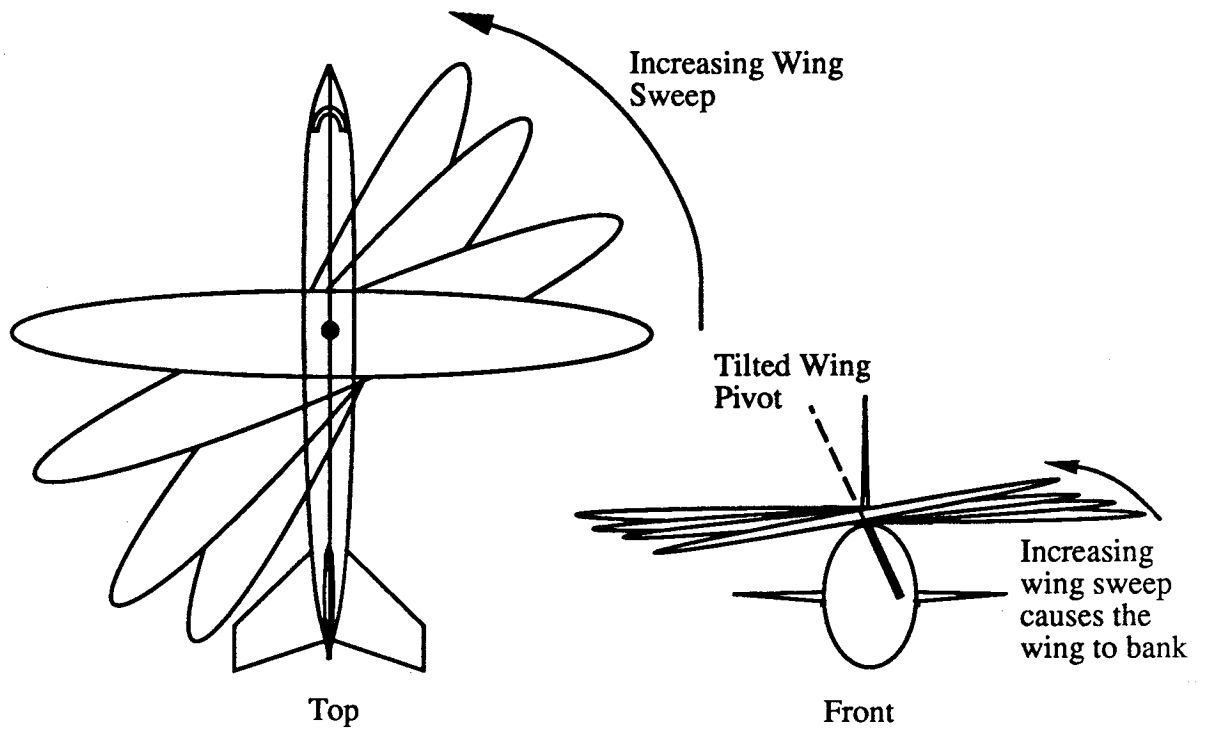
Figure 5.3 effect of pivot axis tilt on wing bank angle

Each design variable is constrained during the synthesis to not exceed a range over which structural weight or total drag would be adversely affected. Table 5.2 lists the limits of the design variables assumed for all design synthesis considered.

$$\text{abs}(\Delta X_{pw}) \leq \frac{C_{ref}}{3}$$

$$\text{abs}(\Delta X_{pf}) \leq C_{ref}$$

$$\text{abs}(\text{ dihedral }) \leq .05$$

$$\text{abs}(\theta_1) \leq 8.0 \text{ (deg)}$$

$$\text{abs}(\theta_2) \leq 20.0 \text{ (deg)}$$

} Implies that the wing bank angle can not exceed 16 (deg) at any sweep angle.

Table 5.2 configuration design variable constraints

The analysis methods required to evaluate the dynamic cost and constraint violations for an arbitrary oblique wing design have been presented in chapters (1-4) and may now be incorporated into the MIDSM objective function calculation. This will be done in the next sec-

156

tions for the cases of several types of OWRA syntheses. Initially, the SAS architecture is assumed to be EMF, so that the optimal SAS gains are computed as part of an optimal control sub-problem at each objective function calculation. This removes the burden from the optimizer of having to search for the optimal gains explicitly. Single flight condition syntheses are performed first to show how the MIDSM method is capable of improving oblique wing handling qualities with the configuration variables considered. Because the configuration variables cannot be altered in flight, they must be chosen for improved dynamic response over a range of flight conditions which is determined by the aircraft's particular mission. The second MIDSM example addresses this issue by synthesizing a a single OWRA for improved handling at both M=0.8, 45 degrees sweep and M=1.6, 65 degrees sweep. In chapter 3 it was noted that the RMF SAS offered advantages in terms of robustness, transient response decoupling, and actuator bandwidth requirements when compared to the EMF SAS. The remaining MIDSM syntheses assume an RMF SAS architecture for the F-8 OWRA which requires that the optimizer explicitly solve for the control gains. This dramatically increases the computation costs of a synthesis when compared to the EMF SAS designs. The influence of SAS architecture on the optimal OWRA configuration is revealed by these results.

5.2.1 MIDSM OWRA Synthesis, EMF SAS, 45° Sweep, M = 0.8

The simplest MIDSM oblique wing synthesis is to simultaneously re-configure the F-8 OWRA and design its SAS for improved handling qualities at a single flight condition (SFC). The flight condition considered in this example is 45° wing sweep, M=0.8, and dynamic pressure = 440 (lb/ft^2). The optimizer solves for four configuration design variables explicitly and 63 control gains implicitly (in the EMF SAS synthesis) to minimize the dynamic cost and satisfy the constraints. The configuration variables are the location of the wing pivot along the fuselage (X_{pf}), chordwise location of the pivot along the wing (X_{pw}), wing bank angle (ϕ_b), and parabolic wing dihedral (η). The wing bank angle (ϕ_b) defines the wing pivot axis angles θ_1 and θ_2 such that when the wing is swept 45° it appears to banked (ϕ_b) (left wing low when viewed from front) with zero incidence change (Fig. 5.4).

157
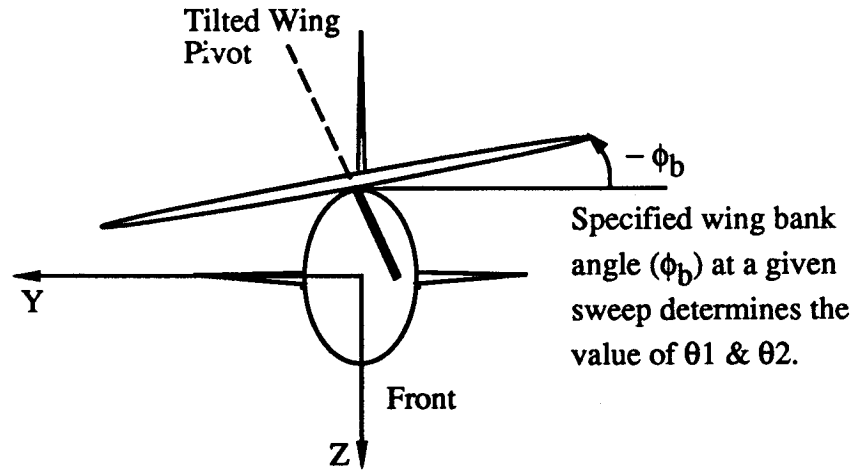
Figure 5.4 specified wing bank angle

Because the EMF SAS architecture assumes full-state feedback, the optimal control gains are computed implicitly by solving the associated ARE at each objective function calculation. This offers the advantage of reduced computational costs for the MIDSM synthesis, but restricts the SAS architecture to the less practical EMF scheme.

The dynamic cost is evaluated as follows:

Dynamic Cost

$$J_d = \int_0^\infty \left\{ (\tilde{y} - \tilde{y}_m)^T Q (\tilde{y} - \tilde{y}_m) + u^T R u \right\} dt$$

J_d is calculated from the [P] matrix (obtained from the solution
of the EMF SAS Riccatti equation) and initial condition information.

$$J_d = \sum_{i=1}^{N_{ic}} y_{o_i}^T P y_{o_i} \qquad N_{ic} = \text{Number of I.C.'s considered}$$

This calculation for J_d is similar to that presented in the EMF SAS design procedure in chapter 3. One important difference is that when only the SAS is synthesized, the resulting values of the optimal control gains are independent of the initial conditions (y_{oi}) that excite the plant. The dynamic cost is dependent upon the plant excitation, but the values of the SAS gains which minimize J_d do not depend on these initial conditions if the system is linear, time invariant, and controllable. In the MIDSM synthesis the type of the initial condi-

158

tions that excite the plant do influence the value of the optimal configuration variables and SAS gains. This is because the integrated design problem no longer has the same mathematical form as the linear optimal control problem. The additional degrees of freedom provided by the configuration variables produce a dependence between J_d and the plant excitation initial conditions. Therefore, it is important in the MIDSM procedure to choose these initial conditions so that they represent anticipated physical disturbances. Examples of these disturbances include pilot commands inputs and atmospheric turbulence. The initial conditions assumed in the F-8 OWRA MIDSM synthesis are:

Plant Excitation for MIDSM Design, F-8 OWRA

$$\tilde{y} = [g_y, g_z, p, q, r, \phi, \delta_{mcroll}, \delta_{mcpitch}, \delta_{mcyaw}]^T$$

Initial Conditions:

step lateral gust $\quad \tilde{y}_{01} = [\ 1\ 0\ 0\ 0\ 0\ 0\ 0\ 0\ 0\ ]^T$

step vertical gust $\quad \tilde{y}_{02} = [\ 0\ 1\ 0\ 0\ 0\ 0\ 0\ 0\ 0\ ]^T$

step roll input $\quad \tilde{y}_{03} = [\ 0\ 0\ 0\ 0\ 0\ 0\ .5\ 0\ 0\ ]^T$

step pitch input $\quad \tilde{y}_{04} = [\ 0\ 0\ 0\ 0\ 0\ 0\ 0\ 1\ 0]^T$

step yaw input $\quad \tilde{y}_{05} = [\ 0\ 0\ 0\ 0\ 0\ 0\ 0\ 0\ .5\ ]^T$

The magnitude of each initial condition reflects the relative importance of the disturbance on the total dynamic response.

The total objective function is given by the the dynamic cost plus penalty functions for the trim and design variable constraints.

$$J_{tot} = J_d + P.F._{trim} + P.F._{design\ varibles}$$

If the plant can be stabilized, the EMF SAS is guaranteed to produce a dynamically stable closed loop system. Therefore, dynamic stability constraints need not be enforced explicitly in the design synthesis. A constraint that the plant can be stabilized may be enforced [Ref. 9] but for the range of configuration variables considered in the MIDSM OWRA synthesis this constraint was found to be unnecessary because it is always possible to stabilize the aircraft.

The Quasi-Newton optimizer solves for the 4 configuration variables and the 63 SAS gains that minimize J_{tot}. Figure 5.5 is a flowchart showing how the integrated design synthesis is accomplished for the F-8 OWRA at a single flight condition. The design synthesis assumes the same model dynamics (Mil.-Spec. F-8785C) , [Q], and [R] weighting matrices used in the EMF SAS design described in chapter 3. The initial guess for the configuration variables corresponds to the nominal F-8 OWRA configuration:

$$X_{pf} = 37.292 \text{ (ft)}$$

$$X_{pw} = 3.1392 \text{ (ft)}$$

$$\phi_b = 0.0 \text{ (deg)}$$

Dihedral $= 0.0$

Table 5.3 configuration variable initial guess values

Figures 5.6 - 5.10 show how the configuration design variables were changed by the optimizer to minimize the total cost. A converged answer was achieved in 20 line searches which required 331 objective function evaluations. The final solution for the optimal control gains and configuration variables is listed in figures 5.11 - 5.13 along with the control surface deflections required for trim.

Figure 5.14 shows a 3-view of the nominal and the MIDSM optimized OWRA configurations. The optimal design has its wing banked (forward wing low) and the entire wing is shifted towards the forward swept tip (planform view). These small changes in the aircraft's configuration have a significant impact on its closed loop dynamic response as is shown in figures 5.15 - 5.20. A 4-g pull up maneuver is simulated for the model, nominal, and MIDSM OWRA. These figures clearly show that the MIDSM OWRA experiences reduced peak lateral acceleration and reduced maximum roll angle. Table 5.4 summarizes the improvements in dynamic decoupling for the F-8 performing the pitch-up maneuver.

	$g_{y \text{ peak}}$	$\phi_{peak} \text{ (deg)}$	$r_{peak} \text{ (deg/sec)}$
Nominal OWRA	-0.38	23.2	-5.0
MIDSM OWRA	-0.034	5.7	1.0
% Reduction	91%	75%	80%

Table 5.4 MIDSM OWRA performance, 45° sweep, EMF SAS

```
Main Code
   │
Read inputs &
initialize variables
   │
Vortex lattice geometry
of initial guess
   │
[AIC] & [VIC]
matrices (store)
   │
[AIC] L-U
decomposition
   │
Call
optimizer  ⟷  QNMDIF
              Quasi-Newton
              Optimizer
   │
Output results
   │
Stop
```

```
                    Objective Function Calculation
                              │
                    Vortex lattice geometry
                    (current configuration variables)
                              │
                    Trim state solution
                              │
                    Stability & control derivatives
                              │
                    Mass Properties
                              │
                    Linear EOM
                              │
                    Solve ARE
                              │
                    SAS gains
```

Dynamic cost

$$J_d = \sum_{i=1}^{N_{fc}} y_o^T [P] \, y_o$$

Penalty functions

Total cost
$$J_{tot} = J_d + \text{penalty functions}$$

Return

Figure 5.5 MIDSM OWRA synthesis, single flight condition, EMF SAS

Total Cost
MIDSM Results, EMF SAS, SFC, 45 (deg) Sweep
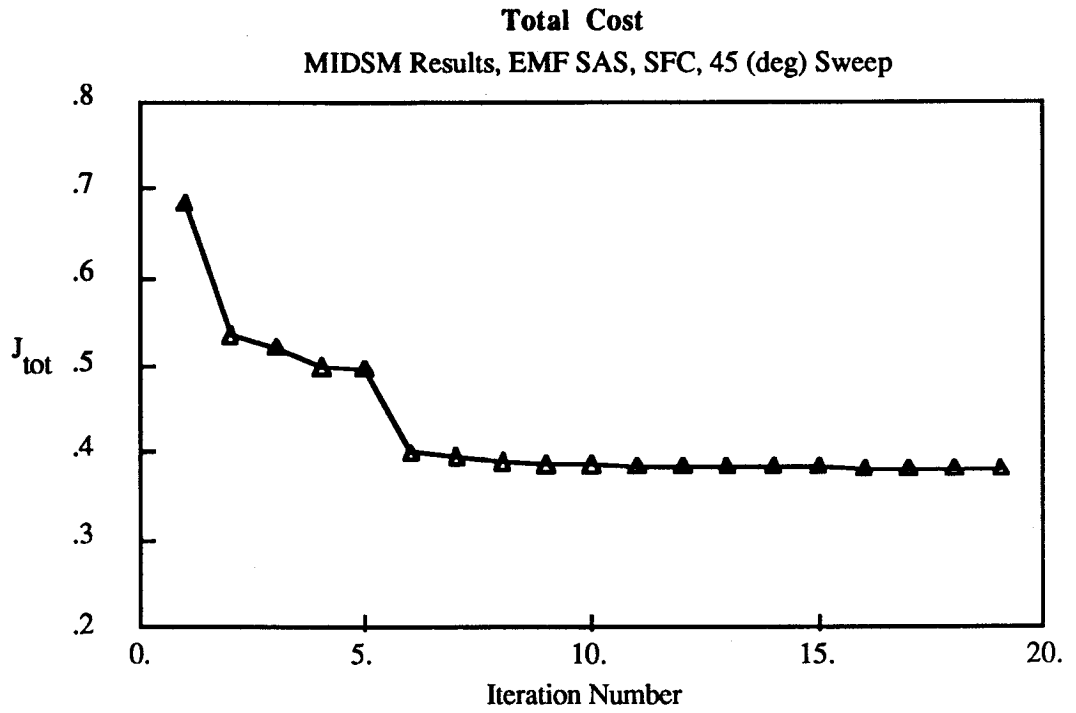
Figure 5.6 total cost vs. optimizer iteration

Wing Bank Angle
MIDSM Results, EMF SAS, SFC, 45 (deg) Sweep
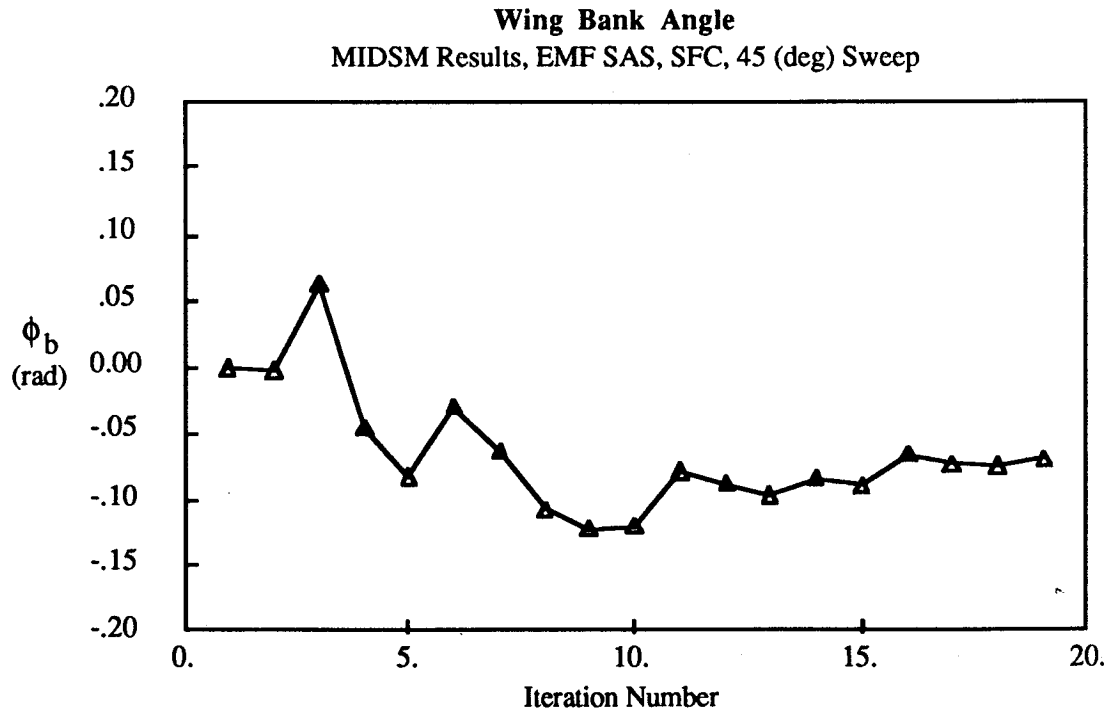
Figure 5.7 wing bank angle vs. optimizer iteration

162

Chordwise Location of Wing Pivot

MIDSM Results, EMF SAS, SFC, 45 (deg) Sweep
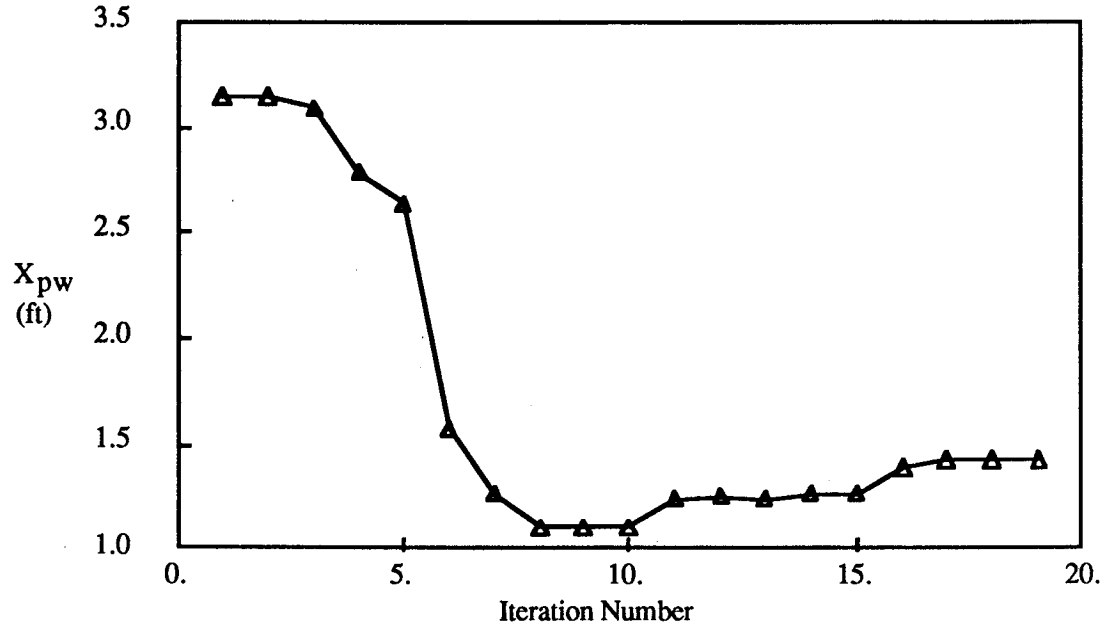
Figure 5.8 chordwise wing pivot location vs. optimizer iteration

Wing Pivot Location Along Fuselage

MIDSM Results, EMF SAS, SFC, 45(deg) Sweep
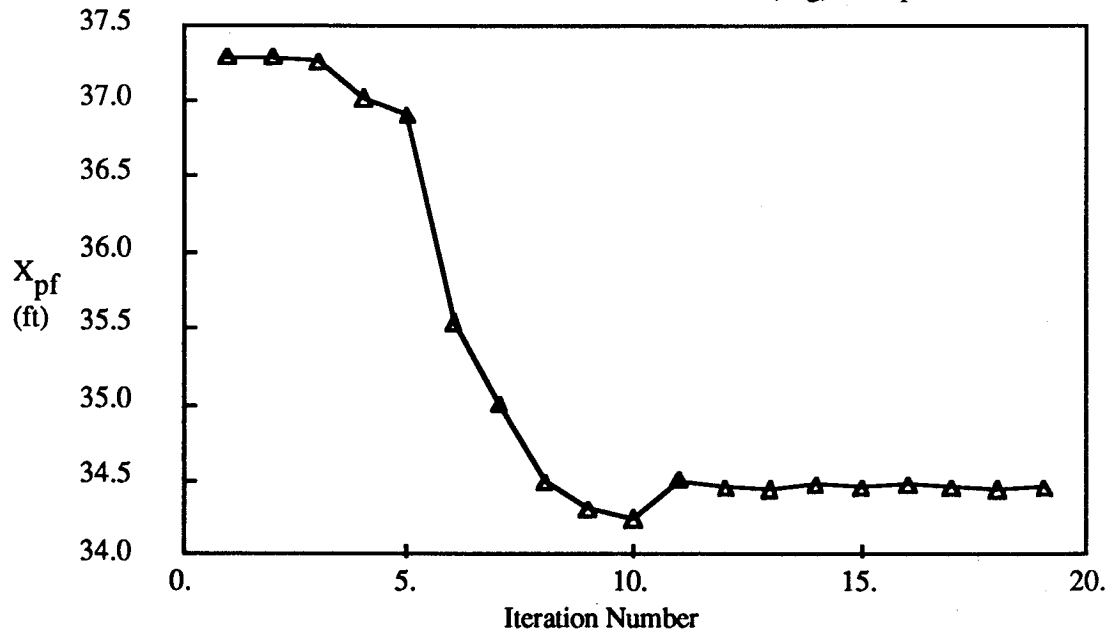
Figure 5.9 fuselage wing pivot location vs. optimizer iteration

163

Parabolic Dihedral

MIDSM Results, EMF SAS, SFC, 45 (deg) Sweep
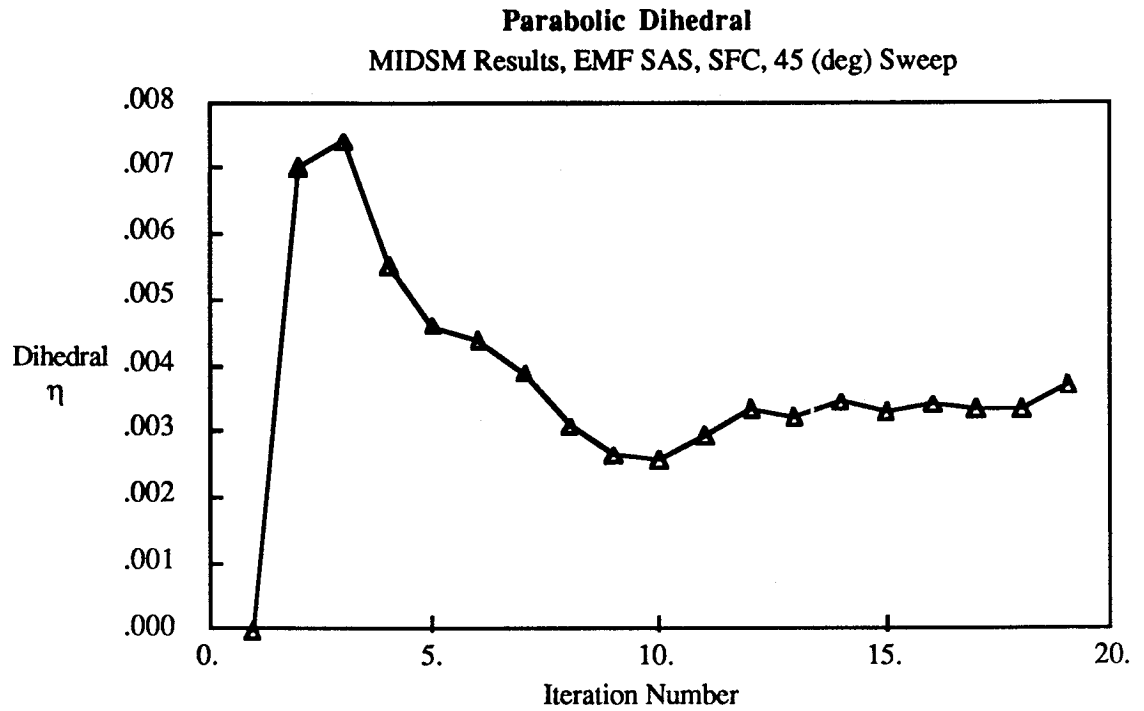
Figure 5.10 parabolic dihedral vs. optimizer iteration

MIDSM Results OWRA Synthesis 45° Sweep

$$Q_{diag} = [\ 1\ \ 1\ \ 1\ \ 0.1\ \ 1\ \ 1\ ] \qquad R_{diag} = [\ 30\ \ 30\ \ 30\ ]$$

$$K_{ff} = \begin{bmatrix} .3770 & -.0136 & .1541 \\ -.0214 & 1.7277 & .0425 \\ .5165 & -.1792 & .4527 \end{bmatrix}$$

$$K_{pf} = \begin{bmatrix} .0202 & -.0095 & .1530 & .0344 & .0390 & .1692 & .0864 & .0300 & .0979 \\ -.0025 & -.0647 & .0041 & .7438 & .0033 & .0092 & .0006 & .6606 & -.0002 \\ .0153 & .0058 & .0993 & -.0391 & .1155 & .1441 & .0633 & -.0346 & .2735 \end{bmatrix}$$

$$K_{fb} = \begin{bmatrix} -.1576 & .0027 & -.0878 & -.0345 & -.2903 & -.0249 & -.1268 & -.0395 & -.4197 \\ -.0869 & .1251 & -.0254 & -.8638 & -.1436 & .0860 & -.0658 & -.8056 & -.1740 \\ -.1271 & -.0279 & -.0170 & .0759 & -.5648 & -.0183 & -.1149 & .0958 & -.5705 \end{bmatrix}$$

Figure 5.11 optimal EMF SAS gains

$$[A] = \begin{bmatrix} -.6692 & .0168 & .7290 & -.1451 & 6.3665 & .4201 & 9.9194 \\ -.3257 & -.9614 & .1888 & -24.2262 & -2.4482 & .4202 & -.2616 \\ 8.2778 & -.0438 & -3.1383 & 2.4444 & .3048 & -8.2664 & 15.1480 \\ .7133 & .1050 & .2866 & -1.1148 & -.0722 & -.7123 & .6816 \\ -1.3627 & .1275 & -.0929 & .2010 & -.4856 & 1.3608 & 1.3831 \\ .0000 & .0000 & 1.0000 & .0000 & .0524 & .0000 & .0000 \\ .0000 & .0000 & .0000 & .0000 & .0000 & .0000 & -25.0000 \\ .0000 & .0000 & .0000 & .0000 & .0000 & .0000 & .0000 \\ .0000 & .0000 & .0000 & .0000 & .0000 & .0000 & .0000 \end{bmatrix}$$

$$[B] = \begin{bmatrix} -10.0276 & .0862 & -56.5160 \\ -.4146 & 65.3697 & .0147 \\ .0000 & .0000 & .0000 \\ .0000 & .0000 & .0000 \\ .0000 & .0000 & .0000 \\ .0000 & .0000 & .0000 \\ 25.0000 & .0000 & .0000 \\ .0000 & 25.0000 & .0000 \\ .0000 & .0000 & 25.0000 \end{bmatrix}$$

([A] continued)
$$\begin{bmatrix} -.3399 & 57.7463 \\ -67.8286 & .0332 \\ 7.0174 & -.2327 \\ 12.6879 & -.3822 \\ -.1019 & 7.2081 \\ .0000 & .0000 \\ .0000 & .0000 \\ -25.0000 & .0000 \\ .0000 & -25.0000 \end{bmatrix}$$

Figure 5.12 MIDSM OWRA linearized equations of motion

MIDSM Configuration   Nominal Configuration

Trim State Solution

α = 2.88 (deg) α = 3.20 (deg)

β = .690 β = -.283

$\delta_{elev\ right}$ = 3.89 $\delta_{elev\ right}$ = -6.38 $\Big\}$ Exceeds Trim Constraint

$\delta_{elev\ left}$ = -5.00 $\delta_{elev\ left}$ = 11.89

δ_{rudder} = -1.83 δ_{rudder} = 1.33

Configuration Variables

X_{pw} = 1.425 (ft) X_{pw} = 3.14 (ft)

X_{pf} = 34.45 (ft) X_{pf} = 37.29 (ft)

ϕ_β = -4.04 (deg) ϕ_β = 0 (deg)

dih = .0037   dih = 0

Figure 5.13 optimal trim state and configuration variables

165
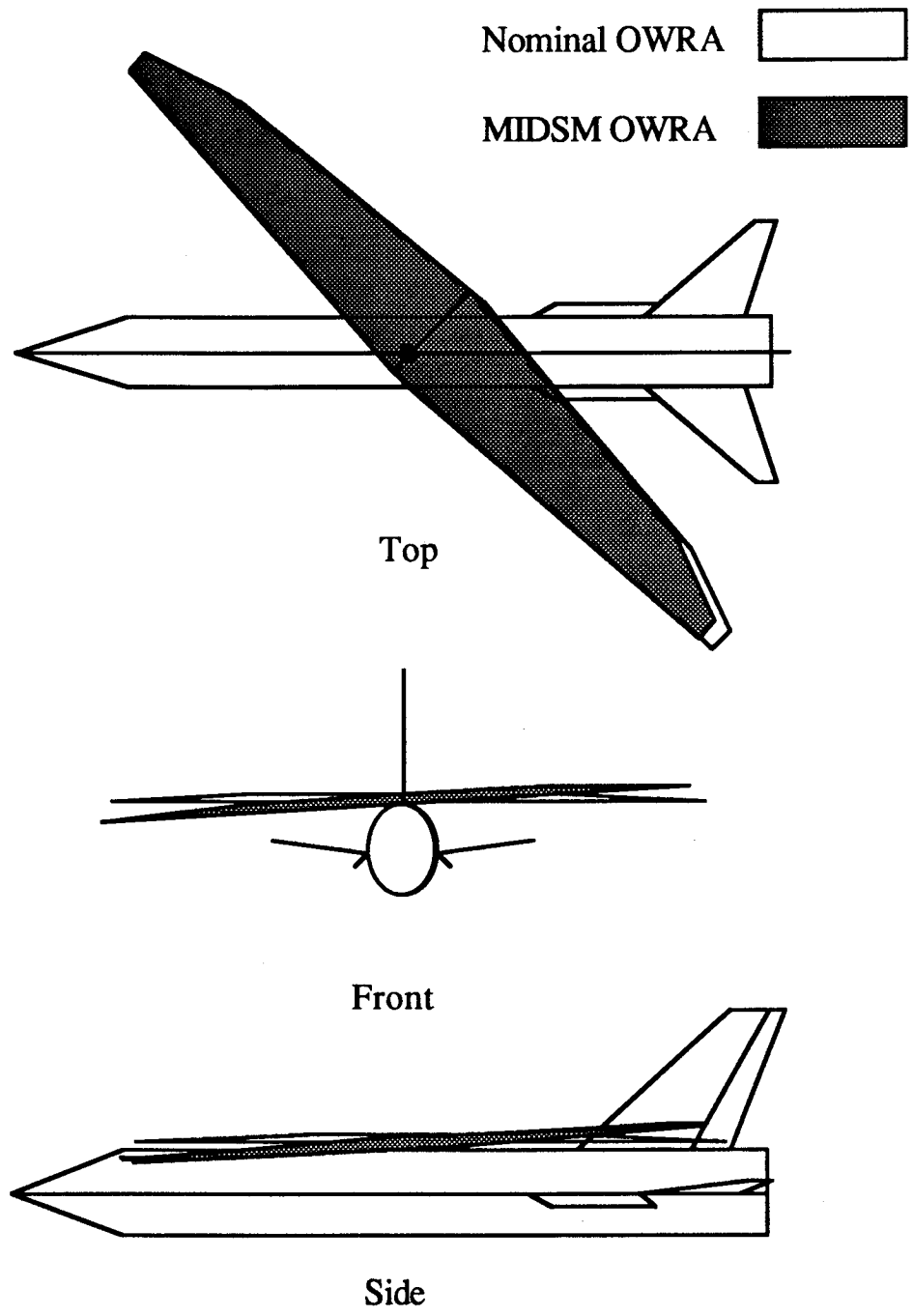
Figure 5.14 nominal and MIDSM OWRA 3-view

Lateral Acceleration vs Time

45 (deg) sweep OWRA, EMF SAS
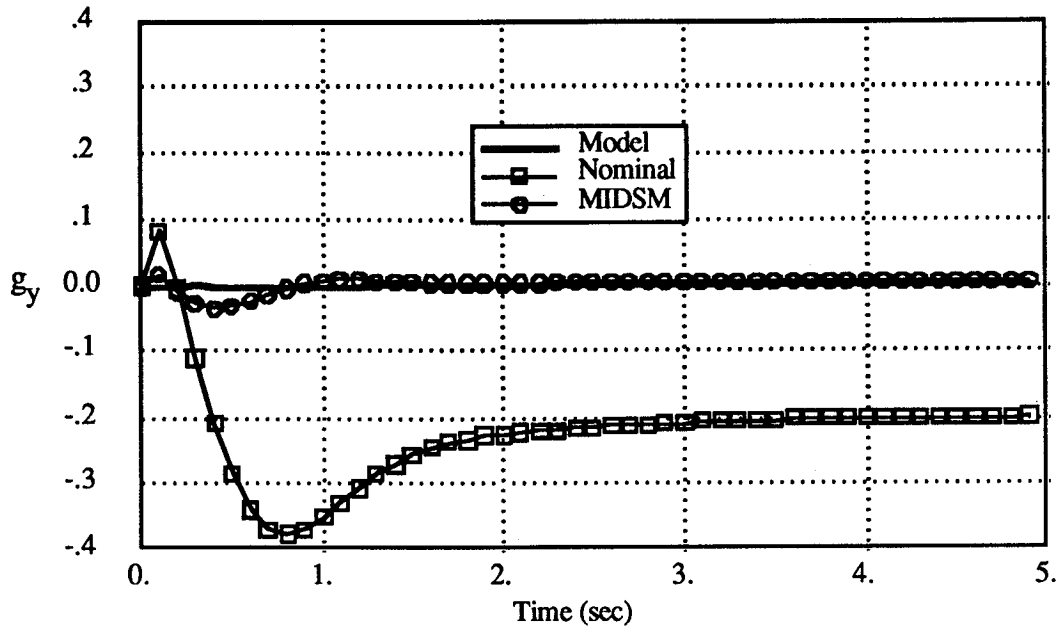
Figure 5.15 lateral acceleration vs. time

Normal Acceleration vs Time

45 (deg) sweep OWRA, EMF SAS
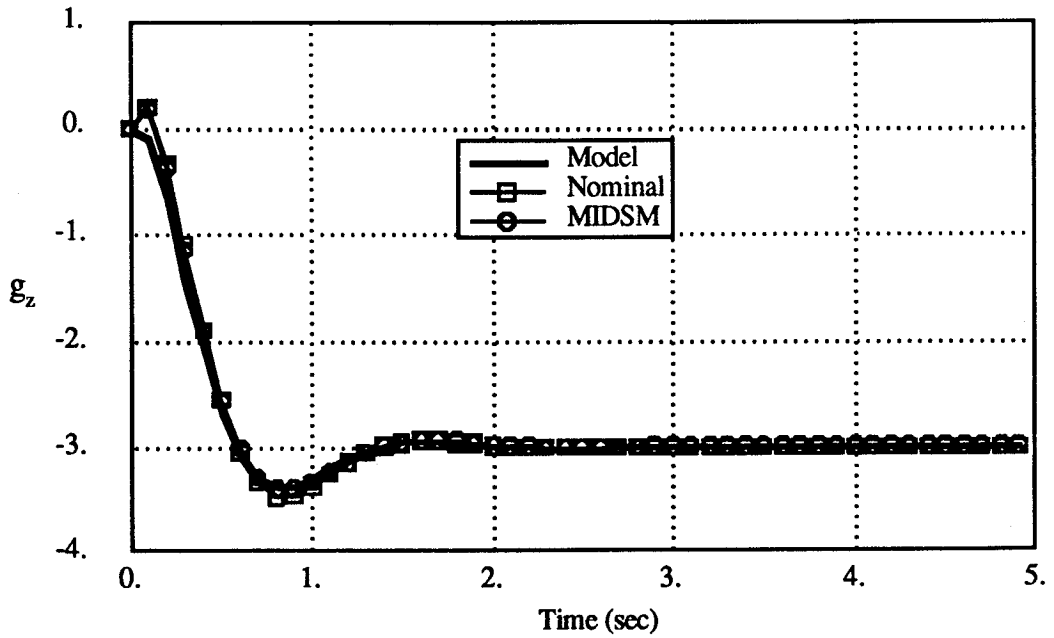
Figure 5.16 normal acceleration vs. time

167

Pitch Rate vs Time

45 (deg) sweep OWRA, EMF SAS
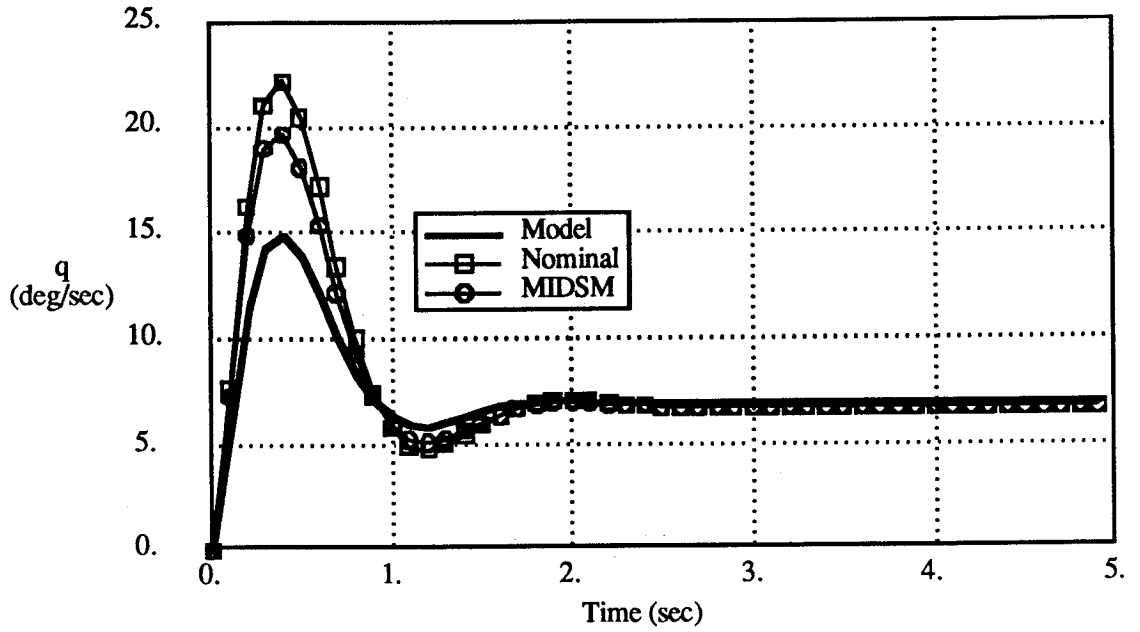
Figure 5.17 pitch rate vs. time

Yaw rate vs Time

45 (deg) sweep OWRA, EMF SAS
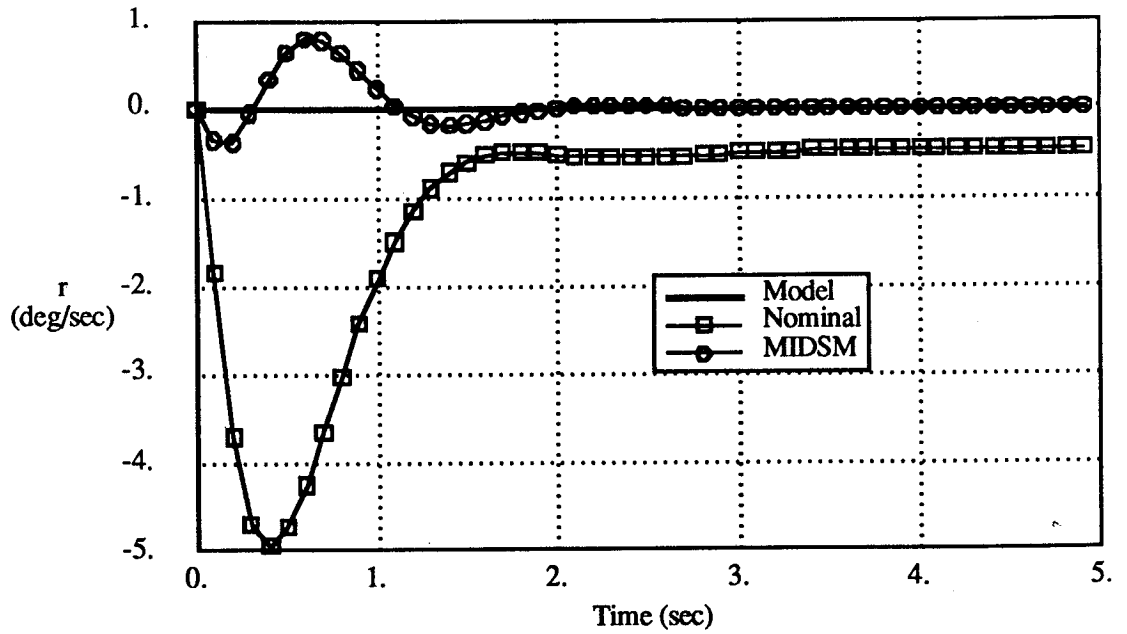
Figure 5.18 yaw rate vs. time

Roll Angle vs Time
45 (deg) sweep OWRA, EMF SAS
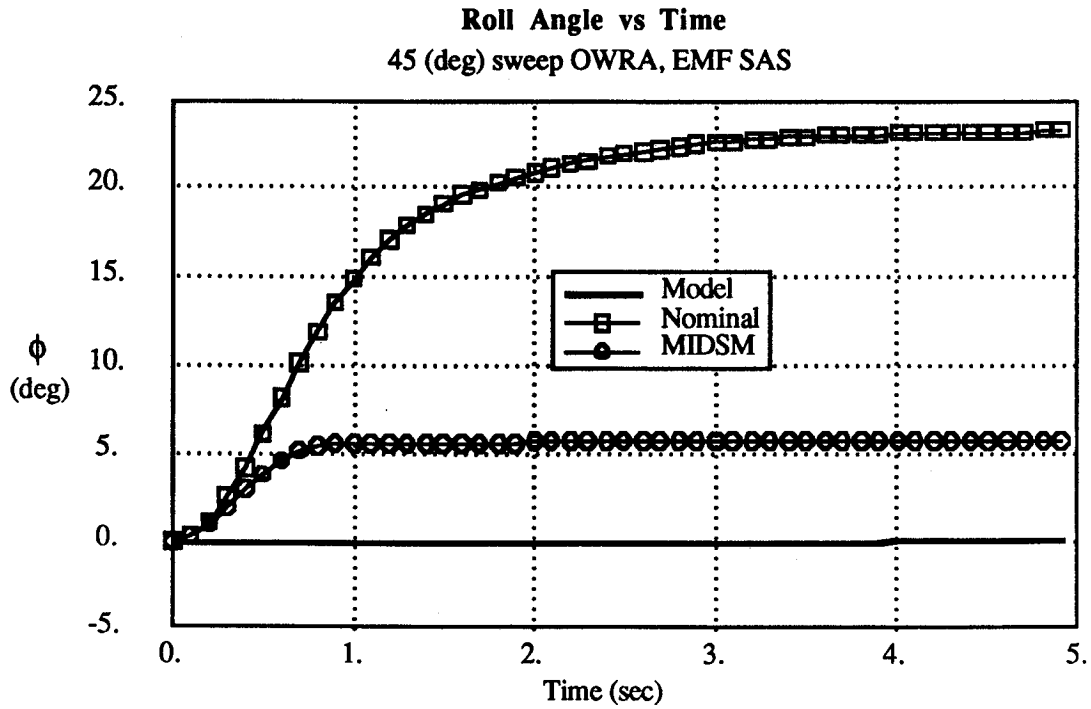
Figure 5.19 roll angle vs. time

Control Surface Deflection vs. Time
45 (deg) Sweep OWRA, EMF SAS
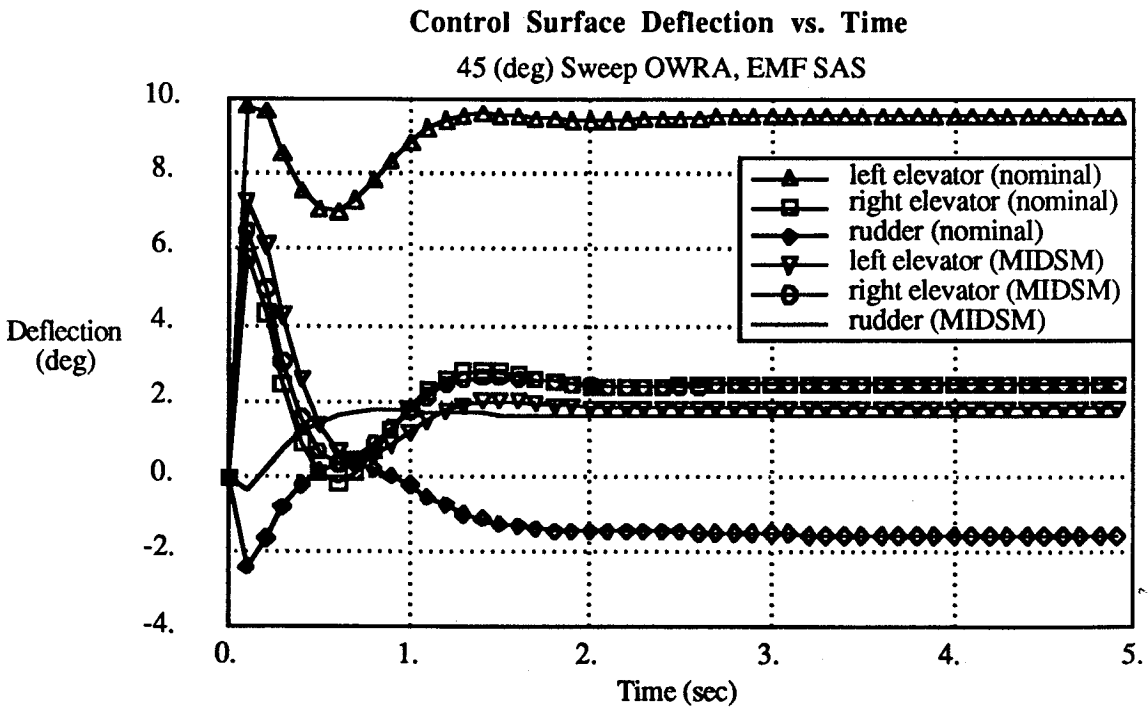
Figure 5.20 control surface deflection vs. time

169

Figure 5.20 shows that the control authority requirements for the MIDSM OWRA are less than for the nominal aircraft.

The reason for the improvement in handling qualities for the MIDSM configured OWRA lies in the values of the aerodynamic coupling terms $C_{l\alpha}$ and $C_{y\alpha}$. Table 5.5 shows the values of these stability derivatives for the two designs:

	Nominal	MIDSM	%Reduction
$C_{y\alpha}$	-.326	-.026	92 %
$C_{l\alpha}$	.0715	.004	94 %

Table 5.5 aerodynamic coupling 45° sweep OWRA

These results show that the MIDSM design has nearly zero values for the sideforce and roll coupling terms. The wing bank (-4.4°) has tilted the resultant of the wing's additional load distribution to be parallel to the x-z body axis plane, thus cancelling the sideforce change due to angle of attack. The chordwise displacement of the wing pivot shifts the wing such that more area projects over the aircraft's right side, placing the centroid of additional load-ing over the x-z plane and cancelling the pitch-roll aerodynamic coupling. The nominal configuration experiences large lateral accelerations due to the leading edge suction compo-nent acting on the unbanked wing. The lack of independent sideforce control dictates that the nominal aircraft must either roll or sideslip excessively to reduce lateral accelerations. The MIDSM configured OWRA avoids this problem by having a minimum coupling of pitch to roll and sideforce. This permits the aircraft's motion to be more easily decoupled by active control of the existing control surfaces.

The configuration changes proposed for the optimized OWRA effect all of the aerodynamic and inertia properties of the aircraft, but the main influence is on the roll and sideforce coupling terms. To further prove this idea, the time histories of lateral acceleration (g_y) and bank angle (ϕ) are plotted for the MIDSM configuration and for the nominal configuration with an EMF SAS designed for the case where $C_{l\alpha}$ and $C_{y\alpha}$ have been deliberately set to zero (Fig. 5.21 - 5.23). These results show that forcing $C_{l\alpha}$ and $C_{y\alpha}$ to zero accounts for most of the handling qualities improvement while the small nonzero values of these

170

terms in the MIDSM results compensate for the affects of inertial coupling and other aero-dynamic effects. (Notice that the MIDSM response is slightly more decoupled than the contrived nominal case).

Lateral Acceleration vs Time

Effect of Aero Coupling
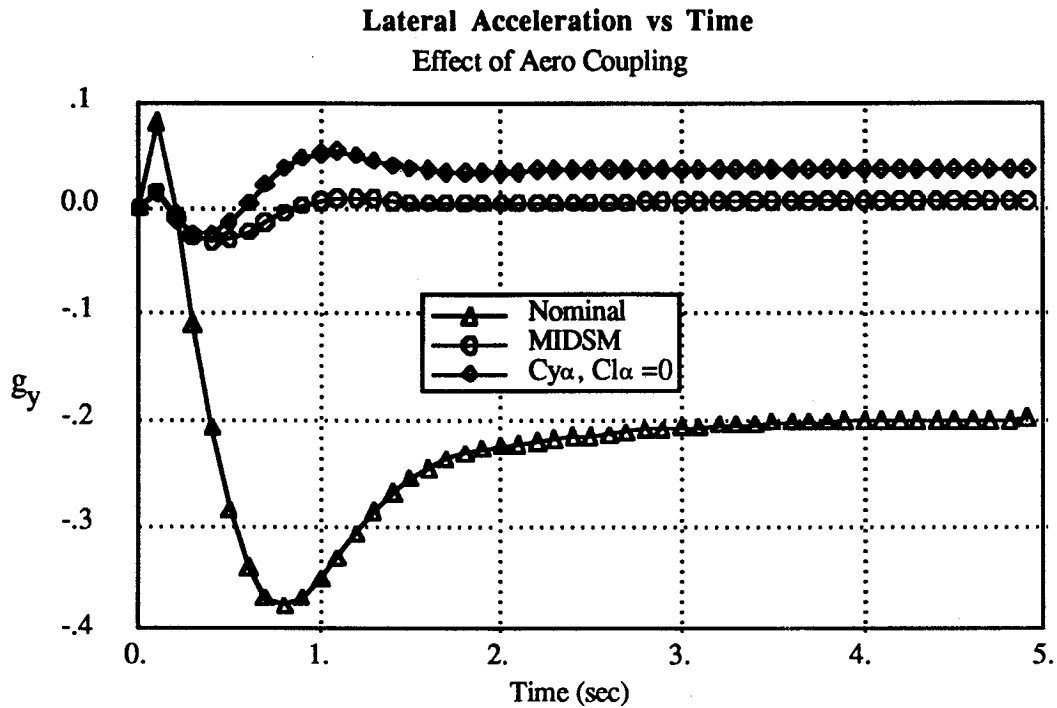
Figure 5.21 lateral acceleration vs. time

Roll Angle vs Time

Effect of Aero Coupling
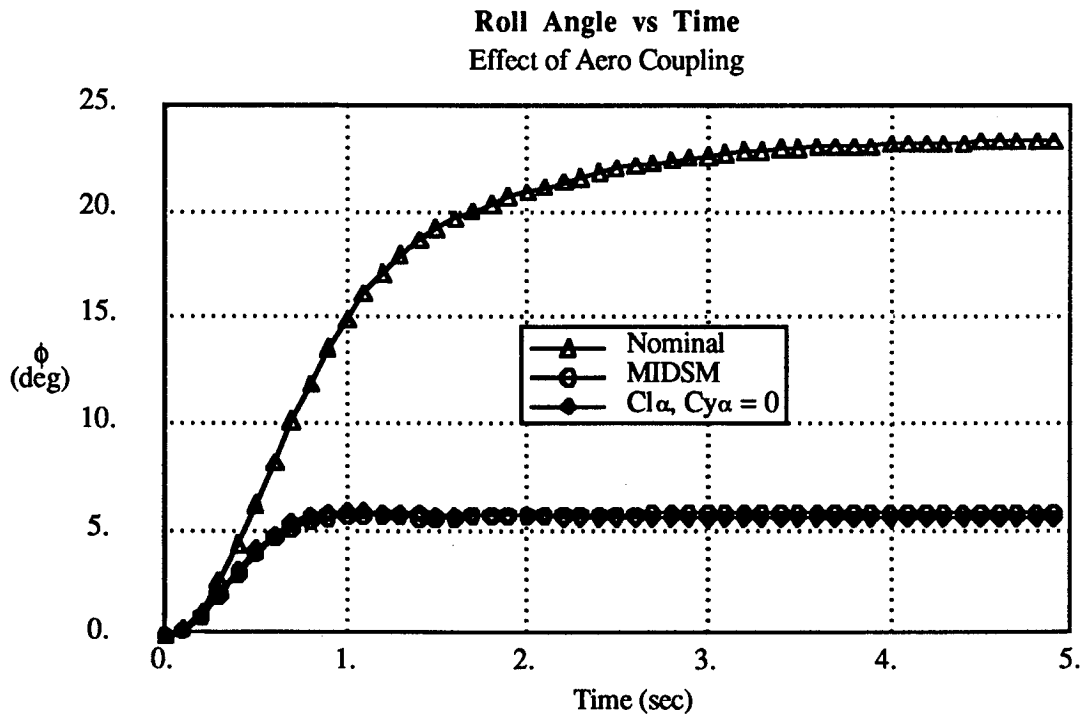
Figure 5.22 roll angle vs. time

171

Control Surface Deflection vs Time
Effect of Aero Coupling
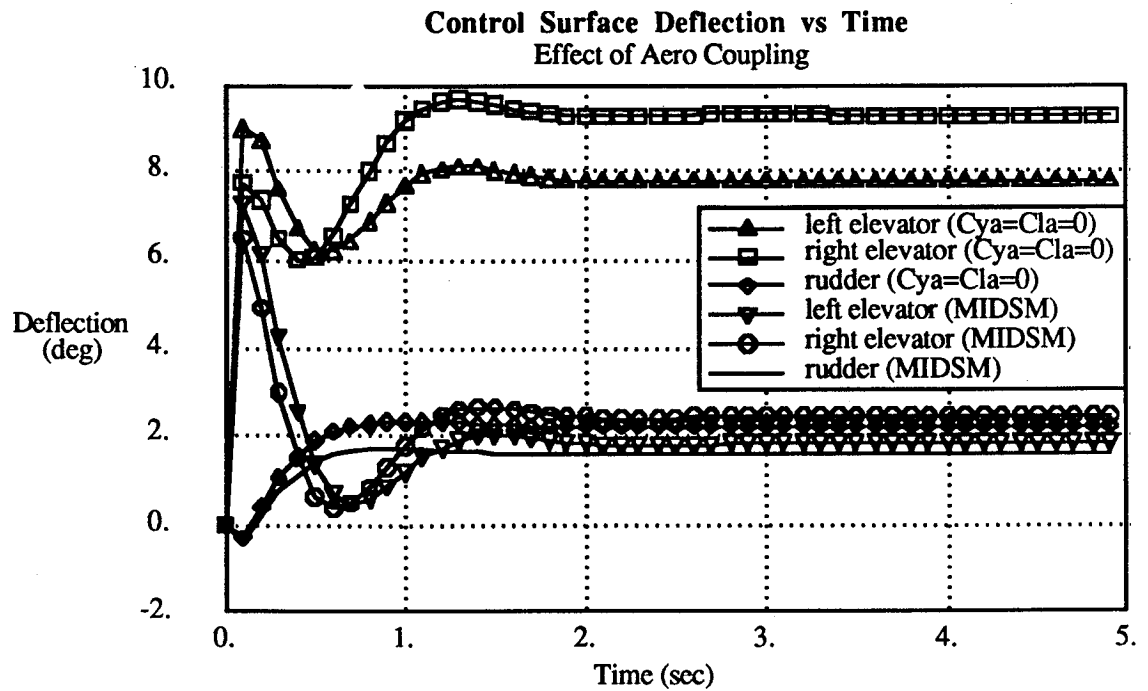
Figure 5.24 control surface deflection vs. time

Figure 5.24 shows also that the MIDSM configured OWRA is able to achieve its performance with lower control effort than the contrived nominal case.

5.2.2 MIDSM OWRA Synthesis, EMF SAS, 65° Sweep, M=1.6

The MIDSM procedure is now repeated for a flight condition corresponding to 65° wing sweep and M=1.6 (q=1180 lb/ft^2) to see if similar performance gains may be obtained in other flight regimes. The formulation of the problem is identical to the 45° sweep synthesis, excepting that the vortex lattice geometry, input weighting matrices, and initial conditions are different. Table 5.6 lists the values of these inputs.

weighting matrices

$$Q_{diag} = [\,1\ \ 1\ \ 1\ \ 0.1\ \ 0.1\ \ 1\,]$$

$$R_{diag} = [\,50\ \ 50\ \ 50\,]$$

Table 5.6 MIDSM OWRA synthesis 65° Sweep, M=1.6, EMF SAS

$$\vec{y} = [g_y, g_z, p, q, r, \phi, \delta_{mcroll}, \delta_{mcpitch}, \delta_{mcyaw}]^T$$

Initial Conditions:

step lateral gust $\qquad \vec{y}_{01} = [1\ 0\ 0\ 0\ 0\ 0\ 0\ 0\ 0]^T$

step vertical gust $\qquad \vec{y}_{02} = [0\ 1\ 0\ 0\ 0\ 0\ 0\ 0\ 0]^T$

step roll input $\qquad \vec{y}_{03} = [0\ 0\ 0\ 0\ 0\ 0\ .5\ 0\ 0]^T$

step pitch input $\qquad \vec{y}_{04} = [0\ 0\ 0\ 0\ 0\ 0\ 0\ 1\ 0]^T$

step yaw input $\qquad \vec{y}_{05} = [0\ 0\ 0\ 0\ 0\ 0\ 0\ 0\ .5]^T$

Table 5.6 (cont.) MIDSM OWRA synthesis 65° Sweep, M=1.6, EMF SAS

The initial guess configuration is once again the nominal F-8 OWRA with no wing bank and 65° wing sweep. The MIDSM synthesis was executed and converged to a solution in 50 line searches (700 objective function evaluations). Figure 5.25 shows the resulting MIDSM optimized OWRA and the nominal configuration. The displacement and banking of the wing are similar to the results obtained at 45° sweep. Table 5.7 lists the values of the optimal configuration variables.

MIDSM Configuration	Nominal Configuration

Trim State Solution

MIDSM Configuration	Nominal Configuration
α = 1.98 (deg)	α = 2.49 (deg)
β = 1.84	β = .633
$\delta_{elev\ right}$ = .8511	$\delta_{elev\ right}$ = -.925
$\delta_{elev\ left}$ = -5.00	$\delta_{elev\ left}$ = 4.02
δ_{rudder} = -3.87	δ_{rudder} = -1.82

Configuration Variables

MIDSM Configuration	Nominal Configuration
X_{pw} = 2.565 (ft)	X_{pw} = 3.14 (ft)
X_{pf} = 33.54 (ft)	X_{pf} = 37.29 (ft)
ϕ_β = -14.2 (deg)	ϕ_β = 0 (deg)
dih = .0105	dih = 0

Table 5.7 MIDSM results 65° sweep OWRA synthesis

The dynamic performance of the nominal and MIDSM configurations is compared in figures 5.26 - 5.30 for the 4-g pull-up maneuver. Once again the MIDSM design achieves significantly better dynamic decoupling than the nominal OWRA and with reduced control effort. The maximum lateral acceleration and roll angles achieved by the two cases are:

	$g_{y\,peak}$	ϕ_{peak} (deg)	r_{peak} (deg/sec)
Nominal OWRA	-0.34	8.0	1.5
MIDSM OWRA	-0.10	4.3	-0.7
% Reduction	67%	46%	53%

Table 5.8 MIDSM OWRA performance, 65° sweep EMF SAS

In the 45° sweep synthesis, improved decoupling occurred because the aerodynamic coupling terms $C_{l\alpha}$ and $C_{y\alpha}$ were minimized. This appears to not be the case for the MIDSM OWRA at 65° sweep because the value of these coupling terms is distinctly non-zero (table 5.9).

	Nominal	MIDSM	%Reduction
$C_{y\alpha}$	-.172	-.116	32 %
$C_{l\alpha}$	.016	.025	-56 %

Table 5.9 aerodynamic coupling 65° sweep OWRA

To better understand why the 65° MIDSM OWRA shows large aerodynamic coupling and the 45° case does not, a test case was studied where $C_{l\alpha}$ and $C_{y\alpha}$ were deliberately forced to zero for the nominal 65° sweep configuration with an EMF SAS. Figures 5.31 and 5.32 show the simulation results comparing the MIDSM design to this contrived nominal configuration.

Both aircraft have similar dynamic response, but the contrived nominal configuration shows slightly better dynamic coupling. The control effort, however, for the MIDSM configured design is significantly less. These results indicate that forcing $C_{l\alpha}$ and $C_{y\alpha}$ to zero will significantly decouple the OWRA's response, but the MIDSM method has found a de-

174

MIDSM

Top

Nominal

MIDSM

Nominal

Front

MIDSM

Nominal

Side
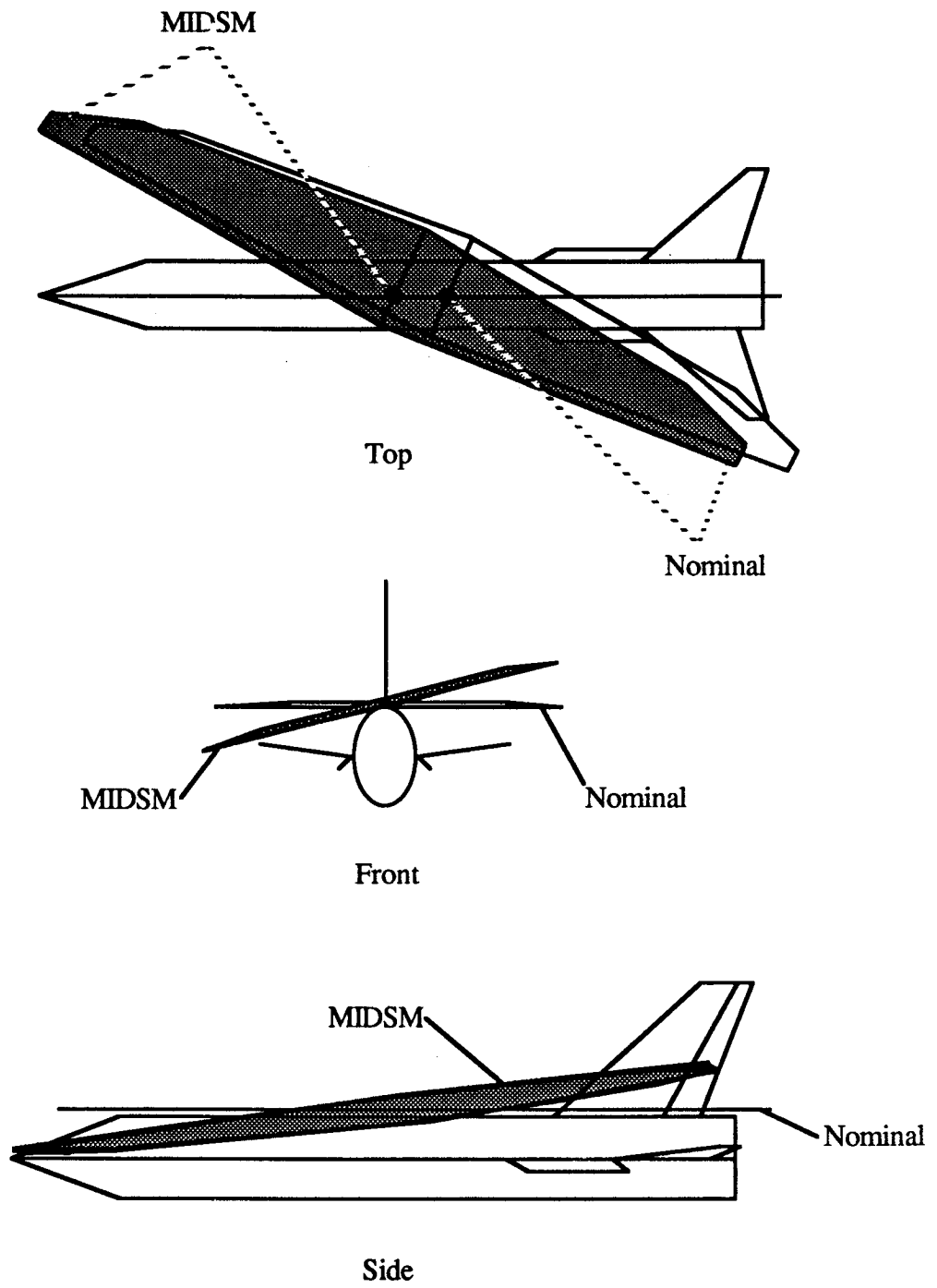
Figure 5.25 MIDSM optimal OWRA configuration, 65° sweep, EMF SAS

Lateral Acceleration vs Time
65° sweep OWRA, EMF SAS
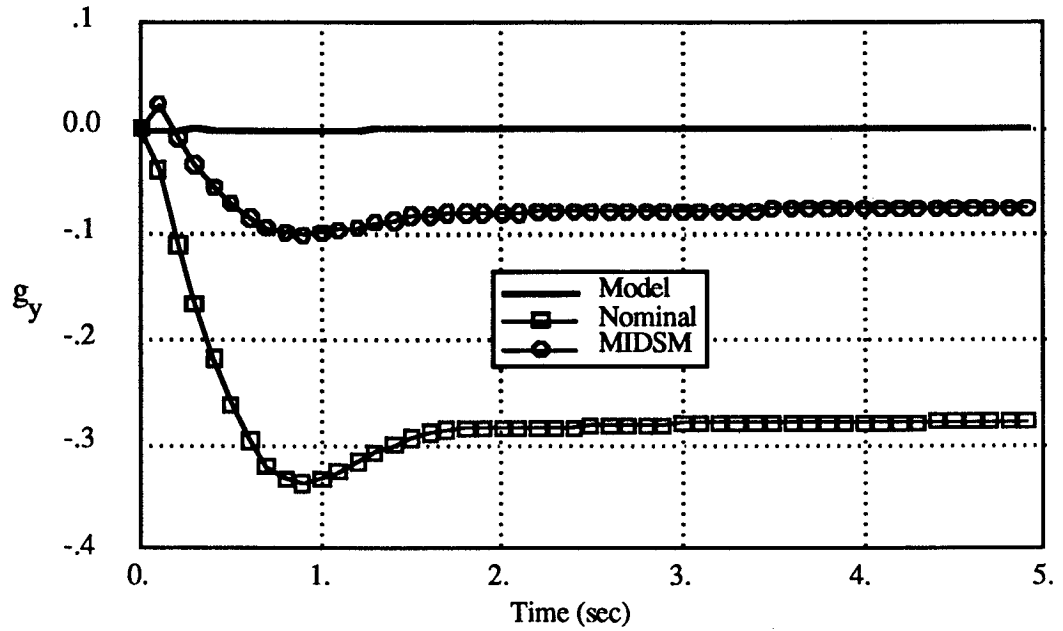
Figure 5.26 lateral acceleration vs. time

Normal Acceleration vs Time
65° Sweep OWRA, EMF SAS
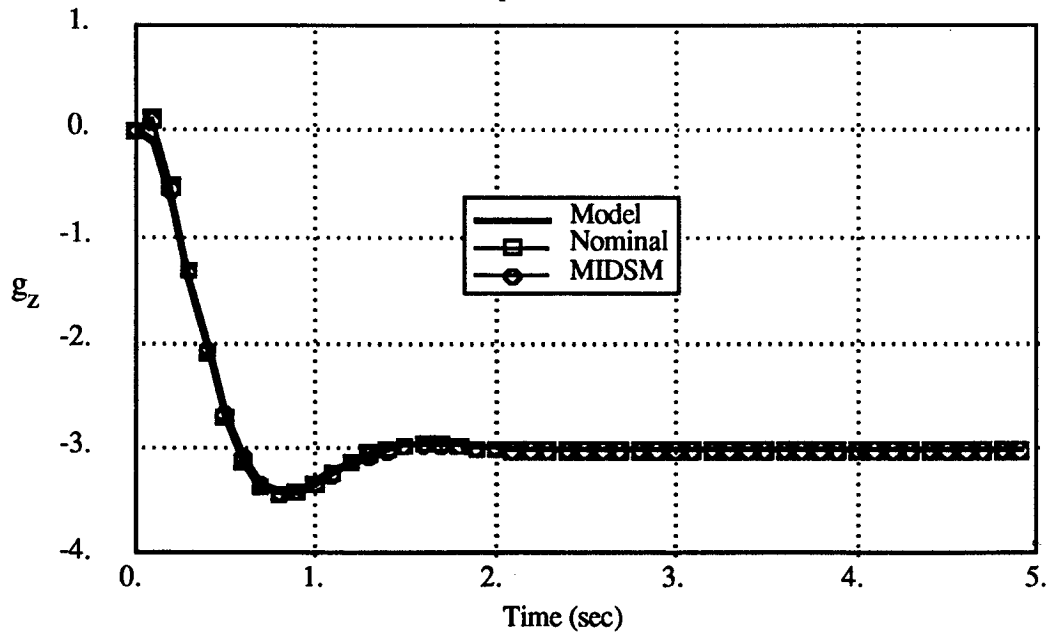
Figure 5.27 normal acceleration vs. time

176

Yaw Rate vs Time

65° sweep OWRA, EMF SAS
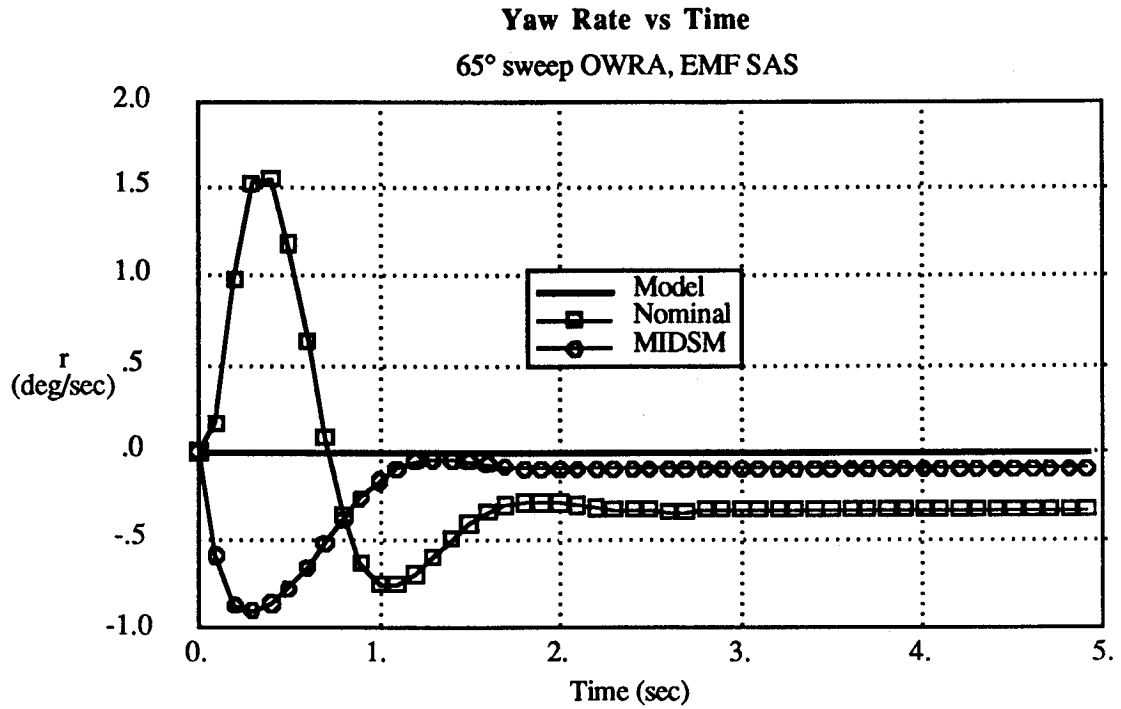
Figure 5.28 yaw rate vs. time

Roll Angle vs Time

65° sweep OWRA, EMF SAS
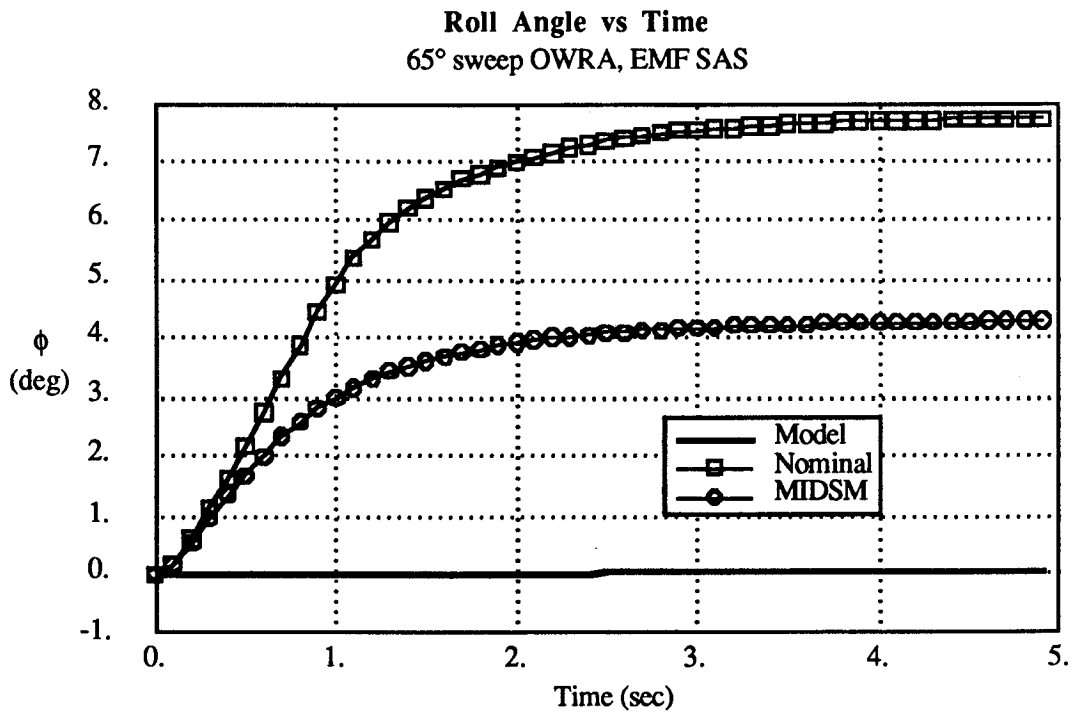
Figure 5.29 roll angle vs. time

177

Control Deflection vs Time
65° Sweep OWRA, EMF SAS
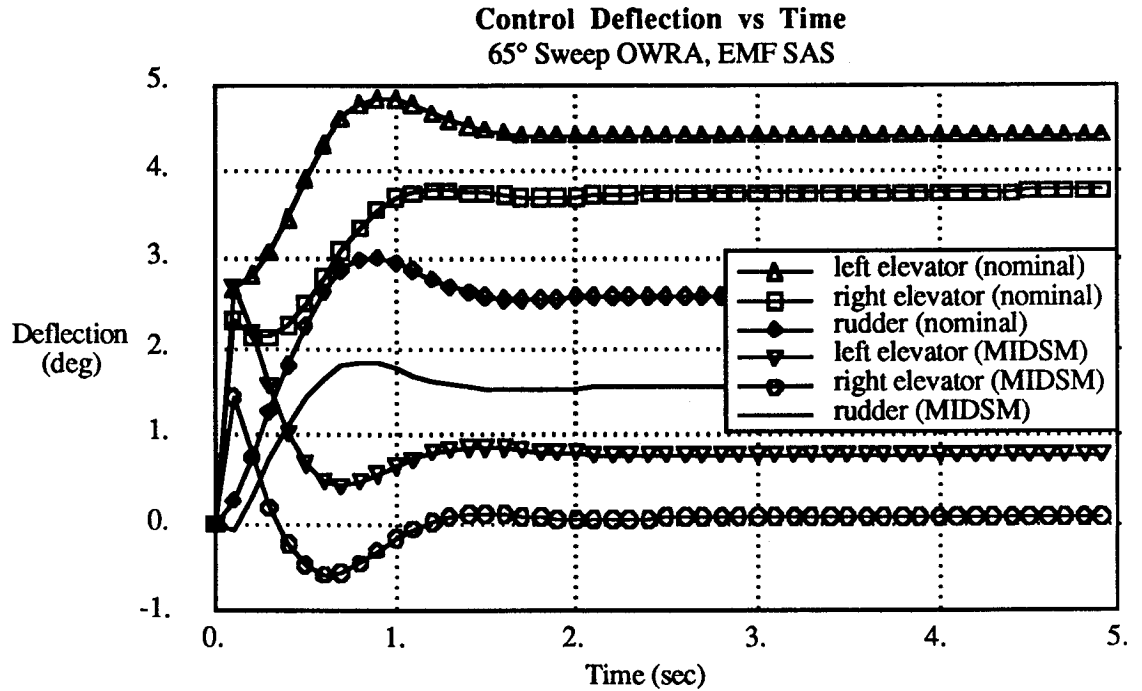
Figure 5.30 control surface deflection vs. time

sign with nearly as great decoupling and significantly lower control effort where $C_{l\alpha}$ and $C_{y\alpha}$ are nonzero. The explanation as to why the MIDSM design strives to minimize control effort at the expense of improved dynamic decoupling can be found in the large values of the weighting matrix [R]. As was noted in chapter 3, the EMF SAS favors higher bandwidth control in the feedback path, and therefore large control effort weighting is required to enforce an actuator bandwidth restriction (5 Hz in this example). For the 65° sweep flight condition, [R] must be substantially greater than at 45° sweep to meet the actuator bandwidth limit of 5 Hz. As a result, the total dynamic cost consists largely of control effort cost and MIDSM minimizes this more than the dynamic coupling. The MIDSM design actually has lower dynamic cost than the nominal design with $C_{l\alpha}$ and $C_{y\alpha}$ set to zero because of its lower control activity (see table 5.10).

$$J_d = \begin{array}{|c|c|} \hline \text{MIDSM} & Cl\alpha, Cy\alpha = 0 \\ \hline 25.47 & 29.29 \\ \hline \end{array}$$

13% Lower

Table 5.10 effect of aero-coupling on dynamic cost, 65° sweep OWRA

178

Lateral Acceleration vs Time
65° sweep OWRA, EMF SAS
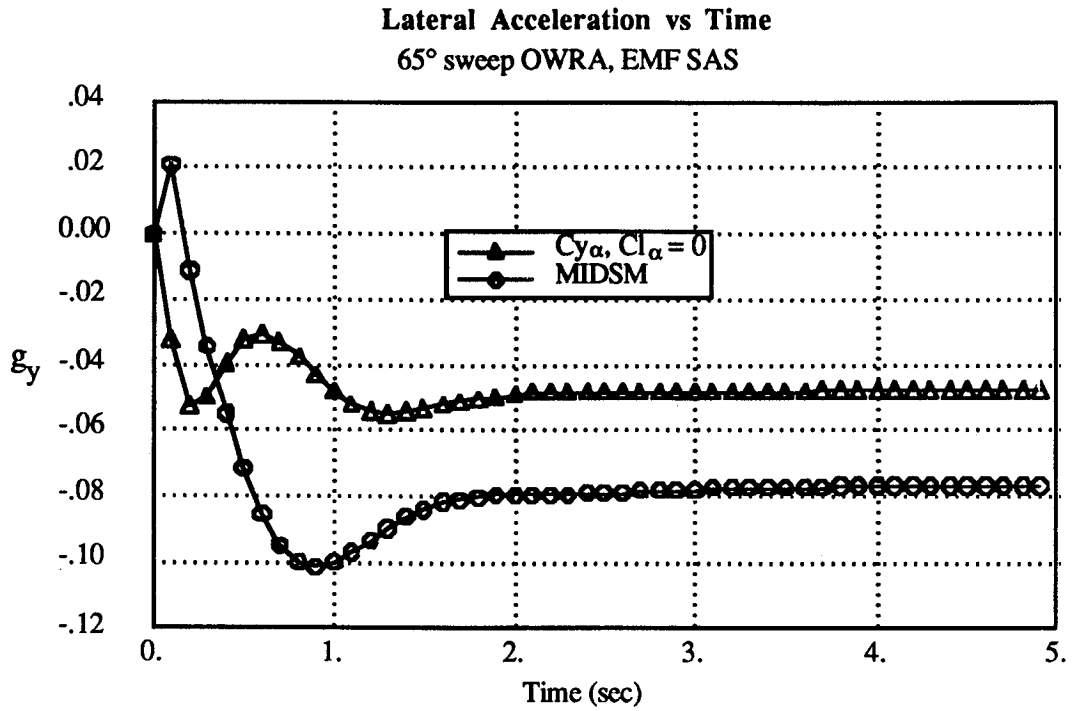
Figure 5.31 effect of aerodynamic coupling on handling qualities
lateral acceleration vs. time

Roll Angle vs Time
65° sweep OWRA, EMF SAS
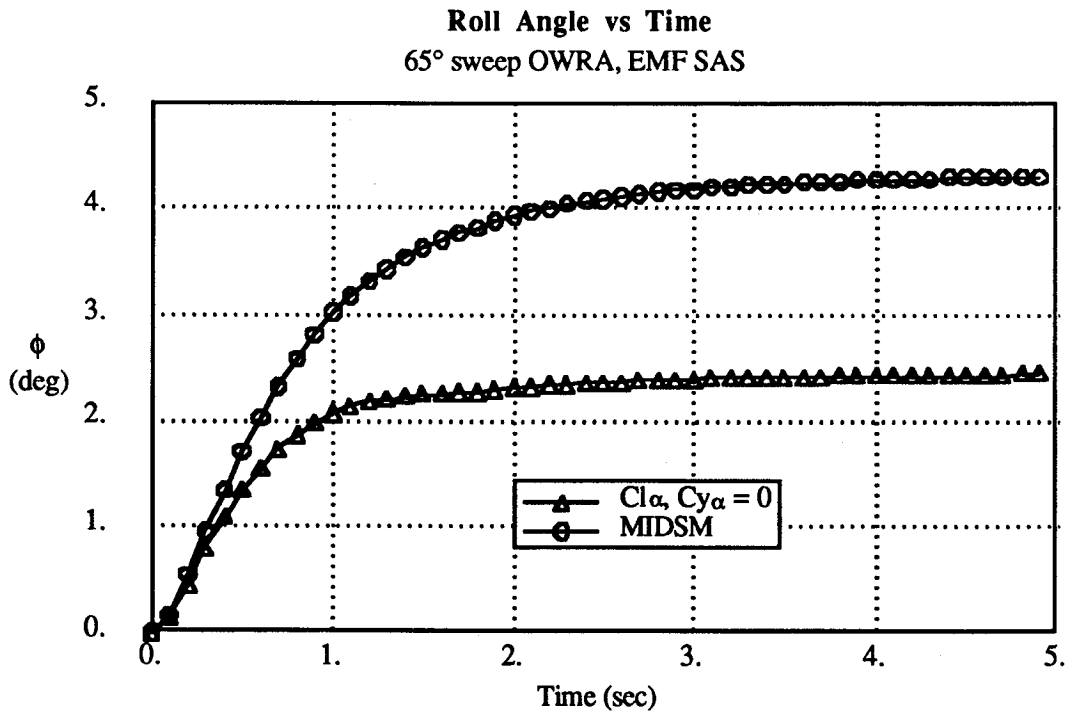
Figure 5.32 effect of aerodynamic coupling on handling qualities
roll angle vs. time

MIDSM has accurately identified the extra weighting placed on control activity and has found a configuration with highly decoupled response that uses very little control effort. Because it is impossible to distinguish between control effort due to large deflections and that due to large frequency of motion in the LQR cost function, the designer is forced to place excessive weight on control activity to enforce bandwidth constraints. When the SAS architecture is switched to the RMF SAS, this problem is avoided because the actuator states are not fed-back, and therefore their bandwidth remains unchanged for any value of [Q] and [R]. It is reasonable to suspect that the 65° sweep MIDSM results are more a function of the assumed SAS architecture (than is the case for the 45° sweep results) because of their strong dependence on control effort weighting.

5.2.3 MIDSM OWRA Synthesis at Multiple Flight Conditions with EMF SAS

In the two previous examples the F-8 OWRA was re-configured for improved handling qualities at 45 and 65° sweep. Unfortunately, the configuration changes required at these flight conditions are not identical, which implies that a configuration optimized for one flight condition will not be optimal at others. It is possible, however, to synthesize a single aircraft with improved performance over a wide range of flight conditions by incorporating the dynamic cost at several flight conditions into the total cost. This idea is similar to the method proposed by Ly [Ref. 24] for the synthesis of robust controllers for linear systems with plant model uncertainties. Ly's method synthesizes a single controller which must improve the response of not only the nominal plant, but also plant models perturbed to reflect plant uncertainties. This idea is extended to the oblique wing synthesis, where a single aircraft must perform well over a range of flight conditions. The example presented here configures the OWRA for improved handling at two flight conditions. New EMF SAS gains are calculated at each flight condition and gain scheduling is assumed to be used for transitioning between flight regimes. This basic technique can be extended to account for the influence of changing wing sweep, nonlinearity of the aerodynamic loads, influence of changing dynamic pressure, etc. on the optimal OWRA configuration.

The two flight conditions considered are described below.

<div align="center">

Multiple Flight Condition OWRA Synthesis

Flight Conditions Considered

</div>

Flight Condition	Sweep	Mach	Dynamic Pressure (lb/ft^2)
1	45	0.8	440
2	65	1.6	1180

An optimal EMF SAS is synthesized at each flight condition using [Q] and [R] matrices appropriate for each wing sweep. Penalty function constraints are implemented to enforce aircraft trim in 1-g level flight at both flight conditions. The total cost function for the multiple flight condition synthesis (MFC) is:

$$J_{tot} = J_{d\,45} + J_{d\,65} + P.F._{trim\,45} + P.F._{trim\,65} + P.F._{design\,var's}$$

This formulation of the total cost weights each flight condition equally, but if the mission requirements invalidate this assumption, weighting factors may be included to reflect the relative importance of each flight mode. Figure 5.33 is a flowchart of the MIDSM MFC design procedure. The synthesis is nearly identical to the SFC cases previously described, except that the dynamic cost must now be evaluated at more than one flight condition.

In the single flight condition synthesis the wing pivot axis orientation was defined in terms of a single variable, ϕ_b, the wing bank angle at a fixed wing sweep. The variable, ϕ_b, has no meaning for the multiple flight condition synthesis because it is impossible to find a single pivot axis orientation which will produce arbitrary wing bank at a specified sweep angle with zero wing incidence. Therefore, the design variables θ_1 and θ_2 are included explicitly in the MFC synthesis.

The MFC synthesis assumes the nominal OWRA configuration for the initial configuration guess. Table 5.12 lists the input parameters used in the synthesis. The optimizer converged to a final solution after 47 line searches (756 objective function evaluations). The resulting optimized configuration variables are:

<div align="center">

$X_{pw} = 2.01$ (ft) $\theta_1 = -1.826$ (deg)

$X_{pf} = 34.80$ (ft) $\theta_2 = -6.138$ (deg)

Dihedral $= .0058$

</div>

Table 5.11 MIDSM OWRA optimal design variables, multiple flight condition case

<div align="center">

181

</div>

45 (deg) Sweep	65 (deg) Sweep

$$Q_{diag} = [\,1 \ \ 1 \ \ 1 \ \ 0.1 \ \ 1 \ \ 1\,] \qquad Q_{diag} = [\,1 \ \ 1 \ \ 1 \ \ 0.1 \ \ 0.1 \ \ 1\,]$$

$$R_{diag} = [\,30 \ \ 30 \ \ 30\,] \qquad\qquad R_{diag} = [\,50 \ \ 50 \ \ 50\,]$$

Plant Excitation for MIDSM Design
(assumed for all flight conditions)

$$y = [g_y, \ g_z, \ p, \ q, \ r, \ \phi, \ \delta_{mcroll}, \ \delta_{mcpitch}, \ \delta_{mcyaw}]^T$$

Initial Conditions:

step lateral gust $\qquad y_{01} = [\,1\ 0\ 0\ 0\ 0\ 0\ 0\ 0\ 0\,]^T$

step vertical gust $\qquad y_{02} = [\,0\ 1\ 0\ 0\ 0\ 0\ 0\ 0\ 0\,]^T$

step roll input $\qquad y_{03} = [\,0\ 0\ 0\ 0\ 0\ 0.5\ 0\ 0\,]^T$

step pitch input $\qquad y_{04} = [\,0\ 0\ 0\ 0\ 0\ 0\ 0\ 1\ 0\,]^T$

step yaw input $\qquad y_{05} = [\,0\ 0\ 0\ 0\ 0\ 0\ 0\ 0\ .5\,]^T$

Configuration Design Variables Initial Guess
(Nominal OWRA Config.)

$$X_{pf} = 37.292 \ (ft)$$

$$X_{pw} = 3.1392 \ (ft)$$

$$\theta_1 = 0.0 \ (deg)$$

$$\theta_2 = 0.0 \ (deg)$$

Dihedral $= 0.0$

Table 5.12 multiple flight condition MIDSM inputs
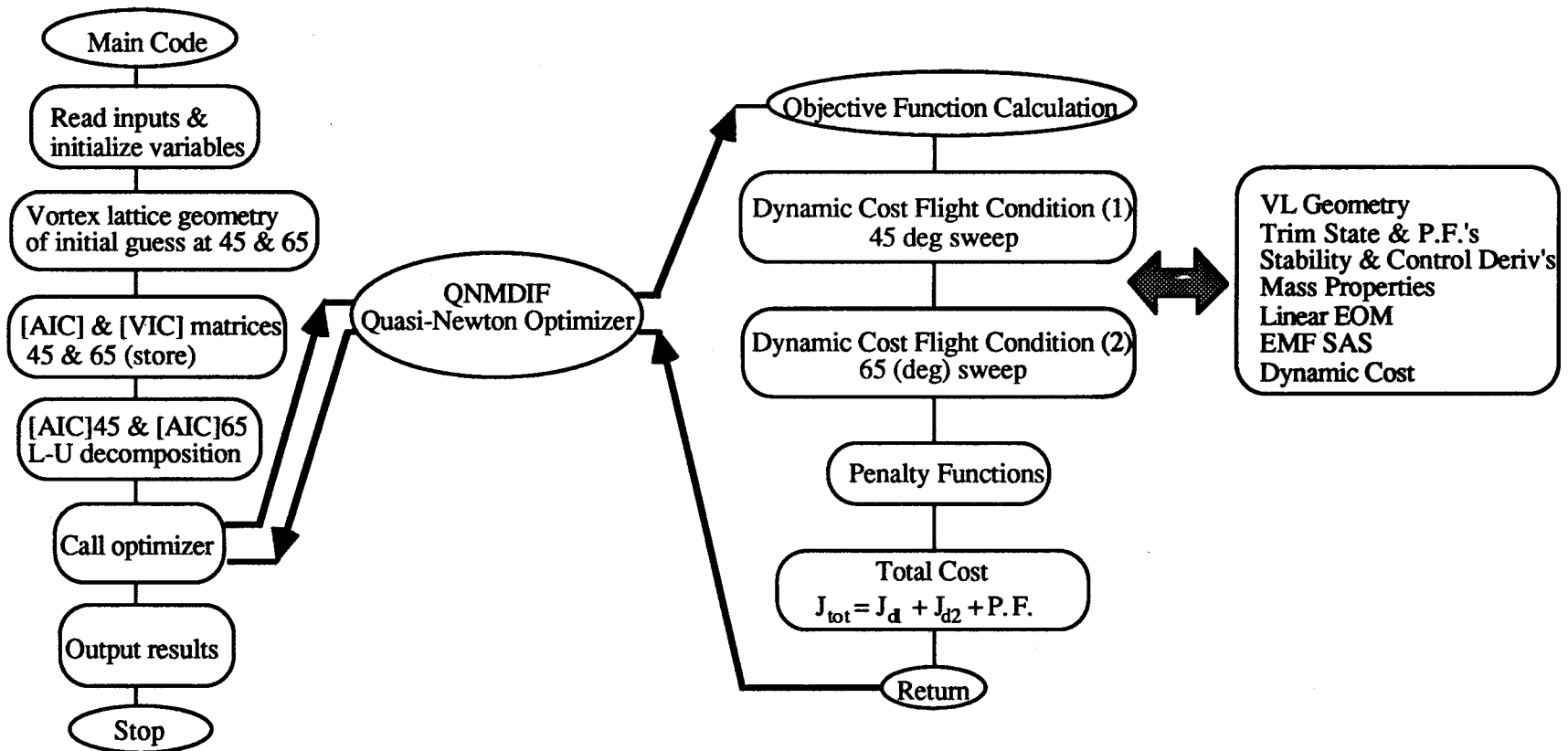
Figure 5.33 multiple flight condition synthesis flowchart, EMF SAS

Figures 5.34 and 5.35 show the nominal and optimized OWRA configurations in 3-view. For both flight conditions the MIDSM design has its wing banked right wing low and the wing is shifted to the aircraft's right side. This is the same trend displayed in the single flight condition synthesis results. The aircraft satisfies the trim constraints at both flight conditions even though the nominal configuration does not. Figures 5.36 - 5.40 are time histories of the various OWRA configurations performing the 4-g pitch-up maneuver. Results from the single flight condition syntheses are also shown for comparison. These results show that the dynamic performance of the MIDSM OWRA is markedly improved over that of the nominal configuration at both flight conditions. The peak lateral acceleration and roll angle are listed in table 5.13 for the various cases.

		MIDSM-MFC	Nominal	% Reduction
45 (deg) Sweep	$g_{y\ peak}$	-.07	-.38	82 %
	ϕ_{peak}	12 (deg)	23 (deg)	48 %
65 (deg) Sweep	$g_{y\ peak}$	-.04	-.33	88 %
	ϕ_{peak}	1.5 (deg)	7.8 (deg)	81 %

Table 5.13 OWRA performance, MIDSM multiple flight condition results
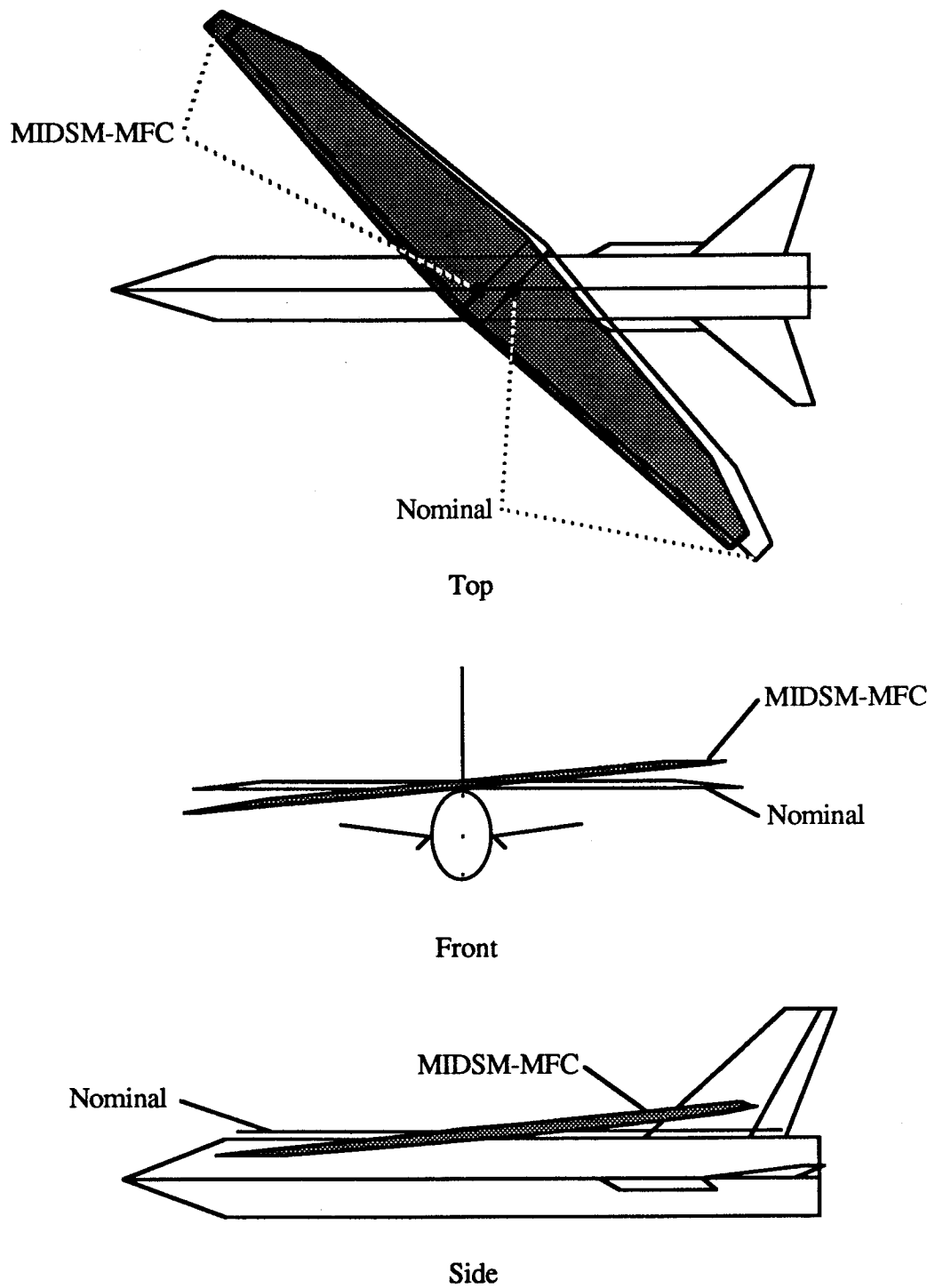
184

Figure 5.34 MIDSM-MFC results, OWRA configuration with 45° sweep

185

Top

Front

Side
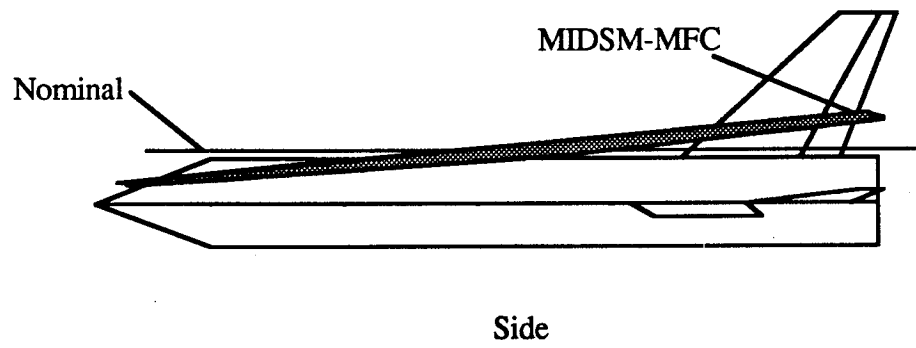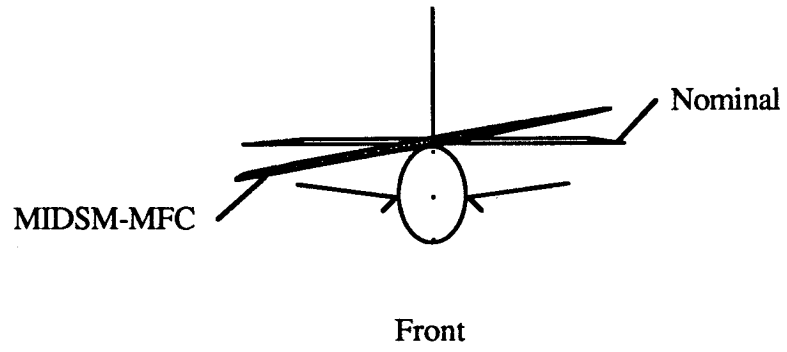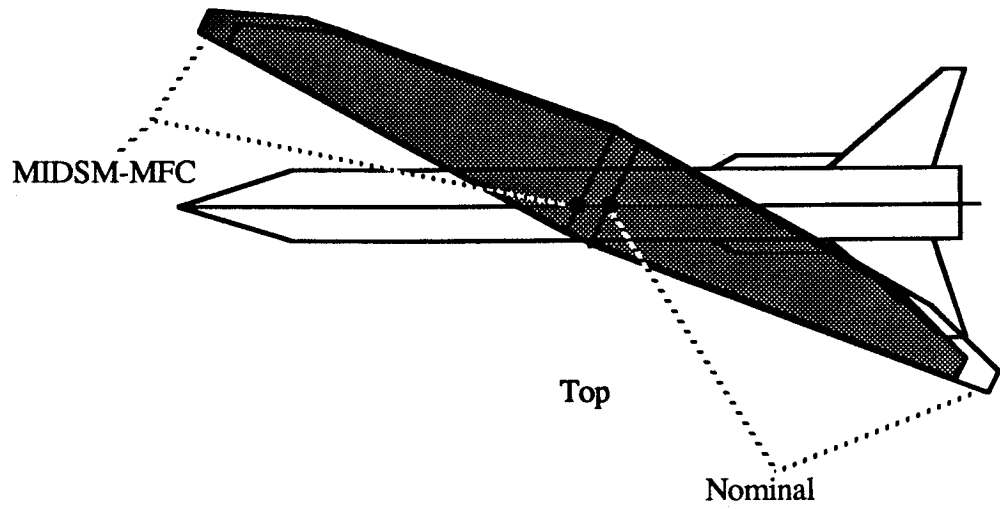
Table 5.35 MIDSM-MFC results, OWRA configuration with 65° sweep

Lateral Acceleration vs Time
45° Sweep OWRA, EMF SAS
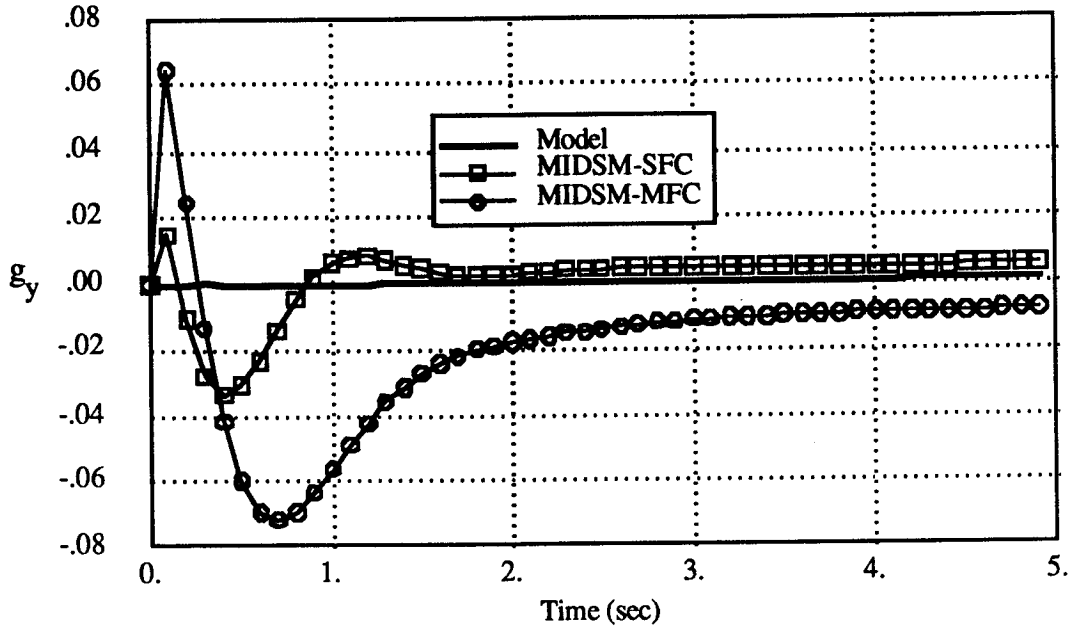
Figure 5.36   lateral acceleration vs. time

Roll Angle vs Time
45° Sweep OWRA, EMF SAS
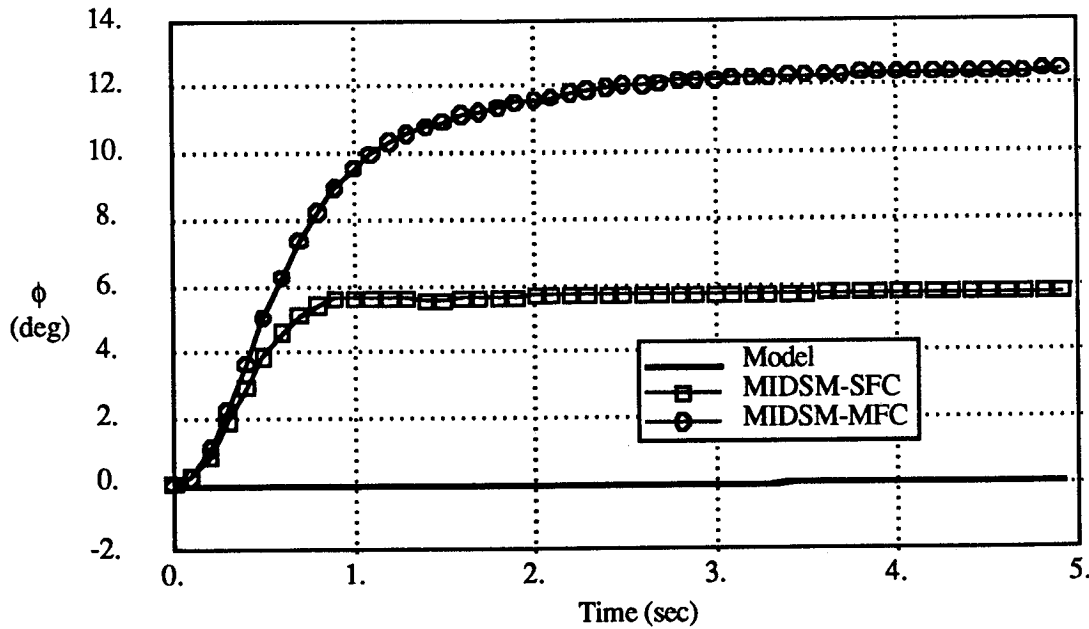
Figure 5.37 roll angle vs. time

187

Lateral Acceleration vs Time
65° Sweep OWRA, EMF SAS
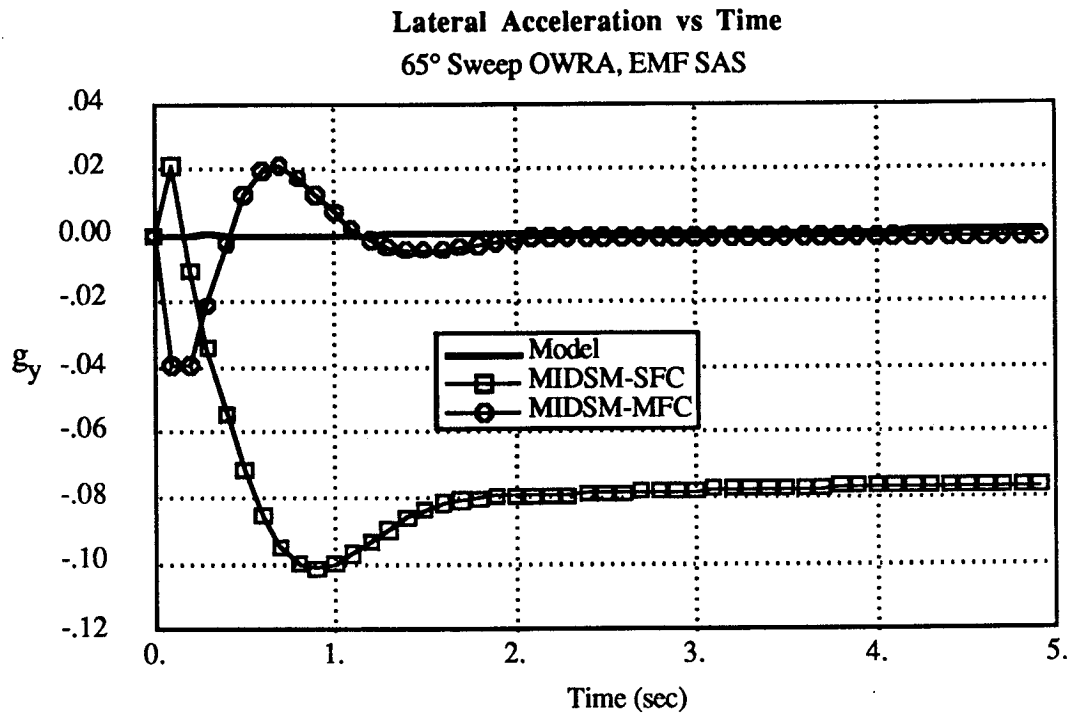
Figure 5.38 lateral acceleration vs. time

Roll Angle vs Time
65° Sweep OWRA, EMF SAS
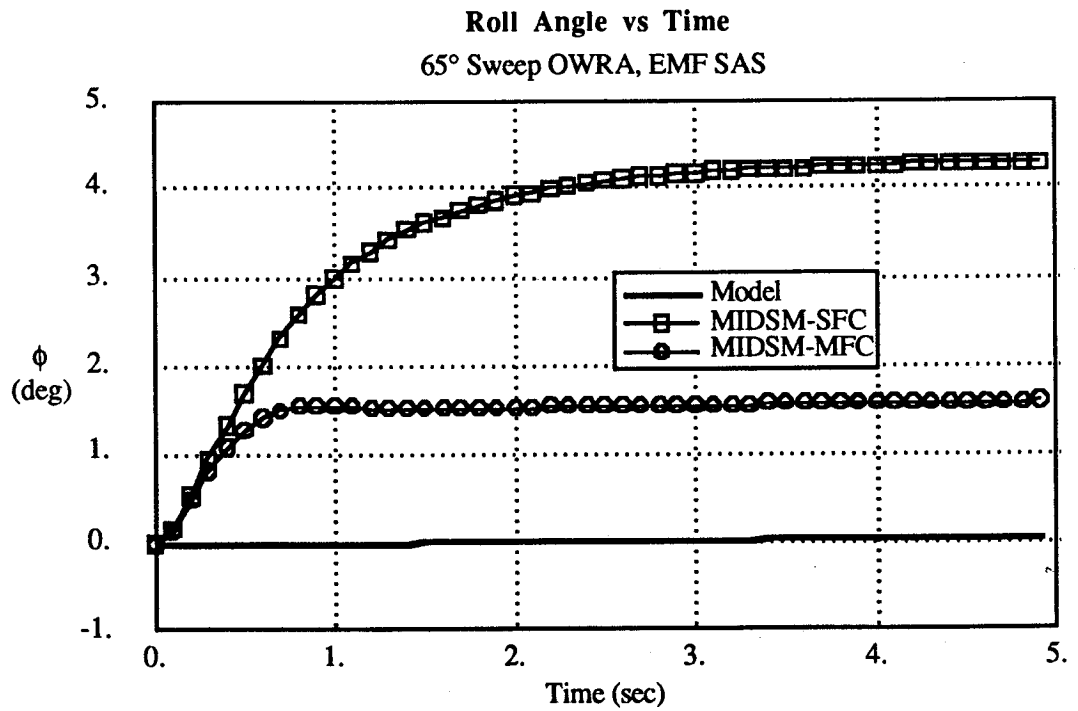
Figure 5.39 roll angle vs. time

Control Surface Deflection vs Time
65° Sweep OWRA, EMF SAS
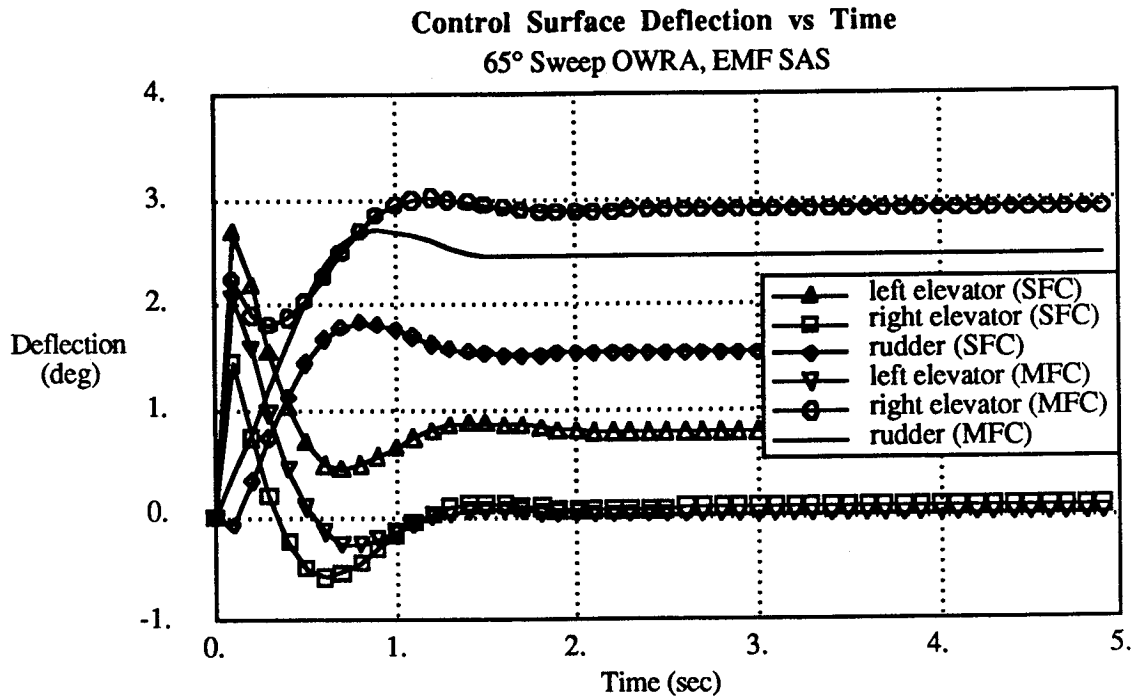
Figure 5.40 control surface deflection vs. time

Figures 5.36 - 5.37 show that at the 45° sweep flight condition the lateral acceleration and roll angle excursions for the OWRA optimized at multiple flight conditions are greater than the SFC optimized OWRA. This result is to be expected, because the MFC design represents a compromise design at any single flight condition. The dynamic response of the MFC OWRA at the 65° sweep flight condition shows lower peak lateral acceleration and roll angle than the SFC result. At first these results seem incorrect, because the SFC design should have superior dynamic response. A more careful examination of the results shows that the dynamic cost is indeed lower for the SFC OWRA, but most of the cost reduction comes from reduced control effort and not reduced peak lateral acceleration and roll angle. This idea is confirmed by figure 5.40 which shows that the MFC OWRA requires more control deflection to achieve its performance than the SFC design. The significant influence of control effort on dynamic cost at the 65° sweep flight condition is once again due to the EMF SAS architecture which desires excessive bandwidth in the feedback path. Changing the SAS to RMF will permit the synthesis of designs with acceptable actuator bandwidth without resorting to excessive control effort weight.

The results of this synthesis show that it is possible to improve the F-8 OWRA's handling

189

qualities significantly over a wide range of flight conditions by re-configuring the aircraft. The required configuration changes are small enough that aircraft drag and structural weight will not be seriously affected. The resulting optimized OWRA is more easily trimmed over the flight envelope and has approximately 1/10 the lateral acceleration response and 1/2 to 1/3 the roll angle excursion during abrupt pitch maneuvers, as the originally proposed F-8 OWRA configuration.

5.2.4 MIDSM OWRA Synthesis, RMF SAS, 45° Sweep, M=0.8

In chapter 3 the reduced order model following (RMF) SAS was shown to have several advantages over the EMF SAS architecture. Because the RMF controller does not require full-state feedback, it is possible to enforce actuator bandwidth constraints by not including the actuator states in the feedback path. Furthermore, the RMF SAS attempts to drive the closed loop plant's unforced response to that of the model's without excessive bandwidth requirements. These features make the RMF SAS a logical choice for a controller that is more practical and well suited for oblique wing aircraft than the EMF SAS. The previous MIDSM synthesis examples have shown how significant improvement in handling qualities may be obtained by simultaneously re-configuring the F-8 OWRA and its SAS. In this example the MIDSM method will be used to perform the same task except that an RMF SAS will be implemented instead of an EMF SAS. This example will also show if the MIDSM OWRA configuration is sensitive to the SAS architecture for the case studied.

The integrated synthesis with an RMF SAS requires a slightly different formulation of the objective function than was used in the previous examples. The RMF synthesis requires that the SAS gains be computed explicitly by the optimizer. The biggest disadvantage of this approach is the increased computational burden when compared to full-state feedback schemes which solve for all of the gains in a single ARE. Dynamic stability constraints must be enforced explicitly in the RMF synthesis, otherwise the solution for the dynamic cost may become unbounded. The total cost for SFC RMF synthesis is given by:

$$J_{tot} = J_d + P.F._{trim} + P.F._{design\ var's} + P.F._{stability}$$

The penalty functions for trim and limits on the design variables are identical to those pre-

sented in the EMF MIDSM examples. The penalty function for dynamic stability is given in chapter 3 by equation 3.68. Figure 5.41 is a flowchart of the RMF synthesis method which shows how the control gains are solved for explicitly by the optimizer.

The integrated design synthesis is carried out for the nominal OWRA configuration at 45° sweep, M=0.8 flight condition. The values of the initial guess variables are identical to those used in the EMF SAS example, except for the following parameters:

$$Q_{diag} = [\, 10 \;\; 5 \;\; 1 \;\; 1 \;\; 1 \;\; 10 \,]$$

$$R_{diag} = [\, 100 \;\; 100 \;\; 100 \,]$$

Actuator pole: $s = -10.0 \pm 0.0\, j$ (rad/sec)
(1.6 Hz Bandwidth Actuator)

MIDSM inputs single flight condition, RMF SAS , 45° sweep

Notice that the actuators are modelled as 1.6 Hz bandwidth devices and that their bandwidth can not be altered by the SAS because only the quantities $\{g_y, g_z, p, q, r, \phi\}$ are sensed and fed-back. The initial guess for the control gains is all zero except for a small amount of roll and yaw damping which is required to stabilize the dutch roll mode (for the initial guess). Because MIDSM must now minimize the total cost with respect to 49 variables (i.e. 45 SAS gains and 4 configuration variables) the number of line searches and the computational cost of each gradient evaluation is much greater than in the EMF MIDSM examples. A converged solution for the RMF MIDSM synthesis was achieved after 56 line searches and 3697 objective function evaluations. Table 5.14 lists the optimal configuration variable values and the optimized RMF SAS gains. A 3-view of the nominal OWRA and the optimal MIDSM configuration is given in figure 5.42.

Optimal RMF SAS Gains

$$K_{ff} = \begin{bmatrix} .3549 & -.2206 & .6895 \\ -.0525 & 1.9225 & .2346 \\ .2564 & -.2725 & 1.4245 \end{bmatrix}$$

$$K_{pf} = \begin{bmatrix} -.0772 & -.0016 & .0449 & 2.1049 & -.2960 & .2059 \\ -.2380 & .0742 & -.3710 & 4.2548 & -1.0057 & -.1918 \\ -.1466 & -.0410 & -.0640 & 2.0628 & -.3334 & .1213 \end{bmatrix}$$

$$K_{fb} = \begin{bmatrix} .2129 & .0131 & -.0866 & -1.4096 & .0067 & -.3269 \\ .3004 & .0026 & .2710 & -3.4882 & 2.0186 & .1056 \\ .2412 & .0465 & .0446 & -1.4056 & .1104 & -.2070 \end{bmatrix}$$

<u>MIDSM Configuration</u>   <u>Nominal Configuration</u>

Trim State Solution

	MIDSM			Nominal	
α	= 3.25 (deg)		α	= 3.20 (deg)	
β	= 2.0		β	= -.283	
$\delta_{elev\ right}$	= 4.24		$\delta_{elev\ right}$	= -6.38	} Exceeds Trim Constraint
$\delta_{elev\ left}$	= -5.00		$\delta_{elev\ left}$	= 11.89	
δ_{rudder}	= -1.82		δ_{rudder}	= 1.33	

Configuration Variables

MIDSM	Nominal
$X_{pw} = 1.734$ (ft)	$X_{pw} = 3.14$ (ft)
$X_{pf} = 35.05$ (ft)	$X_{pf} = 37.29$ (ft)
$\phi_\beta = -5.42$ (deg)	$\phi_\beta = 0$ (deg)
dih = .0037	dih = 0

Table 5.14 MIDSM results OWRA synthesis, 45° sweep, RMF SAS

192
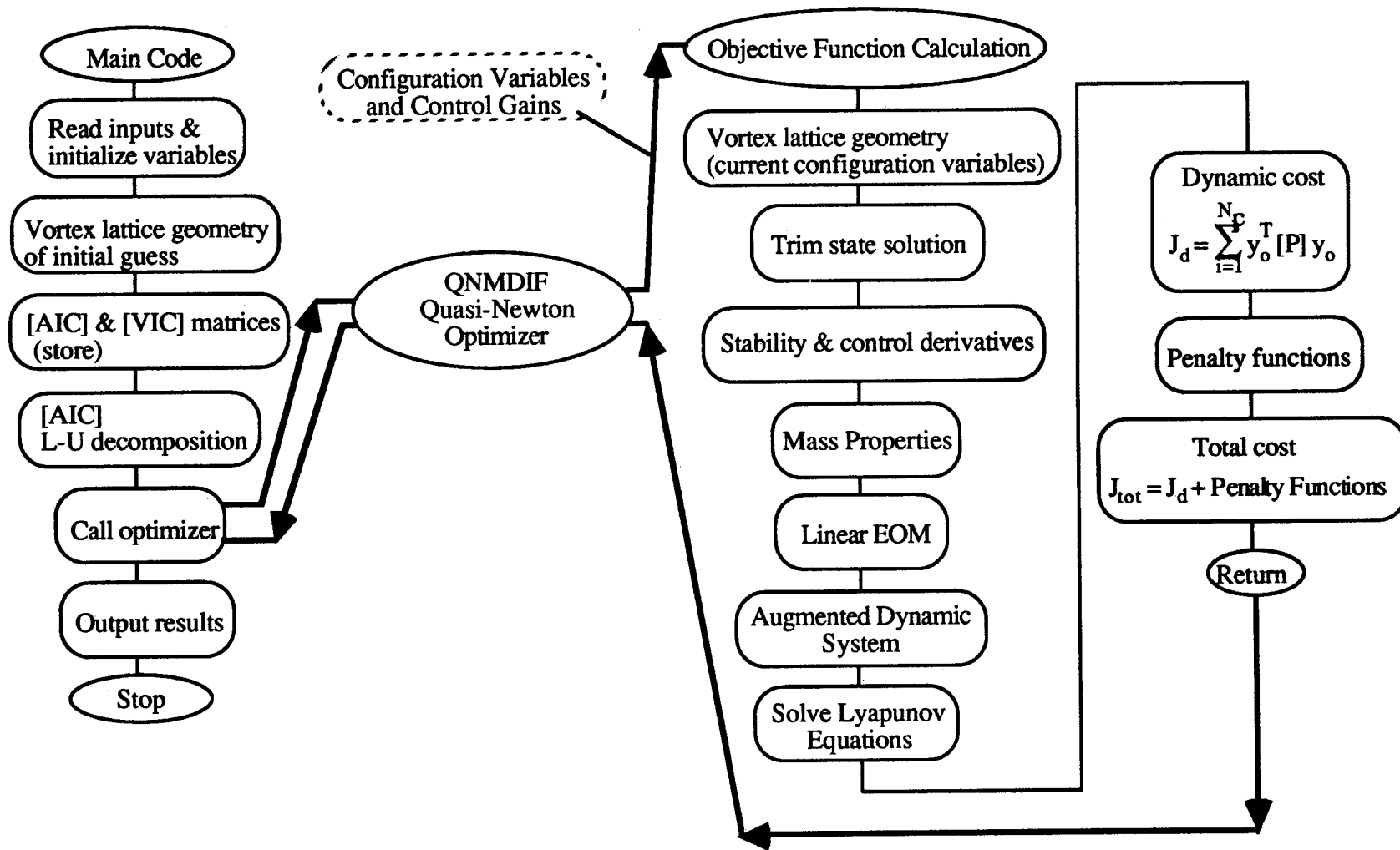
Figure 5.41 MIDSM synthesis, single flight condition, RMF SAS flowchart

Nominal OWRA ▭

MIDSM OWRA ▬

Top

Front

Side
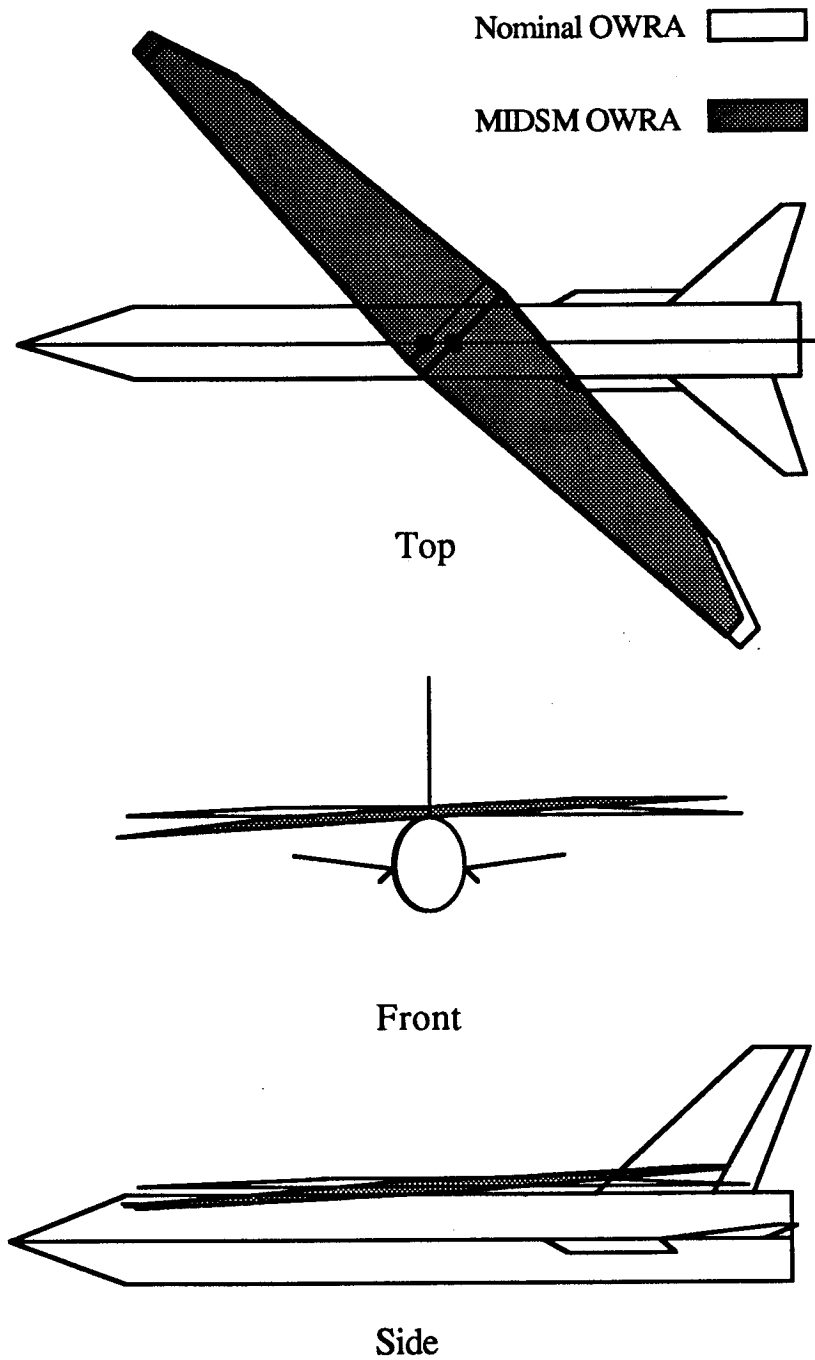
Figure 5.42 MIDSM results, F-8 OWRA configuration

The time histories of the optimized RMF design and the nominal design with RMF SAS are compared to the model's response for the 4-g pull-up maneuver in figures 5.43 - 5.46.

Lateral Acceleration vs Time
45° Sweep, RMF SAS
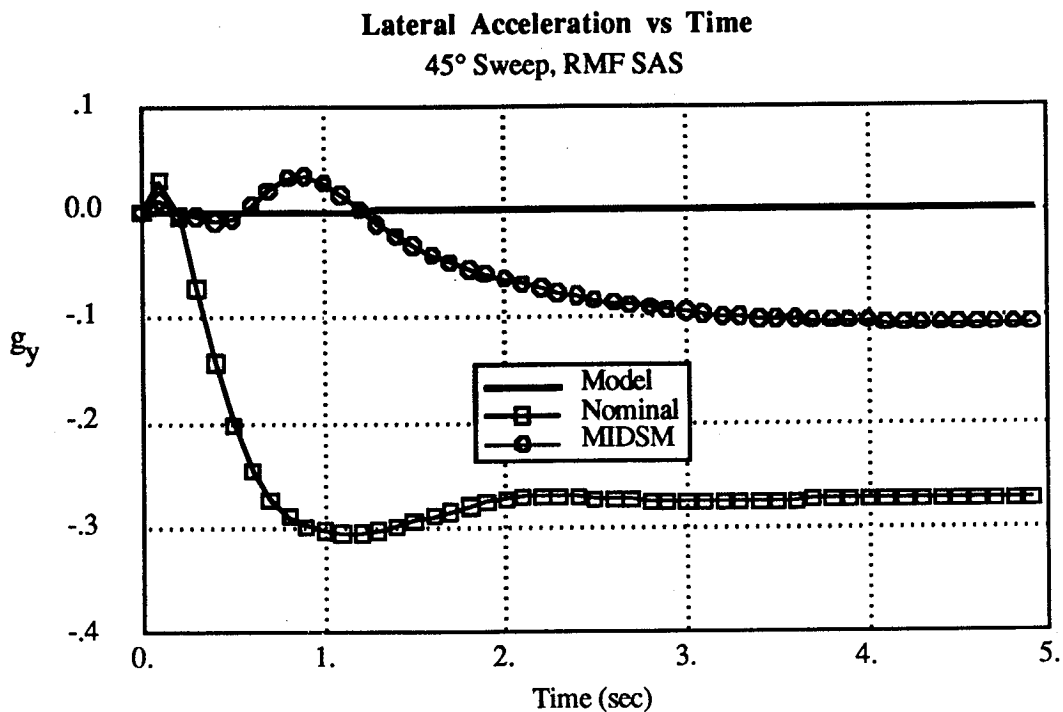
Figure 5.43 lateral acceleration vs. time

Yaw Rate vs Time
45° Sweep, RMF SAS
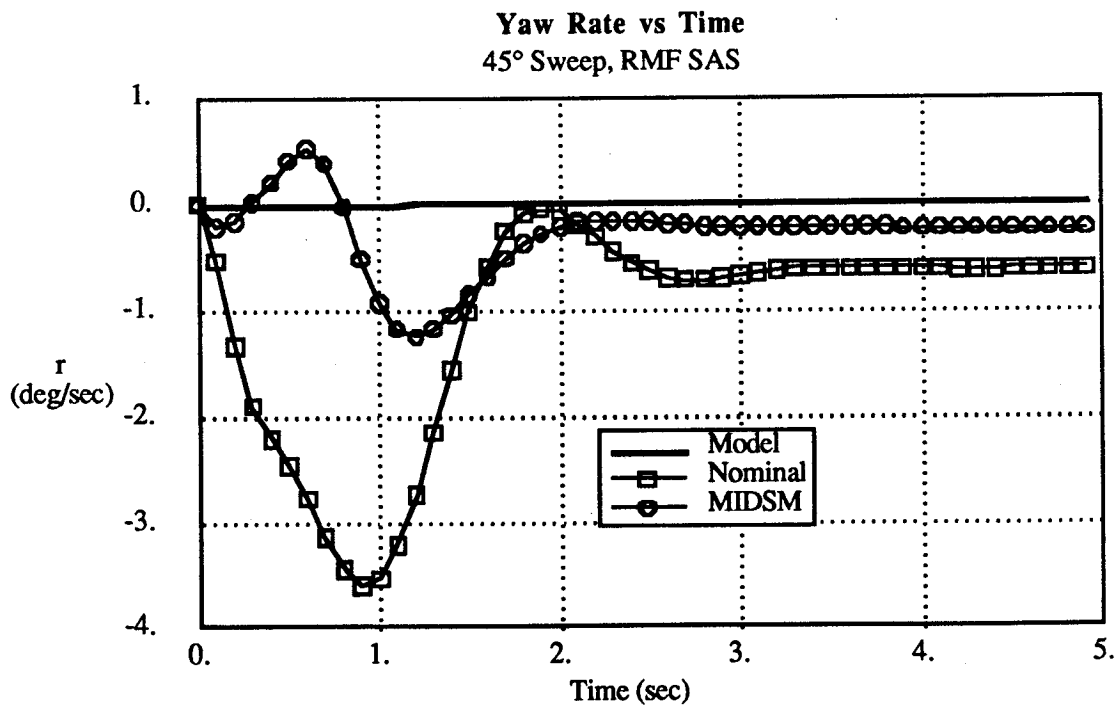
Figure 5.44 yaw rate vs. time

Roll Angle vs Time
45° Sweep OWRA, RMF SAS
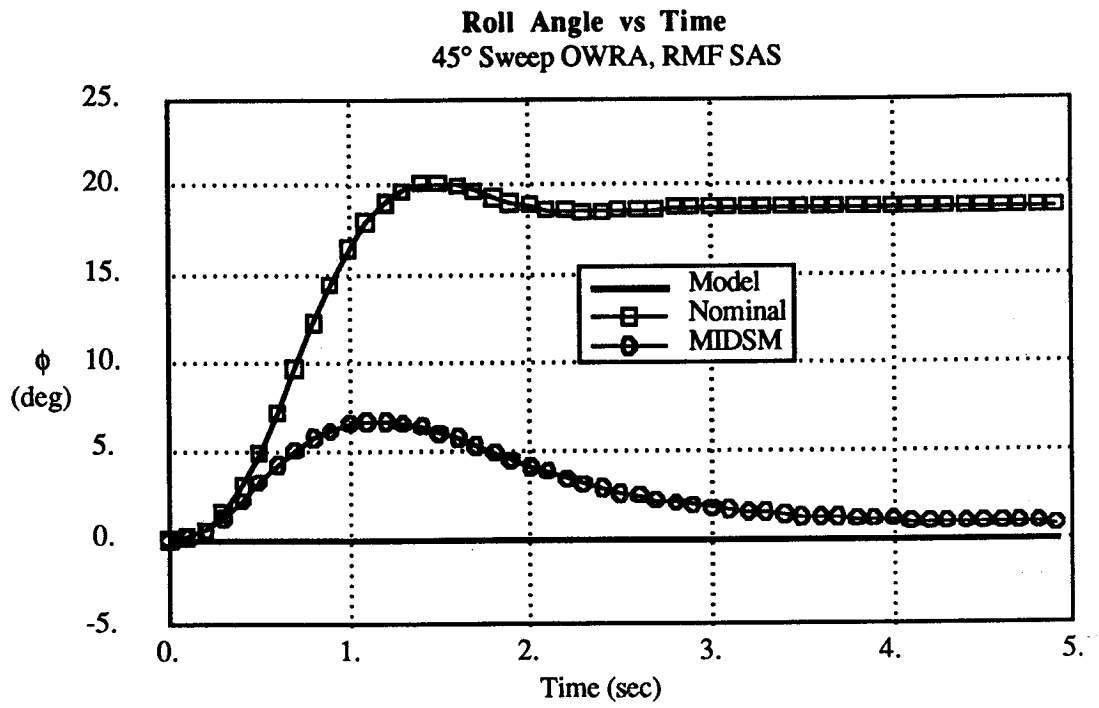
Figure 5.45 roll angle vs. time

Control Surface Deflection vs Time
45° Sweep OWRA, RMF SAS
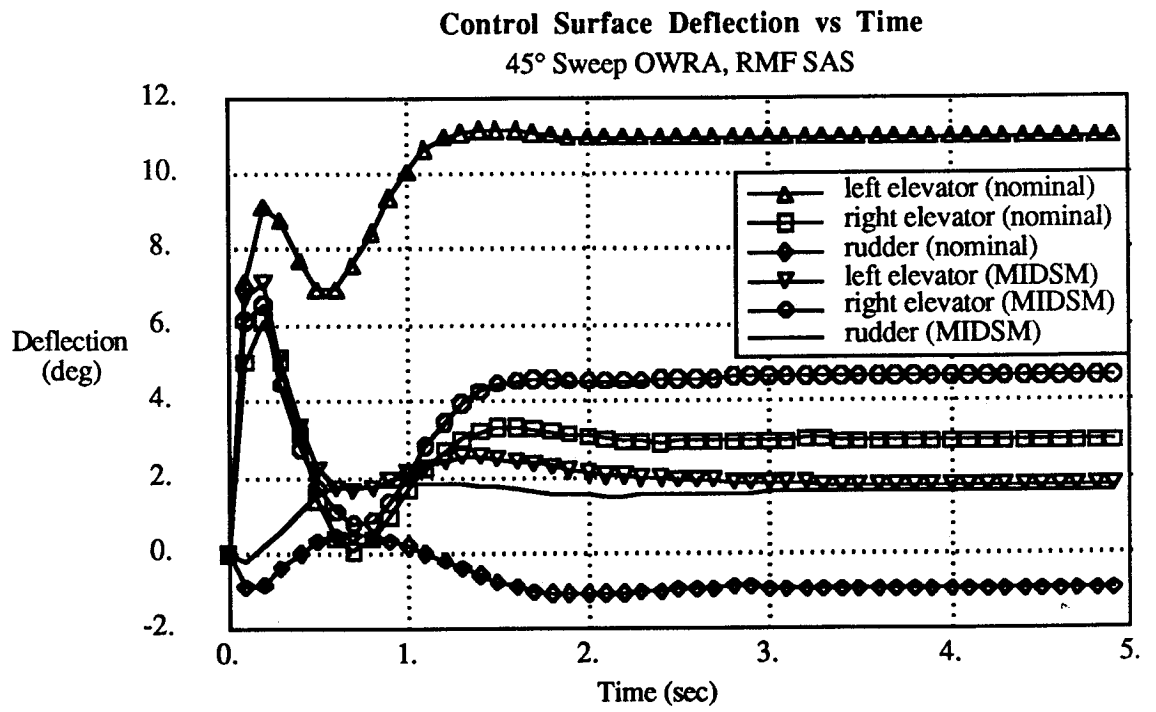
Figure 5.46 control surface deflection vs. time

The optimized configuration with RMF SAS is nearly identical to the EMF OWRA, as can be seen from figures 5.14 and 5.42. In addition, the time histories for the 4-g pull-up maneuver show similar dynamic decoupling and transient response. This indicates that for the 45° sweep flight condition, the optimized OWRA configuration is not very sensitive to the SAS architecture. The RMF OWRA has appropriate wing bank and pivot displacement to force the coupling terms $C_{l\alpha}$ and $C_{y\alpha}$ to be nearly zero, just as is the case for the EMF OWRA. Table 5.15 lists the performance of the aircraft with RMF SAS.

	$g_{y\,peak}$	ϕ_{peak} (deg)	r_{peak} (deg/sec)
Nominal OWRA	-0.31	20.16	-3.7
MIDSM OWRA	-0.10	6.7	-1.1
% Reduction	67%	67%	70%

Table 5.15 MIDSM OWRA performance, 45° sweep RMF SAS

A key aspect of the optimized RMF OWRA is that it achieves dynamic performance similar to the EMF case, but it does so with actuators whose bandwidth is only 1.6 Hz instead of 5 Hz. In figure 5.47 the closed loop eigenvalues of both the RMF and EMF designs are shown. It is clear from this figure that the RMF design has eigenvalues much closer to those of the model (in frequency) than the EMF case. As was discussed in chapter 3, one key advantage of the RMF SAS is that it attempts to match the poles of the closed loop plant to those of the model, which produces the desired model following performance without excessive bandwidth requirements in the feedback path. Figure 5.47 clearly shows that most of the EMF OWRA closed loop poles are at a frequency of 1.6 Hz or greater where most of the RMF OWRA poles are less than 1.6 Hz. All of the remaining synthesis in this work will assume an RMF SAS architecture.

Closed Loop Roots

45° Sweep OWRA
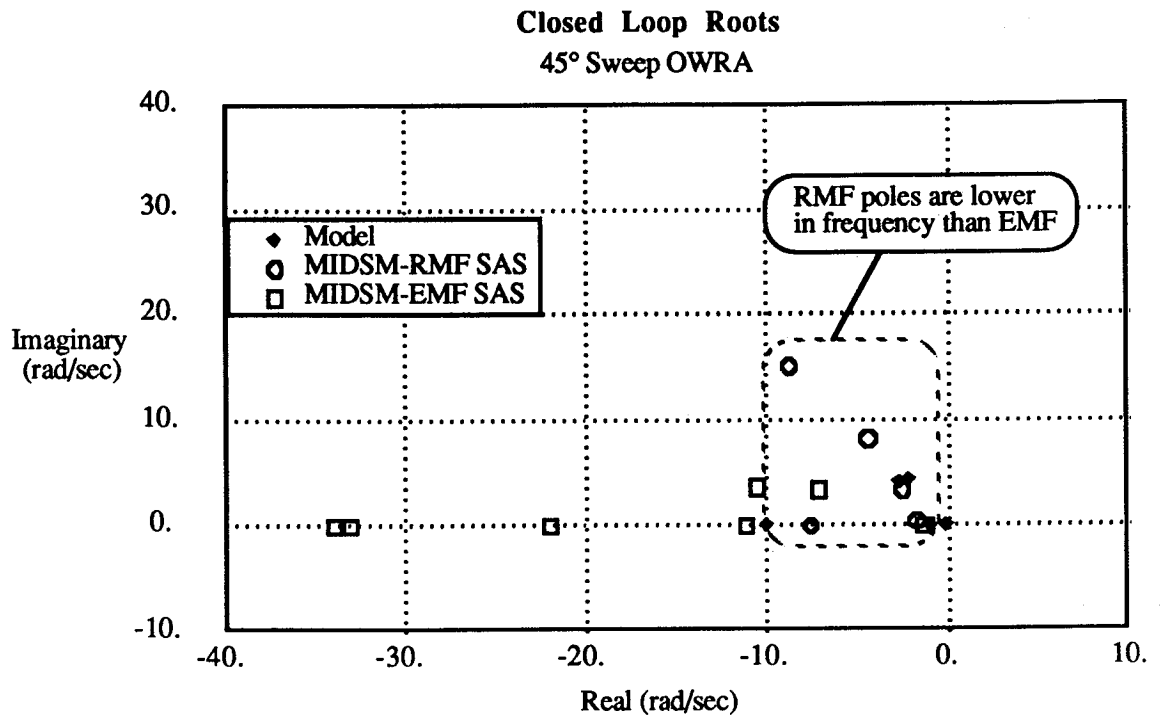
Figure 5.47 closed loop roots, EMF and RMF SAS

5.3 Global Versus Local Minimum in the Optimization Procedure

All of the results presented here used the nominal OWRA configuration as the initial guess for the optimal configuration and the synthesis procedure changed the design until a minimum in the total cost was found. Because all possible combinations of the design variables are not considered, it is possible that there are other configurations that produce a smaller total cost than those designs presented here. To test this theory syntheses were repeated for several different values of the initial guess for the configuration design variables to see if the optimizer would converge to a different answer. In all cases, the converged solution was identical to the one obtained when the nominal OWRA configuration was used as the initial guess. This indicates a reduced likelihood of local minima in the design space of the total cost. This in no way guarantees that an arbitrary synthesis will produce a single minimum and it is the designers responsibility to formulate the total cost function so as to minimize the chances of local minimum. Optimizers which are more robust to local minimum may be used [Ref. 9] but they can have much higher computation costs. The examples pre-

198

sented here show that a wide class of problems may be solved with a straight-forward optimization technique (i.e. Quasi-Newton method) and produce vastly improved designs without evidence of local minima.

5.4 Nonlinear Aerodynamics and Multiple Flight Condition Analyses

In chapter 2 it was shown that many important aerodynamic coupling forces acting on the oblique wing aircraft have significant nonlinear behavior. One shortcoming of a linear dynamics analysis is that it is not possible to accurately account for these nonlinear trends unless the plant model is re-linearized as the state vector changes. For the oblique wing design problem this is a significant issue. For example, the simulation results presented for the nominal OWRA at 65° sweep, M=1.6 flight condition do not display nearly as dramatic sideforce and roll coupling as the VMS simulator results do (figure 3.11). This is because the point of linearization for the airloads ($C_z = 0.1$) happens to occur where the slope of the $C_{l\alpha}$ and $C_{y\alpha}$ terms is very small, giving the illusion of reduced coupling. In reality, as the angle of attack changes during the 4-g pitch-up, the values of $C_{l\alpha}$ and $C_{y\alpha}$ grow nonlinearly and the performance degrades rapidly. To properly account for this in an integrated synthesis (which relies on a linear dynamics analysis) the dynamic cost should be the sum of the cost at several angles of attack that span the range of α experienced during the maneuver. This is identical to idea already presented in the multiple flight condition synthesis where two wing sweeps and Mach numbers were considered. (Note: The results presented for the 45° sweep flight conditions do not experience this 'favorable linearization error' because the point of linearization for their dynamics has nearly maximum slope in all of the coupling variables). All of the analysis tools and techniques required to perform such a synthesis have been presented here, but this work is left for future study so that the present work can focus on the important effects of wing flexibility on oblique wing handling qualities.

Chapter 6

Influence of Wing Flexibility on Oblique Wing Stability and Handling Qualities

In the analyses presented in chapters 1-5, the dynamics model for the oblique wing designs studied assumed a rigid aircraft. Flight test results from the AD-1 oblique wing demonstrator program have shown that aeroelastic deformation of the wing can strongly influence aircraft trim and handling qualities [Ref. 6]. Furthermore, studies of oblique wing flutter [Ref. 27] have shown that the critical aeroelastic instability for wing sweep greater than 25° is a low frequency motion involving wing-bending and aircraft rolling. This flutter instability is unique to oblique wing configurations and may be a critical factor in the structural design of the wing. In this chapter the influence of wing flexibility is included in the linearized equations of motion and in the MIDSM synthesis. First, the 6 DOF EOM are re-derived to include explicitly the influence of wing deformation using an assumed modes model for the wing bending. This formulation retains the rigid aircraft terms in the equations of motion, so that the influence of the flexibility appears explicitly, in addition to the familiar rigid aircraft dynamics. These EOM are then used as a tool to study the aeroelastic instability of the AD-1 configuration and compare the results to previous flutter analyses. Once the validity of the elastic aircraft dynamics model is established, the EOM are incorporated into the MIDSM synthesis so that the F-8 OWRA can be re-designed for improved handling qualities with a deformable wing. The results show that wing flexibility significantly alters the handling qualities of the nominal OWRA configuration and that the optimized OWRA configuration is different from the previous optimized rigid aircraft results. In all cases, the MIDSM OWRA shows dramatic reductions in dynamic coupling and improved handling qualities when compared to both the flexible and rigid wing nominal OWRA.

6.1 Linearized Equations of Motion for a Free-Flying Aircraft with a Flexible Wing

When the oblique wing configuration was first proposed, designers believed that some of its potential advantages would be countered by a structural weight penalty required to keep the forward swept wing from diverging aeroelastically. A study by Jones and Nisbet [Ref. 7] showed, however, that the critical mode of instability is a coupled roll-bend flutter which occurs at speeds significantly higher than the clamped divergence speed of the forward swept wing. Because this instability significantly affects the structural design of the aircraft, it is important to accurately predict this dynamic behavior. The problem is complicated by the fact that the wing flexibility is highly coupled to the rigid aircraft dynamics during flutter. To properly account for this interaction, the linearized equations of motion for a free flying aircraft with a flexible wing are derived. Wing deformation is modeled by N assumed bending modes for the wing. Torsional deformation is not considered initially because its effect on handling qualities and aeroelastic instability (at sweep > 25 °) has been shown to be small [Ref. 6 and 27]. The derivation presented here may be easily extended to include torsional effects if desired. Similarly, a quasi-steady aerodynamics model (i.e. LINAIR) is used to calculate the airloads because the reduced frequency of the flutter mode is typically small (< 0.05). For other problems where unsteady aerodynamic effects are significant, the method may be extended to include apparent mass terms and circulatory aerodynamic terms (using Pade' Approximants).

The equations of motion are derived using Lagrange's energy method presented in a form convenient for analyzing a deformable body. The generalized coordinates (q_i) and speeds (u_i) are carefully chosen to retain the rigid aircraft equations of motion with the effect of flexibility appearing as additional forces and inertia acting on the rigid aircraft.

Lagrange's equations of motion for a single continuous body with possible elastic properties and holonomic constraints may be written as:

Lagrange's Equation of Motion

$$(6.1) \qquad \int_{vol} \left[\rho \frac{I}{V} \cdot \frac{\partial V}{\partial u_i} \right] dVol + \sum_{j=1}^{r} \frac{\partial U}{\partial q_i} W_{ji} = Q_{Ni} \qquad i=1,2, \ldots r$$

201

where:

ρ = Material density

$\dfrac{I}{V}$ = Inertial acceleration

V = Inertial velocity

U = Potential energy

q_i = ith generalized coordinate

u_i = ith generalized speed

W_{ji} = Element of the transform matrix between u & q

Q_{Ni} = ith generalized non-conservative force

r = Number of degrees of freedom

The generalized coordinates and speeds are chosen to be:

$$q = X_I, Y_I, Z_I, \psi, \theta, \phi, \eta_1, \eta_2, ..., \eta_N$$

$$u = u, v, w, p, q, r, \dot{\eta}_1, \dot{\eta}_2, ..., \dot{\eta}_N$$

The assumed mode shape amplitudes are $\eta_1, ...\eta_N$ and X_I, Y_I, Z_I are the inertial position of the undeformed aircraft's mass center expressed in an inertial reference frame. The transform between u and q is given in equation 6.2.

$$(6.2) \qquad W = \begin{bmatrix} T_{B-I} & 0 & 0 \\ 0 & T_{\psi\theta\phi-pqr} & 0 \\ 0 & 0 & I \end{bmatrix}$$

where:

T_{B-I} = Transform from body to inertial coordinates

$T_{\psi\theta\phi-pqr}$ = Transform from body axis angular rates to Euler angles

I = Identity matrix

Because only the wing has modelled flexibility, it is convenient to re-write Lagrange's equations of motion for the rigid fuselage-tail and the elastic wing separately (Eqn. 6.3).

202

(6.3)   Wing

$$\int_{wing}\left[\rho\,\frac{I}{V}\cdot\frac{\partial V}{\partial u_i}\right]dVol + \sum_{j=1}^{r}\frac{\partial U_{wing}}{\partial q_i}\,W_{ji}$$

Fuselage & Tail

$$+\int_{fuse\&tail}\left[\rho\,\frac{I}{V}\cdot\frac{\partial V}{\partial u_i}\right]dVol + \sum_{j=1}^{r}\frac{\partial U_{fuse\&tail}}{\partial q_i}\,W_{ji} =$$

$$Q_{Ni\ wing} + Q_{Ni\ fuse\&tail}\qquad i=1,2,\dots r$$

The wing potential energy term accounts for both the vertical displacement of each wing mass element and the elastic strain energy stored in the deformed structure.

In order to evaluate the kinetic energy terms (volume integrals) in the equations of motion the inertial velocity, V^{P-O}, of each material point (P) must be known (Fig. 6.1).
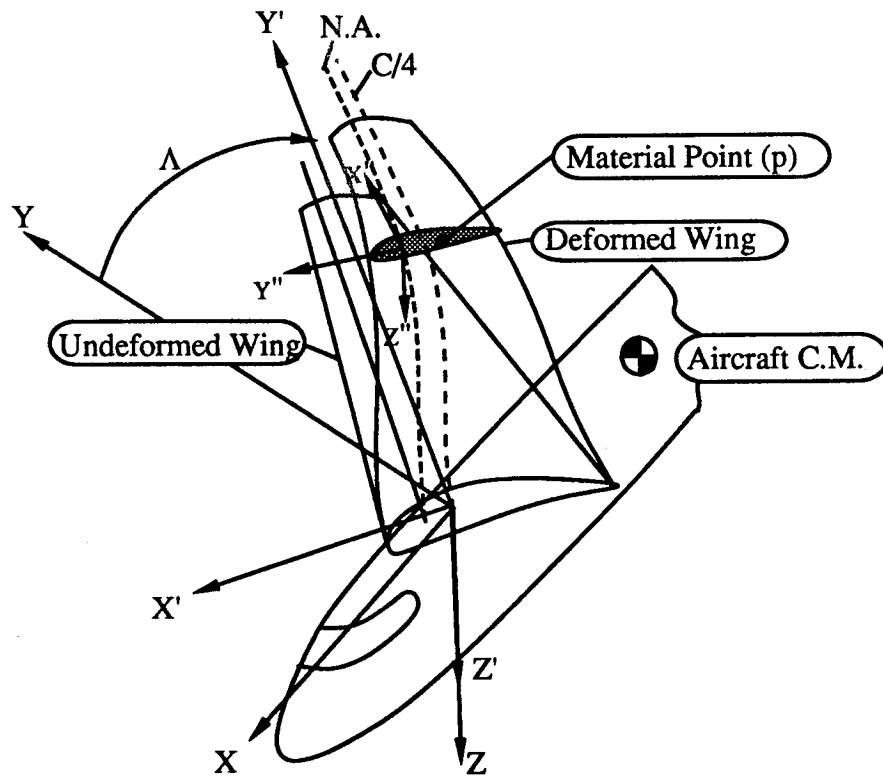
Figure 6.1 definition of axes for the deformable aircraft

$$\delta_b = \sum_{i=1}^{N} \eta_i \, f_i \, (y_i)$$
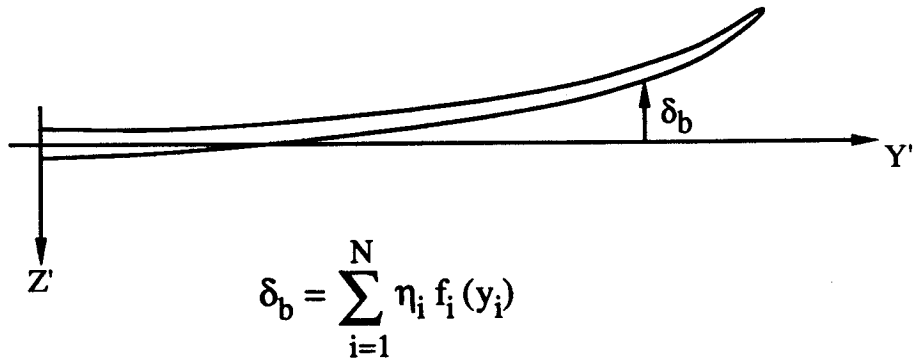
where:

δ_b = local bending deflection

f_i = ith mode shape

η_i = ith mode shape amplitude

Figure 6.2 wing assumed bending modes

$R_B^{cm-p} \equiv$ Distance from the undeformed aircraft C.M. to the point (p)

$$(6.6) \quad R_B^{cm-p} = \begin{bmatrix} X_{cg} \\ 0 \\ Z_{cg} \end{bmatrix} + \begin{bmatrix} T_{B'-B} \end{bmatrix} \begin{bmatrix} X_{NA}' \\ Y' \\ -\delta_B \end{bmatrix} + \begin{bmatrix} T_{B''-B} \end{bmatrix} \begin{bmatrix} X'' \\ 0_{''} \\ Z \end{bmatrix}$$

Where $\begin{bmatrix} T_{B'-B} \end{bmatrix}$ & $\begin{bmatrix} T_{B''-B} \end{bmatrix}$ are coordinate transform matrices from the (') and (")
coordinate system to body axes.

The inertial velocity of material point (p) is V_B^{p-o}

$$(6.7) \quad V_B^{p-o} = \frac{B}{R_B^{cm-p}} + \omega^{B-I} \times R_B^{cm-p} + V_B^{cm-o}$$

where:

$$(6.8) \quad \omega^{B-I} = \begin{bmatrix} p & q & r \end{bmatrix}^T$$

$$(6.9) \quad V_B^{cm-o} = \begin{bmatrix} u & v & w \end{bmatrix}^T$$

Substituting into the volume integral the wing contribution to the
kinetic energy term (linearized about 1-g level flight) is given by
equations 6.10 - 6.15.

Elastic Wing Contribution to Kinetic Energy

<u>Generalized speed</u>   <u>Linearized wing KE term</u>

(6.10)   u : $\dot{u}\, M_w + \int m(-\dot{r}\, Y_{NA} + \dot{q}\, Z_{NA})\, ds' + qw_o M_w$

(6.11)   v : $\dot{v}\, M_w + \int m(-\dot{p}\, Z_{NA} + \dot{r}\, X_{NA})ds' + r\, U_o M_w - pw_o M_w$

(6.12)   w : $\dot{w}\, M_w + \int m(-\dot{q}\, X_{NA} + \dot{p}\, Y_{NA})ds'$

$$-\int (m \sum_{j=1}^{N} f_j \ddot{\eta}_j)ds' - qU_o M_w$$

(6.13)   p : $\dot{p}\, I_{xxw} + \dot{q} I_{xyw} + \dot{r}\, I_{xzw} + \int(-Q_2 I_{xx''} \sum_{j=1}^{N} \frac{\partial f_j}{\partial s'} \ddot{\eta}_j - Y_{NA}\, m \sum_{j=1}^{N} f_j \ddot{\eta}_j)ds'$

$$+ \int m(\dot{r}\, Z_{NA} - r\, U_o Z_{NA} - qU_o Y_{NA} + \dot{w}\, Y_{NA} + p\, w_o Z_{NA})ds'$$

(6.14)   q : $\dot{p}\, I_{xyw} + \dot{q}\, I_{yyw} + \dot{r}\, I_{zyw} + \int(m\, X_{NA} \sum_{j=1}^{N} f_j\, \ddot{\eta}_j - I_{xx''} Q_1 \sum_{j=1}^{N} \frac{\partial f_j}{\partial s'} \ddot{\eta}_j)ds'$

$$+ \int m(\dot{u}\, Z_{NA} - \dot{w}\, X_{NA} + q\, U_o\, X_{NA} + q\, w_o\, Z_{NA})ds'$$

(6.15)   r : $\dot{p}\, I_{xzw} + \dot{q}\, I_{yzw} + \dot{r}\, I_{zzw} + \int m(-\dot{u}\, Y_{NA} + \dot{v}\, X_{NA} + r\, U_o X_{NA} - qw_o Y_{NA} - pw_o X_{NA})ds'$

(6.16) $\dot{\eta}_i$: $\dot{p} \int(-I_{xx''} Q_2 \frac{\partial f_i}{\partial s'})ds' + \dot{q} \int(-I_{xx''} Q_1 \frac{\partial f_i}{\partial s'})ds'$
   i=1,... N

$$+ \int(I_{xx''} \frac{\partial f_i}{\partial s'} \sum_{j=1}^{N} \frac{\partial f_j}{\partial s'} \ddot{\eta}_j + m\, f_i \sum_{j=1}^{N} f_j \ddot{\eta}_j)\, ds'$$

$$+ \int -m\, f_i(-\dot{q}\, X_{NA} + \dot{p}\, Y_{NA} + \dot{w} - qU_o)\, ds'$$

* all integrals are from $-\frac{bs}{2}$ to $\frac{bs}{2}$

where:

m = wing mass per unit length

f_i = ith mode shape function

$I_{xx''}$ = rotational inertia per unit span about the x'' axis (slug-ft)

$\frac{b_s}{2}$ = structural semi-span

S' = spanwise location along the neutral axis

$I_{(\ )(\ )w}$ = undeformed wing inertia (slug-ft^2)

M_w = wing mass

$\eta_{()}$ = mode shape amplitude

Λ = C/4 sweep angle of semi-span

ξ = sweep of neutral axis relative to the C/4

$Q_1 = \sin(\Lambda + \xi)$

$Q_2 = \cos(\Lambda + \xi)$

$\begin{bmatrix} X_{NA} & Y_{NA} & Z_{NA} \end{bmatrix}^T$ = location of the undeformed N.A. at the wing root,
relative to the C.G. in body axes

The potential energy consists of the vertical displacement of the wing mass relative to the center of gravity and the strain energy due to bending deformation.

$$(6.17) \qquad U_{wing} = M_w \, g \left(Z + \sum_{j=1}^{N} f_j \eta_j \right) + \frac{1}{2} \int_{-\frac{bs}{2}}^{\frac{bs}{2}} EI \left(\sum_{j=1}^{N} \frac{\partial^2 f_j}{\partial S'^2} \eta_j \right)^2 ds'$$

A Bernoulli-Euler beam model has been assumed for the wing structure in the formulation of the potential energy expression (Eqn. 6.17). Substituting the wing's contribution to the potential energy into the equations of motion and linearizing:

generalized coordinate		potential energy term (wing)
(6.18)	X_I	$M_w \, g \cos(\theta_0) \, \theta + M_w \, g \sin(\theta_0)$
(6.19)	Y_I	$- M_w \, g \cos(\theta_0) \, \phi$
(6.20)	Z_I	$-M_w \, g \cos(\theta_0) + M_w \, g \sin(\theta_0)$
(6.21)	ψ	0
(6.22)	θ	0
(6.23)	ϕ	0
(6.24)	η_i	$\displaystyle\int_{-\frac{bs}{2}}^{\frac{bs}{2}} \left(EI \sum_{j=1}^{N} \frac{\partial^2 f_j}{\partial S'^2} \eta_j \frac{\partial^2 f_i}{\partial S'^2} \right) ds'$ $+ g \left(-\cos(\theta_0) + \sin(\theta_0) \right) \displaystyle\int_{-\frac{bs}{2}}^{\frac{bs}{2}} m \, f_i \, ds'$

The non-conservative generalized forces acting on the wing are the lift, drag, and quarter chord pitching moment at each spanwise station. Expressions for the nonlinear generalized forces are given here, but these will be linearized after the fuselage and tail contributions have been included.

<table>
<thead>
<tr><th>generalized speed</th><th>associated nonconservative generalized force</th></tr>
</thead>
<tbody>
<tr><td>(6.25) u</td><td>$\int F_{wx} \, ds'$</td></tr>
<tr><td>(6.26) v</td><td>$\int F_{wy} \, ds'$</td></tr>
<tr><td>(6.27) w</td><td>$\int F_{wz} \, ds'$</td></tr>
<tr><td>(6.28) p</td><td>$\int (-F_{wy} Z_{c/4} + F_{wz} Y_{c/4} + M_{wx}) \, ds'$</td></tr>
<tr><td>(6.29) q</td><td>$\int (F_{wx} Z_{c/4} - F_{wz} X_{c/4} + M_{wy}) \, ds'$</td></tr>
<tr><td>(6.30) r</td><td>$\int (-F_{wx} Y_{c/4} + F_{wy} X_{c/4} + M_{wz}) \, ds'$</td></tr>
<tr><td>(6.31) $\dot{\eta}$</td><td>$\int (-f_i F_{wz} + M_{wx} \cos(\Lambda) \dfrac{\partial f_i}{\partial s'} + M_{wy} \sin(\Lambda) \dfrac{\partial f_i}{\partial s'}) \, ds'$</td></tr>
</tbody>
</table>

where:

$$F_w = \begin{bmatrix} F_{wx} & F_{wy} & F_{wz} \end{bmatrix}^T$$

$$M_{wc/4} = \begin{bmatrix} M_{wx} & M_{wy} & M_{wz} \end{bmatrix}^T$$

$$X_{cg-c/4} = \begin{bmatrix} X_{c/4} & Y_{c/4} & Z_{c/4} \end{bmatrix}^T$$

* all integrals are from $-\dfrac{bs}{2}$ to $\dfrac{bs}{2}$

The rigid fuselage and tail contribution to the EOM is evaluated, linearized and combined with the wing contributions (Eqn. 6.10 - 6.31) to produce the intermediate form of the complete EOM's (Eqn. 6.32 - 6.38). Substitutions have been made for the undeformed aircraft inertia, mass and airloads (where appropriate).

207

	<u>Generalized Speed</u>	<u>Contribution to the Linearized EOM</u>

$$(6.32) \quad u: \qquad \dot{u}\,M + q\,w_0\,M + M\,g\cos(\theta_0)\,\theta = F_x$$

$$(6.33) \quad v: \qquad \dot{v}\,M + r\,U_0\,M - p\,w_0\,M - M\,g\cos(\theta_0)\phi = F_y$$

$$(6.34) \quad w: \qquad \dot{w}\,M - q\,U_0\,M + M\,g\sin(\theta_0)\,\theta + \sum_{i=1}^{N}\ddot{\eta}_i \int -m\,f_i\,ds' = F_z$$

$$(6.35) \quad p: \qquad \dot{p}\,I_{xx} + \dot{q}\,I_{xy} + \dot{r}\,I_{xz} + \sum_{i=1}^{N}\ddot{\eta}_i \int (-Q_2\,I_{xx''}\frac{\partial f_i}{\partial s'} - Y_{NA}\,m\,f_i)\,ds' = M_x$$

$$(6.36) \quad q: \qquad \dot{p}\,I_{xy} + \dot{q}\,I_{yy} + \dot{r}\,I_{yz} + \sum_{i=1}^{N}\ddot{\eta}_i \int (m\,X_{NA}\,f_i - I_{xx''}\,Q_1\frac{\partial f_i}{\partial s'})\,ds' = M_y$$

$$(6.37) \quad r: \qquad \dot{p}\,I_{xz} + \dot{q}\,I_{yz} + \dot{r}\,I_{zz} = M_z$$

$$(6.38) \quad \dot{\eta}_i: \qquad \dot{p}\int(-I_{xx''}\,Q_2\frac{f_i}{\partial s'} - m\,Y_{NA}\,f_i)\,ds' + \dot{q}\int(-I_{xx''}\,Q_1\frac{\partial f_i}{\partial s'} + m\,X_{NA}\,f_i)\,ds'$$

$$+ \dot{w}\int -m\,f_i\,ds' + q\,U_0\int m\,f_i\,ds' + \sum_{j=1}^{N}\ddot{\eta}_j \int (I_{xx''}\frac{\partial f_i}{\partial s'}\frac{\partial f_j}{\partial s'} + m\,f_i f_j)\,ds'$$

$$+ \theta\,g\sin(\theta_0)\int m\,f_i\,ds' + \sum_{j=1}^{N}\eta_j \int EI\,\frac{\partial^2 f_i}{\partial s'^2}\frac{\partial^2 f_j}{\partial s'^2}\,ds'$$

$$= \int \left[-f_i\,F_{wz} + (M_{wx}\cos(\Lambda) + M_{wy}\sin(\Lambda))\frac{\partial f_i}{\partial s'}\right]\,ds'$$

$$* \text{ all integrals are from } -\tfrac{bs}{2} \text{ to } \tfrac{bs}{2}$$

where:

I_{xx}, I_{xy}, I_{xz}, etc.	Inertia tensor of the undeformed aircraft about the mass center
M	Total aircraft mass
$\overline{F} = \begin{bmatrix} F_x, F_y, F_z \end{bmatrix}^T$	Net aerodynamic force acting on the undeformed aircraft
$\overline{M_{wc/4}} = \begin{bmatrix} M_{wx}, M_{wy}, M_{wz} \end{bmatrix}^T$	Net aerodynamic moment acting about the wing c/4, on the undeformed aircraft

The aerodynamic terms are now linearized and the equations of motion are re-arranged into a matrix form convenient for stability and control analysis.

(6.39) $[A]\,\dot{x} + [B]\,x = [C]\,x + [D]\,u$

p = number of states (=9+N), m= number of controls

where:

[A] = inertia matrix (pxp)

[B] = kinematics and flexibility matrix (pxp)

[C] = aerodynamics matrix (pxp)

[D] = controls matrix (pxm)

$$x = \left[\, u,\ v,\ w,\ p,\ q,\ r,\ \psi,\ \theta,\ \phi,\ \dot{\eta}_1,\ \eta_1,\ \dots \dot{\eta}_N,\ \eta_N \right]^{T}\ (px1)$$

$$u = \left[\, \delta_{elev\ right},\ \delta_{elev\ left},\ \delta_{rudder} \right]^{T}\ (mx1)$$

Notice that the first (P) terms of the state vector are identical to the state vector for the rigid aircraft as derived in chapter 3. The explicit form of the matrices [A]-[D] are:

$$[A] = \text{(Mass Matrix)} = \begin{bmatrix}
M & 0 & 0 & 0 & 0 & 0 & 0 & 0 & 0 & 0 & 0 & 0 & 0 & \cdots & 0 & 0 \\
0 & M & 0 & 0 & 0 & 0 & 0 & 0 & 0 & 0 & 0 & 0 & 0 & \cdots & 0 & 0 \\
0 & 0 & M & 0 & 0 & 0 & 0 & 0 & 0 & I_{11} & 0 & I_{12} & 0 & \cdots & I_{1N} & 0 \\
0 & 0 & 0 & I_{xx} & I_{xy} & I_{xz} & 0 & 0 & 0 & I_{41} & 0 & I_{42} & 0 & \cdots & I_{4N} & 0 \\
0 & 0 & 0 & I_{yx} & I_{yy} & I_{yz} & 0 & 0 & 0 & I_{61} & 0 & I_{62} & 0 & \cdots & I_{6N} & 0 \\
0 & 0 & 0 & I_{zx} & I_{zy} & I_{zz} & 0 & 0 & 0 & 0 & 0 & 0 & 0 & \cdots & 0 & 0 \\
0 & 0 & 0 & 0 & 0 & 0 & 1 & 0 & 0 & 0 & 0 & 0 & 0 & \cdots & 0 & 0 \\
0 & 0 & 0 & 0 & 0 & 0 & 0 & 1 & 0 & 0 & 0 & 0 & 0 & \cdots & 0 & 0 \\
0 & 0 & 0 & 0 & 0 & 0 & 0 & 0 & 1 & 0 & 0 & 0 & 0 & \cdots & 0 & 0 \\
0 & 0 & I_{11} & I_{41} & I_{61} & 0 & 0 & 0 & 0 & I_{811} & 0 & I_{812} & 0 & \cdots & I_{81N} & 0 \\
0 & 0 & 0 & 0 & 0 & 0 & 0 & 0 & 0 & 0 & 1 & 0 & 0 & \cdots & 0 & 0 \\
0 & 0 & I_{12} & I_{42} & I_{62} & 0 & 0 & 0 & 0 & I_{821} & 0 & I_{822} & 0 & \cdots & I_{82N} & 0 \\
0 & 0 & 0 & 0 & 0 & 0 & 0 & 0 & 0 & 0 & 0 & 0 & 1 & \cdots & 0 & 0 \\
\vdots & \vdots & \vdots & \vdots & \vdots & \vdots & \vdots & \vdots & \vdots & \vdots & \vdots & \vdots & \vdots & & \vdots & \vdots \\
0 & 0 & I_{1N} & I_{4N} & I_{6N} & 0 & 0 & 0 & 0 & I_{8N1} & 0 & I_{8N2} & 0 & \cdots & I_{8NN} & 0 \\
0 & 0 & 0 & 0 & 0 & 0 & 0 & 0 & 0 & 0 & 0 & 0 & 0 & \cdots & 0 & 1
\end{bmatrix}$$

Equation 6.40

209

Kinematics and elasticity matrix [B] =

$$[B] = \begin{bmatrix}
0 & 0 & 0 & 0 & 0 & 0 & 0 & 0 & 0 & 0 & 0 & 0 & 0 & \cdots & 0 & 0 \\
0 & 0 & 0 & 0 & 0 & 0 & 0 & 0 & 0 & 0 & 0 & 0 & 0 & \cdots & 0 & 0 \\
0 & 0 & -Mw_o & Mw_o & 0 & MgC\theta_o & 0 & 0 & 0 & 0 & 0 & 0 & 0 & \cdots & 0 & 0 \\
0 & 0 & -MU_o & MU_o & 0 & 0 & -MgC\theta_o & 0 & 0 & 0 & 0 & 0 & 0 & \cdots & 0 & 0 \\
0 & 0 & 0 & 0 & 0 & MgS\theta_o & 0 & 0 & 0 & 0 & 0 & 0 & 0 & \cdots & 0 & 0 \\
0 & 0 & 0 & -\sec(\theta_o) & 0 & 0 & 0 & 0 & 0 & 0 & 0 & 0 & 0 & \cdots & 0 & 0 \\
0 & -1 & 0 & 0 & 0 & 0 & 0 & 0 & 0 & 0 & 0 & 0 & 0 & \cdots & 0 & 0 \\
0 & 0 & -\tan(\theta_o) & 0 & 0 & 0 & 0 & 0 & 0 & 0 & 0 & 0 & 0 & \cdots & 0 & 0 \\
-1 & 0 & 0 & 0 & 0 & 0 & 0 & 0 & 0 & 0 & 0 & 0 & 0 & \cdots & 0 & 0 \\
-I_{11}U_o & I_{11}gS\theta_o & 0 & 0 & 0 & 0 & 0 & I_{911} & 0 & I_{912}\cdots I_{91N} & 0 & 0 & 0 & \cdots & 0 & 0 \\
0 & 0 & 0 & 0 & -1 & 0 & 0 & 0 & 0 & 0 & 0 & 0 & 0 & \cdots & 0 & 0 \\
-I_{21}U_o & I_{21}gS\theta_o & 0 & 0 & 0 & 0 & 0 & I_{921} & 0 & I_{922}\cdots I_{92N} & 0 & 0 & 0 & \cdots & 0 & 0 \\
0 & 0 & 0 & 0 & 0 & 0 & 0 & 0 & 0 & 0 & -1 & \cdots & 0 & & 0 & 0 \\
-I_{1N}U_o & I_{1N}gS\theta_o & 0 & 0 & 0 & 0 & 0 & I_{9N1} & 0 & I_{9N2}\cdots I_{9NN} & 0 & 0 & 0 & \cdots & 0 & 0 \\
0 & 0 & 0 & 0 & 0 & 0 & 0 & 0 & 0 & -1 & 0 & 0 & 0 & & 0 & -1 \\
\end{bmatrix}$$

Equation 6.41

210

Aerodynamics Matrix [C]=

$$[C]=\begin{bmatrix}
\frac{\partial F_x}{\partial u} & \frac{\partial F_x}{\partial w} & \frac{\partial F_x}{\partial v} & \frac{\partial F_x}{\partial p} & \frac{\partial F_x}{\partial q} & \frac{\partial F_x}{\partial r} & 0 & 0 & 0 & \frac{\partial F_x}{\partial \dot\eta_1} & \frac{\partial F_x}{\partial \eta_1} & \frac{\partial F_x}{\partial \dot\eta_2} & \frac{\partial F_x}{\partial \eta_2} & \cdots & \frac{\partial F_x}{\partial \dot\eta_N} & \frac{\partial F_x}{\partial \eta_N} \\
\frac{\partial F_y}{\partial u} & \cdots & & & & & & & & \cdots & & & & & & \\
\frac{\partial F_z}{\partial u} & \cdots & & & & & & & & \cdots & & & & & & \\
\frac{\partial M_x}{\partial u} & \cdots & & & & & & & & \cdots & & & & & & \\
\frac{\partial M_y}{\partial u} & \cdots & & & & & & & & \cdots & & & & & & \\
\frac{\partial M_z}{\partial u} & \cdots & & & & & & & & \cdots & & & & & & \\
0 & \cdots & & & & & & & & \cdots & & & & & & \\
0 & \cdots & & & & & & & & \cdots & & & & & & \\
0 & \cdots & & & & & & & & \cdots & & & & & & \\
\frac{\partial I_{101}}{\partial u} & \cdots & & & & & & & & \cdots & & & & & & \\
0 & \cdots & & & & & & & & \cdots & & & & & & \\
\frac{\partial I_{102}}{\partial u} & \cdots & & & & & & & & \cdots & & & & & & \\
0 & \cdots & & & & & & & & \cdots & & & & & & \\
\vdots & & & & & & & & & & & & & & & \\
\frac{\partial I_{10N}}{\partial u} & \cdots & & & & & & & & \cdots & & & & & & \\
0 & \cdots & & & & & & & & \cdots & & & & & &
\end{bmatrix}$$

Equation 6.42

211

$$\text{Controls Matrix } [D] = \begin{bmatrix} \dfrac{\partial F_x}{\partial \delta_1} & \dfrac{\partial F_x}{\partial \delta_2} & \cdots\cdots & \dfrac{\partial F_x}{\partial \delta_m} \\[2ex] \dfrac{\partial F_y}{\partial \delta_1} & \cdots\cdots\cdots\cdots \\[2ex] \dfrac{\partial F_z}{\partial \delta_1} & \cdots\cdots\cdots\cdots \\[2ex] \dfrac{\partial M_x}{\partial \delta_1} & \cdots\cdots\cdots\cdots \\[2ex] \dfrac{\partial M_y}{\partial \delta_1} & \cdots\cdots\cdots\cdots \\[2ex] \dfrac{\partial M_z}{\partial \delta_1} & \cdots\cdots\cdots\cdots \\[2ex] 0 & \cdots\cdots\cdots\cdots \\[1ex] 0 & \cdots\cdots\cdots\cdots \\[1ex] 0 & \cdots\cdots\cdots\cdots \\[2ex] \dfrac{\partial I_{100}}{\partial \delta_1} & \cdots\cdots\cdots\cdots \\[2ex] 0 & \cdots\cdots\cdots\cdots \\[2ex] \dfrac{\partial I_{102}}{\partial \delta_1} & \cdots\cdots\cdots\cdots \\[2ex] 0 & \cdots\cdots\cdots\cdots \\[1ex] \vdots \\[1ex] \dfrac{\partial I_{10N}}{\partial \delta_1} & \cdots\cdots\cdots\cdots \\[2ex] 0 & \cdots\cdots\cdots\cdots \end{bmatrix}$$

Equation 6.43

212

The equations of motion include terms required to account for the wing flexibility which are weighted integrals ($I_{(...)}{}_{(...)}$) of mass, flexibility, and aerodynamic properties over the wing span. Equations 6.44 - 6.48 and figure 6.3 define these integrals.
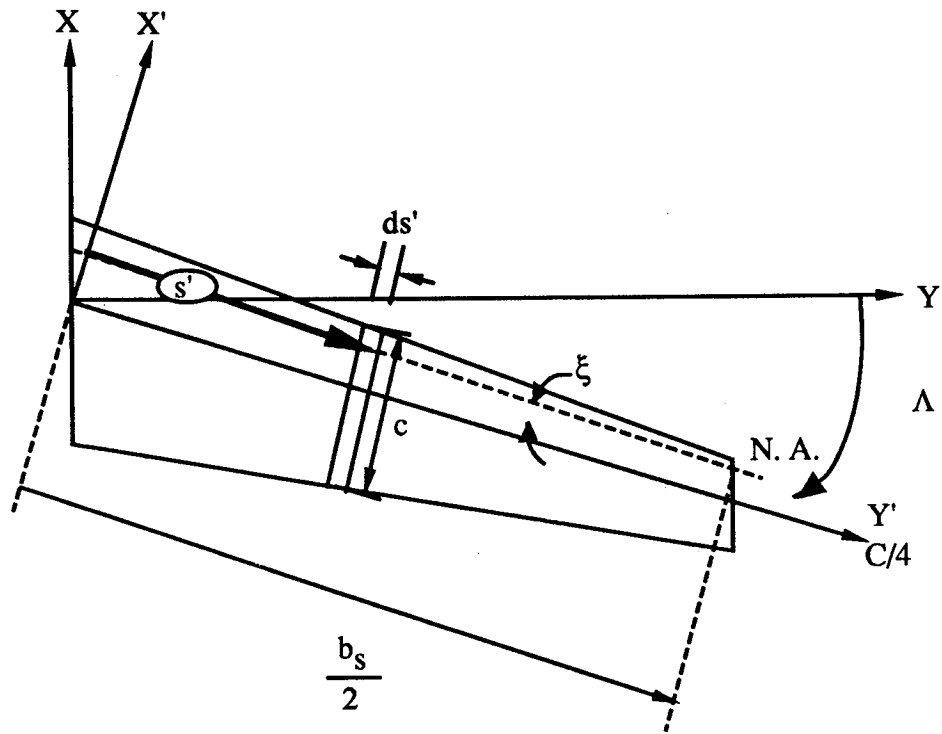

Figure 6.3 wing flexibility spanwise integrals - undeformed wing, top view

Definition of the Spanwise Integrals

$i = 1,2, ...p$

$j = 1,2, ...p$

(6.44) $\qquad I_{1i} = \int -m\, f_i\, ds'$

(6.45) $\qquad I_{4i} = \int (-Q_2\, I_{xx''}\, \dfrac{\partial f_i}{\partial s'} - Y_{NA}\, m\, f_i\,)\, ds'$

(6.46) $\qquad I_{6i} = \int (m\, X_{NA}\, f_i - I_{xx''}\, Q_1\, \dfrac{\partial f_i}{\partial s'}\,)ds'$

(6.47) $\qquad I_{8ij} = \int (\, I_{xx''}\, \dfrac{\partial f_i}{\partial s'}\, \dfrac{\partial f_j}{\partial s'} + m\, f_i\, f_j\,)\, ds'$

(6.48) $\qquad I_{10i} = \int (-f_i\, F_{wz} + (\, M_{wx}\, \cos(\Lambda) + M_{wy}\, \sin(\Lambda))\, \dfrac{\partial f_i}{\partial s'}\,)\, ds'$

* all integrals are from $-\frac{bs}{2}$ to $\frac{bs}{2}$

213

The integrals $I_{(1, 4, 6, 8, 9)}$ involve the normalized assumed mode shape functions, f_i, and the wing mass and stiffness properties. The integral (I_{10i}) is a function of the spanwise loading in the (z) body axis direction and quarter chord moment per unit span (i.e. F_{wz} & $M_{wc/4}$). The spanwise load distribution as a function of the state vector is predicted by the vortex lattice method (LINAIR) which is also used to predict the remaining stability and control derivatives in the EOM.

The linearized EOM may be re-arranged into the following form:

$$[A]\,\dot{x} = \{[C] - [B]\}x + [D]\,u$$

or

(6.49)

The portions of the matrices [A]-[D] labeled "Rigid Aircraft" contain terms identical to those in the rigid aircraft 6 DOF linearized EOM derived in chapter 3. The influence of wing flexibility appears explicitly in the portions marked "Wing Flexibility Terms". The formulation of the EOM in this way allows the designer to analyze the influence of flexibility on an aircraft whose rigid aerodynamic properties may already be well known. This separated form of the EOM also permits the designer to see the influence of flexibility explicitly as a deviation from the rigid aircraft's dynamics. Current aeroelastic analysis methods stress the influence of structural flexibility and unsteady airloads on the stability of the de-

214

forming aircraft structure, but are not easily adapted to analyze unrestrained motion. Similarly, most stability and control analyses are not easily adapted to account for the dynamics associated with aeroelastic phenomenon. The equations presented here show how these two areas may easily be combined into a single formulation which may be used to solve problems spanning the fields of aeroelasticity and stability and control.

The linearized equations of motion are now reduced to their final form for the purpose of stability and control analysis (Eqn. 6.52).

$$[A] \dot{x} = \{[C] - [B]\}x + [D] u$$

(6.51) $\dot{x} = [A]^{-1}\{[C]-[B]\}x + [A]^{-1}[D]u$

or

(6.52) $\dot{x} = [\tilde{A}]x + [\tilde{B}]u$

where:

(6.53) $[\tilde{A}] \equiv [A]^{-1}\{[C] - [B]\}$

(6.54) $[\tilde{B}] \equiv [A]^{-1}[D]$

The system matrices [A] and [B] require that the following information be known to evaluate the equations of motion:

1) Aircraft geometry including the C.G. and elastic axis location

2) Flight condition- altitude, velocity

3) Aerodynamic stability and control derivatives of the rigid aircraft

4) Mass properties of the rigid aircraft

5) Assumed bending mode shape functions

6) Aerodynamic derivatives involving the spanwise variation of wing loading

All of the aerodynamic derivatives for the cases considered in this work are calculated numerically using the vortex lattice method LINAIR (chapter 2). The mass and elasticity integrals are evaluated by numerically integrating the appropriate quantities along the structural wingspan. The process of generating the EOM for the flexible wing aircraft has been automated in a FORTRAN code and linked to an eigensystem solver, dynamics simulation, arid the MIDSM synthesis code to permit detailed analysis of oblique wing aircraft with wing flexibility.

6.2 Aeroelastic Stability of Oblique Wing Aircraft

Flight tests of the AD-1 oblique wing demonstrator aircraft revealed that wing bending can seriously influence handling qualities for oblique wing sweep greater than 30°. Unlike a conventional symmetric aircraft, the bending deformation of an obliquely swept wing produces large pitch and roll moments which can overwhelm the aerodynamic coupling effects present in the rigid aircraft. Figure 6.4 shows the influence of static aeroelastic wing deformation on various force and moment coefficients as load factor varies. These results were obtained from flight test results for the AD-1[Ref. 6].
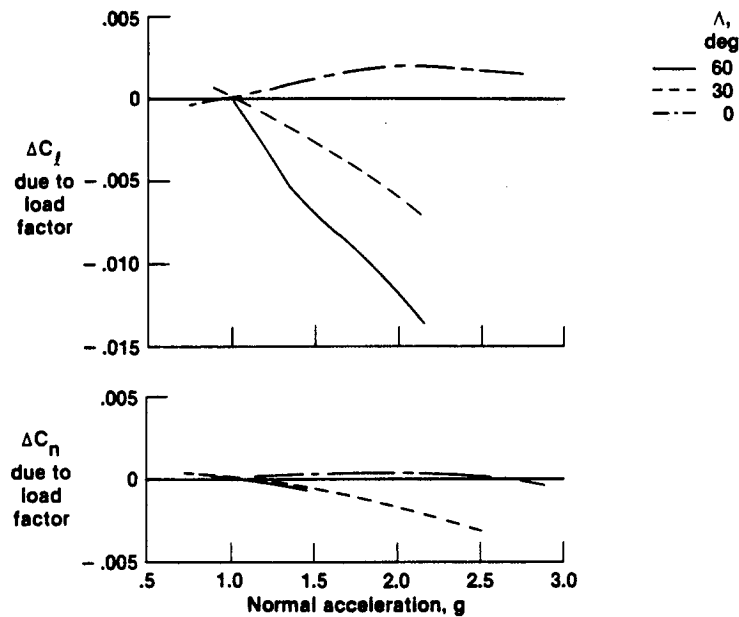
Figure 6.4 effect of wing flexibility on aerodynamic coupling, AD-1 flight test results

Increasing load factor causes the wing to bend upwards which increases the local angle of attack on the forward swept portion of the wing and decreases it on the aft. This shifts the centroid of the span load towards the forward swept wing panel which produces a roll-left, pitch-up tendency as the wing bends under positive loading. If the load factor is changing due to angle of attack change, the aeroelastic effect on the aerodynamic coupling acts opposite the coupling present in the rigid aircraft over a wide range of the flight envelope. The influence of wing flexibility can be a dominant factor in trim, stability, and control of an oblique wing design. Even so, many analyses of oblique wing designs (such as the VMS handling qualities study for the F-8 OWRA) neglect this important phenomenon. In this

216

chapter the influence of wing deformation is included in the design of an oblique wing aircraft for improved handling qualities.

When the oblique wing configuration was first analyzed, designers believed that the critical mode of aeroelastic instability would be a divergence of the forward swept wing panel at high sweep angles. Jones and Nisbet [Ref. 7] showed that this conclusion is incorrect because the assumption of a clamped fuselage boundary condition is inaccurate for the free flying oblique wing aircraft. Instead, a low frequency flutter characterized by a coupling of the wing-bending and rolling motion of the aircraft occurs. Most importantly, this mode becomes unstable at dynamic pressure which may exceed the clamped divergence value by more than a factor of 4. Rutkowski [Ref. 27] calculated in greater detail the critical flutter modes of the AD-1 design using NASTRAN and FLUT numerical analyses. The results showed that for oblique sweep greater than 30° the roll-wing bend flutter mode is critical. The frequency of this mode is low (4Hz for the AD-1) and its sensitivity to torsional stiffness was shown by Rutkowski to be very small.

In order to verify the aeroelastic analysis proposed in this chapter (section 6.1), the AD-1 configuration is analyzed using the proposed method and the flutter results compared to Rutkowski's calculations using NASTRAN and FLUT. The data shown in table 6.1 is used to model the AD-1.

Weight	1700 (lbs)
Span	32.3 (ft)
Wing Area	93 (ft^2)
Taper Ratio	0.39
Section Thickness	12%
Mach Number	0.5
Air Density	.002377 (slug/ft^3)
Modulous of Elasticity	3.8e6 (psi)
Wing Skin Thickness	.16 (in) to .04 (in), linearly tapered
Material Density	Glass = 121 (lb/ft^3) foam = 2 (lb/ft^3)
Number of Assumed Bending Modes	6 polynomial modes
Aerodynamics Model	Quasi-Steady Vortex Lattice (LINAIR)

Table 6.1 AD-1 aeroelastic stability analysis input parameters

217

Figure 6.8 shows the vortex lattice model for the AD-1 along with a 3-view of the aircraft. The flutter speed, assuming only the wing contributes to the airloads (as per Rutkowski), is calculated for wing sweeps of 30, 40, and 60 degrees and is compared to Rutkowski's results in figure 6.7. The flutter speed is calculated by solving the eigensystem of the aircraft's linearized equations of motion at increasing airspeed until an instability is detected. The eigenvector corresponding to the unstable mode defines the flutter mode shape. Similar cases are studied where the fuselage is assumed clamped and divergence of the forward swept wing is critical. All of the flutter analyses assume that the aircraft is free to roll, pitch and plunge. The results show that the method presented here accurately predicts the roll - bend flutter mode. The flutter frequency for all sweep angles (except 60°) is approximately 4 Hz, the same as Rutkowski's results. Calculated divergence speed differs by as much as 30% due to an overly stiff structural model of the AD-1 wing. It was assumed that the skin thickness varied linearly across the span (in the absence of exact information of Rutkowski's model) and this is an overly stiff wing structural model. The flutter speeds compare very well (within 15%) for all wing sweeps except 60 ° where the proposed method predicts a switch in the flutter mode to a very low frequency roll-plunge motion instability. If this low frequency rigid body instability is ignored the next critical flutter mode is a roll - bend mode and this occurs at a speed of 700 (ft/sec), which is much closer to Rutkowski's results. It is not known if Rutkowski's work discovered a similar low frequency instability and ignored it as a "rigid body mode" or if this discrepancy is a valid one. It is typical to ignore unstable low frequency modes in an aeroelastic analysis where the aircraft is only given partial freedom of motion and the total aircraft is not modeled (i.e. no tail). The method proposed here is capable of predicting the free flying dynamics of the aircraft and this instability may very well be physical for the contrived case of a wing-only aircraft with roll, pitch, and plunge DOF. Another potential source of discrepancy is the doublet lattice aerodynamic model used in Rutkowski's work. For a thin lifting surface model a doublet lattice method is not capable of predicting the important leading edge suction forces which can strongly influence the rolling moment and sideforce of an oblique wing design. Nonetheless, the two methods show good comparison and ability to predict this unique aeroelastic instability.
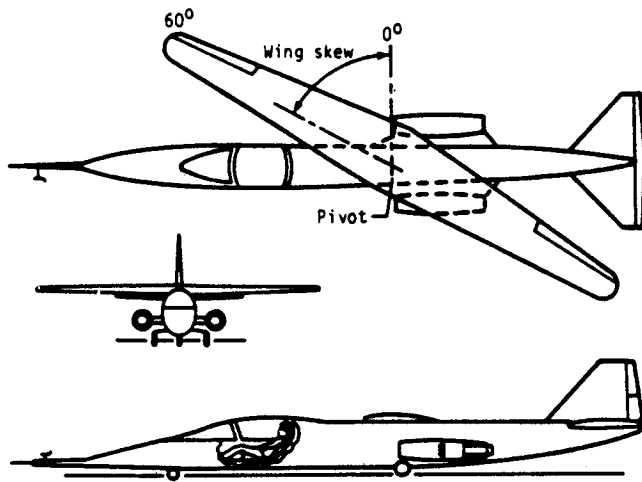
Figure 6.5 3-view of the AD-1 oblique wing demonstrator

V_∞

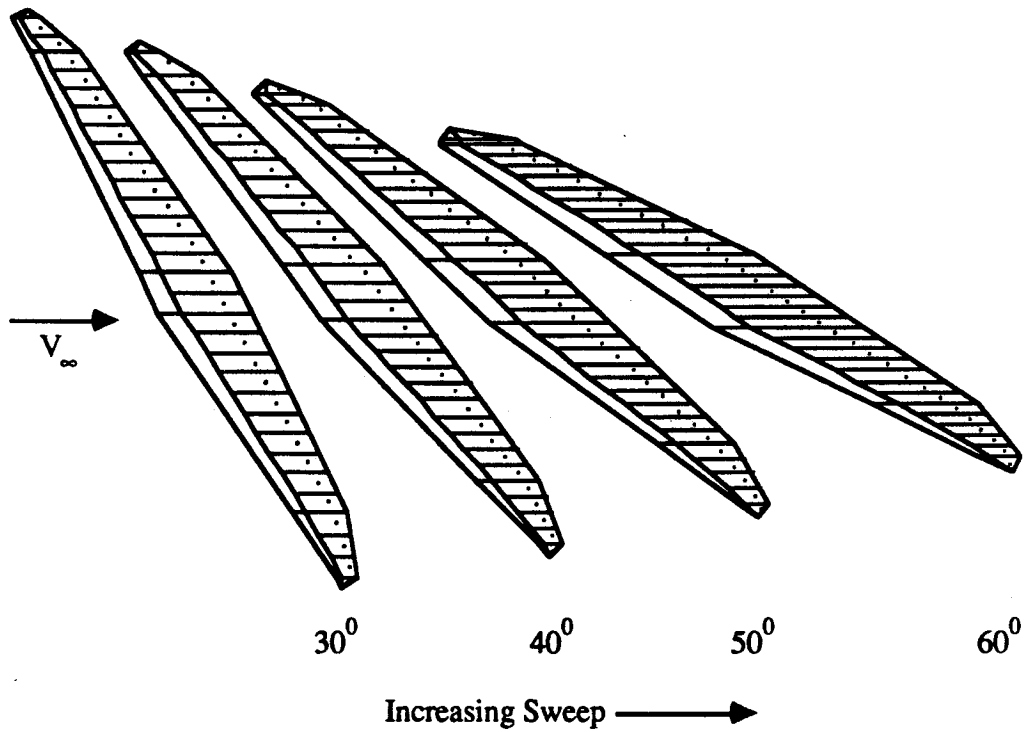30^0 $\qquad$ 40^0 $\qquad$ 50^0 $\qquad$ 60^0

Increasing Sweep $\longrightarrow$

Figure 6.6 AD-1 vortex lattice geometry, wing only

219

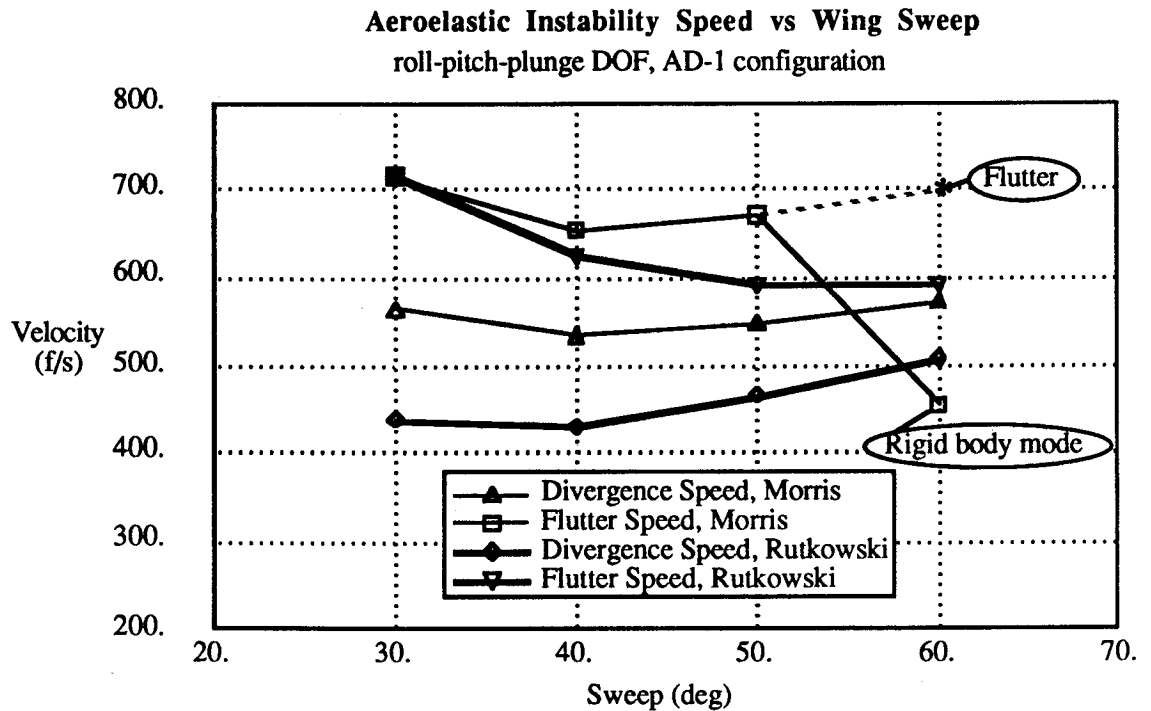## Aeroelastic Instability Speed vs Wing Sweep
### roll-pitch-plunge DOF, AD-1 configuration

Figure 6.7 AD-1 aerolelastic instability speed vs. wing sweep

The effects of full 6 DOF, complete aircraft aerodynamics, fuselage inertia, and tail size on oblique wing flutter will now be considered. First, the influence of the full 6 DOF on the flutter mode will be studied. Figure 6.8 shows the vortex lattice model for the AD-1 at 45° wing sweep. A root locus of the natural modes as flight velocity increases is shown in figure 6.10. The action of the lowest wing bending mode and the roll mode can be clearly seen as these two modes become combined in the unstable flutter mode. The effect of wing flexibility and increasing dynamic pressure on the stability of the short period, dutch roll, and other rigid body modes is seen to be small. Also shown in figure 6.9 is a root locus for the same aircraft with roll degree of freedom and wing bending. The flutter speed and frequency for these two cases is nearly identical, indicating that the reduced degree of freedom model is useful for studying flutter. Simulation results for the 6 DOF aircraft undergoing flutter are presented in figures 6.11 - 6.13 along with a frame by frame pictorial simulation of the aircraft flutter motion (front view) in figure 6.14. These results show that the flutter mode consists mostly of wing bending and fuselage roll even for the 6 DOF case. The left and right wing tips move nearly in phase with each other and the right (forward) tip deflects almost twice as much as the left.

220
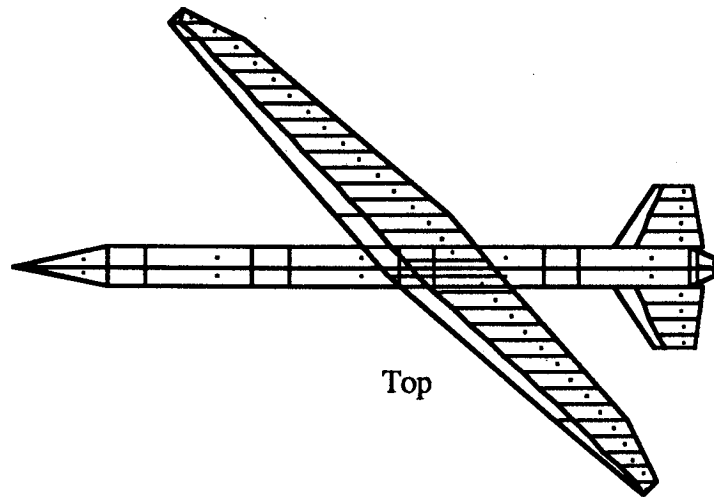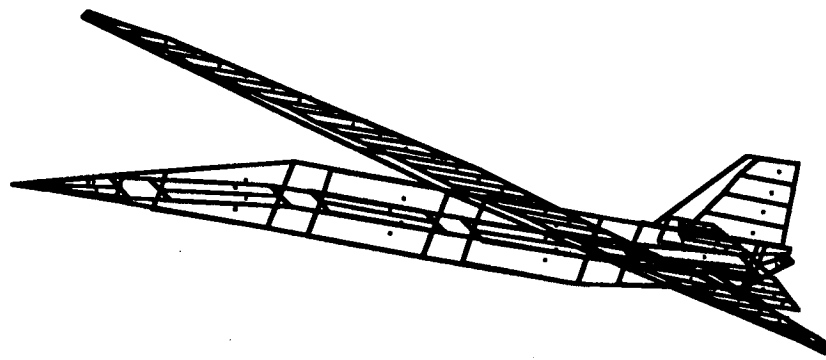
Top
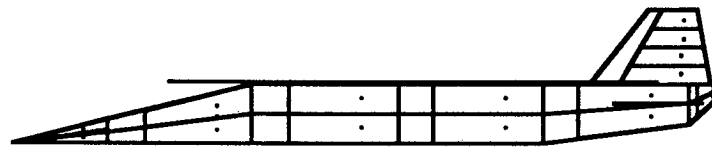
Side
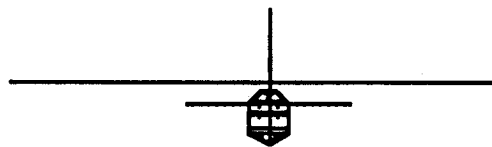
Front

Figure 6.8 vortex lattice model AD-1 oblique wing research aircraft 45° sweep

Flutter Root Locus
AD-1, 45 (deg) Sweep, Roll-Wing Bend DOF Only
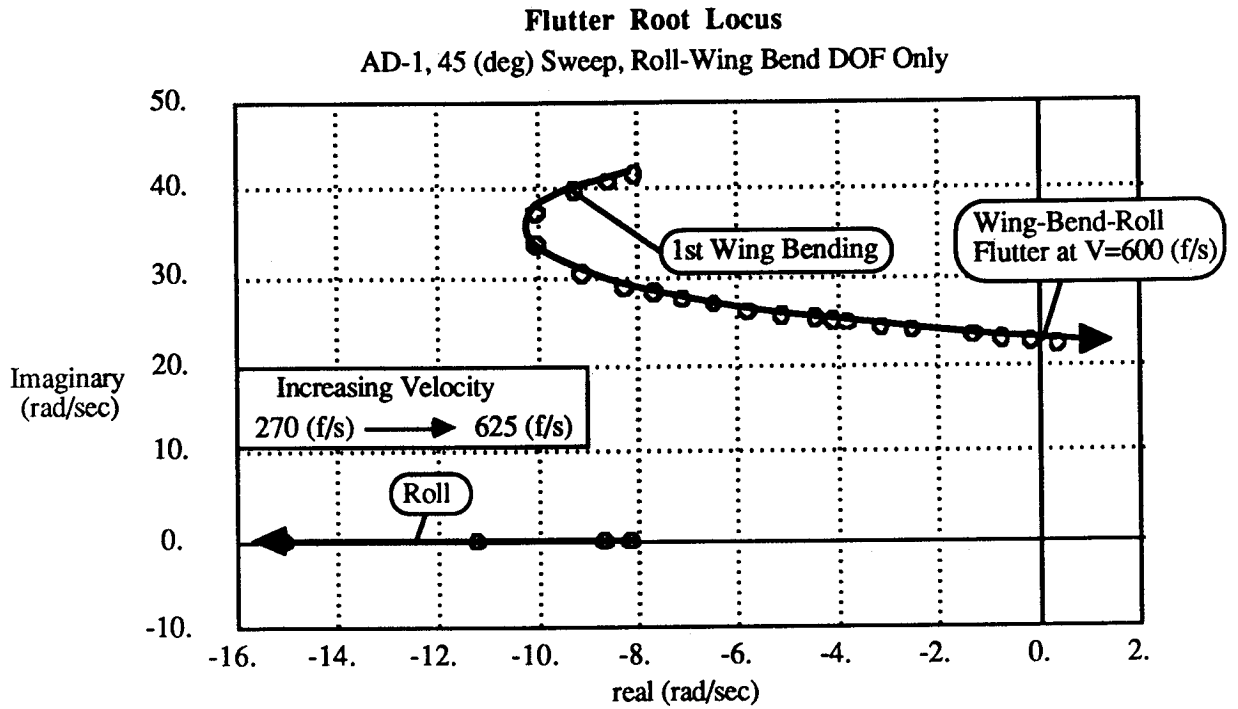
Figure 6.9 AD-1 flutter root locus, roll-wing bend DOF

Flutter Root Locus
AD-1, 45 (deg) Sweep, 6 DOF, 6 Bending Modes
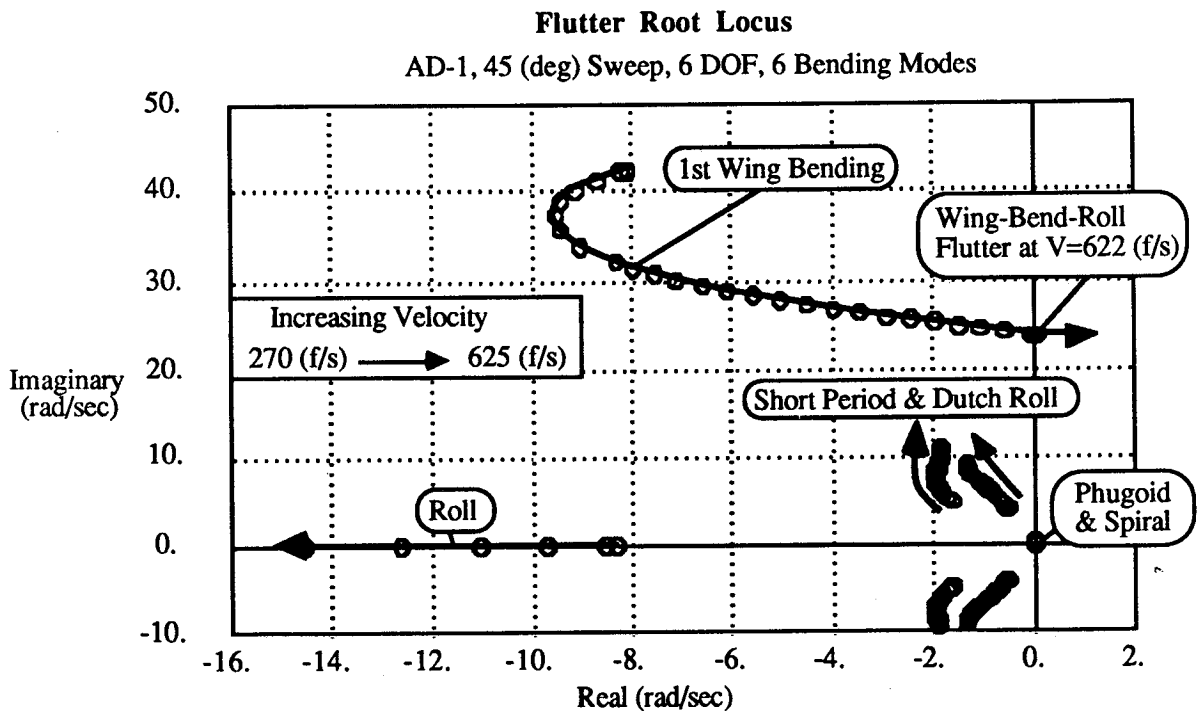
Figure 6.10 AD-1 flutter root locus, 6 DOF and wing bend

222

Translational Velocity vs Time
AD-1 Flutter, 6DOF & Wing Bend, Uo = 624 (f/s)
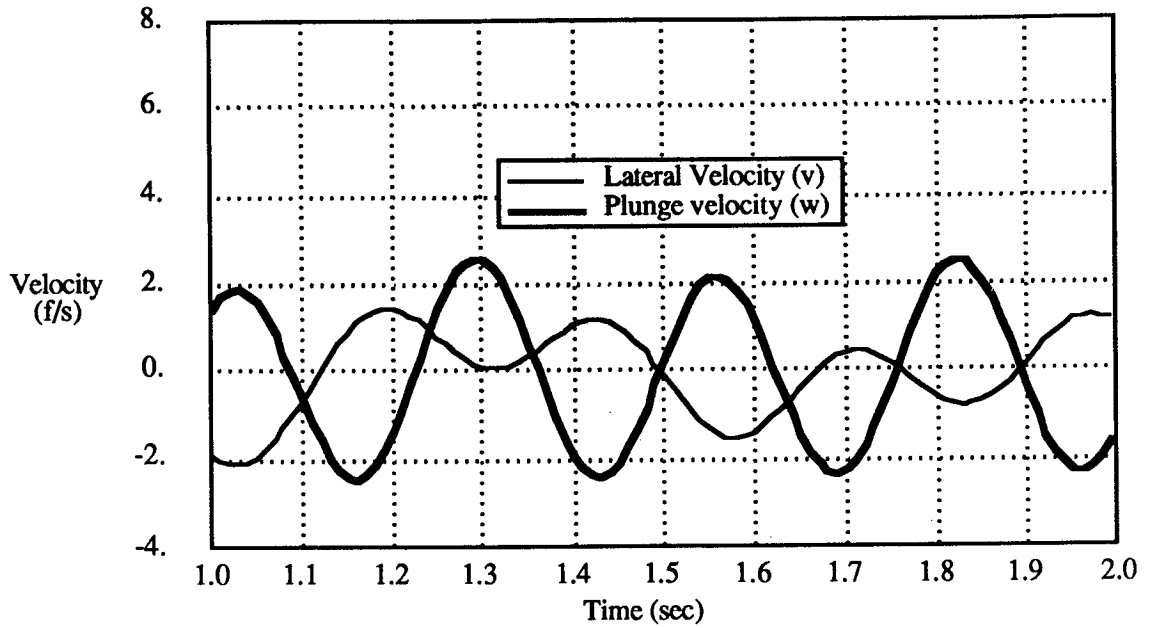
Figure 6.11 velocity vs. time

Euler Angle vs Time
AD-1, 6DOF & Wing Bend, Uo=624 (f/s)
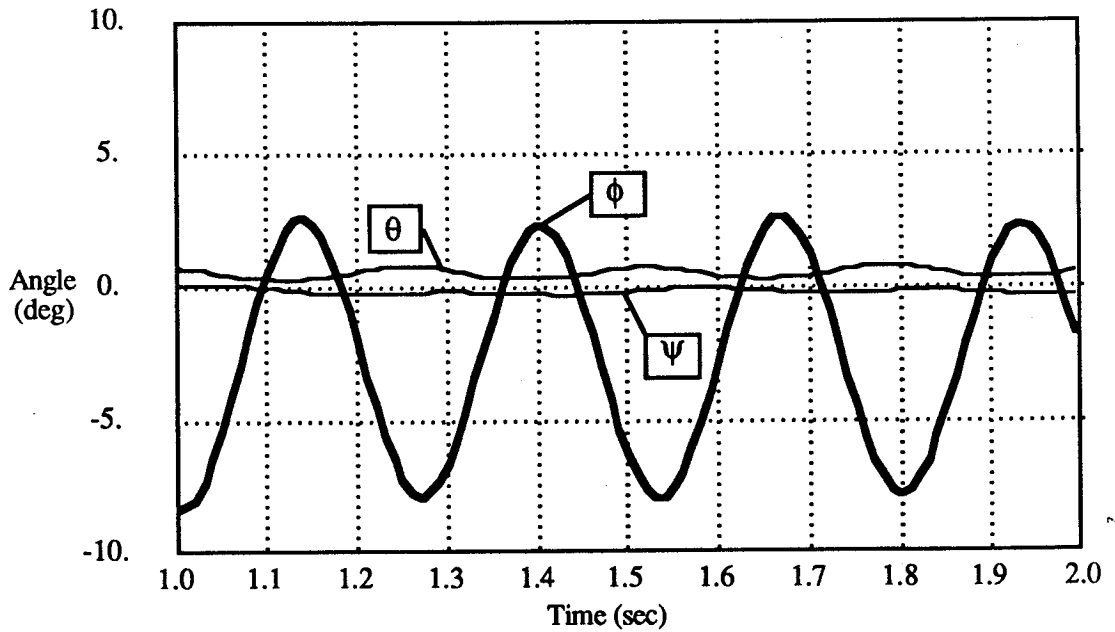
Figure 6.12 Euler angles vs. time

223

Tip Deflection vs Time

AD-1, 6 DOF & Wing Bend, Uo=624(f/s)
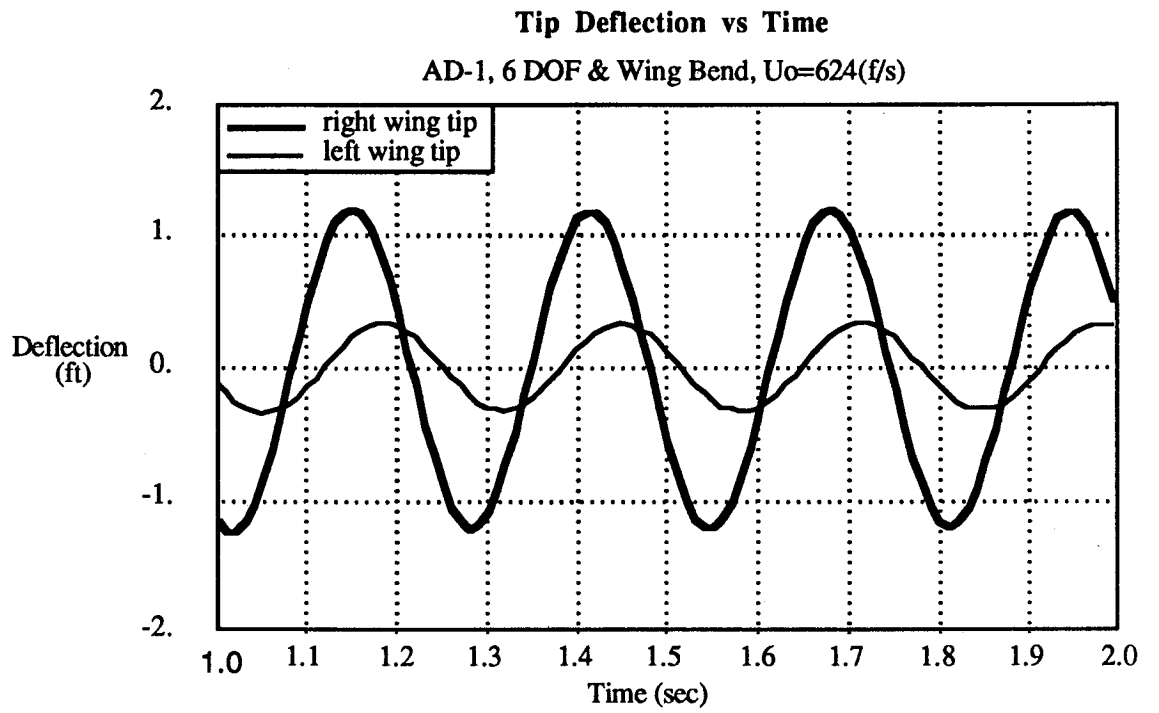
Figure 6.13 tip deflection vs. time
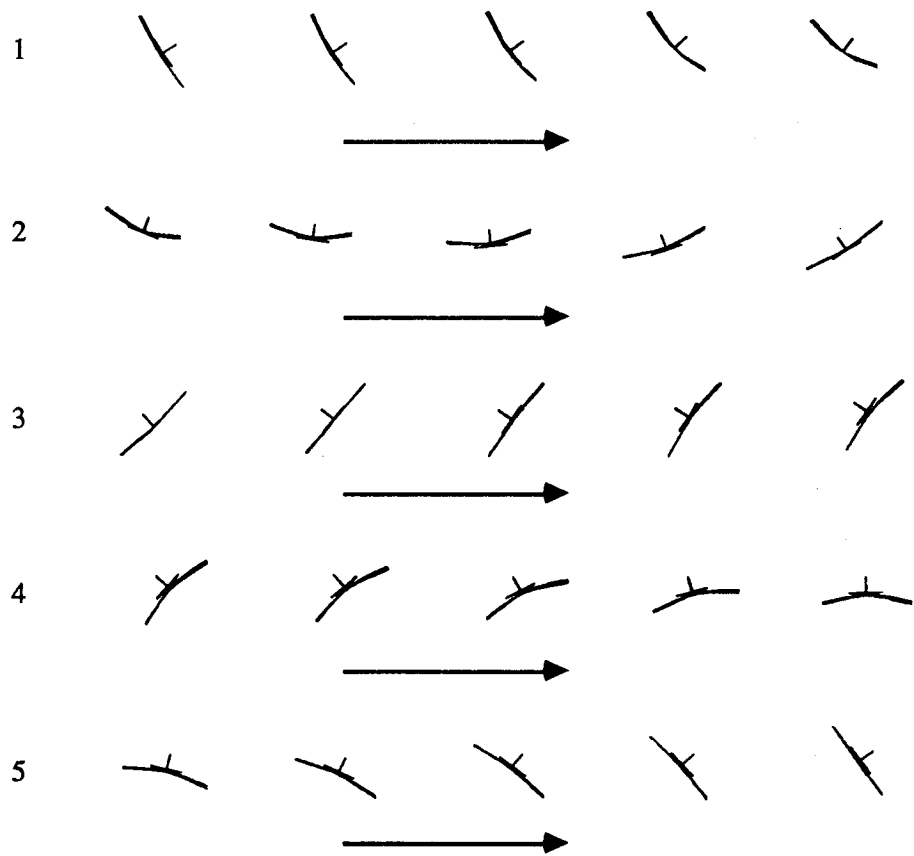
Figure 6.14 6 DOF flutter simulation AD-1, 45° sweep (front view)

224

The influence of wing flexibility on stability is shown in figure 6.15 where the natural modes are plotted as the wing stiffness is decreased by an order of magnitude from the actual AD-1 values. Notice that the AD-1, unlike the F-8 OWRA, has a stable dutch roll mode at 45° sweep. This plot shows that decreasing wing flexibility at a fixed flight velocity will produce the roll wing-bend flutter instability and not significantly affect the stability of the other modes. The coupling of the aircraft's dynamic response is significantly affected by changes wing stiffness and this will be discussed in the next section.

Root Locus on Wing Flexibility
AD-1, 45° Sweep
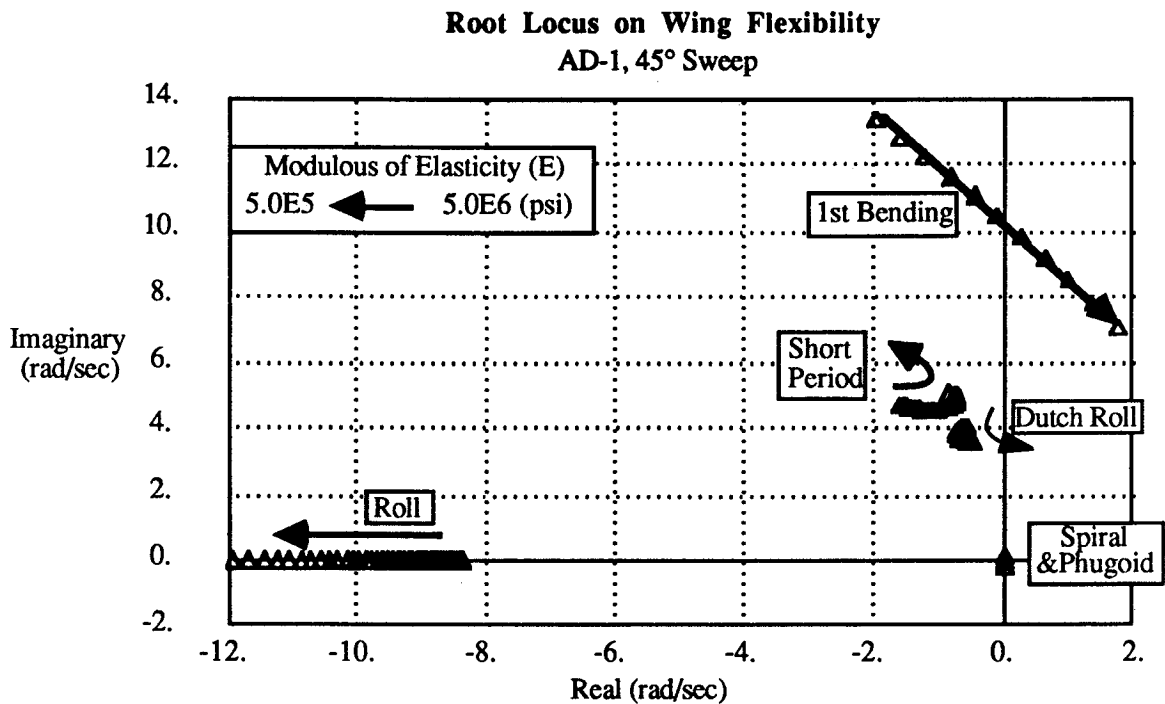
Figure 6.15 effect of wing flexibility on aeroelastic stability (6 DOF)

Jones and Nisbet first suggested that fuselage roll inertia can have a significant effect on oblique wing flutter speed because large inertia causes the fuselage to behave as though it is clamped. This lowers the flutter speed to that of the clamped divergence value as the fuselage inertia becomes infinite. Figures 6.16 - 6.17 show this effect for the AD-1 with 45° sweep, where flutter speed and frequency are plotted versus fuselage inertia. Most apparent from these results is that the flutter speed initially drops off quite dramatically as fuselage inertia increases. For zero fuselage inertia the flutter speed is 3.1 times the clamped divergence speed. The AD-1 flutter speed is only 11% greater than the clamped divergence value.

Flutter Speed vs Fuselage Inertia Ratio
AD-1, 45° Sweep, Roll-Bend DOF, Wing Only

Figure 6.16 flutter speed vs. fuselage inertia ratio

Flutter Frequency vs Fuselage Inertia Ratio
AD-1, 45° Sweep, Roll-Bend DOF, Wing Only

Figure 6.17 flutter frequency vs. fuselage inertia ratio
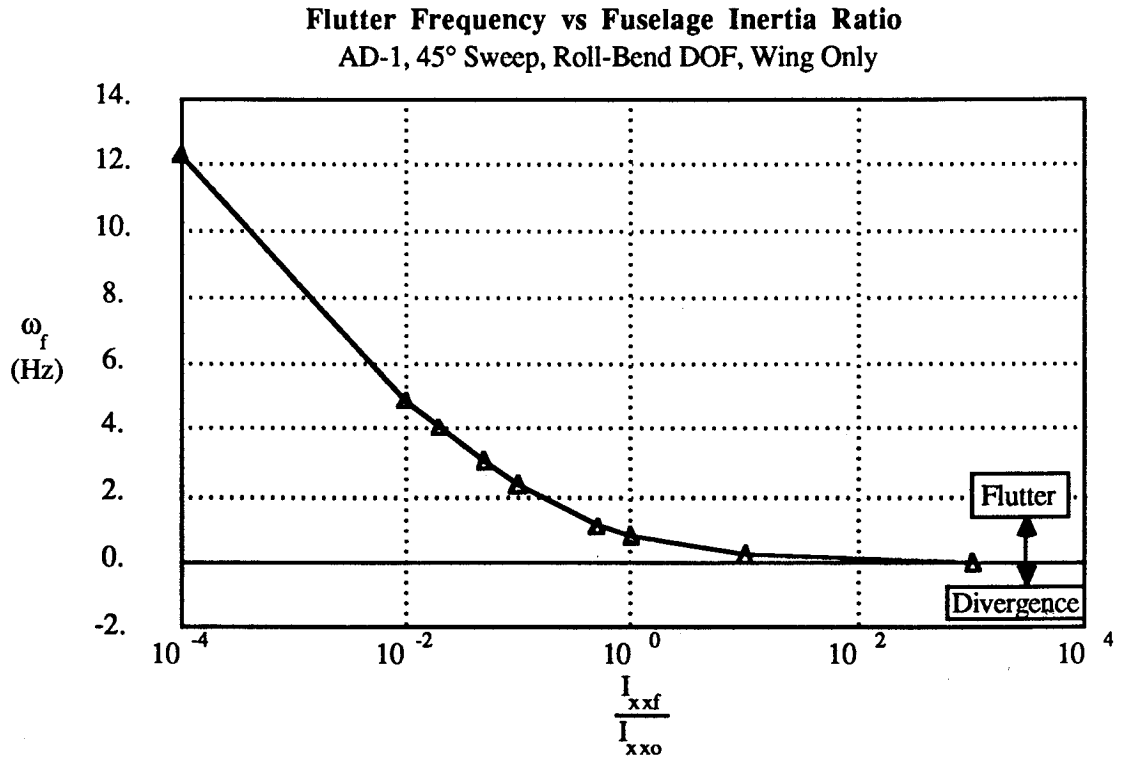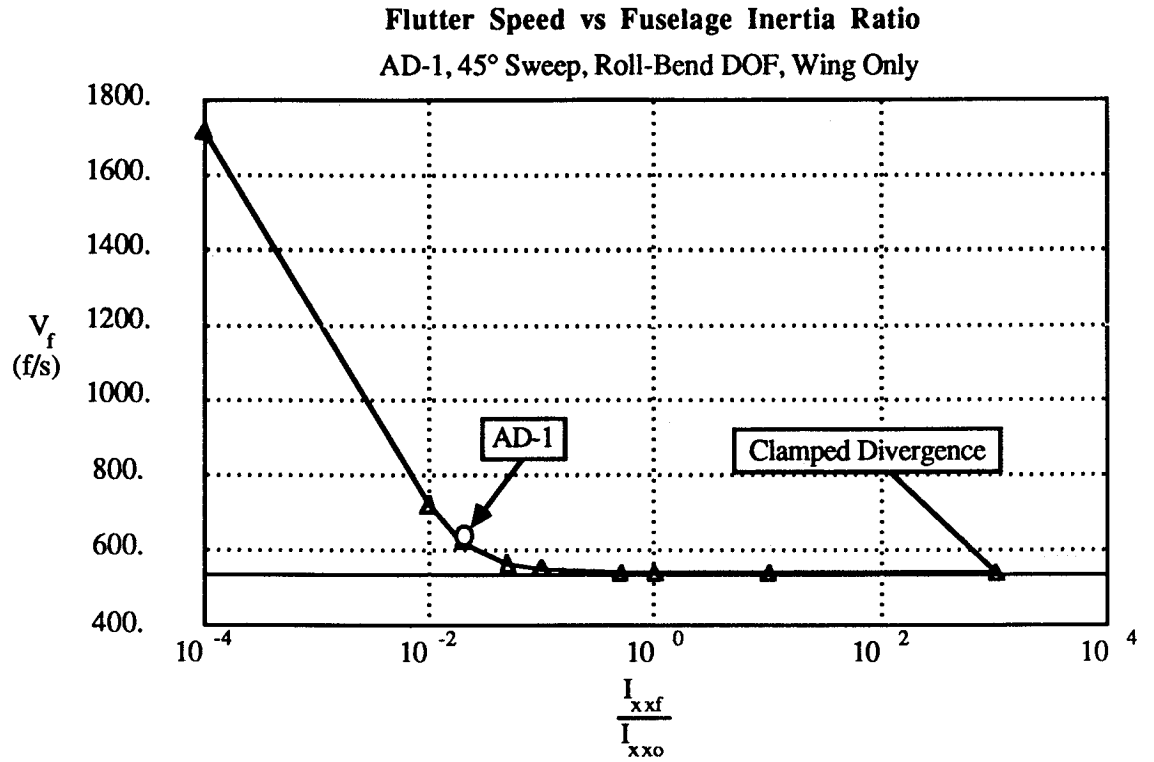
The horizontal and vertical tail size can also influence flutter speed because they affect the aircraft's overall roll damping. To demonstrate this, the AD-1 configuration with 45° sweep is studied with various size tails and the flutter speed and frequency is plotted as tail size increases (assuming no affect on inertia) in figures 6.18 and 6.19. Figure 6.18 shows that flutter speed initially increases with increasing tail size because the additional roll damping removes energy from the flutter mode. As the tail size continues to increase the roll damping becomes detrimental as it resists the rolling motion and effectively clamps the fuselage. Typically, the tail size required for this negative effect to occur is unrealistically large and in general the tail's influence on flutter speed is favorable.

Flutter Speed vs Tail Roll-Damping

AD-1, 45° Sweep, Roll-Bend DOF
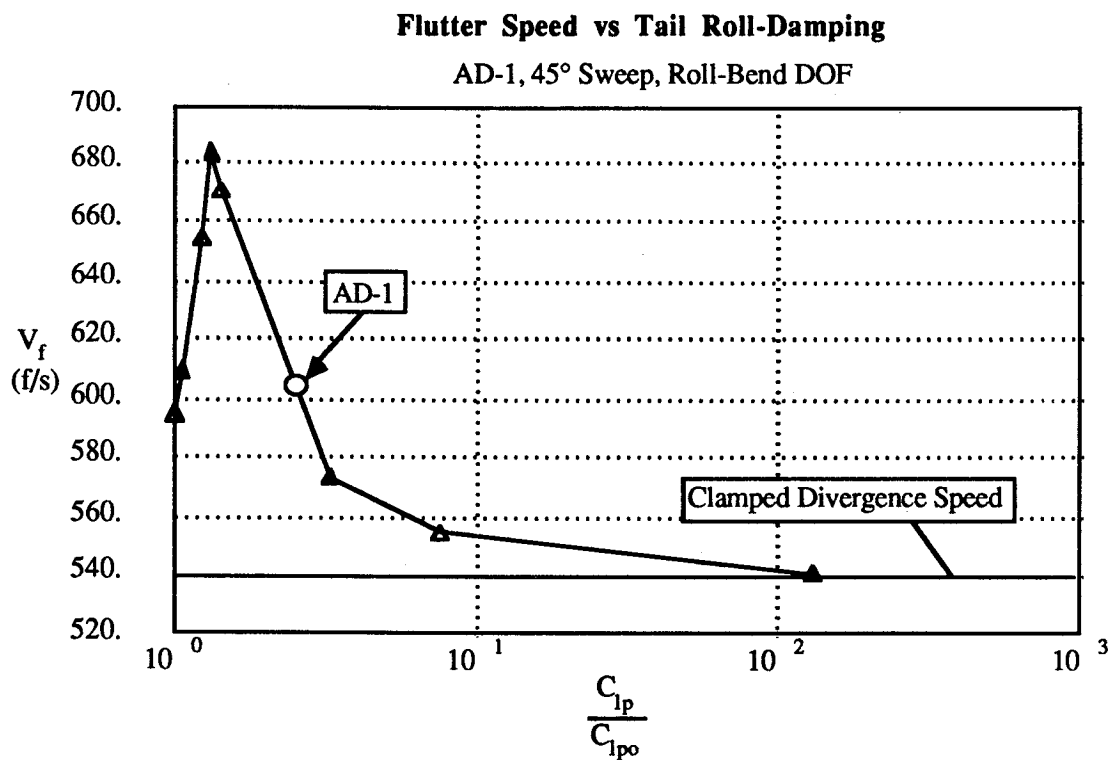
Figure 6.18 flutter speed vs. tail roll-damping

Flutter Frequency vs Tail Roll-Damping
AD-1, 45° Sweep, Roll-Bend DOF
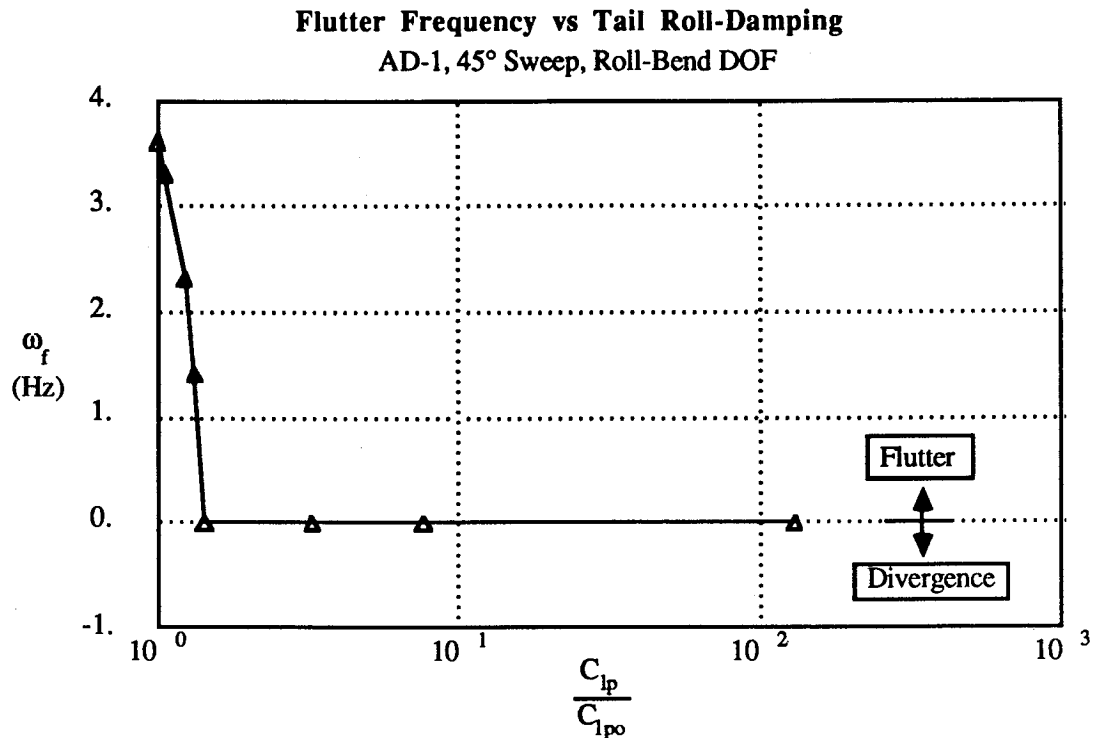
Figure 6.19 flutter frequency vs. tail roll-damping

6.3 Influence of Wing Flexibility on the Closed Loop Handling Qualities of the F-8 OWRA

To asses the impact of wing flexibility on oblique wing handling qualities, the closed loop performance of the F-8 OWRA is studied, with and without an elastic wing. An RMF SAS for the nominal configuration OWRA with a rigid wing has already been discussed (chapter 3) and this synthesis is repeated here with an additional degree of freedom for wing bending. A single parabolic wing bending mode is included in the aircraft's dynamics model to account for the affects of aeroelastic wing deformation on the airloads and the dynamic lag of wing bend during maneuvers. The dynamics model used in the synthesis is the Mil. Spec. F-8785C model previously presented in chapter 3, but augmented to include dummy states which represent zero wing deformation. In the synthesis, the RMF SAS attempts to force the flexible OWRA's dynamic response to be most like that of the rigid model's. This synthesis could be extended to include flutter suppression (in future work) if the flight condition is chosen so that flutter is critical, more bending modes are assumed for the wing, and aileron control surfaces are modeled. Because the dynamics model is rigid and

stable, the SAS would attempt to stabilize the flutter and restore handling qualities most like that of the rigid decoupled aircraft. This differs from conventional flutter suppression designs where only flutter stability is the goal.

The synthesis is carried out identically to the RMF SAS synthesis described in 3, except that the EOM are now calculated using the linearized EOM for the free-flying aircraft with an elastic wing (section 6.1). The structural model for the F-8 OWRA's wing is chosen to produce the same first bending frequency and 1-g wing tip deflection as the preliminary design results [Ref. 21] predict. Figure 6.20 shows the assumed mass and stiffness distribution for the wing which meets these requirements.

Wing Bending Stiffness vs Semi-Span
F-8 OWRA 300 (ft^2) Wing

$x10^7$

EI (lb-ft^2)

Semi-Span (ft)

Vaccum Bending Frequency = 5.73 Hz

1-g Tip Deflection = 9.6 inches
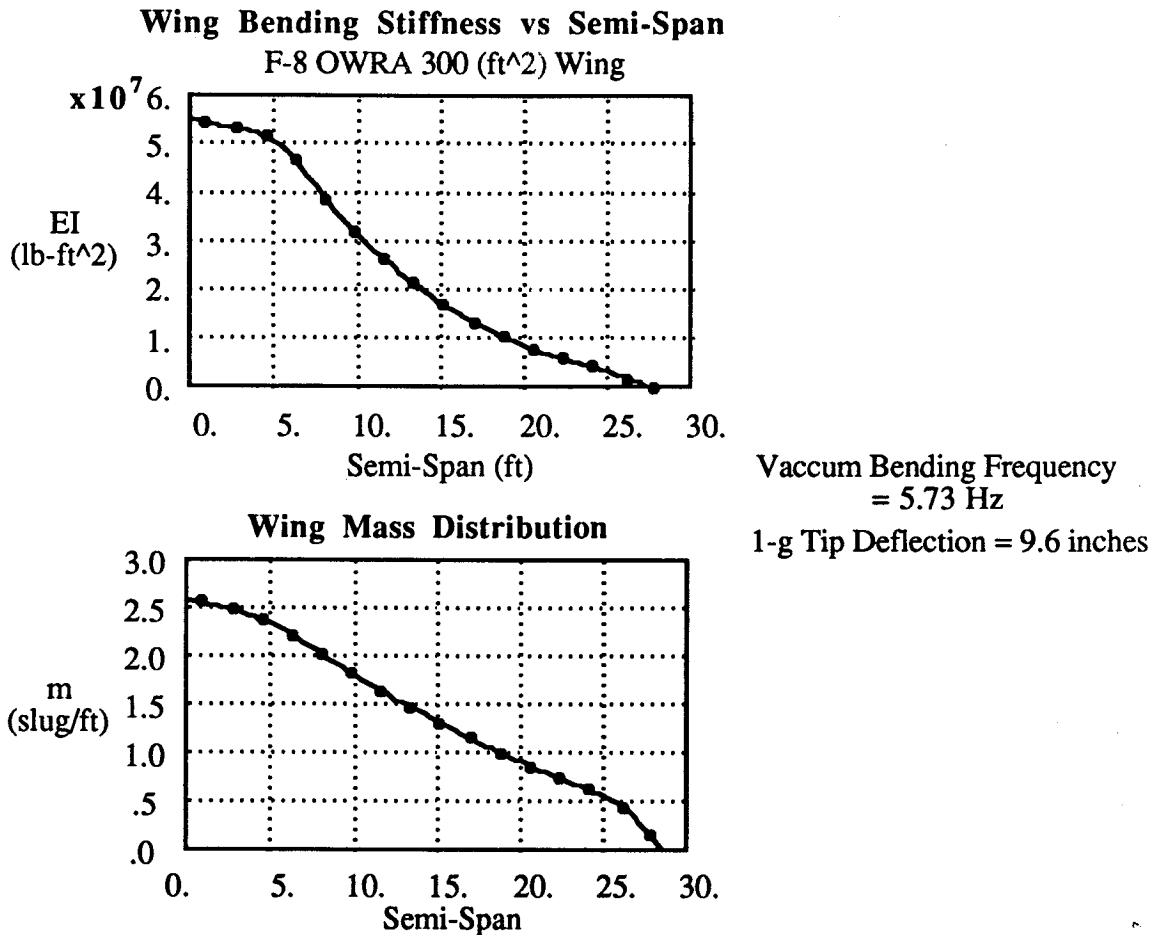
Wing Mass Distribution

m (slug/ft)

Semi-Span

Figure 6.20 F-8 OWRA wing structural model

The weighting matrices and initial conditions assumed for the synthesis are identical to those in section 3.3.2.3, except that no weight is placed on the wing tip deflection states (table 6.2).

Output error weighting

$$[Q] = \text{diag} \; \overset{g_y \;\; g_z \;\; p \;\; q \;\; r \;\; \phi}{[\; 10, \; 5, \; 1, \; 1, \; 1, \; 10 \;]}$$

Control effort weighting

$$[R] = \text{diag} \; \overset{\delta_{roll} \;\; \delta_{pitch} \;\; \delta_{yaw}}{[\; 100, \; 100, \; 100 \;]}$$

Pilot command washout filter pole location

$\varepsilon = 2.0$

Actuator pole location

$s = 10.0 \; (1.6 \; \text{Hz B.W.})$

RMF SAS Initial Conditions

vertical gust $\quad \tilde{y}_o = [\; 0, \; 0.5, \; 0, \; 0, \; 0, \; 0, \; 0, \; 0, \; 0, \;]^T$

lateral gust $\quad \tilde{y}_o = [\; 0.5, \; 0, \; 0, \; 0, \; 0, \; 0, \; 0, \; 0, \; 0 \;]^T$

roll input $\quad \tilde{y}_o = [\; 0, \; 0, \; 0, \; 0, \; 0, \; 0, \; 0.5, \; 0, \; 0, \;]^T$

pitch input $\quad \tilde{y}_o = [\; 0, \; 0, \; 0, \; 0, \; 0, \; 0, \; 0, \; 1.0, \; 0 \;]^T$

yaw input $\quad \tilde{y}_o = [\; 0, \; 0, \; 0, \; 0, \; 0, \; 0, \; 0, \; 0, \; 0.5 \;]^T$

Table 6.2 flexible wing OWRA RMF SAS synthesis input parameters

The performance of the closed loop OWRA (with RMF SAS and flexible wing) performing the 4-g pitch-up maneuver is shown in figures 6.21 - 6.27.

Lateral Acceleration vs Time
Nominal OWRA, 45° Sweep
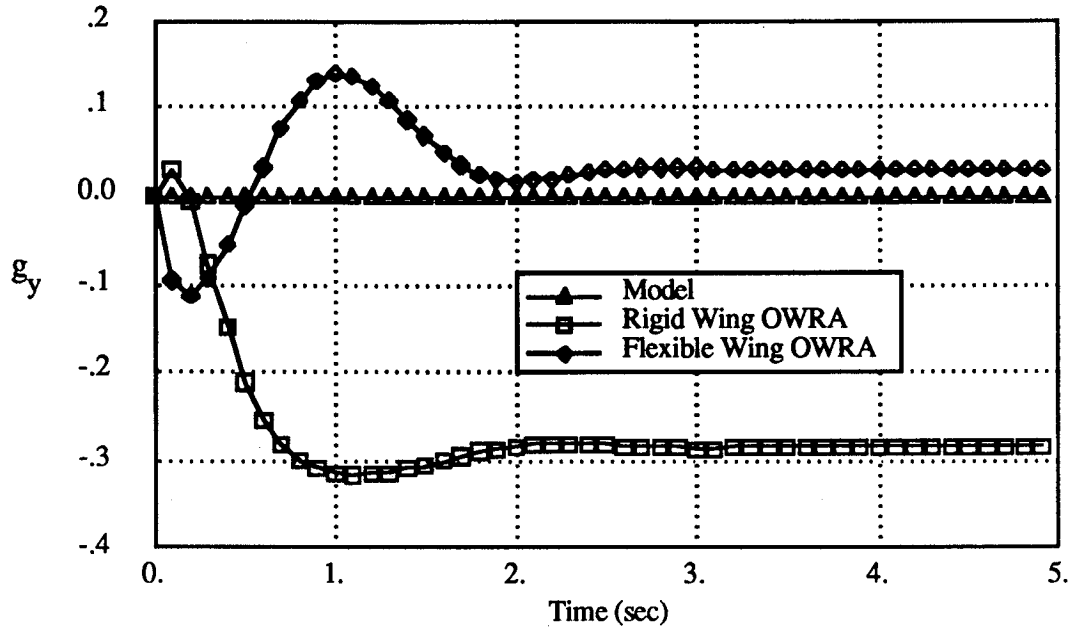
Figure 6.21 lateral acceleration vs. time

Normal Acceleration vs Time
Nominal OWRA, 45° Sweep
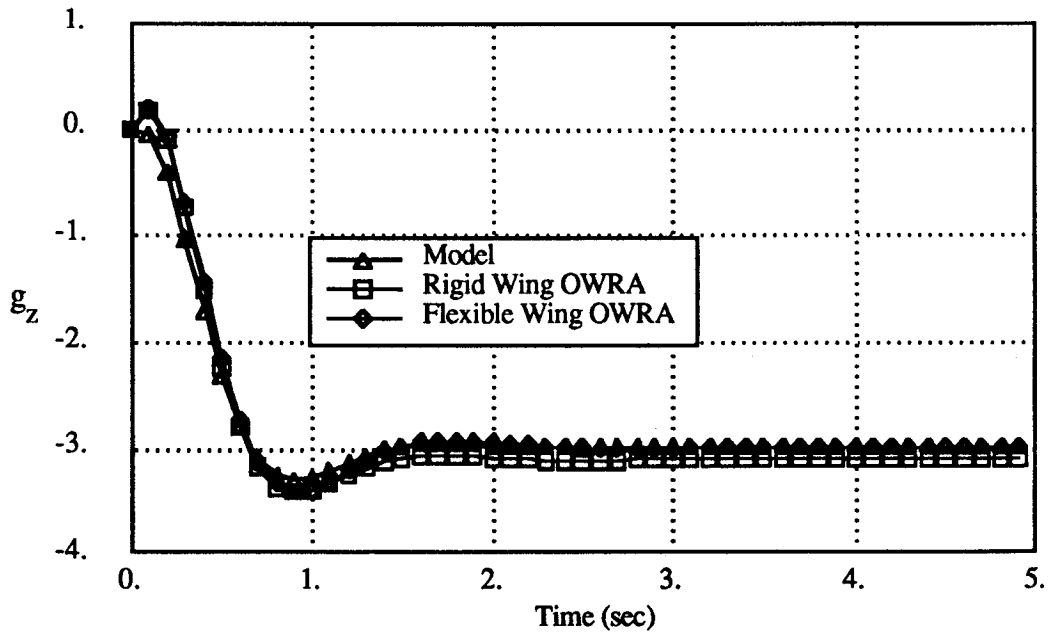
Figure 6.22 normal acceleration vs. time

231

Pitch Rate vs Time
Nominal OWRA, 45° Sweep

Figure 6.23 pitch rate vs. time

Yaw Rate vs Time
Nominal OWRA, 45° Sweep

Figure 6.24 yaw rate vs. time

Roll Angle vs Time
Nominal OWRA, 45° Sweep
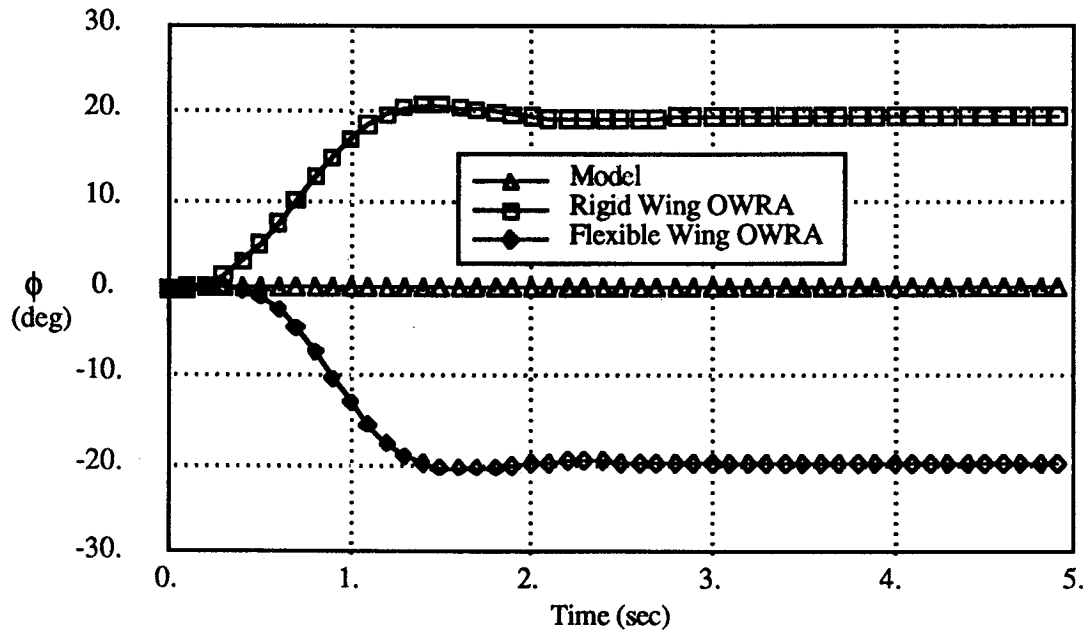
Figure 6.25 roll angle vs. time

Tip Deflection vs Time
Nominal OWRA With Flexible Wing, 45° Sweep
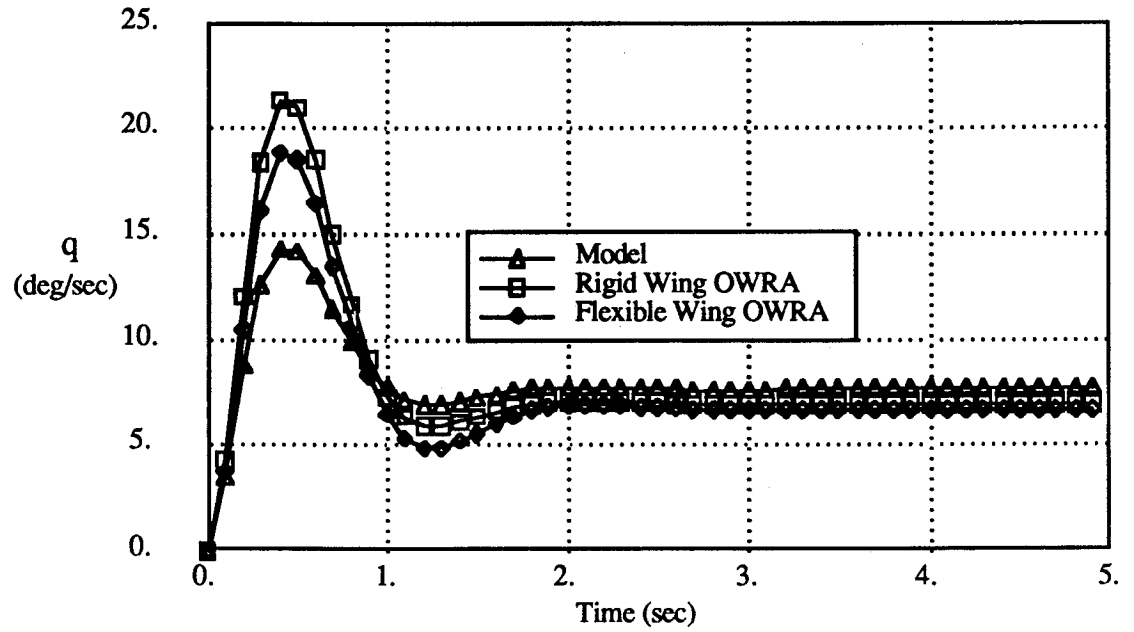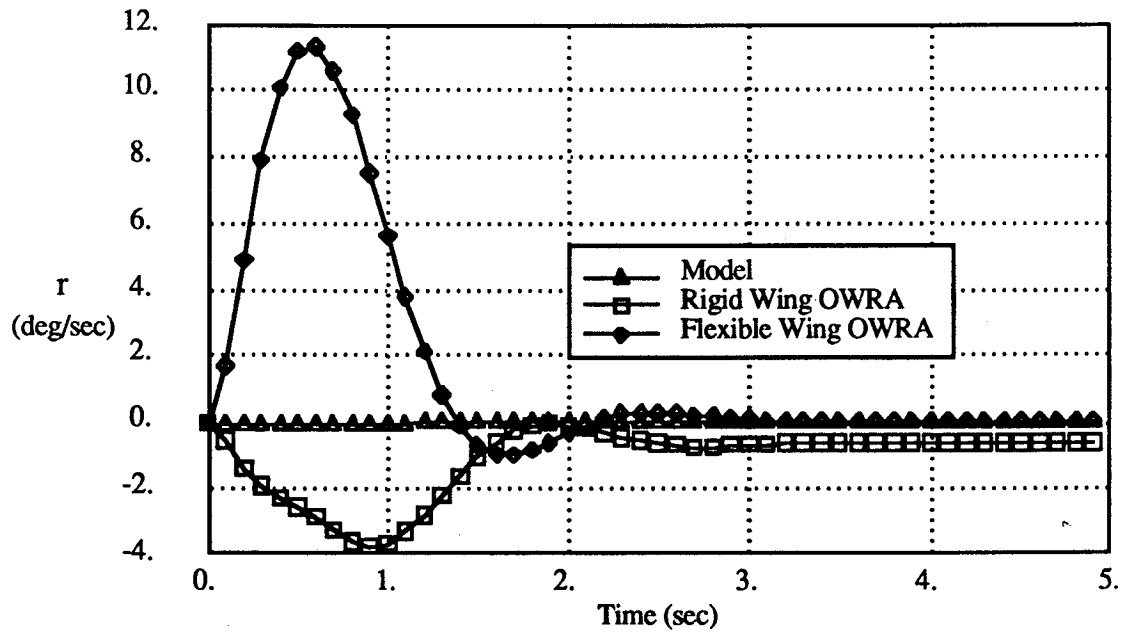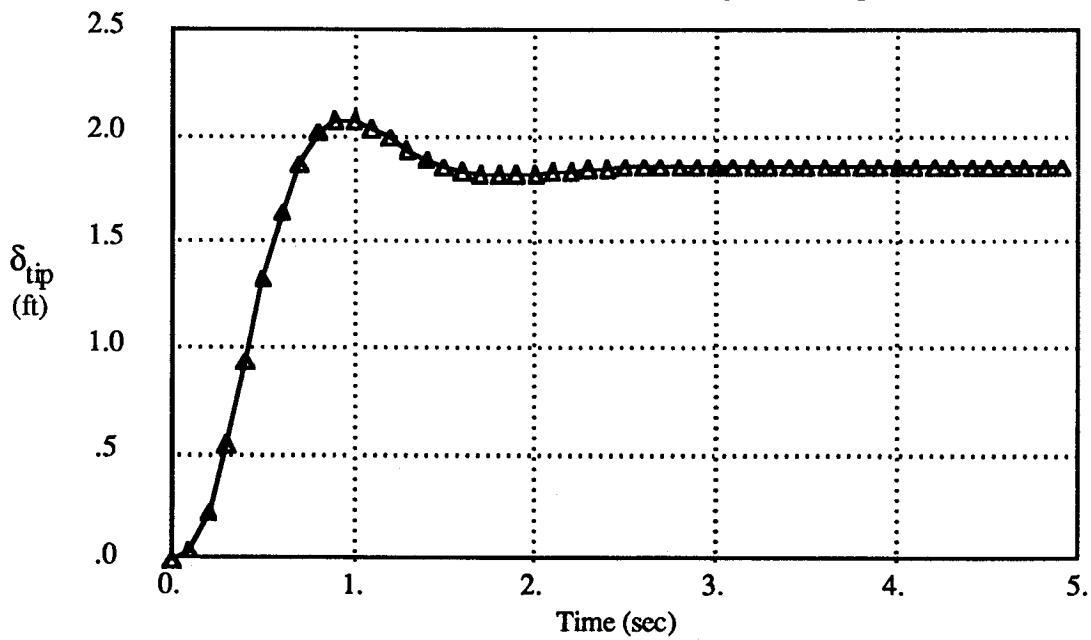

Figure 6.26 wing tip deflection vs. time

233

Control Surface Deflection vs Time
Nominal OWRA, 45° Sweep
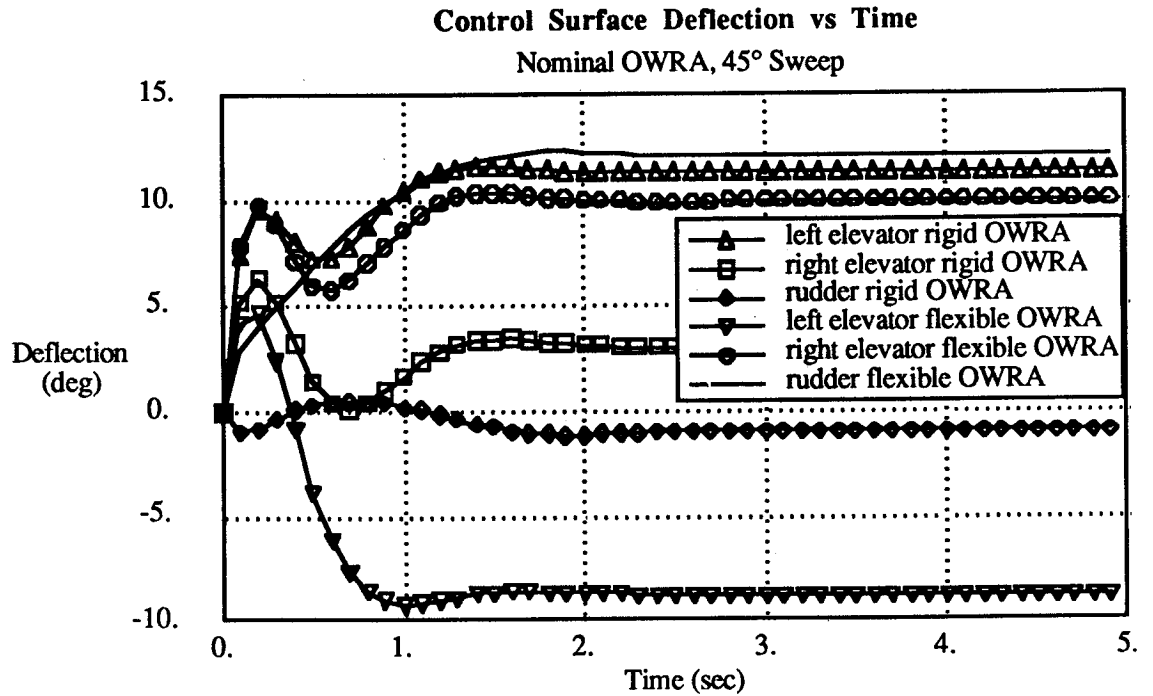
Figure 6.27 control surface deflection vs. time

The excursions in lateral acceleration, yaw rate, and roll angle are still large for the nominal closed loop OWRA with a flexible wing, which indicates that wing flexibility has not significantly contributed to the aircraft's controllability and therefore, re-design of the configuration is still needed. The flexible aircraft shows reduced lateral acceleration during the pitch-up maneuver, but increased yawing motion. The elastic wing design is using excessive sideslip (8 °) to limit excursions in lateral acceleration, where as the rigid aircraft merely rolled right. A most noticeable difference between the response of the two aircraft is that the rigid one rolls right (+20° roll) during the maneuver, where as the elastic one rolls left (-20°). The strong influence of wing bending , which produces a roll-left coupling with increased normal load, is clearly dominating the response of the OWRA with the elastic wing. These results show that it is a gross error to assume that a rigid wing model adequately describes the dynamics of the OWRA and furthermore, that a SAS designed for the rigid aircraft has little in common with an appropriate SAS for the flexible design. Wing flexibility must be included in even the preliminary assessments of handling qualities of oblique wing designs.

6.4 MIDSM Synthesis of the F-8 OWRA
with a Flexible Wing,
45° Sweep, M=0.8

The previous example has demonstrated that the F-8 OWRA with wing flexibility still has insufficient controllability to produce acceptable closed loop handling qualities and that wing elasticity significantly alters the aircraft's dynamic response. These results indicate that the optimal OWRA configuration with wing flexibility may be very different from the optimal rigid configuration. To test this hypothesis, MIDSM is used to re-design the flexible wing OWRA at 45° sweep and M=0.8. AN RMF SAS is assumed and all of the inputs are identical to those in the previous example. The configuration design variables considered are:

ϕ_b	= Wing bank angle relative to the fuselage
X_{pw}	= Root chordwise location of the wing pivot
X_{pf}	= Location of the wing pivot along the fuselage
dihedral	= Tip deflection due to jig-built parabolic dihedral

Table 6.3 design variables for OWRA synthesis with wing flexibility

Notice that the dihedral now defines the jig built value, so that the trim solution automatically accounts for the additional 1-g deformation that occurs at trim. The results from MIDSM are presented in figures 6.28 - 6.34. A comparison of the optimized rigid and flexible wing OWRA configurations with the nominal design is given in figure 6.28. The optimized flexible wing OWRA shows significantly more wing bank and different wing displacement than the optimal rigid wing design, verifying that wing flexibility alters the optimal oblique wing configuration.

ϕ_b	= -8.5 (deg)
X_{pw}	= 4.79 (ft)
X_{pf}	= 38.81 (ft)
dihedral	= -.008

Table 6.4 optimal configuration variables
45° sweep OWRA, RMF SAS, flexible wing

235

Nominal OWRA

MIDSM OWRA
(flexible)

Top

Front

Side
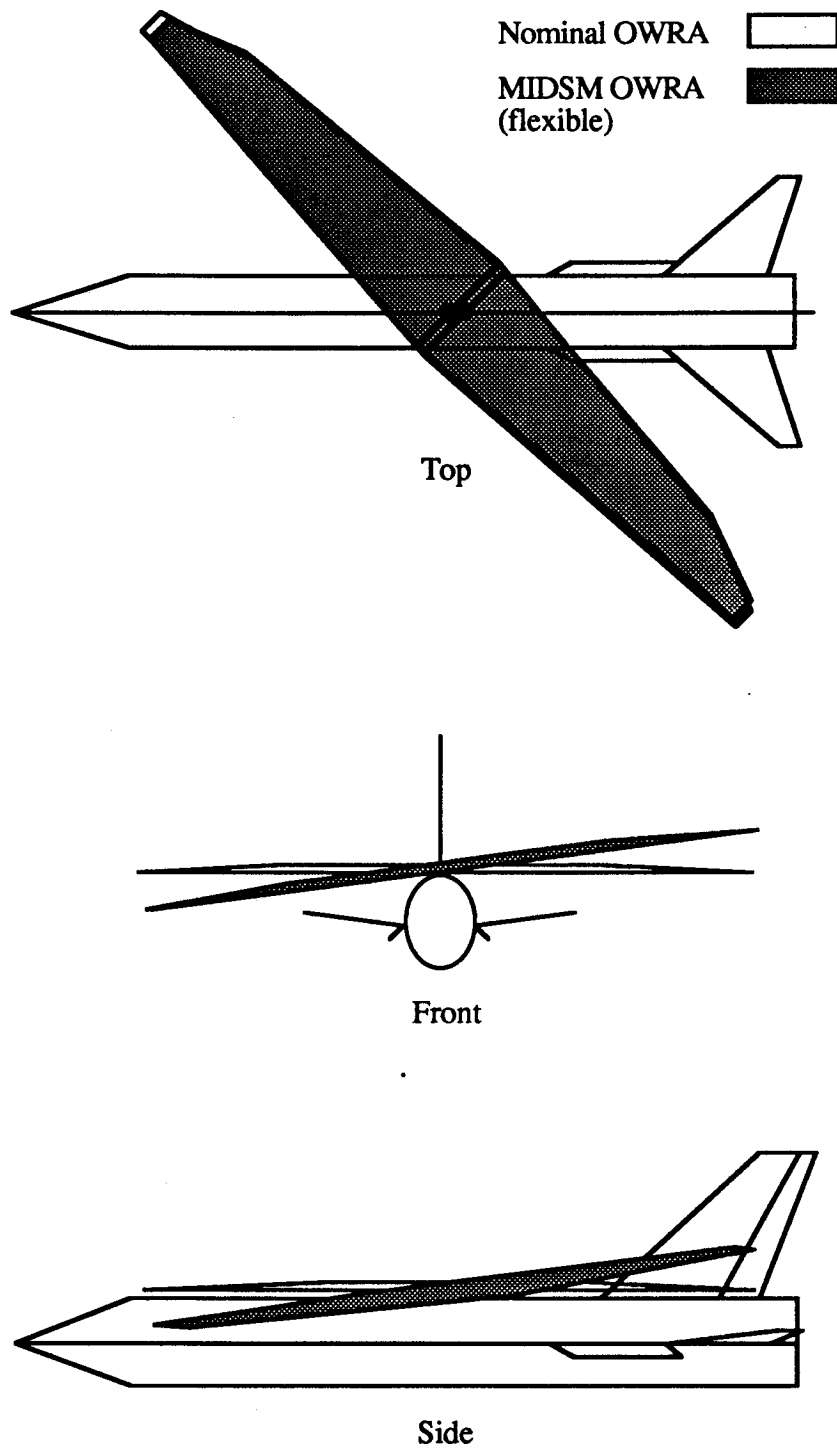
Figure 6.28 MIDSM F-8 OWRA with flexible wing

236

Lateral Acceleration vs Time
45° Sweep OWRA
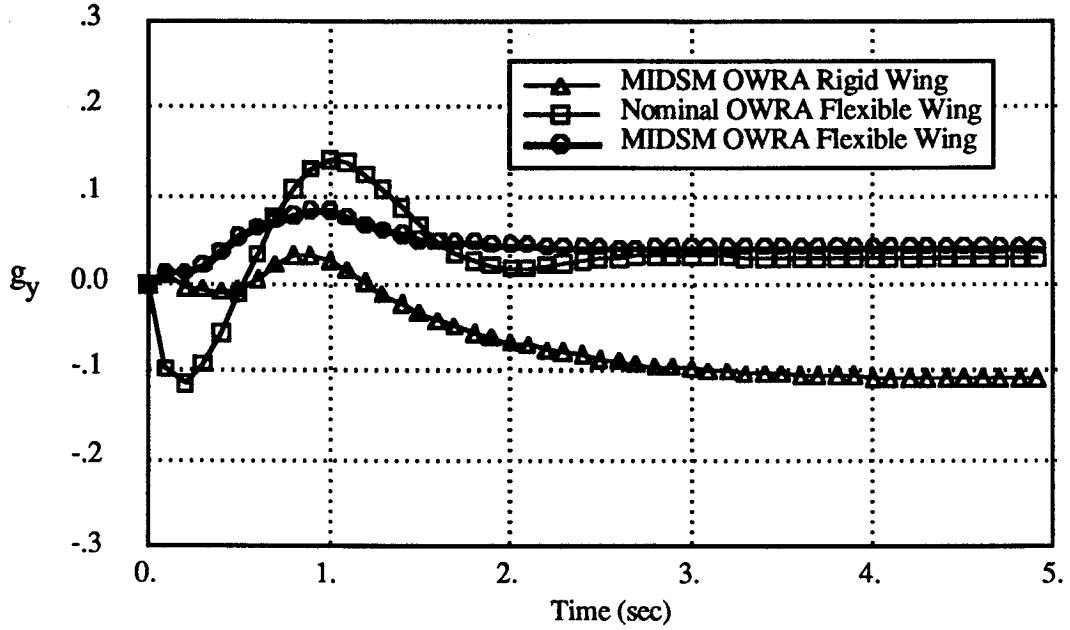
Figure 6.29 lateral acceleration vs. time

Normal Acceleration vs Time
45° Sweep OWRA
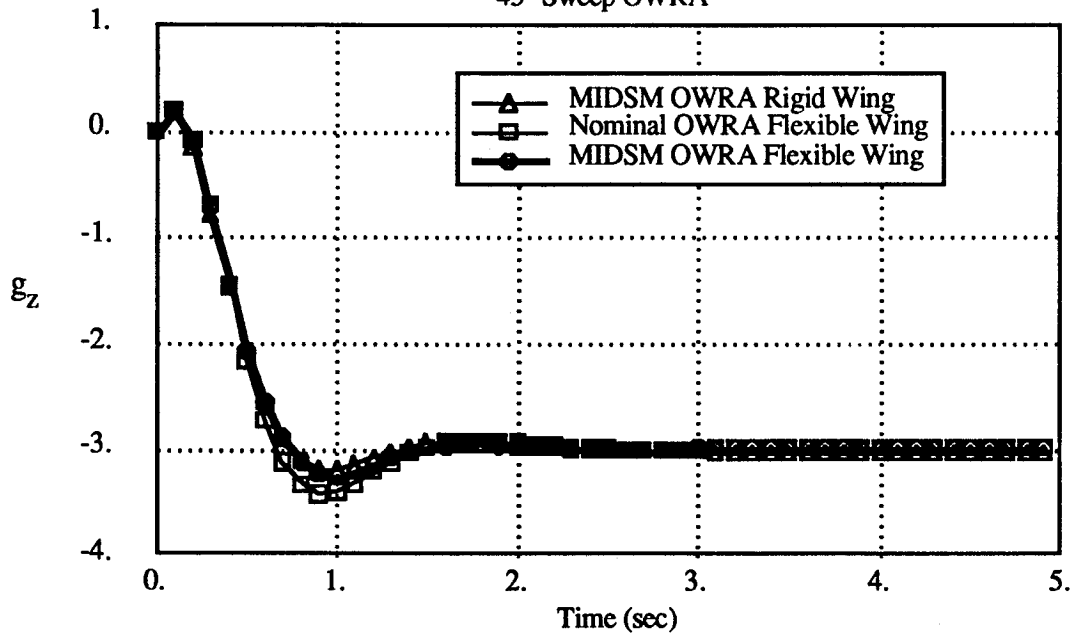
Figure 6.30 normal acceleration vs. time

237

Yaw Rate vs Time
45° Sweep OWRA
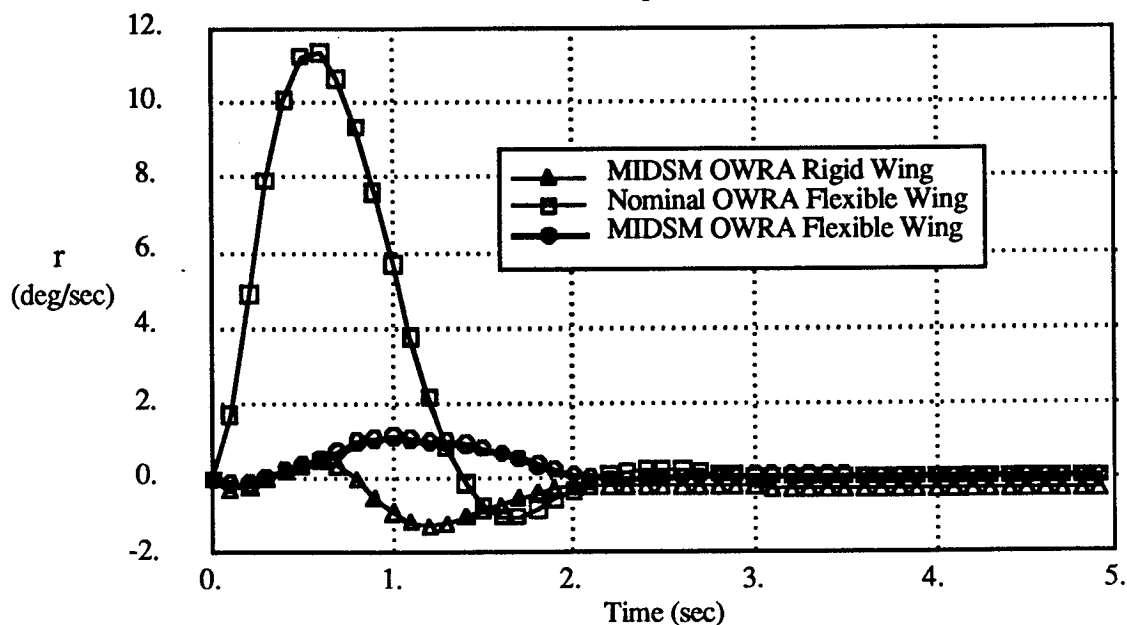
Figure 6.31 yaw rate vs. time

Roll Angle vs Time
45° Sweep OWRA
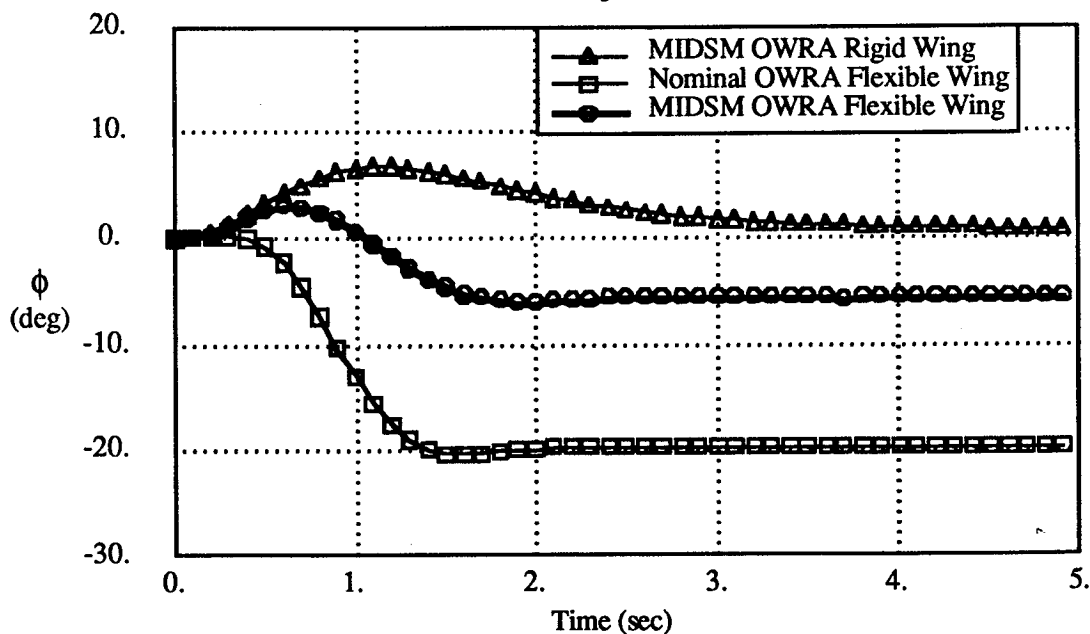
Figure 6.32 roll angle vs. time

238

Wing Tip Deflection vs Time
45° Sweep OWRA
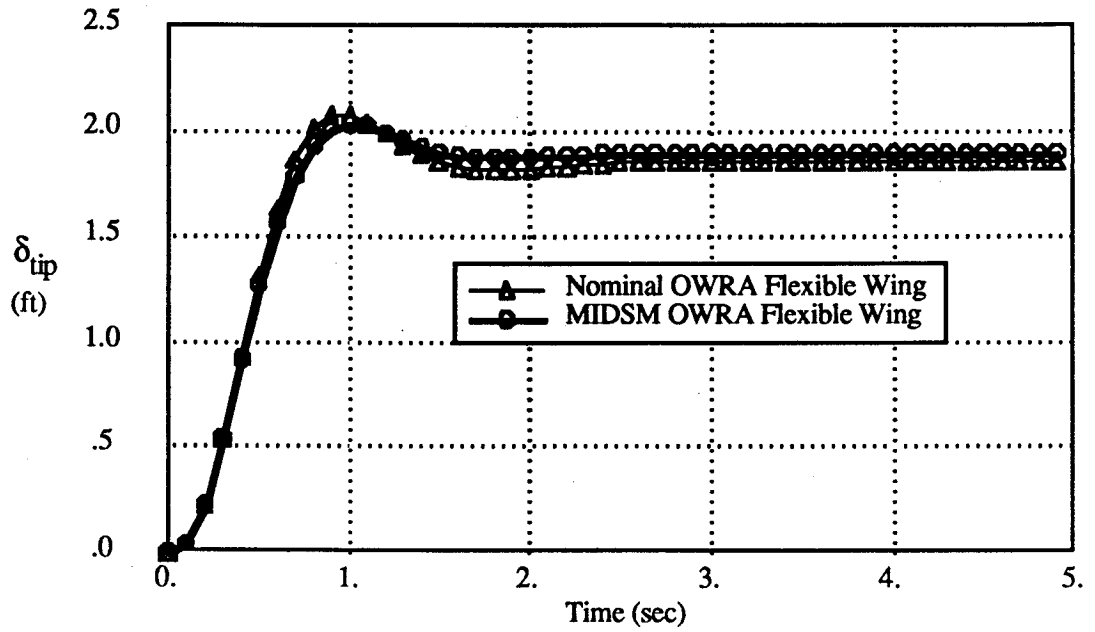
Figure 6.33 tip deflection vs. time

Control Surface Deflection vs Time
45° Sweep OWRA
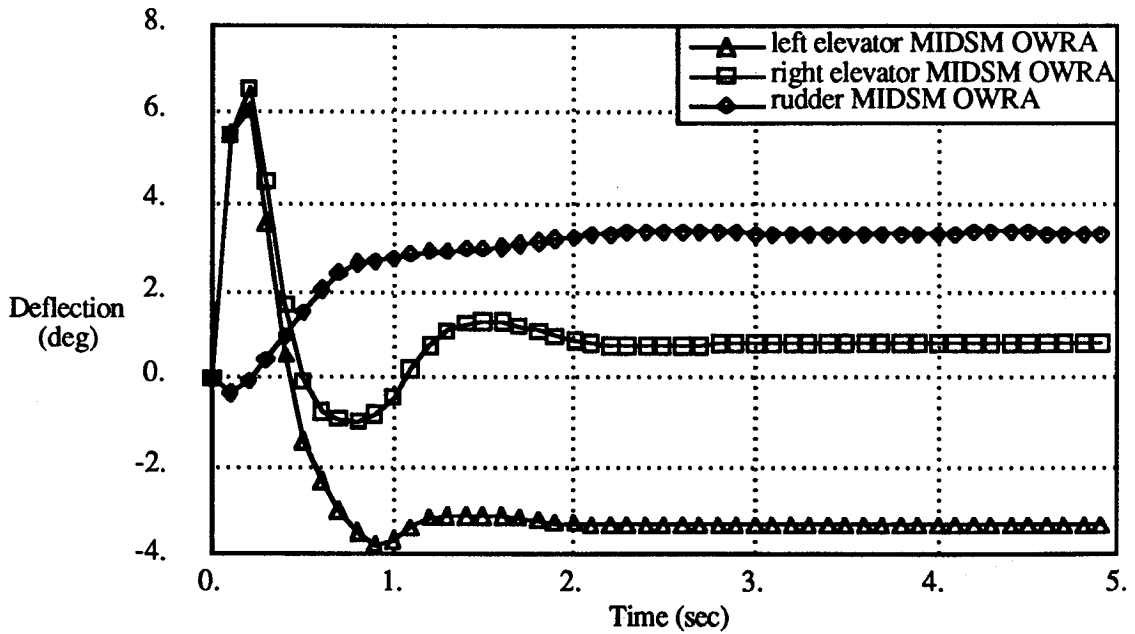
Figure 6.34 control surface deflectoin vs. time

239

The impact of the design changes on the OWRA's handling qualities is shown in the simu-
lated 4-g pitch-up maneuver in figures 6.29 - 6.34. Table 6.5 summarizes the peak excur-
sions in the coupling variables for the nominal, optimal rigid, and optimal elastic designs.

	Nominal OWRA Flexible Wing	MIDSM OWRA Flexible Wing	% Improvement	MIDSM OWRA Rigid Wing
g_{ypeak}	0.12	.07	42%	-.11
ϕ_{peak} (deg)	-19	-6	68%	6.7
r_{peak} (deg/sec)	11.5	1.1	90%	-1.2

Table 6.5 optimized flexible wing OWRA performance summary

These results show that the dynamic response of the flexible wing OWRA is significantly
improved by the MIDSM re-design and its performance is equal to or better than the opti-
mized rigid aircraft. Even though the optimal rigid and elastic wing designs have similar
values of the peak coupling variables, their dynamic responses are quite different. Com-
parison of figures 6.29 - 6.34 reveals that the optimal rigid OWRA rolls right during the
pitch-up maneuver, where as the flexible aircraft first rolls right and then left. The elastic
wing aircraft is designed with an excess amount of wing bank so that the initial roll motion
is to the right, but as the wing reaches its maximum deformation (1 second later) the
coupling of wing displacement and wing bend causes a left roll which keeps the overall roll
excursion very small. The initial right-roll also reduces the amount of lateral acceleration to
the left. The improved response is obtained by a re-configuring of the aircraft that not only
accounts for the effects of static wing deformation on the response, but is also dependent
upon the dynamic deflection of the wing itself. For example, the correct amount of wing
"overbanking" is highly dependent upon the time lag associated with the wing bending in
order to produce the proper reversal in roll rate during the pitch-up. The optimized rigid
OWRA designs obtained most of their dynamic response improvement by re-configuring
the aircraft for reduced $C_{l\alpha}$ and $C_{y\alpha}$ coupling. It is reasonable to assume that a similar
process has occurred in the flexible wing design, except that the static aeroelastic values of
the coupling terms are made small. Table 6.6 presents these coupling terms for the various
designs so that this theory can be investigated.

	Nominal OWRA (Rigid Wing)	Nominal OWRA (Elastic Wing)	MIDSM OWRA (Elastic Wing)
$C_{y\alpha}$	-.2751	-.2417	.1882
$C_{l\alpha}$	.0574	-.1046	-.0114
$C_{m\alpha}$	-1.3112	.6428	.433
$C_{n\alpha}$	-.0397	-.0694	-.0419

Table 6.6 aerodynamic coupling of the optimized flexible wing OWRA
(static aeroelastic values)

The static aeroelastic value of $C_{l\alpha}$ is significantly reduced in the optimized design, but the values of $C_{y\alpha}$ and $C_{n\alpha}$ are not made small. Notice also that the $C_{y\alpha}$ term is reversed in sign and made large by the wing "overbanking". These results demonstrate that the optimal design is not merely an "aeroelastic decoupling" of the nominal OWRA configuration, but is instead a highly integrated design which depends upon the detailed dynamic interaction between aircraft motion and wing flexibility. These results further stress the importance of wing elasticity as a significant phenomenon in the preliminary design of an oblique wing aircraft, perhaps more so than for a conventional symmetric aircraft.

6.5 OWRA Synthesis for Optimal Wing Flexibility

Because wing flexibility can produce changes in the aerodynamic coupling which oppose the coupling present in the rigid aircraft, perhaps there is an optimal amount of wing flexibility for improved handling qualities (in an oblique wing design). To test this idea, the previous synthesis is repeated with the wing modulus of elasticity (E) as an additional design variable. The inputs are identical to the previous example, and the initial guess for E is 10×10^6 (psi). The MIDSM results show that the optimized OWRA has the same values for the configuration variables as the previous optimized elastic wing design, and the optimal wing stiffness is 18×10^6 (psi), which is twice the nominal value. Figures 6.35 - 6.37 compare the dynamic response of this design to the optimized rigid and flexible wing OWRA's. Table 6.7 summarizes the peak excursions of the coupling variables.

	Rigid Wing	Elastic Wing	Elastic Wing Optimal (E)
g_{ypeak}	-.11	.07	.045
ϕ_{peak} (deg)	6.7	-6	6.
r_{peak} (deg/sec)	1.2	1.1	-1.56

Table 6.7 performance comparison optimized wing flexibility OWRA
45° Sweep, RMF SAS

Lateral Acceleration vs Time
45° Sweep OWRA
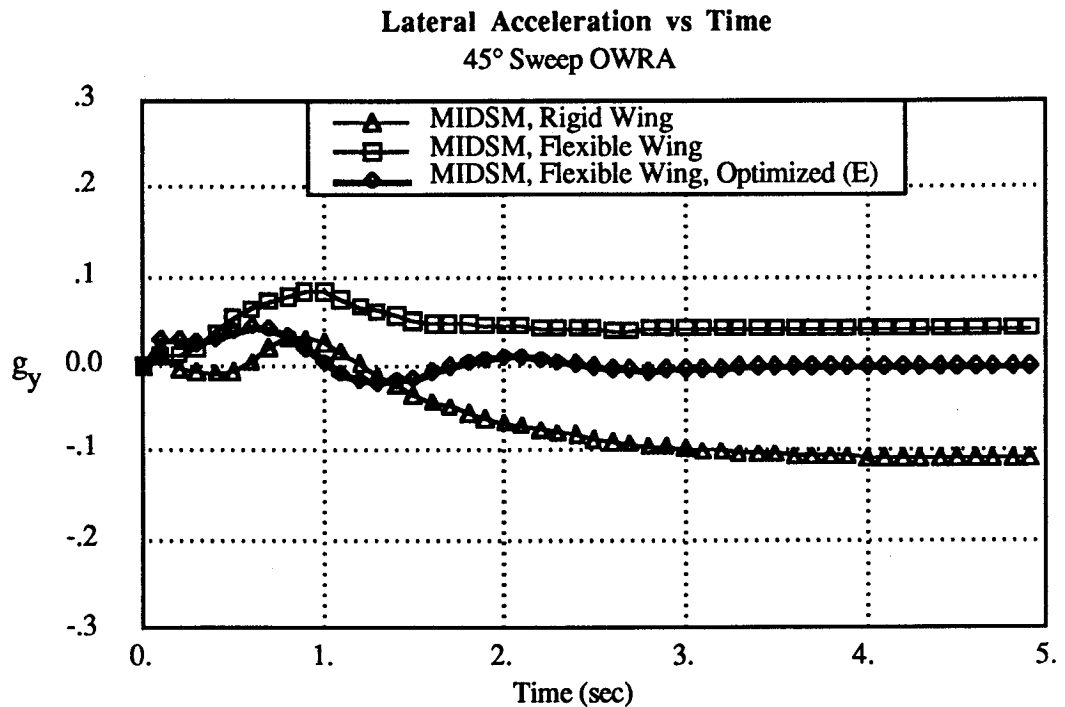
Figure 6.35 lateral acceleration vs. time

Roll Angle vs Time
45° Sweep OWRA
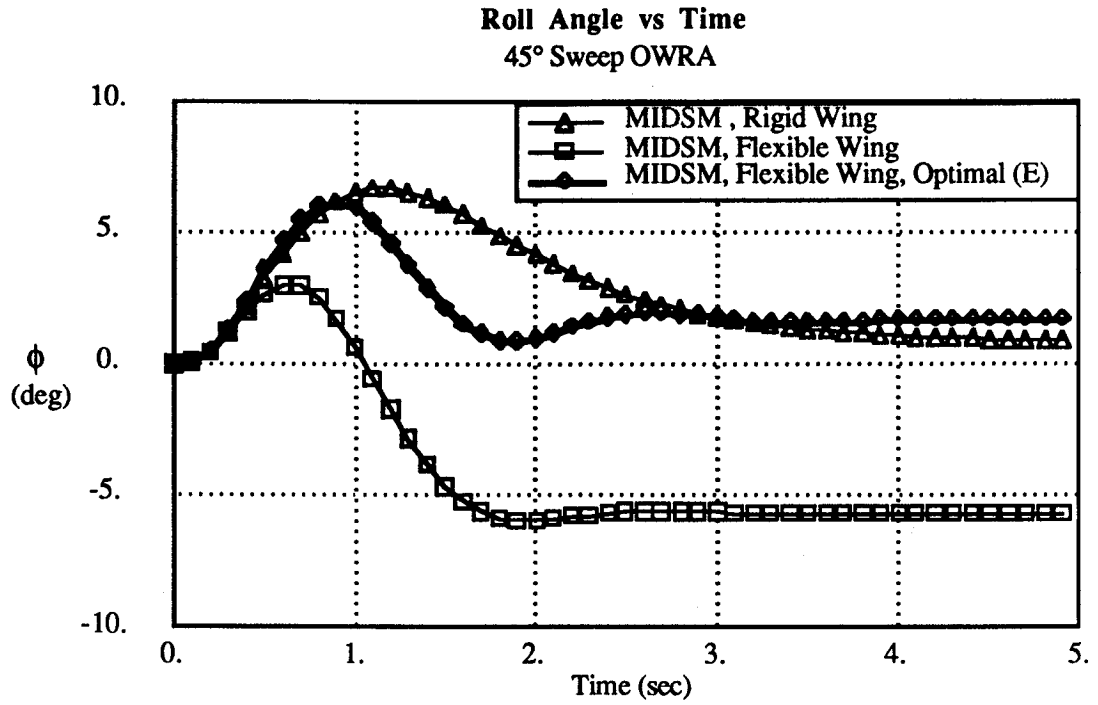
Figure 6.36 roll angle vs. time

Control Surface Deflection vs Time
45° Sweep OWRA, optimized wing stiffness
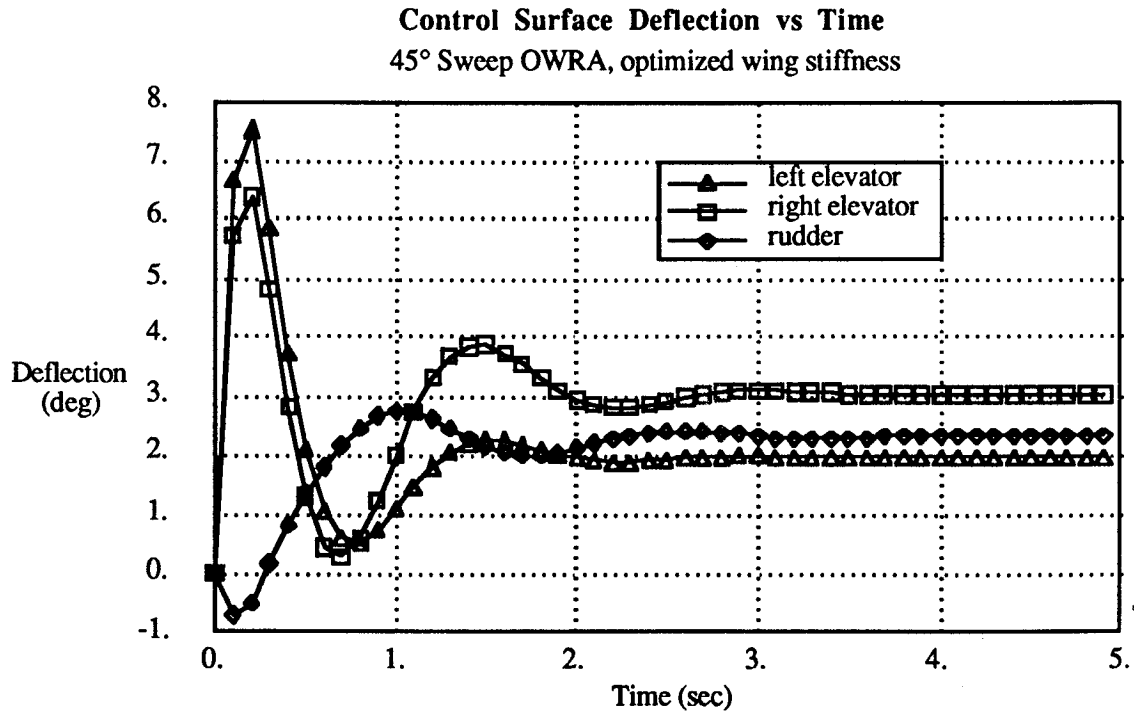
Figure 6.37 control surface deflection vs. time

243

The optimized stiffness design is superior in performance to the other cases considered (by a small margin) and achieves must of its performance in reduction of lateral acceleration and control activity. The time histories show more clearly that the model following error of this design is less than the optimal rigid and flexible designs previously considered. These results indicate that there is an optimum amount of wing flexibility for improved handling qualities in an oblique wing design and that an overly stiff wing can be just as detrimental as one that is too flexible. Furthermore, this example demonstrates that MIDSM is capable of integrating many disciplines (structures, aerodynamics, and controls in this case) into a single design synthesis method which is capable of improving aircraft performance where sequential methods would otherwise fail.

Chapter 7

Conclusions and Recommendations
for Future Work

7.1 Contributions

This work has demonstrated several new ideas and methods for the integrated synthesis of oblique wing aircraft and aircraft in general. The following list summarizes these contributions.

1) A method for accurately analyzing the forces and moments of an arbitrary oblique wing configuration (in the attached flow regime) has been developed and tested (LINAIR). The airloads are calculated using a vortex lattice method which uses a nearfield flow solution to predict suction forces and loads normal to the panels. LINAIR accurately predicts the non-linear trends present in the aerodynamic coupling loads for the flow region where separation and supersonic leading edges are not present. The coupling between angle of attack and yawing moment is not well predicted by this analysis.

2) The nature of the unusual coupling between angle of attack and yawing moment has been discovered. The mutual interference between the obliquely swept wing (with thickness) and the fuselage produces an asymmetric flow over the forward part of the fuselage. The resulting pressure peak near the aircraft's nose produces a strong yaw moment (away from the forward swept wing) even at the zero lift condition. This effect can be captured by a panel code such as PANAIR.

3) A new model following SAS synthesis method has been developed. The reduced model following SAS (RMF) shows several advantages over previously implemented explicit and implicit model following controllers. The RMF controller attempts to match both the forced and the unforced response of the model's dynamics without any restrictions on the SAS architecture, except that it be linear. In the case where the controllability is reduced or the

245

control authority weighting is large, the performance of this controller degrades such that the linear quadratic cost function representing the model following error plus control effort is minimized. Because the RMF SAS attempts to match both the forced and unforced response of the model, the bandwidth of the feedback control can be substantially less than that required for an explicit model following SAS (which does not attempt to match the unforced response of the model). The freedom to implement partial state feedback in the RMF controller permits the designer to enforce bandwidth restrictions on actuators and other devices without excessive adjustment of the weighting matrices. Comparisons of the SAS designs have shown that the RMF SAS can achieve dynamic response performance equal to the EMF SAS but with less control effort, lower bandwidth actuators, and partial state feedback for an oblique wing aircraft SAS.

4) The linearized equations of motion for a free flying aircraft with a flexible wing have been derived and tested. This approach combines the aeroelastic affects of dynamic wing deformation with the full 6 DOF associated with free flight, so that the interaction between aircraft flexibility and unrestrained motion is fully represented. Current methods for flutter analysis stress structural flexibility effects and are not well suited to model the dynamics of the rigid aircraft; similarly, the equations of motion normally used for stability and control studies often neglect all of the dynamics necessary to accurately predict flutter. The derivation presented in this work does not compromise in either of these fields and is therefore capable of predicting unusual flutter modes such as the oblique wing aircraft's roll wing-bend flutter as well as the oblique wing aircraft's handling qualities. The equations can be reduced to study only the effects of flexibility or rigid aircraft dynamics, if so desired. The form of the EOM preserves all of the terms present in the equations for the rigid 6 DOF aircraft so that the influence of flexibility on the aircraft's dynamics can be seen explicitly.

5) Analysis of the 6 DOF oblique wing aircraft with a flexible wing has verified that the critical flutter mode (roll-bend) is still the critical mode of instability when all 6 DOF are included in the analysis. Previous work had only considered roll, pitch and plunge DOF with wing isolated aerodynamics. This work has extended these results to include complete aircraft aerodynamics and 6 DOF motion.

6) An integrated design synthesis method (MIDSM) which permits the designer to trade handling qualities for other types of mission performance is presented and demonstrated. Configuration design variables which determine the aircraft's layout, structure, etc. are included, along with (optional) control system gains, as design variables with which to minimize a composite objective function representing handling qualities and other specified types of mission performance. The MIDSM procedure finds the configuration and SAS which minimizes the total mission cost in a single integrated design synthesis. By varying the weight between handling qualities and other types of mission performance, an aircraft is synthesized for the greatest performance with a fixed level of handling quality. Examples presented in this work have shown that this procedure can design aircraft with performance that exceeds those designed sequentially (i.e. airframe first then SAS).

7) Integrated synthesis of an oblique wing aircraft and its control system for improved handling qualities was performed. Designs were synthesized for the aircraft at several flight conditions, rigid and elastic wing models, improved performance over a range of flight conditions, and with several types of SAS. In all cases studied the MIDSM method is able to significantly improve the controllability of the F-8 OWRA and therefore improve its closed-loop handling qualities. The results indicate that reductions in lateral acceleration and rolling motion during pitch maneuvers is large enough to raise the handling quality rating of the F-8 OWRA to an acceptable level.

7.2 Conclusion Summary

The MIDSM approach to the integrated design of oblique wing aircraft is capable of improving the aircraft's controllability for improved handling qualities by making minor configuration changes to the aircraft. This work has identified that nonlinearities due to changing flight condition and the influence of wing flexibility on the dynamic response are two factors which must be included in a final synthesis of an oblique wing design for a specific mission. A new type of model-following SAS (RMF SAS), which shows improved performance over other types of SAS architectures, shows great promise as a candidate controller in a future oblique wing design. Integrated designs of the F-8 OWRA with modeled wing flexibility and an RMF SAS have been presented and the method required to carry out this synthesis for a single aircraft at multiple flight conditions has also been demonstrated.

247

These examples provide the basic tools for the integrated design a final oblique wing aircraft configuration, once a mission specification is known. The aerodynamics, dynamics, and integrated design methods developed specifically to solve the oblique wing synthesis problem may also be applied to a host of other analysis and integrated synthesis studies involving non-oblique wing configurations.

7.3 Recommendations for Future Work

1) Improvements in the MIDSM synthesis:

  a) Incorporate the option for finite time integral evaluation of the dynamic cost as in reference 23.

  b) Calculate the gradients of the dynamic cost with respect to the control gains using the analytic expressions derived in reference 23.

2) Apply MIDSM in more detail to an oblique wing synthesis for a specific mission. This would include the design of a single aircraft for improved handling over the entire flight envelope with wing flexibility modelled.

3) Application of MIDSM to integrated design problems in other fields:

  a) Aeroservoelastic flutter suppression and possibly composite tailoring for flutter stability and improved handling qualities with minimum weight. Use MIDSM to design the structure and the SAS of an aircraft for improved handling with minimum weight when aeroelastic effects are significant.

  b) Analyze the trade-off between handling qualities and trimmed drag (and/or) improved maneuverability for aircraft with relaxed longitudinal stability. Use MIDSM to calculate optimal static margin and configuration.

  c) Application to non-aircraft problems such as minimum weight space structures with maximum active/passive damping to disturbances.

4) RPV study of oblique wing handling qualities. Use a small-scale, subsonic, remotely-piloted-vehicle with active control to verify the improvements in handling qualities that MIDSM calculates for oblique wing aircraft.

References

[1] Kroo, I., "The Aerodynamic Design of Oblique Wing Aircraft," AIAA-86-2624, Oct. 1986.

[2] Nelms, P., "Applications of Oblique-Wing Technology - An Overview," AIAA-76-943, Sept. 1976.

[3] Sim, A., Curry, R., "Flight Characteristics of the AD-1 Oblique-Wing Research Aircraft," NASA TP-2223, March 1985.

[4] Kempel, R., McNeill, W., Gilyard, G., Maine, T., "A Piloted Evaluation of an Oblique-Wing Research Aircraft Motion Simulation With Decoupling Control Laws," NASA TP-2874, Nov. 1988.

[5] Enns, D., Bugajski, D., Klepl, M., "Flight Control for the F-8 Oblique Wing Research Aircraft," *Proceedings of the 1987 American Control Conference*, Minneapolis, 1987, p. 1112.

[6] Curry, R., Sim, A., "In-Flight Forces, Moments, and Static Aeroelastic Characteristics of an Oblique-Wing Research Airplane," NASA TP-2224, Oct. 1985.

[7] Jones, R., Nisbet, J., "Aeroelastic Stability and Control of an Oblique Wing," *Aeronautical Journal*, Aug. 1976, pp. 365 - 369.

[8] Zeiler, T., Weisshaar, T., "Integrated Aeroservoelastic Tailoring of Lifting Surfaces," *Journal of Aircraft*, Vol. 25, No. 1, Jan. 1988, pp. 76-83.

[9] Sawaki, E., Kobayakawa, M., Imai, H., "A Design Method of an Aircraft with ACT by Nonlinear Optimization," *Trans. Japan Soc. of Aerospace Sciences*, Vol. 29, No. 85, Nov. 1986, pp. 142-162.

[10]. Jones, R., "Theoretical Determination of the Minimum Drag of Airfoils at Supersonic Speeds," *Journal of the Aeronautical Sciences*, Vol. 19, No. 12, Dec. 1952, pp. 813-822.

[11] Clarke, A., "Test of the 0.058-Scale VFMX Oblique Wing Model in the Rockwell International Trisonic Wind Tunnel," TFD-83-1354, Rockwell International, Dec. 1983.

[12] Kennelley, R., Carmichael, R., Kroo, I., Strong, M., Wind Tunnel Test of a NASA Designed 250 sq. ft. Wing for the F-8 OWRA, Personal Contact, NASA Ames Research Center.

[13] Kennelley, R., Carmichael, R., Kroo, I., "Transonic Wind Tunnel Test of an Oblique Wing for the F-8 OWRA," NASA TM Draft, June 1988.

[14] Kennelley, R., Carmichael, R., Kroo, I., "Transonic Wind Tunnel Test of a 14% Thick Oblique Wing," NASA TM Draft, March 1989.

[15] Sidwell, K., Baruah, P., Bussoletti, J., "PAN AIR - A Computer Program for Predicting Subsonic or Supersonic Linear Potential Flows About Arbitrary Configurations Using a Higher Order Panel Method. Vol. II User's Manual (Version 1.0),"
NASA CR-3252, 1980.

[16] Kroo, I., "LinAir — A Discrete Vortex Weissenger Method for Rapid Analysis of Lifting Surfaces," Desktop Aeronautics, 1987.

[17] Carmichael, R., Aerodynamic Load Predictions Using PANAIR for the F-8 OWRA, Personal Contact, NASA Ames Research Center.

[18] Schlichting, H., Truckenbrodt, E., "Aerodynamics of the Airplane,"
McGraw Hill, 1979.

[19] Gill, P., Murray, W., Pitfield, R., "The Implementation of Two Revised Quasi-Newton Algorithms for Unconstrained Optimization," National Physical Laboratory Rpt. NAC 11, April 1972.

[20] "Military Specification Flying Qualities of Piloted Airplanes (MIL-F-8785C)," Nov. 1980.

[21] White, S., "A Feasibility Design Study for an F-8 Oblique Wing Research Demonstrator - Final Report," Rockwell International NA-84-1135, July 1984.

[22] Tyler, J., "The Characteristics of Model Following Systems as Synthesized by Optimal Control," IEEE Transactions on Automatic Control, Vol. AC-9, Oct. 1964, pp. 485-498.

[23] Ly, U. "A Design Algorithm for Robust Low-Order Controllers", Stanford University, SUDAAR 536, Nov. 1982.

[24] Cooper, G., Harper, R., "The Use of Pilot Rating in the Evaluation of Aircraft Handling Qualities," NASA TN D-5153, April 1969.

[25] Golub, G., Nash, S., Van Loan, C., "A Hessunburg-Schur Method for the Problem $AX + XB = C$", IEEE Transactions on Automatic Control, Vol. AC-24, No. 6, Dec. 1979, pp. 909-913.

[26] Schweger, J., Sensburg, O., Berns, H., "Aeroelastic Problems and Structural Design

of a Tailless CFC Sailplane," 2nd International Symposium on Aeroelasticity in Structural Dynamics, 1985.

[27] Rutkowski, M., "Aeroelastic Stability Analysis of the AD-1 Manned Oblique-Wing Aircraft," *Journal of Aircraft*, Vol. 16, No. 6, June 1979, pp. 401-406.